UNIVERSITY OF LIVERPOOL

Highly Water Repellent Polymer-Nanoparticle Composite Coatings: Moving Towards Real World Applications

Rebekah Upton

January 2022

Declaration

I, Rebekah Upton, confirm that the work detailed within this PhD thesis is my own. I confirm that any information which has been sourced from within the literature has been referenced, and any work carried out by/in collaboration with others has been clearly stated.

Acknowledgements

Firstly, I would like to thank my supervisor, Dr Colin Crick, who gave me the opportunity to carry out my PhD, and embark on the journey of starting his research group. I greatly appreciate your continuous support throughout the entirety of my PhD, and everything that you have taught me/the opportunities you have provided over the last four years. I would also like to extend my thanks to the rest of the Crick group – Yasmin, Emma and Ravi – for their support and laughter; it has been a pleasure to work with you all. Additionally, I would like to thank my secondary supervisor, Dr Tom Hasell, who has provided constructive advice and guidance, while always inviting me on Hasell group nights out!

To everyone who has assisted me and helped me throughout my PhD – Zoe Manifold, Dr Marco Marcello, Dr Keith Arnold, Dr Matt Bilton, Dr Karl Dawson, Aleksandra Fedosyuk, Dr Mark Isaacs, Amy Lunt and Romy Dop – I can't thank you enough, as this thesis wouldn't have been complete without your contributions, which are greatly appreciated.

Finally, I would like to thank my family and friends, who have helped me every step of the way with their encouragement and support. To Mum, Dad, Nan, Tom and Milo, thank you for always supporting me throughout my degree and PhD. To Jess, Jess and Sophie, thank you for always being there through the ups and downs, and always being on hand to buy me a drink in the AJ and to put some Tina Turner on the duke box. To Amy, thank you for your continuous support and for making me laugh, even when times were challenging. I couldn't have done this without you all!

Abstract

Synthetic superhydrophobic materials are frequently inspired by those found in nature. Artificial surfaces have been heavily documented throughout the years, as many innovative fabrication routes have been reported within the literature, and a diverse range of materials have been employed; a broad overview of the field of superhydrophobic materials design will be discussed in chapter 1. Generally, highly water repellent materials display several inherent properties that are deemed to be commercially and industrially desirable. Yet, typically lack the level of resilience that would be required to commercially roll-out materials. Although there has been much diversity within this field, polymer-nanoparticle composites have received particular attention, for reasons addressed within the introductory chapter.

The research presented within this thesis, first details a novel design principle that can be used to systematically optimise highly water repellent materials that comprise a range of hydrophobic polymers (**chapter 2**). In doing so, the effects that component composition has on surface hydrophobicity, microstructure and resultant functionality (self-cleaning performance) are investigated, with the aid of confocal fluorescence microscopy and other standard imaging techniques. In further experimental work, routes of imparting resilience into coatings are explored, while applying the defined design principle throughout to ensure full materials optimisation. Firstly, the UV instability issues that surround superhydrophobic pigmented coatings that comprise photoactive nanoparticles, are tackled. Whereby, alternative pigments are investigated, and both polymeric and molecular composites are studied (**chapter 3**). Following this, the physical durability and underwater stability issues, associated with external superhydrophobic coatings, are simultaneously addressed (**chapter 4**). Here, the introduction of a high-strength additive and use of an alternative design approach is used as a combined tool, to demonstrate that mechanical strength and underwater plastron stability can be significantly enhanced. Finally, the closing experimental chapter investigates the use of more sustainable hydrophobic polymers, which comprise a natural organic crosslinker and waste by-product of the petrochemical industries, for their use as multi-functional superhydrophobic coatings (**chapter 5**).

Contents

Abbreviations

General Abbreviations

AACVD	Aerosol Assisted Chemical Vapour Deposition
AFM	Atomic Force Microscopy
BET	Brunauer-Emmett-Teller
CAH	Contact Angle Hysteresis
CFU	Colony Forming Units
CNF	Carbon Nanofiber
CVD	Chemical Vapour Deposition
DDS	Dimethyldiethoxysilane
DIDP	Diisodecyl Phthalate
DMF	Dimethylformamide
DSC	Differential Scanning Calorimetry
E_D	Net free energy change
EDX	Energy Dispersive X-ray Spectroscopy
E_g	Band Gap Energy
FAS	Fluoroalkylsilane
FIB	Focused Ion Beam
FITR	Fourier-Transform Infrared
HDPE	High Density Polyethylene
HMDS	Hexamethyldisilazane
LB	Lysogeny Broth
MIBK	Methylisobutylketone
MWCNTs	Multi-Wall Carbon Nanotubes
PDMS	Polydimethylsiloxane
PER	Perillyl Alcohol
PET	Polyethylene Terephthalate
PBS	Phosphate Buffered Saline
PMMA	Poly(methylmethacrylate)
PTFE	Polytetrafluoroethylene

PVA	Polyvinyl alcohol
PVC	Polyvinyl Chloride
PVDF	Polyvinylidene Difluoride
PXRD	Powder X-Ray Diffraction
Rz	Resazurin
SAM	Self-Assembled Monolayer
SEM	Scanning Electron Microscopy
SLIPS	Slippery Liquid-Infused Porous Surfaces
SPNC	Superhydrophobic Polymer-Nanoparticle Composite
S-TEM	Scanning Transmission Electron Microscopy
TA	Tilting Angle
TEM	Transmission Electron Microscopy
TEOS	Tetraethylorthosilicate
T_g	Glass Transition Temperature
THF	Tetrahydrofuran
TMES	Trimethylethoxysilane
TMS	Trimethylsilyl
XPS	X-ray Photoelectron Spectroscopy

Chemical Abbreviations

Al_2O_3	Aluminium Oxide
Ag	Silver
CeO_2	Cerium Oxide
CH_4	Tetrafluoromethane
$CHCl_3$	Chloroform
HCl	Hydrochloric Acid
MnO_2	Manganese oxide
NaOH	Sodium Hydroxide
SiO_2	Silicon Dioxide
S_8	Elemental Sulfur
TiO_2	Titanium Dioxide
ZnO	Zinc Oxide

Symbols and Equations

θ	Water contact angle
γ_{SV}	Solid-vapour interfacial tension
γ_{SL}	Solid-liquid interfacial tension
γ_{LV}	Liquid-vapour interfacial tension
θ_e	Equilibrium contact angle
θ_w	Wenzel contact angle
θ_A	Advancing contact angle
θ_D	Apparent contact angle
θ_R	Receding contact angle
θ_C	Critical contact angle
A	Adhesion tension
f_1	Area of solid-liquid interface
f_2	Area of liquid-vapour interface
ϕ_S	Solid-liquid fraction
$1\text{-}\phi_S$	Liquid-vapour fraction
r	Roughness factor
S_1	Force vector representing solid-vapour interface
S_{12}	Force vector representing solid-liquid interface
S_2	Surface tension of the liquid
$\mathbf{r}_{poly}$	Theoretical polymer thickness
$\mathbf{r}_{sphere}$	Average radius of the particle core
$\mathbf{r}_{poly+sphere}$	Average radius of the [particle core + polymer shell]
h^+	Hole
e^-	Electron
λ	Wavelength
E	Energy
P	Hydrostatic Pressure
ρ	Density
h	Height of cylinder

Constants

h	Planks constant (6.626×10^{-34} m^2kgs^{-1})
c	Speed of light (2.998×10^{8} ms^{-1})
J to eV	Conversion factor (6.242×10^{8})
g	Acceleration of gravity (9.81 ms^{-2})

Publications and Presentations

Publications:

Highly rough surface coatings via the ambient temperature deposition of thermosetting polymers. Y.A. Mehanna, R. L. Upton and C. R. Crick. *J. Mater. Chem. A*, 2019, **7**, 7333-7337.

A general formulation approach for the fabrication of water repellent materials: how composition can impact resilience and functionality. R. L. Upton, Z. Davies-Manifold, M. Marcello, K. Arnold and C. R. Crick. *Mol. Syst. Des. Eng.*, 2020, **5**, 477-483.

Pigmented self-cleaning coatings with enhanced UV resilience *via* the limitation of photocatalytic activity and its effects. R. L. Upton and C. R. Crick. *Mol. Syst. Des. Eng.*, 2020, **5**, 876-881.

The challenges, achievements and applications of submersible superhydrophobic materials. Y.A. Mehanna, E. Sadler, R. L. Upton, A. G. Kempchinsky, Y. Lu and C. R. Crick. *Chem. Soc. Rev.*, 2021, **50**, 6569-6612.

Carbon nanofiber/SiO_2 nanoparticle/HDPE composites as physically resilient and submersible water-repellent coatings on HDPE substrates. R. L. Upton, A. Fedosyuk, J. B. Edel and C. R. Crick. *ACS Appl. Nano Mater.*, 2021, **4**, 10090-10102.

Patent:

'Improvements Relating to Superhydrophobic Surfaces (Publication No. WO/2020/183149)', published 17/09/20. Inventors: C. R. Crick and R. L. Upton.

Oral Presentations:

Functional Nanomaterials Symposium (Berlin, 2019)

Lean Launch Programme Pitch (Belfast, 2019) – ICURe NorthByNorthwest

Poster Presentations:

Young Researchers Meeting (Dublin, 2018) – Macro Group UK

7th EuCheMS Chemistry Congress (Liverpool, 2018) – European Chemical Sciences

Chapter 1

Introduction

1.1 Thesis Overview

Water – the most abundant and essential molecule on planet earth. Although all ecosystems, including human life, rely on this simple molecule to survive, there are circumstances where repelling water becomes more practical. Whether that be in nature, where species have been able to adapt and use ingenious water repelling mechanisms to their advantage, e.g. plants who actively use falling rainwater to clean their external leaf surface, or insects, such as water striders, who showcase their ability to 'walk on water'.[1,2] Alternatively, it may be synthetic coatings, designed to improve our way of living by preventing water-related damage through integrating new functional properties into materials. Nonetheless, the development of highly water repellent materials is predicted to be crucial as we move towards the future.

The interaction of water with any surface is complex and can differ dramatically, owing to the unique chemical properties and geometric morphology of each individual surface.[3] This will be addressed in the introduction, alongside relevant routes to fabricating highly water repellent materials. This area of coating fabrication can be considered broad, as a diverse range of materials has been utilized (both synthetic and natural), some of which will be highlighted and discussed throughout this chapter.[4] Finally, the intrinsic properties exhibited by these surface coatings that have effectively driven all industrial and commercial interest into water repellent technologies, in particular self-cleaning (Lotus effect), will be explored as the introduction concludes.[5]

The durability and consequently the lifespan of superhydrophobic materials is an ongoing challenge. Although the same is true for naturally occurring water repelling surfaces, these often display inherent regenerative mechanisms that can restore superhydrophobicity in the event of any surface damage. As a result, any artificially designed commercial coatings that are currently on the market (e.g. NeverWet) can only be employed for short-medium term usage, before a reapplication is required.[6,7] This PhD research extensively examines how the composition of polymer-nanoparticle precursor formulations can heavily impact the resultant hydrophobicity, microstructure and functional properties of synthetic coatings (**chapter 2**). Furthermore, it details novel methods of enhancing the resilience of hydrophobic materials, with respect to both, UV stability (**chapter 3**) and generic durability (physical resilience and underwater stability, **chapter 4**) to increase the commercial viability by introducing possible long-term coating solutions. Before finally, investigating the use of alternative, more sustainable polymers for their prospective use in superhydrophobic coating design, and suspected superior functionalities (**chapter 5**).

1.2 Biomimetic Surfaces

Multi-scale surface roughness, combined with a low surface-energy material (see section 1.3) is key in generating surfaces that display extreme water repellency.[8] Nature has provided us with various intricate surface designs in the form of insects and plants, many of which show remarkable morphological features and regenerative mechanisms that are often too complex for scientists to accurately replicate.[9] Nonetheless, the discovery and long-term study of these topological designs has driven the artificial development of countless biomimetic materials.

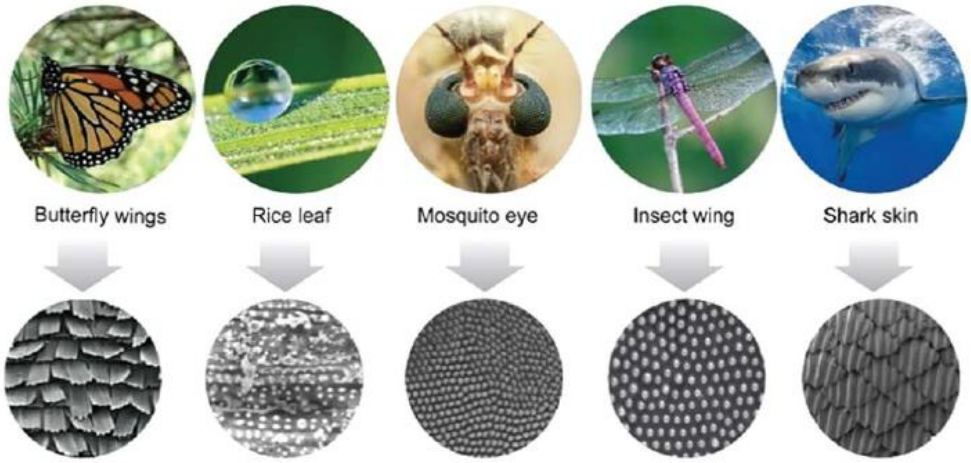

Figure 1.01: Examples of natural superhydrophobic surface designs and corresponding scanning electron microscopy (SEM) micrographs, highlighting morphological features. Figure taken from ref [10].

Several different approaches have been taken to replicate nature's designs, with various natural templates being studied (see Fig. 1.01). Some research groups have produced direct replicas, carried out with the use of moulding techniques (section 1.4.1.1.2), and others have fabricated structural replicas, built to resemble the unique morphologies using a range of innovative techniques.[10] An interesting biomimetic surface that has been reported widely in the literature is the 3D printed array of 'egg-beater' head structures, inspired by the *Salvinia molesta* leaves (see Fig. 1.02). The *Salvinia molesta* leaves have unique structural surface properties as the terminal cells, of the otherwise hydrophobic 'egg-beater' structures, lack wax crystals. Subsequently, this leads to high underwater stability. Hence, these surfaces have been mostly replicated for potential applications in the maritime sector (e.g. anti-fouling of ship hulls and drag/fuel reduction), that would require long-term underwater submersion of superhydrophobic coatings.[11–14] In a different approach, Liu *et al.* reported a replica moulding process, where they prepared biomimetic films based on shark skin. A polydimethylsiloxane

(PDMS)/silica (SiO_2) particle base was moulded from the skin, followed by hydrophobic treatment.[15] Coatings that displayed excellent self-cleaning and drag reducing properties – designed to target applications that required fluidic drag reduction – were attained.

Moving away from the laboratory, biomimetic designs have already found interest, commercially. In similar work to that reported above, Speedo engineered a full-body swimsuit in 2000 based on the micro-grooves (dermal denticles) on the surface of shark skin, to reduce viscous drag for Olympic swimmers.[16] For many years, natural surfaces and their biomimetic counterparts have inspired pioneering research from many different angles, in the hope that superhydrophobic coatings can be widely implemented as innovative technologies at the forefront of solving real-world problems.[17,10]

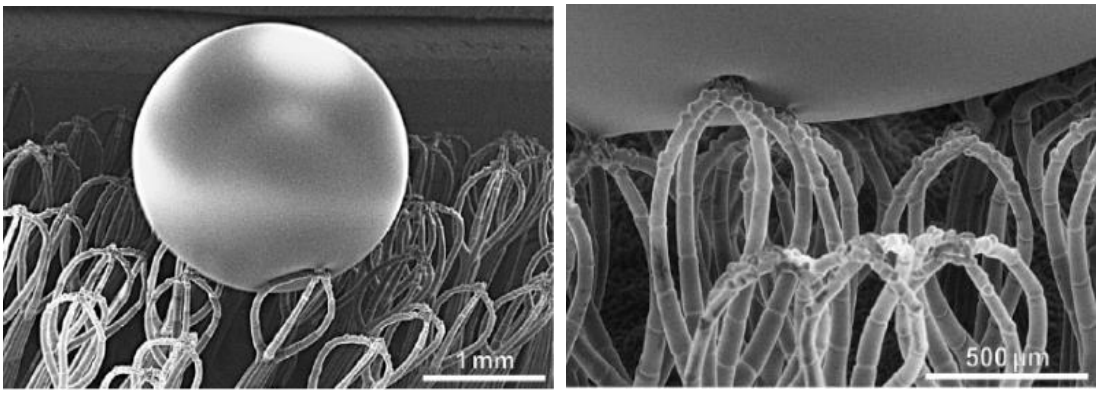

Figure 1.02: Low-temperature SEM micrograph of a *Salvinia molesta* leaf showing a droplet of a water-glycerol solution on the surface (**left**) and a higher magnification image highlighting droplet pinning to the terminal cells of the 'egg-beater' microstructures. Scale bars are shown. Figure taken from ref [13].

1.2.1 Lotus Effect

Arguably, the most well reported superhydrophobic surface is that of the Lotus leaf (*Nelumbo nucifera*). This natural surface is the origin of the term 'Lotus Effect', which is used to describe the superhydrophobic self-cleaning phenomenon.[2] Both microstructures and nano-sized features, encapsulated in a waxy leaf coating, can be seen on the surface of the Lotus leaf, and serve as a platform for generating hierarchical surface roughness (see Fig. 1.03).

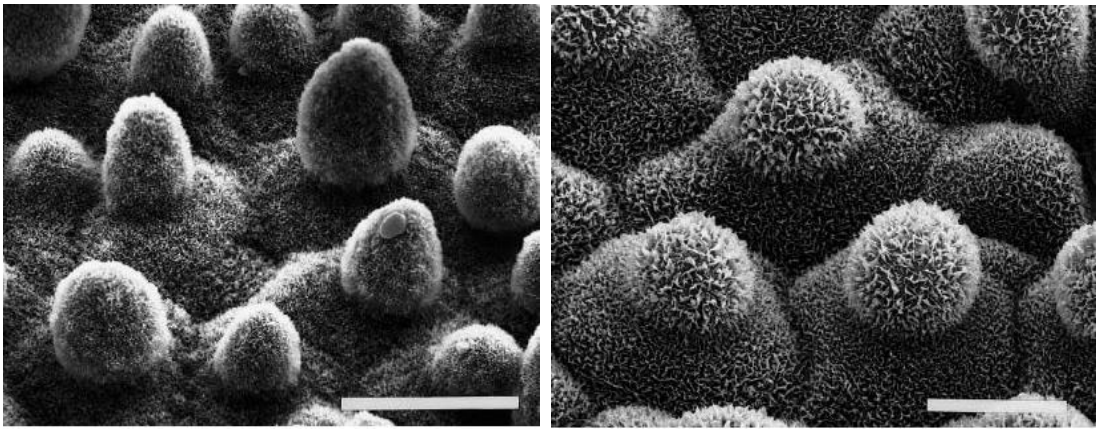

Figure 1.03: SEM micrographs, highlighting the hierarchical surface structure of the Lotus leaf at low magnification (**left**) and high magnification (**right**). Scale bar 20 µm. Figure taken from ref [2].

As falling rainwater encounters the surface of the leaf, it is coerced into near-spherical droplets that actively roll off the surface, transporting with them any unwanted surface-bound contaminants (e.g. dirt particulates and/or bacteria, see Fig. 1.04).[18] This phenomenon is only made possible by the low frictional adhesion of water to the surface, owed to the highly textured surface designs that many plant leaves possess. Self-cleaning mechanisms are considered to be one of the most desirable properties that are displayed by highly water repellent materials, which if integrated into existing technologies, could prove extremely useful. As a result, many synthetic self-cleaning coatings have been developed (examples outlined throughout sections 1.4 and 1.5; commercial coatings discussed in section 1.7).

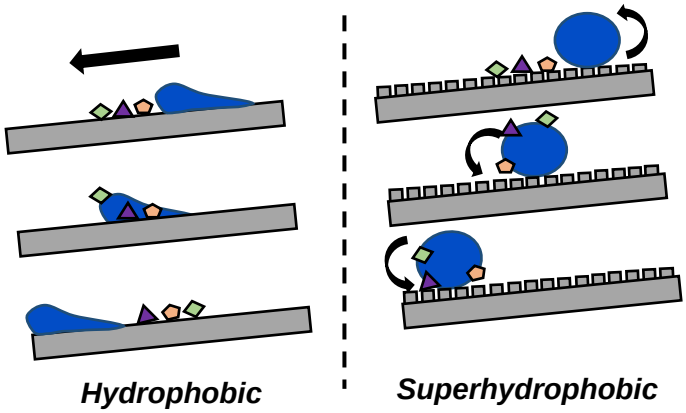

Figure 1.04: Illustration picturing the rolling motion of a water droplet across a superhydrophobic surface, removing any surface-bound contaminants (**right**), compared with that of a hydrophobic surface, where contaminants remain as water slides over them (**left**).

1.3 Wettability

The wettability of a surface is generally defined by its static water contact angle; the angle between the plane of the solid surface and the tangent of the liquid-vapour interface (θ). The contact angle is characteristic of the wetting behaviour of a solid, and can generally be used to categorise surface wettability. A favourable interaction with water places a material in the hydrophilic ($\theta < 90°$) or superhydrophilic ($\theta < 5°$) category, depending on the degree of water spreading across the surface. Whereas, materials which display limited interaction with water can be labelled as hydrophobic ($\theta > 90°$) or superhydrophobic ($\theta > 150°$), as seen in Figure 1.05.[19]

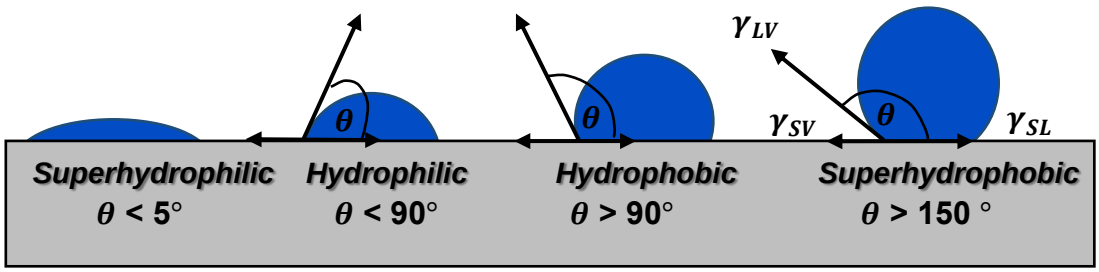

Figure 1.05: Illustration categorising surface wettability and the corresponding contact angle ranges.

Surface texture plays a crucial role when designing materials of extreme hydrophobicity, as surface chemistry alone cannot give rise to such surface properties.[20] Decker *et al*. reported that a planar surface modified with an array of $–CF_3$ groups displayed a maximum contact angle of 120°, in comparison to an array of $–CH_3$ groups, which displayed a contact angle of 111°.[21–23] Despite using a low surface energy material, contact angles that tend towards 180° cannot be attained; a low surface energy material refers to a solid where the energy difference between the bulk material and the surface is small, so that there is no driving force to create a new interface with water – reflected by Youngs equation, where the contact angle is seen to increase with a decreasing solid surface free energy. For example, regularly aligned hexagonal close-packed $-CF_3$ groups, owing to the low polarizability of fluorine. However, it is only when the surface area of the solid is enhanced (per unit area), that larger contact angles are observed.

1.3.1 Youngs Equation

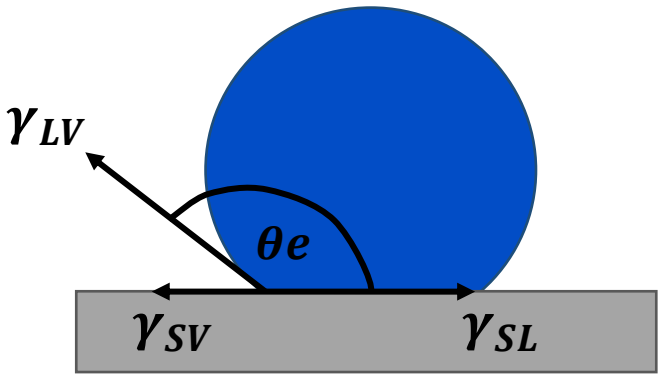

Figure 1.06: Illustration of Youngs model, detailing the equilibrium water contact angle (θe) and interfacial surface tensions (γ_{SV}, γ_{SL} and γ_{LV}) of a static water droplet on a flat surface, as seen in eqn 1.

The most straightforward wetting model that exists is based on an "idealised surface" i.e., flat and chemically homogenous. The contact angle, in this case, can be simply determined using Youngs equation (eqn 1, see Fig. 1.06):

$$\gamma_{SV} = \gamma_{SL} + \gamma_{LV} \cos\theta_e \quad \textbf{(1)}$$

Contact between the droplet and surface leads to the formation of a dynamic three-phase contact line, in which the three phases of the system co-exist. When the interfacial tensions of the three-phase boundaries [solid-vapour (γ_{SV}), which can also be described as the solid surface free energy), solid-liquid (γ_{SL}), and liquid-vapour (γ_{LV})] balance and reach a thermodynamic equilibrium – to achieve the lowest possible surface free energy – the equilibrium contact angle is determined (θ_e, eqn 2). If the material exhibits a hydrophobic wetting behaviour (low surface-energy material), the solid-liquid interfacial energy (per unit area) is greater than that of the solid surface free energy (per unit area), resulting in a non-wetting surface – as water spreading would be energetically unfavourable. Thus, water changes shape to minimise the surface area of the free liquid, and in doing so, limits the solid-liquid interfacial area. In the case of hydrophilic surfaces (high surface-energy material), the reverse is true and full surface wetting is observed, owed to the solid surface free energy (per surface area) exceeding that of the solid-liquid interfacial energy (per unit area).[24,25]

$$\cos\theta_e = \frac{\gamma_{SV} - \gamma_{SL}}{\gamma_{LV}} \quad \textbf{(2)}$$

1.3.2 Non-Ideal Surfaces

Youngs equation works under the premises of a 2D, flat surface model that is in a state of thermodynamic equilibrium. However, this is an idealized view which is almost certainly not valid when applied to real-life solids, as the interaction of water at different contact points on the surface is not accounted for (surface defects).[26] To elucidate this, two surface models were proposed to determine the realistic interaction of water with 'everyday' surfaces i.e., incorporating a roughness factor that accounts for surface non-homogeneity (see Fig. 1.07). Surface roughness is expressed as a ratio in both models, by what is referred to as the roughness factor, comparing the actual roughness to that of the geometric surface:[27, 28]

$$\text{Roughness factor } (\mathbf{r}): \frac{Actual\ surface}{Geometric\ projected\ surface} \qquad (\mathbf{3})$$

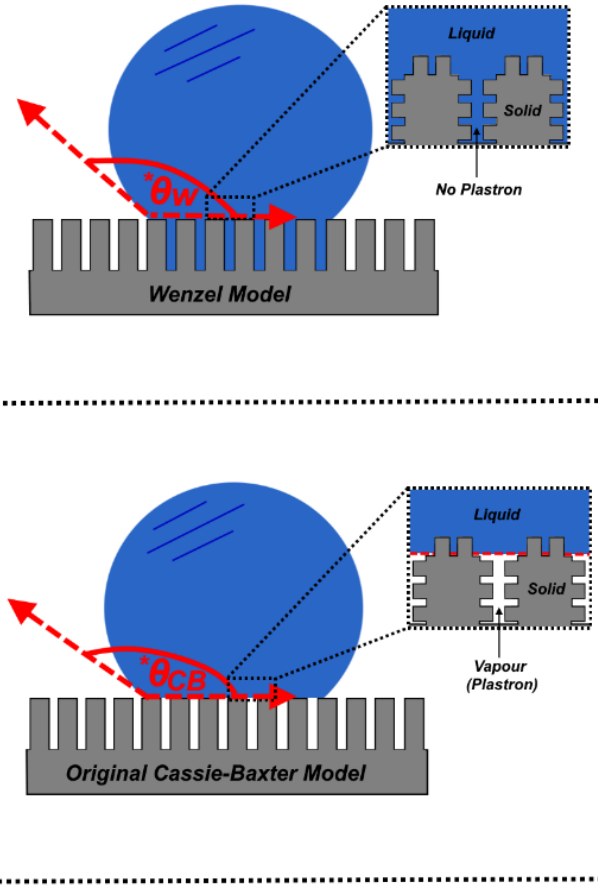

Figure 1.07: The interaction of water with a roughened solid surface as predicted in; the Wenzel model (**top**) and the Cassie-Baxter model (**bottom**).

1.3.2.1 Wenzel Wetting Model [28,29]

As previously discussed, wetting is generally determined by thermodynamic considerations. This model uses the net change in specific surface free energy content (per unit area) of the dry surface *vs* the wetted surface, to explain whether water will spontaneously spread or bead-up, upon contact with the surface. The extent of the net free energy change can also govern the rate at which water spreading will occur. When a surface is roughened, the area of the surface and therefore, the intensity of the total specific surface free energy, within a particular unit area, will increase with respect to the same unit area of the geometric (smooth) surface (see Fig. 1.08). An additional way to imagine this is that area **a-b-c-d** of the geometric surface has the same total specific surface free energy as area **e-f-g-h** of the roughened surface (see Fig. 1.09).

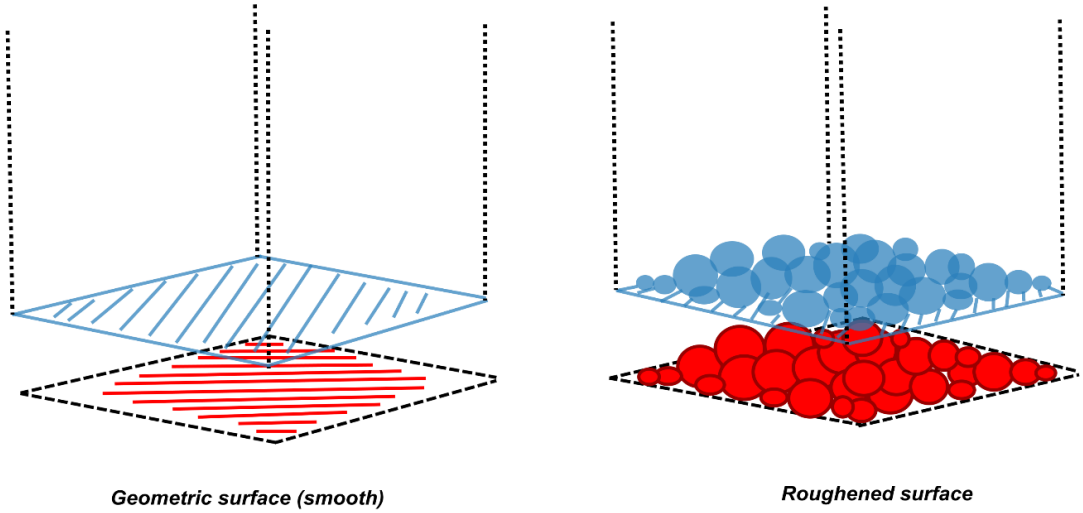

Figure 1.08: Illustration comparing the same unit area of the geometric (smooth, **left**) surface and the roughened surface (**right**). Roughening the surface has resulted in an increased volume of surface, and therefore, a corresponding intensification in specific surface free energy within that particular unit area.

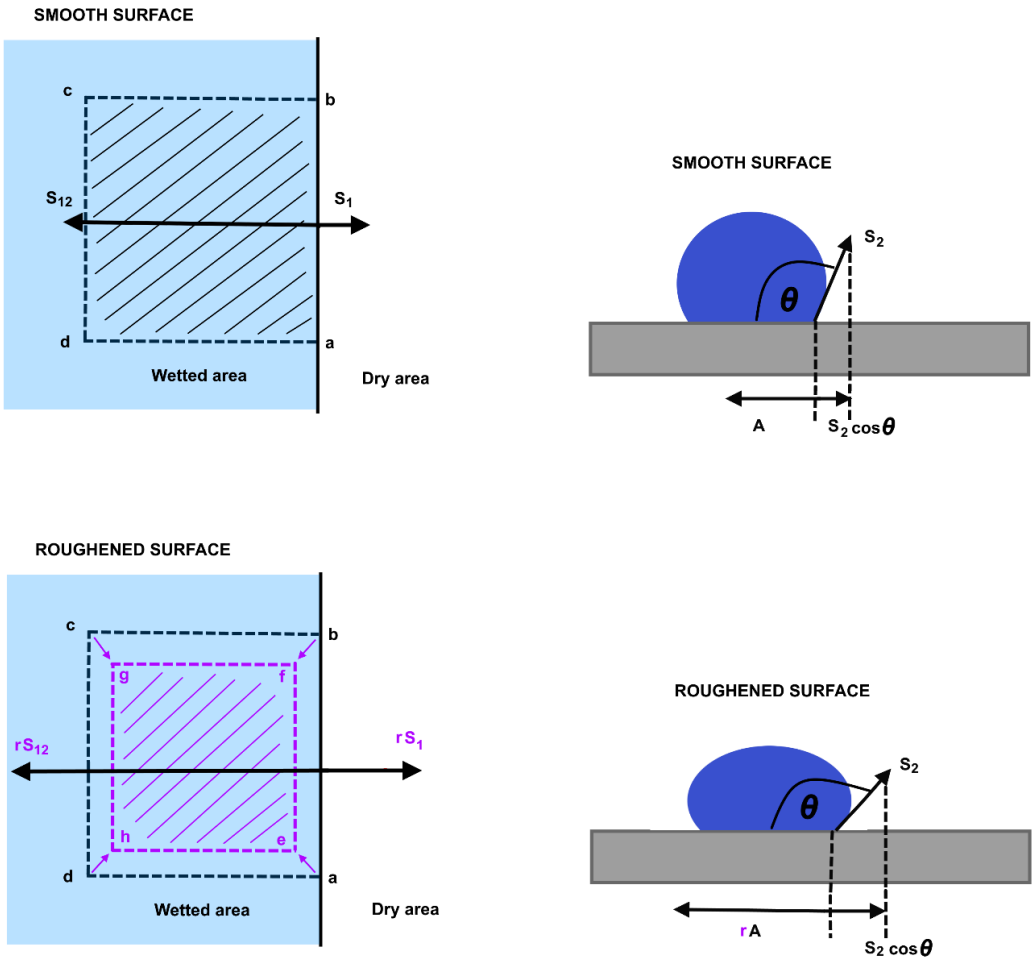

Figure 1.09: Illustration comparing how the surface force vectors act upon the same unit area **a-b-c-d** for a geometric hydrophobic surface (**top**) and a roughened hydrophobic surface (**bottom**). [29] The roughened surface has a greater total specific surface free energy within area **a-b-c-d**. Hence, when the roughened surface is wetted, an amplified net energy change occurs and a larger apparent contact angle is observed to counteract this. **e-f-g-h** represents the area of the roughened surface that has an equal specific surface free energy to area **a-b-c-d** of the geometric surface. S_1, S_2 and S_{12} represent force vectors (defined below in section 1.3.2.1), A represents the adhesion tension and **r** represents the roughness factor.[29]

The Wenzel model refers to a homogenous wetting system, whereby water retains full contact with the surface at all points beneath the droplet [see Fig. 1.07 (**top**)]. Therefore, the degree of surface roughening is directly relatable to the wetting characteristics of the solid. Although the specific surface free energy values themselves cannot change, the increased volume of surface within a particular unit area, will result in an intensified change in net energy upon formation of a new interface (solid-liquid, per unit area). The apparent contact angle can now be expressed as:

$$\cos\theta_w = \boldsymbol{r}\cos\theta_e \qquad \textbf{(4)}$$

where θ_w is the apparent Wenzel contact angle, **r** is the roughness factor (defined in Eqn 3) and θe is the equilibrium contact angle determined from Youngs equation.

Force vectors are used to describe the wetting characteristics of both smooth and roughened surfaces; S_1 is used to represent the dry area (solid-vapour interface) and S_{12} to represent the wetted area (solid-liquid interface) of a given unit length along the advancing boundary of the wetted surface (**a-b**). The difference between these force vectors is referred to as the adhesion tension (A). The adhesion tension will have a negative value if the surface opposes wetting, as the force acting upon the solid-liquid interface (S_{12}) will be greater, in order to minimize the solid-liquid interfacial area and prevent water spreading.

$$A = S_1\text{-}S_{12} \qquad \textbf{(5)}$$

Dependent on whether the surface has been roughened, the adhesion tension across a unit length of the advancing boundary (**a-b**) can be further expressed as:

$$A = S_2 \cos\theta_e \ (\textbf{\textit{smooth}}) \quad or \quad \textbf{\textit{r}}A = S_2 \cos\theta_e \ (\textbf{\textit{roughened}}) \quad \textbf{(6)}$$

The adhesion tension of a surface will be intensified if the surface has been roughened (forces must counteract the greater net free energy change of the roughened surface), reflected here by ***r****A* in Eqn 6. Therefore, for an inherently hydrophobic surface (θ_e > 90°), the adhesion tension will become more negative, in line with increasing surface roughness. As anticipated, the apparent contact angle increases as the adhesion tension becomes increasingly negative, confirming that superhydrophobicity can be attained when the respective surface is roughened – verified by subbing increasingly negative values into (r)A, using Eqn 7 below [considering the surface tension (S_2) is independent and remains as a constant value]. The opposite is said to be true for a hydrophilic surface, where the apparent contact angle tends towards 0°.

$$\theta_w = cos^{-1}\left(\frac{(r)A}{S_2}\right) \quad \textbf{(7)}$$

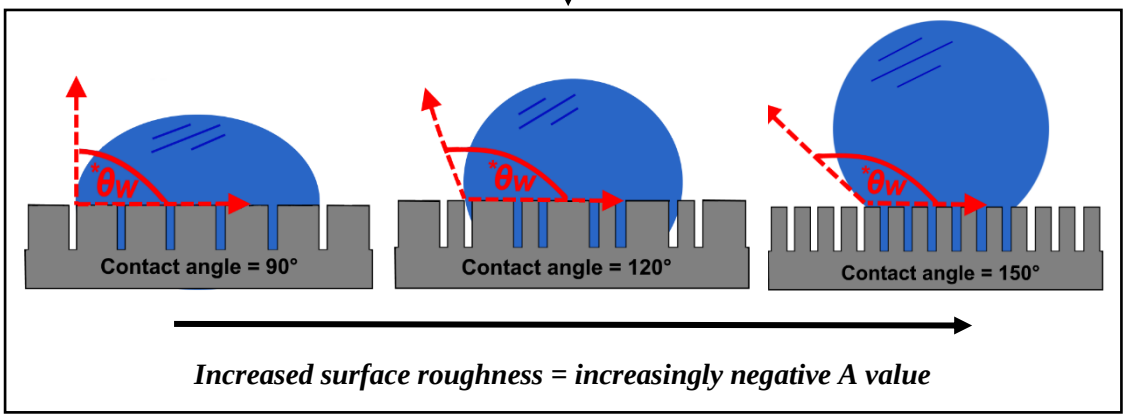

Figure 1.10: Illustration which highlights the increase in contact angle and hydrophobicity for a surface with Wenzel wetting, upon further roughening of the surface. As surface roughness becomes greater, the value of (r)A becomes increasingly more negative (adhesion tension is negative for an inherently hydrophobic surface), which when input into Eqn 7, results in larger values of θ_w.

1.3.2.2 Cassie-Baxter Wetting Model[30]

The second wetting model describes the interaction of water with porous surfaces. Free liquid bridges the tops of surface protrusions and makes contact with only a fraction of the solid surface as interfacial air, retained within the surface porosity, accounts for all other contact beneath the droplet. As a result, a new liquid-vapour interface is generated. In this model, interfacial areas and interfacial energies are used to describe the water repellency of a surface. Upon wetting, an area of the solid-vapour interface is destroyed and two new interfaces are created (solid-liquid and liquid-vapour), resulting in an overall net free energy change (E_D); for a non-wetting surface, replacement of the solid-vapour interface is energetically unfavourable. E_D, which will ultimately govern the extent of surface wetting – based on the specific interfacial free energies for any given surface – can be expressed as follows:

$$E_D = f_1 \gamma_{SL} - f_1 \gamma_{SV} + f_2 \gamma_{LV} \quad \textbf{(8)}$$

Furthermore, the contact angle of the advancing edge of the water droplet (θ_A) can be related to the interfacial surface energies using Youngs equation:

$$\cos\theta_A = \frac{\gamma_{SV}-\gamma_{SL}}{\gamma_{LV}} = \frac{-E}{\gamma_{LV}} \qquad \textbf{(9)}$$

where E is the energy required to form a geometrical unit area of the solid-liquid interface. If θ_A of a surface can be obtained, this value can be used to determine the interfacial areas, f_1 (solid-liquid interfacial area) and f_2 (liquid-vapour interfacial area, see Fig. 1.11). To derive the apparent contact angle of a porous surface, the following equation can be used:

$$\cos\theta_D = \frac{-E_D}{\gamma_{LV}} = f_1 \cos\theta_e - f_2 \qquad \textbf{(10)}$$

Where cos θ_D is the apparent contact angle and θe is the equilibrium contact angle, as defined earlier. If the surface has been roughened but has no porosity i.e., the liquid-vapour interfacial area is equal to zero, the second term (f_2) can be disregarded, and Eqn 10 is now said to equal Eqn 4. This directly relates to both wetting equations (Wenzel and Cassie-Baxter) as f_1 is assumed to be the solid-liquid interfacial area which corresponds to the roughness factor, **r**.

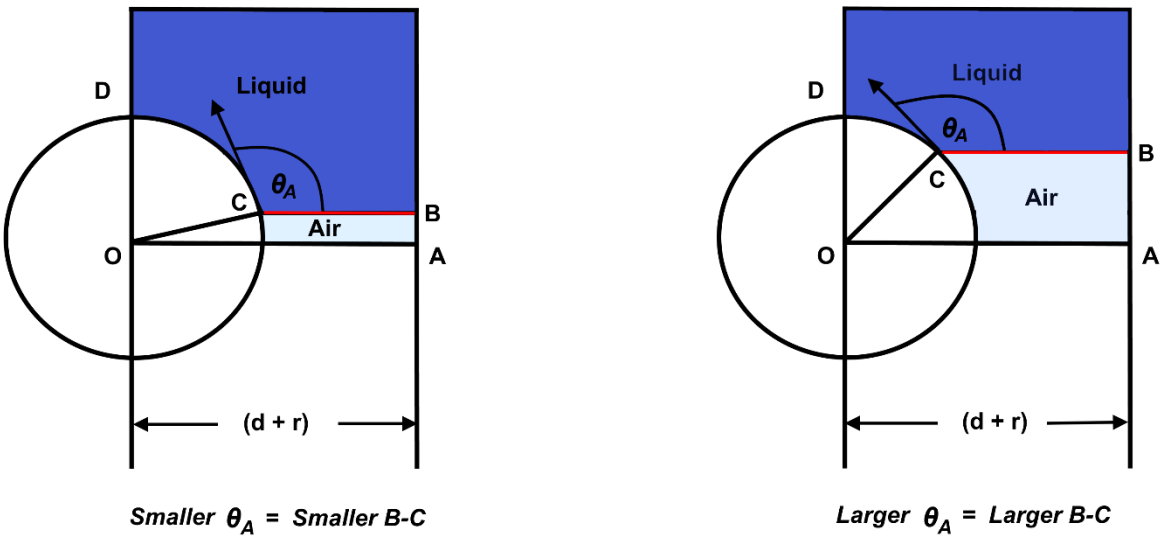

Figure 1.11: Illustration highlighting the repeating unit (O-A) of the cross-sectional area of a fibre (porous surface of repeating parallel fibres), presenting a smaller θ_A value (**left**) and a larger θ_A value (**right**). B-C is the liquid-vapour interface. From θ_A values, the interfacial areas (f_1 and f_2) may be derived.

The Cassie-Baxter equation can be further simplified by assuming the solid-liquid and liquid-vapour interfaces, in a unit of plane geometrical area parallel to the rough surface, to be co-planar i.e., the interfaces are considered to be flat (see Fig. 1.12).[31]

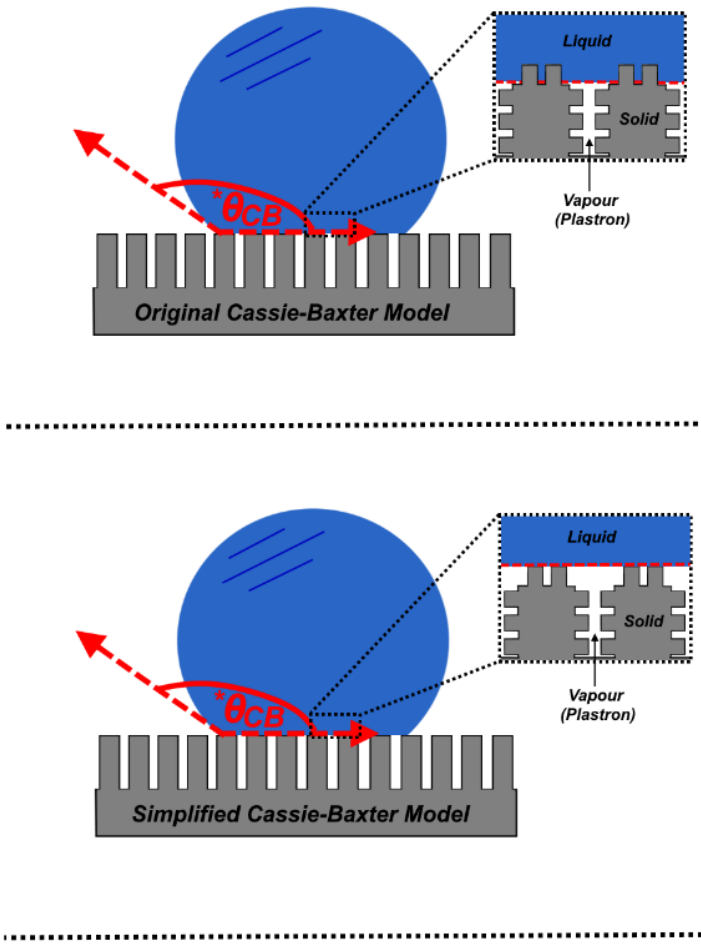

Figure 1.12: The interaction of water with a roughened solid surface as predicted by the original Cassie-Baxter model (**top**), whereby a roughness factor for the solid-liquid interface is included, and the simplified Cassie-Baxter model (**bottom**) which considers the solid-liquid interface to be flat.[31]

Hence, the sum of both fractional areas can then be said to equal 1:

$$\cos\theta_{CB} = f_1 \cos\theta_e + f_2 \cos\theta_{AIR} \qquad (f_1 + f_2 = 1) \qquad \textbf{(11)}$$

From this, we can assign fractional areas to f_1 (solid-liquid fraction, ϕ_S) and f_2 (liquid-vapour fraction, 1-ϕ_S), and compute the contact angle of air ($\cos\theta_{180} = -1$) to give the simplified equation:[32]

$$\cos\theta_{CB} = \phi_S \cos\theta_e + \phi_S - 1 \qquad \textbf{(12)}$$

The apparent contact angle can be seen to change with ϕ_S. For example, an interface structured from 5-10 % solid that displays an equilibrium contact angle of 110-120°, can yield a resultant contact angle of ~160-170°. As ϕ_S is increased, the apparent contact angle will become increasingly smaller, due to the reduction in the liquid-vapour interfacial area.[33] This model differs considerably from the Wenzel model, where any increase in the solid-liquid interfacial area results in an increased apparent contact angle.

1.3.3 Favoured States and Transitions

Although both wetting models (Wenzel and Cassie-Baxter) are good theoretical tools, it is possible that solids may not take on either wetting state in its exclusive form. In fact, wetting state transitions have been widely reported throughout the literature, easily differentiated by their inherent 'sticky or slippery' surfaces, as quoted by Quéré *et al*.[34] This alludes to the existence of metastable intermediate states, whereby retained air and partial wetting of microstructures can co-exist. Often, either the Wenzel or Cassie-Baxter state will be favoured, and can be anticipated by considering various factors. If a droplet is carefully deposited onto a surface from above, it will likely take on the Cassie-Baxter wetting state and bridge between surface microstructures. However, if a water droplet is condensed from the gas phase onto a surface, it has been reported to take the Wenzel wetting state, and pin strongly to features on the underlying substrate.[24] Lafuma *et al.* reported deposition *via* both of these methods; deposition from above yielded a contact angle of 164°, and deposition *via* condensation gave a contact angle of 141 ± 3°. Following this, they induced the direct transition between states by increasing the pressure exerted onto a droplet, positioned between two micro-structured substrates, by compressing it gradually with a micrometric screw (see Fig. 1.13). Initially, a plateau in contact angle could be observed, owing to the resistance from air pockets retained within the surface structure. As the pressure surged, the contact angle decreased indicating that the droplet began to sink into the surface microstructure, adopting a Wenzel wetting state. The final contact angle after the application of ~250 Pa was 145 ± 3°, aligning well with the initial contact angle observed for the condensed droplet.[35]

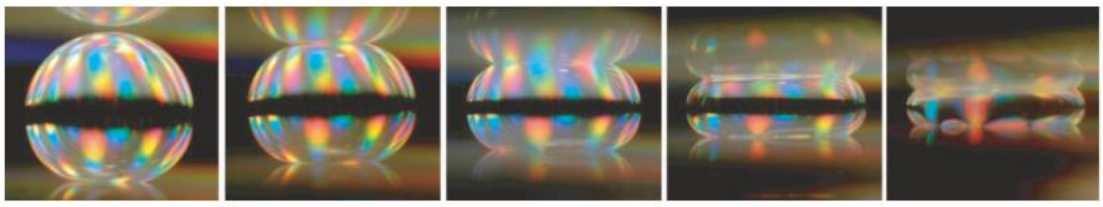

Figure 1.13: Visual images showing the compression of a water droplet between two identical substrates. Taken from ref [35].

Furthermore, the adopted wetting state and the rate at which the transitional state change may occur when an external stimulus is applied relies heavily upon the aspect ratio of surface microstructures (amongst other factors, e.g. droplet size).

Shirtcliffe *et al.* documented how the equilibrium contact angle of an epoxy-based photoresist (SU-8), patterned with evenly spaced 15 μm diameter circular pillars, ranging in aspect ratio up to 7, increased in line with increasing microstructure height. This was observed for SU-8 surfaces pre-treated with a fluorocarbon which reached a maximum contact angle of 145°, and also untreated surfaces (flat surface yielded a contact angle of 80°) that displayed a final contact angle of 143°. When the aspect ratio was ≥ 1, the apparent contact angle appeared to plateau for both surfaces.[36] Ultimately, surface roughness is essential when designing surfaces that adopt a Cassie-Baxter style of wetting, as surfaces that display diluted features (printed pillars or spikes, as mentioned above) often favour Wenzel wetting and display lower observed contact angles. This was reported by Quéré *et al.* who equated the critical contact angle (threshold between both states) to be $\cos \theta_C = (\phi_S - 1)/(r - \phi_s)$, and described how a heterogeneous wetting state would only be favoured for a highly roughened surface with a Youngs contact angle that exceeded the critical contact angle (conditions: $\theta_e > 90°$ for $r \rightarrow \infty$).[34] However, there is still much debate about whether a stable wetting state can be achieved and how transitions between states occur.

1.3.4 Contact Angle Hysteresis (CAH)

Throughout the introduction thus far, the idea of different wetting regimes being associated with either 'sticky or slippery' surfaces has been discussed. When a water droplet is deposited onto a 'real-life' surface (non-homogenous with surface defects), a singular equilibrium contact angle is not obtained. Instead, a range of stable contact angles that reside between the advancing (θ_A, highest) and receding (θ_R, lowest) contact angles are known to exist.[37] These can differ greatly for each surface, due to changes in topography and surface chemistries. The difference between the advancing and receding values of a static water droplet, resting on a tilting surface, is used to determine the CAH and estimate the force required to set the droplet into motion (see Fig. 1.14 and eqn 13). This can also be estimated more arbitrarily by assessing the tilting angle. Typically, for a Cassie-Baxter style surface, the tilting angle is below 10° and droplets can move freely across the surface.[38]

$$\text{CAH} = \theta_A - \theta_R \quad \textbf{(13)}$$

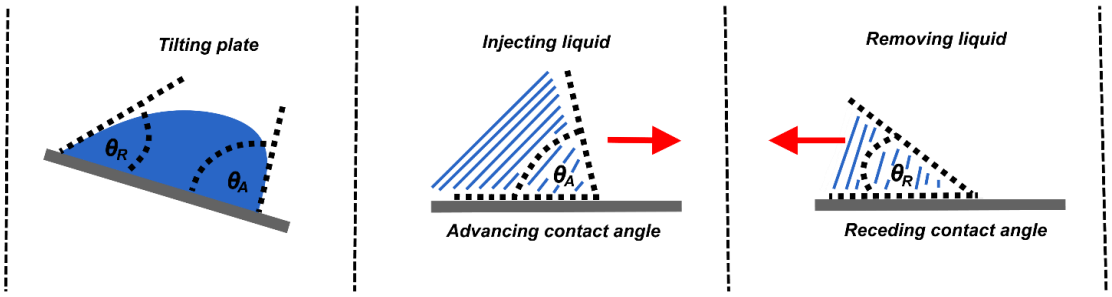

Figure 1.14: Two alternative methods of determining the advancing and receding contact angles; the tilting plate method (**left**) and injection/removal of liquid into/from a droplet (**middle/right**).

The tilting method is not the only commonly used technique to quantify CAH. The advancing contact angle can be determined by injecting liquid into a droplet resting on a horizontal surface and recording the angle at which the droplet sets into motion. Likewise, the receding contact angle can be determined by removing liquid from a droplet and observing the angle where the solid-liquid interfacial area begins to recede.[39,40] This can be thought of, simply, by using an absorbent (e.g. paper towel) to remove a droplet from a surface; if there is a very low CAH, the droplet is removed instantly. However, if the CAH is high, the volume of liquid can be seen to decrease, but attachment to the surface remains and the droplet will need to be blotted more than once.

1.4 Engineering Highly Water Repellent Surfaces

Highly water repellent materials have two fundamental requirements; hierarchical surface roughness and a low surface energy material, as seen and inspired by those found in nature (see section 1.2). Although a diverse range of fabrication techniques, used to induce micro- and nano-scale surface texturing have been reported in the literature, all techniques generally fall into two categories; (**i**) the removal of bulk material ('top-down' approach) or (**ii**) the addition of material ('bottom-up' approach), as seen in Figure 1.15.[41] Both approaches have the same consideration; whether hydrophobization or surface roughening is considered first. Low-surface energy and textured surfaces can be fabricated by either the direct roughening of a bulk hydrophobic material (e.g. hydrophobic polymer) or by the assembly of smaller hydrophobic building blocks (e.g. hydrophobic particles).[42] Alternatively, roughening of a hydrophilic material *via* either of the aforementioned methods (e.g. metal oxide, *via* either method), followed by post-treatment with a low surface-energy material, would result in the same outcome.[42] Both approaches have found equal success, and highlighted examples from the literature can be found in the following sections (sections 1.4.1 and 1.4.2).

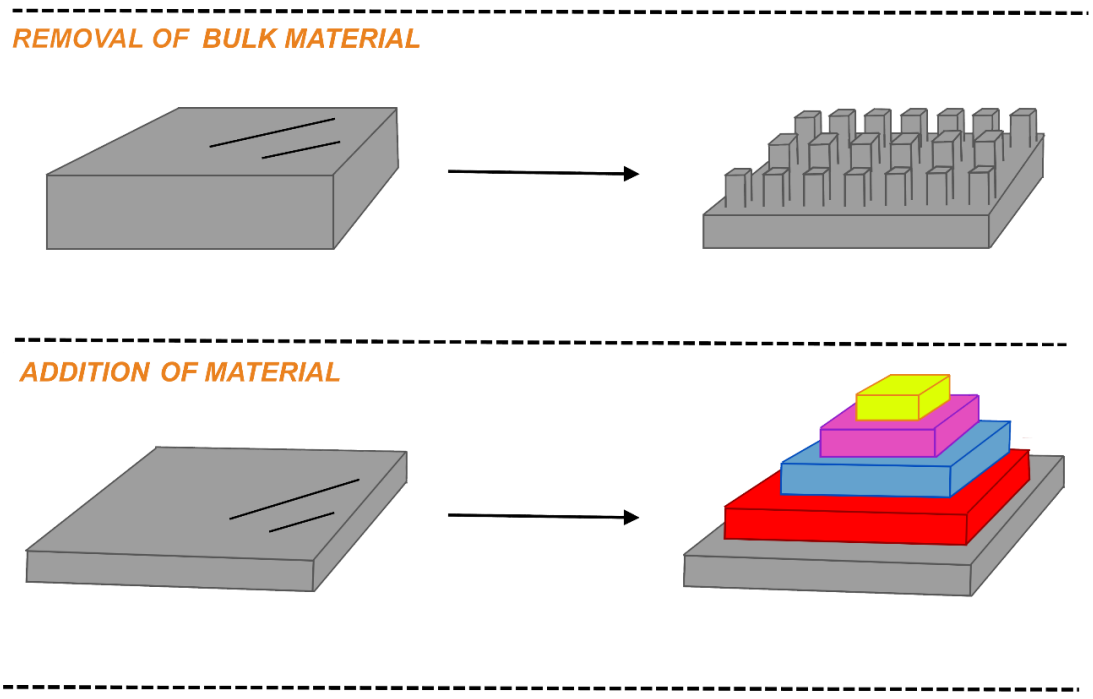

Figure 1.15: Illustration showing the two general fabrication approaches used to generate surface roughness, when fabricating highly water repellent materials; the 'top-down' approach (**top**) and the 'bottom-up' approach (**bottom**).

1.4.1 Removal of Bulk Material

The 'top-down' approach employs a bulk material and modifies it accordingly, to create well-defined arrays of surface features that give rise to precise structural designs, that are considerably more difficult to achieve when using most 'bottom-up' fabrication techniques. The removal of bulk material is often accomplished using methods, such as etching, machining and moulding; many fabrication techniques fall under this category, a summary of which are included within this section.

1.4.1.1 Lithography

Lithography is a widely established technique used to produce small-scale surface patterning on thin films and bulk substrates. This is often carried out by employing a master (patterned surface) and using its negative to create a replica, which can then be transferred to a chosen substrate material.[43] Lithography is a broad area of materials design and fabrication, and is a general term that covers different variations of lithographic techniques, depending on the method being employed to induce substrate patterning. The primary techniques used, will be briefly discussed below.

1.4.1.1.1 Photolithography

Generally, the most common form is photolithography, which is a long-established process and involves the use of UV radiation, to transfer a geometric pattern from an optical mask to a substrate that has been previously coated with a thin layer of light-sensitive photoresist. As a result, specific areas of the substrate are exposed and susceptible to modification, typically *via* a series of chemical treatments or etching.[43,4] Dependent on the substrate, post-treatment with a surface modifier is often required to generate superhydrophobicity.[44,45] Öner and McCarthy prepared a series of silicon surfaces with hexagonally arrayed square posts, varying in size (from 2 μm x 2 μm to 128 μm x 128 μm) and height (20-140 μm), in addition to designing arrays of rhombus-shaped posts, indented square shape posts and four-point star-shaped posts (see Fig. 1.16).[44] A vast range of surface architectures with defined shapes and dimensions were possible here with the use of different masks and etching times. Post-treatment with different silanization reagents (dimethyldichlorosilane, *n*-octyldimethylchlorosilane or heptadecafluoro-1,1,2,2-tetrahydrodecyldimethylchlorosilane) was carried out to generate surface hydrophobicity.

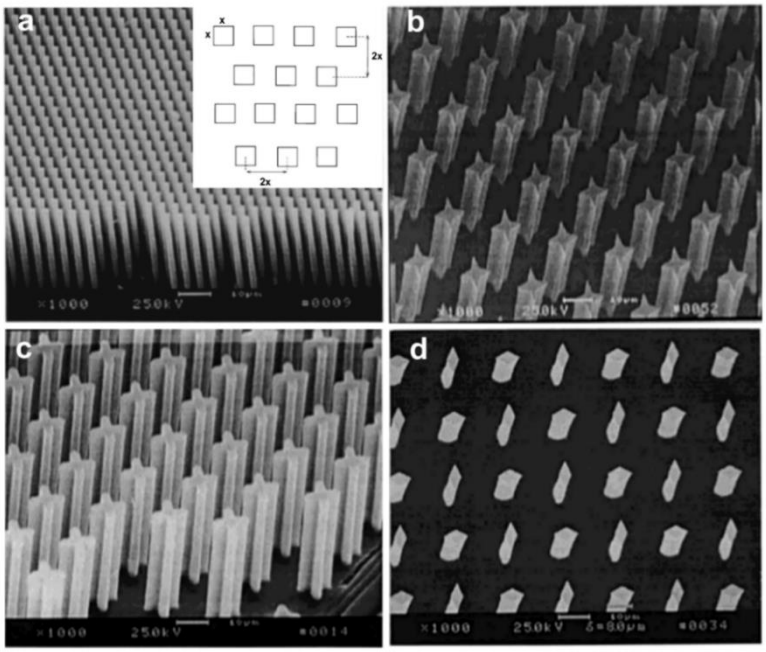

Figure 1.16: SEM micrographs of a series of differently shaped silicon surface arrays; (**a**) square posts 2 μm x 2 μm x 100 μm (inset; 2-dimensional representation of the series of silicon surfaces); (**b**) four-armed star-shaped posts; (**c**) indented square posts; and (**d**) staggered rhombus posts. Figures taken from ref.[44]

1.4.1.1.2 Soft Lithography

In contrast, techniques enabling the direct transfer of natural surface designs, *via* the process of moulding a soft material (e.g. PDMS), are also widely employed; termed soft lithography.[46] Soft lithography has been used on various natural templates, including; the lotus-leaf, mosquito compound eyes, the rice leaf etc., and is an inexpensive and simplistic technique that facilitates biomimetic surface designs.[47–49] Chen *et al.* developed superhydrophobic biomimetic wood surfaces with integrated functional properties that were directly replicated from taro leaves with the use of a silicone elastomer mould (PDMS with a fluorinated coating to lower the surface-energy and avoid sticking).[46] The primary replica served as a stamp to modify the surface morphology of PDMS/Fe_3O_4 nanoparticle-coated wood, by casting the negative impression of the leaf (see Fig. 1.17). The resultant coatings yielded a water contact angle of 152 $\pm$ 2°, and were shown to also repel other common liquids (food/beverage-related).

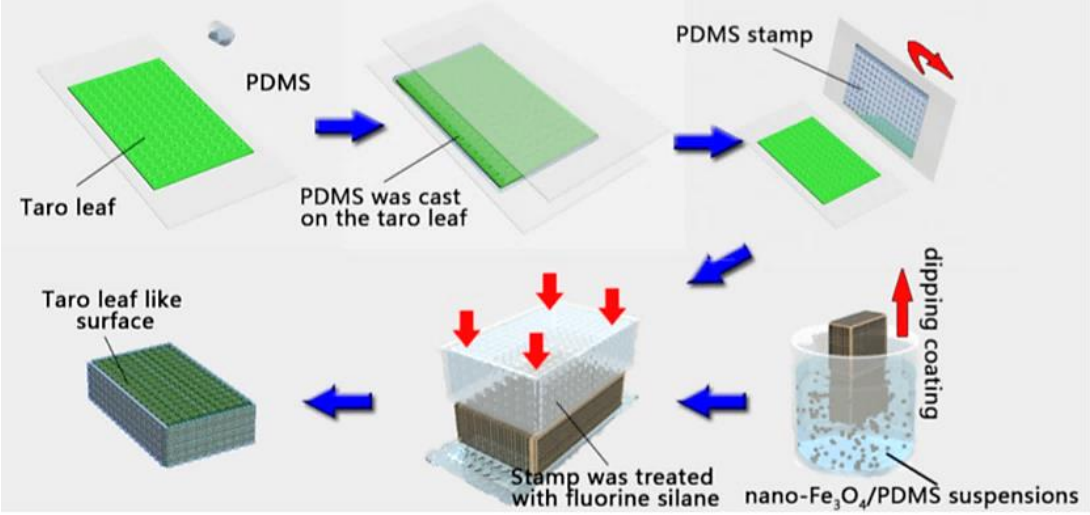

Figure 1.17: Fabrication process of superhydrophobic PDMS/Fe_3O_4-coated wood surfaces, using a PDMS first-time replica stamp to transfer the negative impression of a taro leaf onto the surface (soft lithography). Figure taken from ref.[46]

1.4.1.1.3 Nanoimprinting

A more recently discovered form of lithography is nanoimprinting, first reported in 1996 by Chou *et al*.[50] Upon its discovery, Chou *et al.* reported a synergistic compression moulding and etching process to transfer a pattern into a thermoplastic polymer *via* mechanical deformation, using a silicon/SiO_2 mould. A temperature is used which exceeds the glass transition temperature (T_g) of the polymer i.e., the temperature at which a polymer changes from a glassy state to a rubbery state (see section 5.3.1.1 for further definition). The use of rigid materials gave rise to extremely high-resolution features that were reported to reach sub-50 nm, which is typically quite challenging when using conventional lithographic techniques. This process was termed hard-mould nanoimprinting lithography.[51,50] Furthermore, overlap with soft lithography has been introduced, and soft-mould nanoimprinting lithography has also been established to address problems often associated with the use of a hard mould (defect control of the mould, wearing and breakage of mould etc.).[52] Structures of high complexity have been reported, as intricate nano-patterns (cone, pillar, hole and line shapes) have been etched into larger microstructures, as seen in Figure 1.18, where a silicon master mould was employed to produce polyvinyl alcohol (PVA) replica moulds.[53] Excellent design control was demonstrated

here, however, one restriction is that components must be compatible with the moulding process, potentially limiting material selection.

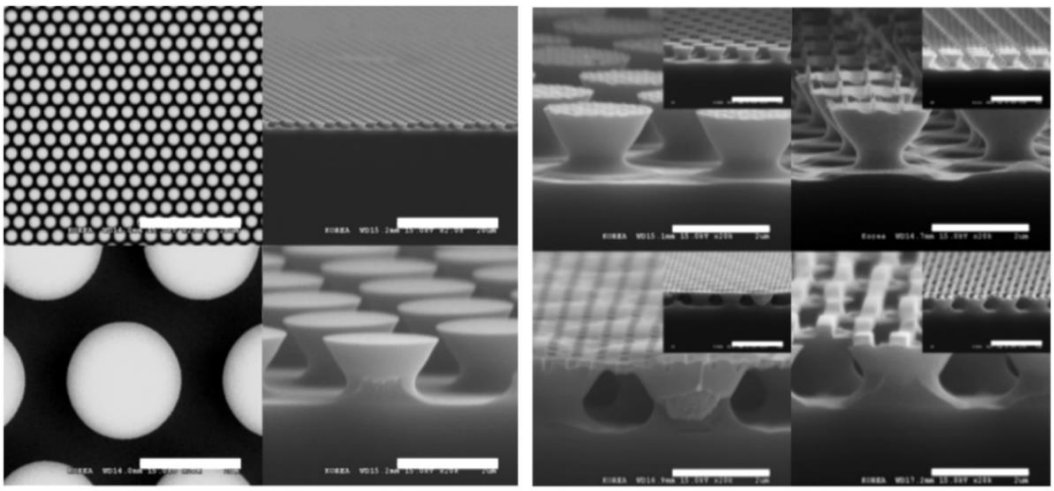

Figure 1:18: SEM micrographs showing overhang microstructure at low magnification (scale bar 20 μm) and high magnification (scale bar 2 μm), (**left**). SEM micrographs of nano-patterned overhang structures [cone (**top left**), pillar (**top right**), hole (**bottom left**) and line (**bottom right**) shaped] with a scale bar of 5 μm. Figures taken from ref.[53]

1.4.1.2 Etching

Many variations of etching techniques exist, that have been implemented independently or in combination with other fabrication approaches to generate hierarchical surface texturing. Generally, etching results in the removal of surface material through either isotopic etching i.e., uniform etching in all directions (chemical/electrochemical reactions) or anisotropic etching i.e., uniform etching in a specific direction (possible *via* plasma etching).[54]

1.4.1.2.1 Chemical Etching

Chemical etching is considered to be a facile, low-cost procedure that generally uses strong acidic or basic solutions to perform a series of redox reactions, resulting in the removal of substrate material – typically, the oxidation of the substrate material, followed by the dissolution of the oxidized material.[55] This type of etching has been primarily implemented for texturing metallic substrates which are often more susceptible to selective etching, due to lattice structure irregularities.[56] Lomga *et al.* outlined how durable superhydrophobic aluminium surfaces with self-cleaning/anti-fogging properties could be obtained by simply placing aluminium substrates into an etchant solution of aqueous sodium hydroxide (NaOH), and carefully controlling parameters such as, etchant concentration and etching time.[57]

Textured aluminium substrates were obtained, confirmed by atomic force microscopy (AFM) and SEM, that were then functionalised in an ethanolic solution of lauric acid (a long chain hydrocarbon, see Fig. 1.19). The untreated aluminium substrate displayed a contact angle of 70.6°, which increased significantly, in line with hydrophobicity, to 168.2° after 180 minutes of immersion in NaOH solution (5 g/L). Etching initiated the process of pitting, promoting the trapping of air at the surface, and therefore, resulting in Cassie-Baxter wetting. Although chemical etching is a convenient technique with substantial benefits, there are drawbacks associated with this procedure; a large volume of chemicals are required to maintain consistent etching rates (not eco-friendly) and process control is limited. Therefore, alternative dry etching technologies of higher precision have been established.

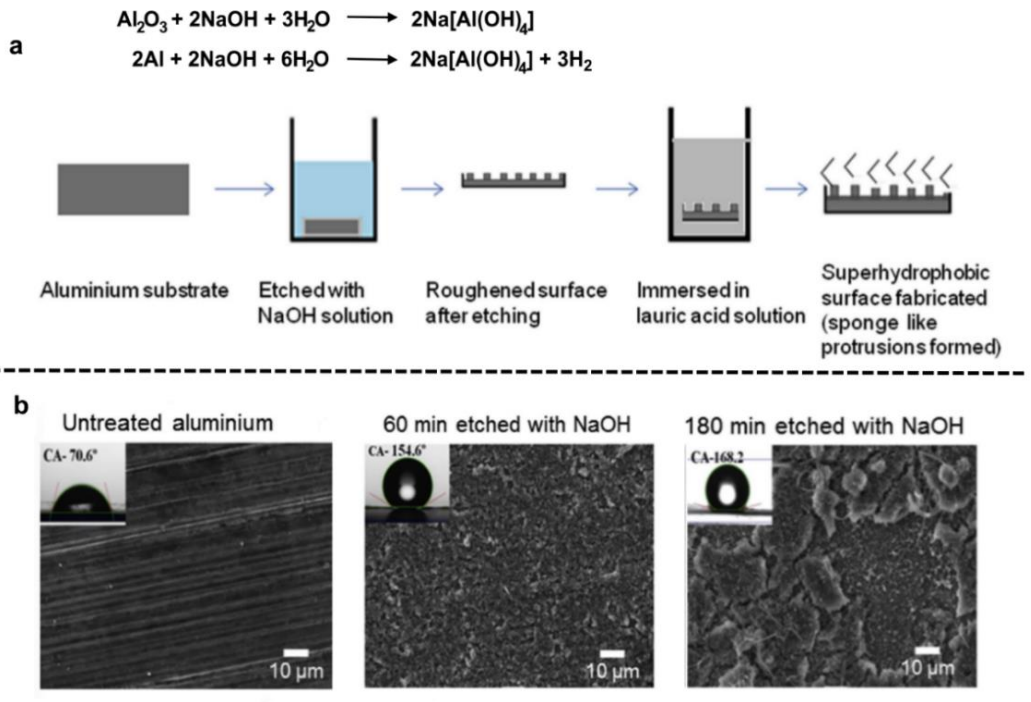

Figure 1.19: (a) Illustration outlining the chemical etching process of aluminium substrates in NaOH (chemical equations included), followed by post functionalisation with lauric acid. **(b)** SEM micrographs showing the incremental change in surface morphology and corresponding contact angles of aluminium substrates in a NaOH etchant solution of 5 g/L concentration at different etching times. Scale bars are shown. Figures taken from ref.[57]

1.4.1.2.2 Plasma Etching

Plasma is an ionised gas that is produced when high energy is supplied to a neutral gas, resulting in charged ions and electrons, and has been frequently implemented in dry etching technologies. Plasma etching is based on the selective erosion of material by combining the

bombardment of ions (sputtering) with the presence of reactive species that can selectively attack surface material. Where applicable, an optical mask may be applied to the substrate to facilitate micro- and nano-patterning.[58,59] Hou *et al.* designed micro-cubic arrays on silicon surfaces with the use of plasma etching, followed by fluorination with an ethanolic solution of fluoroalkylsilane (FAS) to achieve superhydrophobicity and ant-icing properties.[60] A SU-8 photoresist was first applied to the substrate, followed by a photomask which was used to transfer a geometric pattern onto the substrate. Plasma was used to etch the substrate material, resulting in coatings that displayed water contact angles approaching 154.2°.

Direct plasma etching of polymers has also been largely reported in the literature, more specifically the etching of low surface-energy polymers that then require no hydrophobic post-treatments, e.g. fluorinated polymer polytetrafluoroethylene (PTFE – better known as Teflon®, see Fig. 1.20).[61,62] PTFE displays several desirable characteristics, including high chemical stability, strong water repellency and a non-stick nature, due to the low polarizability of C-F bonds, making it ideal for robust superhydrophobic materials. Additionally, PTFE has been successfully etched by various types of plasma, for example, argon, tetrafluoromethane (CF_4), nitrogen and oxygen, as reported by Takahashi *et al*., who compared topographical changes of a PFTE surface as plasma etching rates were investigated (see Fig. 1.21).[63] Plasma etching has been incredibly successful in generating materials that display extreme superhydrophobicity. Nonetheless, plasma is not always employed exclusively for etching, in particular CF_4 plasma, which has been reported to synergistically etch a material, while lowering the overall surface-energy by increasing the fluorine content of the surface.[64]

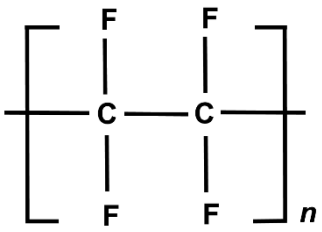

Figure 1.20: Chemical structure of PTFE repeating unit.

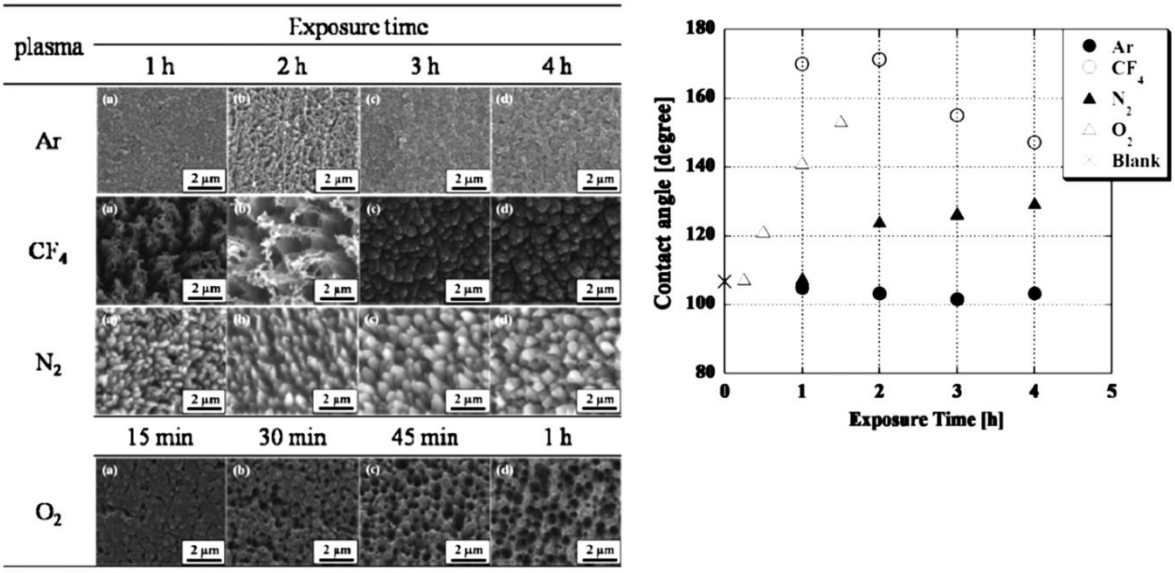

Figure 1.21: SEM micrographs picturing the change in PTFE surface structure as four different types of plasma were employed and the exposure time was varied (**left**). A graph to show the change in hydrophobicity with plasma exposure time (**right**). Figures taken from ref.[63]

1.4.1.3 3D Printing

The possibilities for sculpturing different surface features are infinite, even down to the nano-scale, as seen in section 1.4.1.1. 3D printing employs a layer-by-layer design process to deposit material and build intricate structures, so therefore, is technically categorised as a 'bottom-up' technique.[65] However, as this technique is often utilized to fabricate organised 3D arrays – similar to 'top-down' techniques (as seen above) – it has been discussed within this section. Different printing processes have been developed, some of which have been reported as methods for designing superhydrophobic materials. Simple patterned structures, such as porous PDMS meshes, built from extruded filaments of PDMS', have been developed.[66] Furthermore, 3D printing is often regarded as one of the best techniques for generating surface features of the highest intricacy – designs that are likely not achievable using conventional fabrication techniques. Arguably one of the most complex examples of 3D printed structures, designed specifically to exhibit superhydrophobicity, are those that mimic the 'egg-beater' structures present on the *Salvinia molesta* leaves, as briefly discussed in section 1.2. Yang *et al.* used a novel printing process to tailor a photocurable resin (E-glass), infiltrated with multi-wall carbon nanotubes (MWCNTs, for enhanced structural stability and surface roughness), into the unusual 'egg-beater' structures. Interestingly, a hydrophilic composite was used (contact angle of 65° on a flat surface), and yet contact angles as high as 170° were attained.[12] Although, materials were seen to have high tilting angles, which was desirable in this case.

High surface superhydrophobicity was speculated to be directly related to the limited contact area between the water droplet and the substrate, and thus, the entrapment of air between surface microstructures. This was late reflected by a decrease in contact angle, upon reducing the number of arms of each 'egg-beater' (N value, see Fig. 1.22).

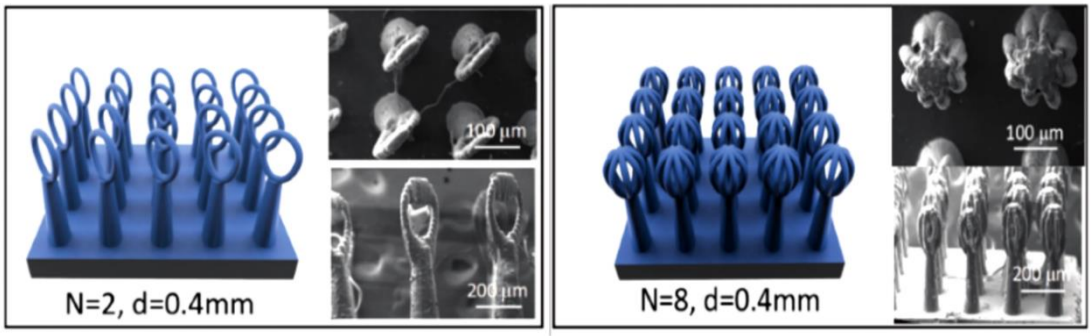

Figure 1.22: 'Egg-beater' arrays with corresponding SEM micrographs (side-on and top-down), highlighting the morphological differences between structures with varying numbers of arms (N); 2 arms (**left**) and 8 arms (**right**). In both arrays, structures were 0.4 mm distance apart. Scale bars are shown. Figures taken from ref.[12]

The common factor that relates 3D printed materials – whether the design is simplistic or complex – is that independent printing in the absence of other technologies, can only result in microstructures, due to the limitations in printing resolution.[67] As a result, printed materials that comprise nano-scale surface roughness, are challenging to obtain. Innovative methods to overcome this have been reported, for example; Lv *et al.* introduced hydrophobic nano-SiO_2 into a PDMS ink before printing and Zhang *et al*. employed PTFE particles in a precursor matrix, followed by sintering to fuse particles and achieve nano-scale surface roughness.[68,69] Nonetheless, printing resolution is the primary challenge associated with the 3D printing of superhydrophobic materials and poses many limitations on what design architectures can be achieved.

1.4.2 Addition of Material

As seen in the above sections, 'top-down' methods typically involve the generation of periodic arrays of surface structures with set dimensions (pillars, spikes, etc.). This can be advantageous for speciality applications that require precise architectural designs, but often result in relatively diluted surface features. As previously mentioned, (see section 1.3.3), Quéré *et al.* stated that in order to generate materials of extreme superhydrophobicity, surface roughness is crucial to minimize the solid-liquid interfacial area; 'bottom-up' techniques often refer to the deposition of nanomaterials in a disorganized manner, hence, generating nano-

scale surface texturing. For this reason, 'bottom-up' fabrication approaches are often more suitable and successful in fabricating highly water repellent materials that display stable Cassie-Baxter wetting states, reflected by their greater apparent contact angles/lower tilting (see Fig. 1.23).[70]

Figure 1.23: Static water droplet with a reported water contact angle of 178°. Figure taken from ref.[70]

1.4.2.1 Electrospinning

Electrospinning has been implemented widely as a relatively simple, yet versatile, technique used to produce synthetic filaments (sub-micron scale) and induce hierarchical surface texturing. By applying a strong electric field to charge liquid droplets that are protruding from the narrow tip of a small needle, the charged liquid is ejected, during which the solvent evaporation/solidification processes – induced by whipping instability – results in the formation of solid threads.[71]

The feed is typically a polymer solution or polymer melt, due to the desirable properties these often display (e.g. high chemical resistance, high mechanical strength etc.).[72] Current research has documented the use of various polymeric materials, e.g. polystyrene dissolved in dimethylformamide (DMF) for use as oil-water separation membranes, hybrid polymers (PDMS and polymethylmethacrylate) dissolved in a mixed solvent system of tetrahydrofuran (THF) and DMF to generate distillation membranes, melted polypropylene pellets for applications in protective clothing and so on, highlighting the versatility of the process.[73–75] However, the process is not limited to polymers, additives can be introduced to further elevate surface roughness. Liu *et al*. outlined the production of superhydrophobic membranes generated from electrospun polyvinylidene difluoride (PVDF)/zinc oxide (ZnO) nanoparticle precursors, with the addition of a silanization reagent to further lower the surface-energy of membranes.[76] The introduction of a roughening agent led to an enlargement in average fibre diameter (consequential of the increased viscosity of precursor suspensions), and increased the texturing of individual fibres (see Fig. 1.24). Ultimately, this resulted in enhanced superhydrophobicity, where an increase in contact angle from 146 $\pm$ 1° to 171 $\pm$ 5° was observed at an optimal ZnO loading of 8 wt %, respectively.

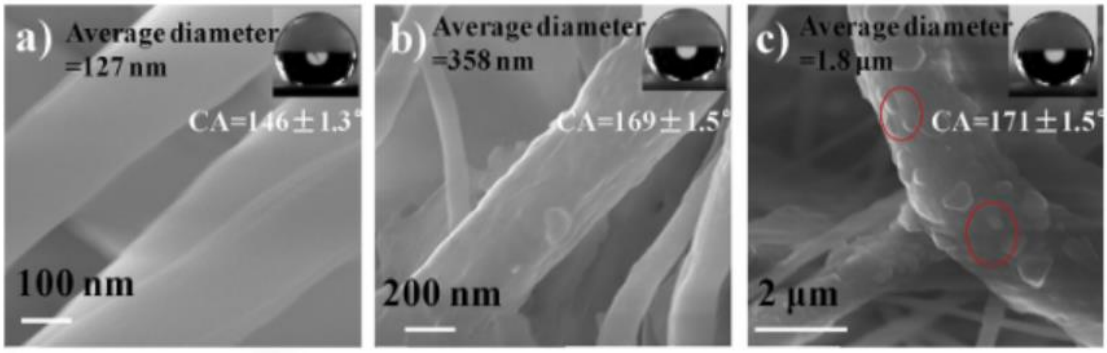

Figure 1.24: SEM micrographs highlighting the change in surface morphology of electrospun fibres from (**a**) pure PVDF to (**b**) the addition of 5 wt % ZnO and (**c**) the addition of 10 wt % ZnO. Corresponding contact angles and fibre diameters are displayed. Scale bars are shown. Figures taken from ref.[76]

1.4.2.2 Chemical Vapour Deposition (CVD)

The process of CVD involves the formation of a solid film, resulting from the deposition of compounds from the vapour phase.[77] Briefly, vaporised reactants are supplied and transported throughout the deposition rig, generally *via* a pressure imbalance or carrier gas, where they are deposited onto a surface, before chemically reacting to form a solid film. Unwanted reaction products remain in the gaseous phase as they are removed from the system.[78] A range of CVD methods have been developed, using different activation techniques and processes (thermal for conventional CVD, plasma-enhanced, photo-assisted etc.).[79] A technique largely reported for its use in depositing superhydrophobic thin films, is aerosol assisted CVD (AACVD), where a precursor aerosol containing the reactants is generated (see Fig. 1.25). Subsequently, reactants no longer need to be volatile, only soluble in the chosen solvent used to formulate aerosol droplets. Hence, significantly expanding the range of precursor molecules that can be used.[80] Although, solubility limitations can still prevent the use of some species.

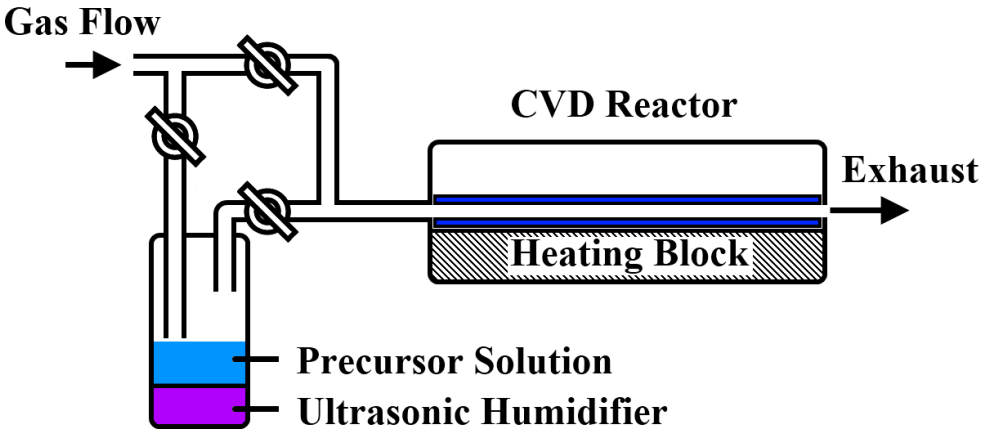

Figure 1.25: Schematic representation of a typical AACVD deposition rig, using an ultrasonic humidifier to generate a precursor aerosol, and nitrogen carrier gas to transport aerosol droplets through the rig, for chemical reaction/deposition onto the substrate. Any unwanted vaporised molecules are removed *via* the exhaust. Figure taken from ref.

Crick *et al*. have contributed significantly in this field of superhydrophobic materials development, reporting on the use of AACVD to prepare Sylgard-184 (PDMS) films that comprised of various nanoparticles [colbalt (II) oxide, iron (II/III) oxide, nickel, gold, SiO_2 and titanium dioxide (TiO_2)], *via* the use of chloroform-based precursor solutions and an ultrasonic humidifier to generate aerosols.[81] Hybrid films displayed promising features, e.g. dual superhydrophobicity and photocatalysis when incorporating photocatalytic TiO_2 nanoparticles, showing great potential for self-cleaning applications.[82] In further advances, superhydrophobic films deposited from Sylgard-184/chloroform aerosols, in the absence of a nanoparticle framework – which is conventionally used to aid surface texturing – were reported with contact angles ranging from 150-167°. Surface hydrophobicity was seen to generally increase, showing lower variability in contact angle when the deposition temperature was enhanced, as this facilitated complete polymer curing and homogenous coatings.[83]

More recently, AACVD was reported as a technique used to fabricate optically transparent superhydrophobic coatings, which are usually fabricated *via* conventional sol-gel processes (see section 1.5.1). Transparency, although extremely useful for certain applications e.g. optical lenses, can be difficult to obtain synergistically with surface superhydrophobicity. Roughness-induced light scattering is a competing factor when considering transparent superhydrophobic coatings – surface roughness must be less than the wavelength of light to avoid substantial light scattering.[84,85] However, irrespective of the associated challenges, researchers have developed methods to overcome this; in a novel approach, Tombesi *et al*. studied the multilayer deposition of functional alkoxysilane films to generate SiO_2

nanoparticle coatings. This was carried out *via* a series of acid hydrolysis and condensation reactions using hydrochloric acid (HCl) as a catalyst. In prior work by Crick *et al.*, it was established that SiO_2 particle size could be controlled by the deposition temperature.[86] Hence, the deposition temperatures of each layer were varied, in order to produce both nano- and micro-SiO_2 particles, before applying a final layer of FAS as a modifying agent to lower the surface energy. The relationship between AACVD deposition time and the optical transparency (400-760 nm) of films was investigated, where a 10 % decrease in transparency was reported for a deposition time of 5 minutes, yielding coatings with a contact angle of 165° and a tilt angle of < 1° (see Fig. 1.26).[87] Transparency was seen to be considerably reduced (50 % relative to initial) as the deposition time was extended to 10 minutes. This was attributed to the increased volume of deposited particles, that subsequently led to a level of surface roughness which exceeded the limit of optical transparency.

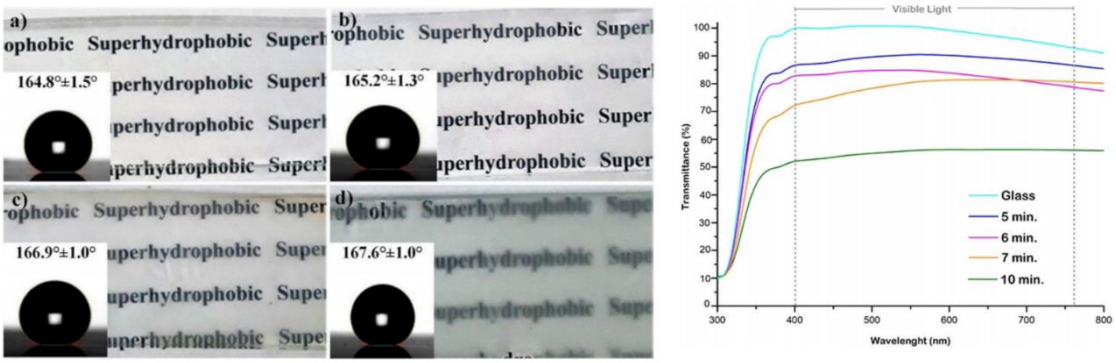

Figure 1.26: Optical images highlighting the change in optical transparency of AACVD-deposited films, with increasing deposition time; (**a**) 5 minutes, (**b**) 6 minutes, (**c**) 7 minutes and (**d**) 10 minutes and their corresponding water contact angles **(left)**. Overlaid UV-Vis spectra of superhydrophobic films, highlighting the change in transmittance with respect to deposition time (**right**). Figures taken from ref.[87]

1.4.2.3 Conventional Techniques

Thus far, the 'bottom-up' techniques that have been discussed have required specialised equipment and/or show some limitations with respect to precursor materials that can be used. For these reasons, simple deposition techniques, such as spray-coating, dip-coating and spin-coating, are widely established and have been universally implemented as integral tools across all fields of superhydrophobic materials design. The only prerequisite that these techniques present is that precursors must be either soluble, or able to suspend, in a solvent with a moderately low boiling point, to facilitate solvent evaporation during coating deposition. Hence, a broad range of surface coatings has been reported, from natural materials such as

waxes and plant-based spores, to synthetic polymers and colloidal suspensions, in addition to many more.[88–91] The generation of large-scale surface coatings on both rigid and flexible substrate materials (e.g. glass, metals, textiles, paper and sponge) has also been shown to be feasible, particularly *via* spray-coating, enhancing the applicability to industrial processes and production of commercial products.[92,93]

1.5 Inorganic Nanoparticle Composites

Inorganic nanoparticles, in particular metal oxides, have been used comprehensively as support scaffolds for generating hierarchical surface roughness within highly water repellent surface coatings. Their tuneable surface chemistry, high redox stability (in most cases) and high thermal stability, in addition to the unique optical properties shown by many, make inorganic nanoparticles highly suitable for use in superhydrophobic formulations. The sol-gel method will be explored within this section, alongside particle modification methods (molecular and polymeric), that have enabled the fabrication of a diverse range of surface coatings, some of which have already been discussed in section 1.4.

1.5.1 Sol-Gel Method

The sol-gel process typically results in the synthesis and chemical deposition of inorganic metal oxide clusters, *via* a series of hydrolysis and condensation reactions (acid or base catalysed), using a precursor solution of metal alkoxides.[8, 25] This results in covalently linked 3D molecular networks that act as nucleation sites for colloidal particle growth, under basic conditions (see Fig. 1.27).[94] Once the colloidal solution has formed, conventional deposition techniques, e.g. spray-coating, dip-coating or spin-coating, are often used to deposit films.

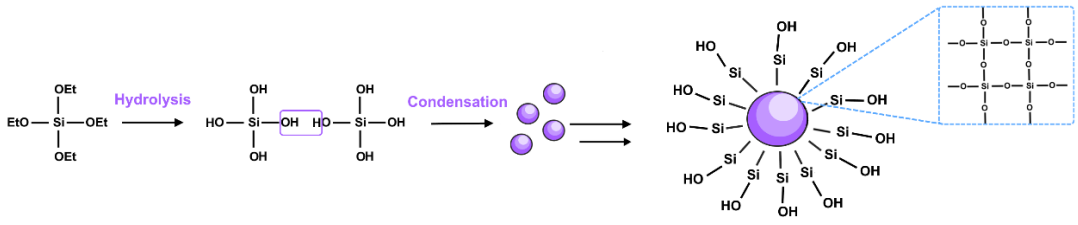

Figure 1.27: Illustration outlining the synthesis process of SiO_2 nanoparticles *via* the sol-gel process; the first step is the hydrolysis of tetraethylorthosilicate (TEOS), followed by condensation of tetrahydroxysilane molecules to form a molecular network.[8,95]

The sol-gel process presents the capability of synthesising homogenous, monodispersed particles of varying size by simply controlling reaction parameters, such as precursor concentrations, water concentration, catalyst concentration, and reaction temperature. All of which, impact either the concentration of nucleation sites or the rate of hydrolysis and condensation reactions, consequently affecting the diameter of the resultant particles.[96,97] The ability to fine-tune particle size is particularly useful when fabricating transparent superhydrophobic films, as discussed earlier (section 1.4.2.2), as it is desirable to produce

particles that are monodisperse, to better control surface roughness.[98] Hence, silanes are commonly employed, due to their high process compatibility and known use in generating films of high optical transparency.[99,100] The sol-gel method has also been frequently used to engineer TiO_2-based and SiO_2/TiO_2 composite superhydrophobic coatings for applications which include, surface patterning and self-cleaning technology, owing to the photocatalytic behaviour that is native to TiO_2 nanoparticles.[101,102]

Inorganic metal oxides are inherently hydrophilic materials, due to the presence of surface-bound hydroxyl groups. Therefore, to ensure high water repellency, particles are often modified with a low surface-energy reagent to form inorganic-organic hybrids *via* (**i**) the use of a co-precursor with one or more hydrophobic groups (see Fig. 1.28 **i**) or (**ii**) post-functionalisation of synthesised particles (see Fig. 1.28 **ii**).

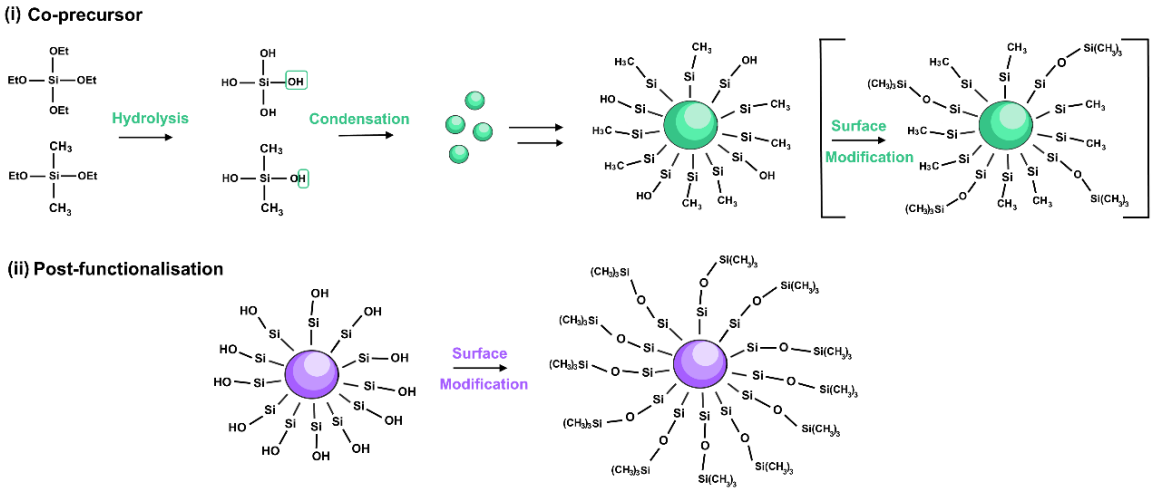

Figure 1.28: Illustrations outlining two alternate routes of synthesising hydrophobic SiO_2 nanoparticles; (**i**) the use of a co-precursor that contains ≥ 1 hydrophobic group [dimethyldiethoxysilane (DDS) used here] for direct incorporation of surface hydrophobicity, however, further functionalisation may be required to modify remaining hydroxyl groups or (**ii**) post-treatment with hydrophobic groups, e.g. hexamethyldisilazane (HMDS), in an additional step.[8,95]

The incorporation of an organo-functionalised co-precursor is a convenient route to introducing and tuning surface hydrophobicity. The resultant surface wettability of the modified inorganic siloxane network will ultimately depend on the density of low surface-energy groups exposed at the surface of particles, as reported by Latthe *et al.*, who investigated the molar ratio between TEOS and trimethyethoxysilane (TMES) precursors. An increase in contact angle from 15° to 151°, in addition to a decrease in tilt angle from 78° to 8°, was achieved when the molar ratio was changed from 0:1 to 1:1 [TMES: TEOS].[98] This aligned

well with work reported by Zhang *et al*. who reported the co-condensation of TEOS and dimethyldiethoxysilane (DDS, as seen in Fig. 1.29b). In this work, coatings never attained superhydrophobicity at any molar ratio until HMDS was used to post-functionalise the remaining surface hydroxyl groups, which is often necessary if sufficient surface hydrophobicity cannot be attained during coating self-assembly. Films deposited from sols that had a ratio > 0.6 [DDS: TEOS] saw almost no change in contact angle after HMDS modification, indicating that the limiting factor was now the remaining number of surface hydroxyl groups that were available for surface functionalisation.[104] Hence, the chemical structure of precursor materials is an important consideration when designing superhydrophobic materials.

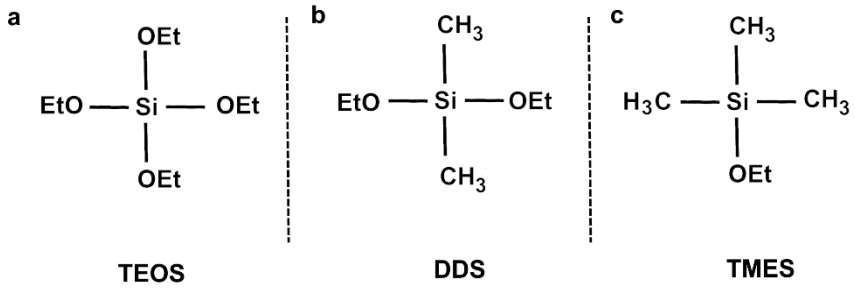

Figure 1.29: Chemical structures of different alkoxysilanes; (**a**) TEOS, (**b**) DDS, and (**c**) TMES.

1.5.2 Molecular Functionalisation

The post-treatment of synthesised nanoparticles enables creativity when designing hydrophobic hybrid materials, resulting from the comprehensive range of molecular groups that can be grafted onto the surface of nanoparticles.

1.5.2.1 Hydrocarbon Modification

A simplistic path to functionalising SiO_2 nanoparticles, that has been heavily documented in the literature as a fluorine-free route, is the reaction with the hydrophobic molecule HMDS, as seen in Figure 1.30.[105–107] Lai *et al.* reported the fabrication of ZnO/SiO_2-HMDS nanorod coatings, targeting the corrosion protection of zinc substrates, where an increase in contact angle from 26.3° (zinc substrate with ZnO nanorods) to 152° was obtained after the application of a SiO_2-HMDS surface coating.[108] The introduction of trimethylsilyl (TMS) groups reduce the surface-energy of particles significantly, enabling the direct formation of

superhydrophobic films, as seen above, or enhanced compatibility for further processing (see section 1.5.3.3).

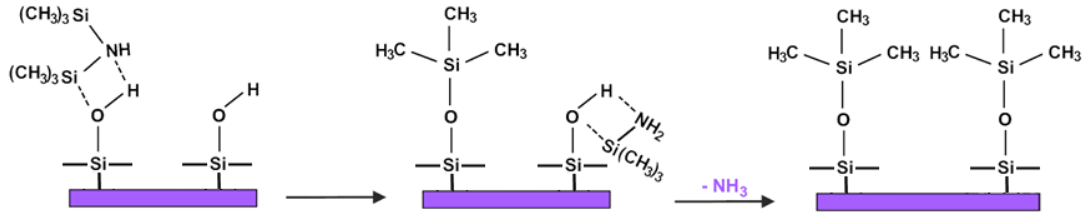

Figure 1.30: Illustration outlining the proposed two-step mechanism of HMDS with SiO_2 nanoparticles. Isolated silanol groups are illustrated on the surface of SiO_2 nanoparticles.[110] An alternative mechanism has also been suggested – the hydrolysis of HMDS to form 2[$Si(CH)_3OH$] and NH_3, if an aqueous environment is used – as reported by Lai *et al.*, so the exact mechanism of functionalisation is still debated.[108]

Functionalisation results in the replacement of silanol groups with triple branched CH_3 groups, subsequently resulting in a dense layer of hydrophobic groups at the surface (if full coverage is obtained).[111] Similarly, bonding of linear hydrocarbon groups can also render surfaces hydrophobic, where chain length has been shown to be an important factor.[112,113] This was outlined by Wang *et al.*, who showed that the chain length of self-assembled monolayers (SAMs) of n-alkanoic acids [$CH_3(CH_2)_nCOOH$, n = 1-16] directly affected the apparent contact angle of roughened surfaces (nanoparticle/microclusters) and smooth copper surfaces. [113] On roughened surfaces, a contact angle of ~ 0° was seen for arrays of molecules with a chain length of n = 1; this was seen to increase sharply, before plateauing at ~ 160° for $n \geq 9$. As the chain length increases, the packing of hydrophobic groups at the surface becomes denser and more ordered, inducing the trapping of air and preventing the exposure of the underlying substrate material (tilting angle < 5° for $n \geq 9$). The same trend was observed for the smooth surface, however, the change in contact angle was not as extreme, as retained air was no longer a contributing factor. Further advances have been made, developing coatings from naturally derived hydrophobic materials; cinnamic acid derived from cinnamon and myristic acid derived from nutmeg, were applied to nano-/micro-structured copper surfaces as detailed by Razavi *et al.*, where advancing contact angles of 154 $\pm$ 2° and 165 $\pm$ 2° were observed.[114]

Besides imparting hydrophobicity, SAMs can be employed to covalently link nanoparticles when blended with a crosslinker to produce superhydrophobic organic-inorganic hybrid networks, as studied by Lee *et al*. Here, Al_2O_3 nanoparticles were initially functionalised with a combination of octadecylphosphonic acid (for hydrophobicity) and 2-hydroxyethyl methacrylate ester (to provide groups for cross-linking, see Fig. 1.31), followed by the addition

of a molecule containing bifunctional vinyl groups, and finally, UV irradiation to induce cross-linking.[115] Superhydrophobicity was reported, where a contact angle of 155° and a tilting angle <5° was attained for coatings with a ratio of 7:3 octadecylphosphonic acid: 2-hydroxyethyl methacrylate ester), in addition to other unique properties (see section 1.6).

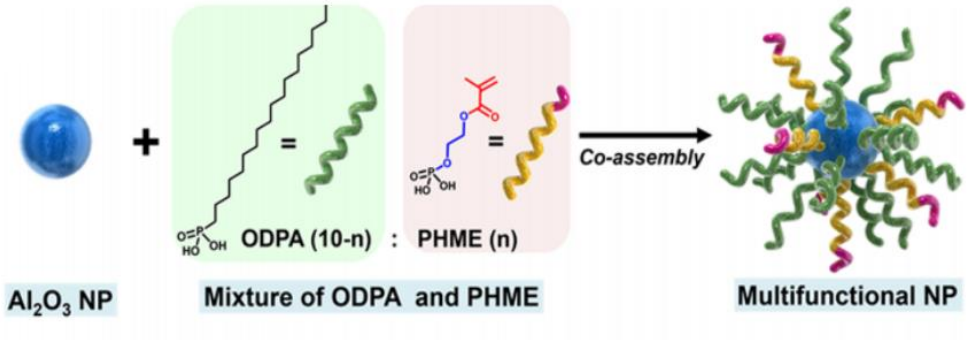

Figure 1.31: Schematic representation of the formation of a SAM of octadecylphosphonic acid (to induce hydrophobicity) and 2-hydroxyethyl methacrylate ester (to enable cross-linking between particles) on Al_2O_3 nanoparticles. Figure taken from ref.[115]

1.5.2.2 Fluorinated Modification

Hydrocarbon modification is often the preferential form of surface functionalisation, as fluorinated analogues are considered as high cost and environmentally hazardous.[116,117] Nonetheless, greater water repellency is often seen with fluorinated surface chemistries (see section 1.3). FASs are a class of hydrophobic molecules that are commonly used to modify particles and promote superhydrophobicity, as outlined in examples throughout section 1.4. Molecules are structured from a long tail of fluorinated alkyl chains, bonded to a functional group that is susceptible to hydrolysis – often trichlorosilyl or triethoxysilyl (e.g. 1H, 1H, 2H, 2H-perfluorooctyltriethoxysilane as seen in Fig. 1.32). The conversion to reactive silanol groups allows for the self-assembly of FAS monolayers onto the solid surface *via* a condensation mechanism.[118,119] Ke *et al*. reported aluminium nanoparticles coated with a SAM of FAS molecules, where a static contact angle of 152.8° and a tilting angle of 3.4° was achieved.[120] Particles were shown to be highly stable, retaining hydrophobicity even after 12 months of storage. In other work, Wang *et al*. reported a higher contact angle of 160° with a tilting angle of 1° for FAS-coated SiO_2/TiO_2 hybrids, highlighting the affinity of FAS coatings for different metal oxide particles.[121]

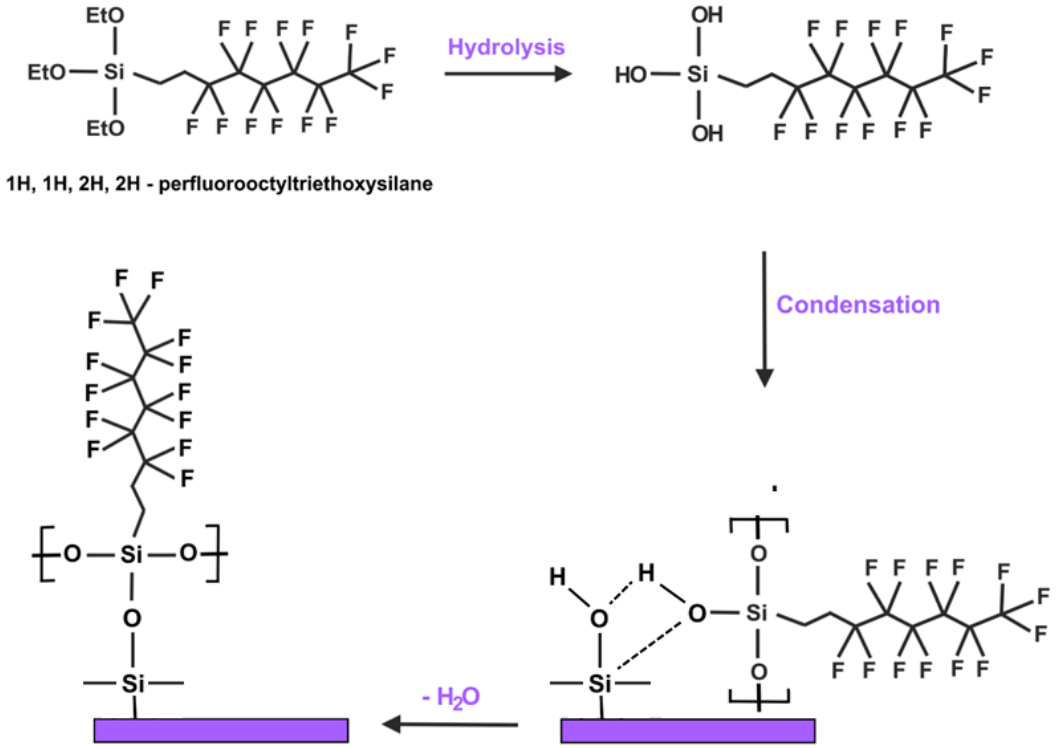

Figure 1.32: Illustration outlining the proposed functionalisation mechanism of SiO_2 nanoparticles with 1H, 1H, 2H, 2H-perfluorooctyltriethoxysilane .[122]

1.5.3 Polymeric Composites

The field of superhydrophobic polymer-nanoparticle composite materials design is extremely broad, as numerous innovative fabrication approaches have been developed over the years. Some approaches have involved the covalent grafting of nanoparticles and polymers to form crosslinked networks, or interlinking layers between particles and the substrate material, and others that simply rely on intermolecular interactions between components, expanding the range of polymeric materials that can be employed. A brief overview of the wider field will be outlined within the following sections, with further discussion taking place in chapter 2.

1.5.3.1 In-situ Nanoparticle Surface Growth

Variations of *in-situ* nanoparticle growth, to create polymeric materials with embedded nanoparticles, have been published. Although this route does not typically involve the direct coating of particles with a polymer, interesting surface designs have been reported. However, there is often a requirement for molecular surface functionalisation in order to yield high water repellency.[123,124] Farbod *et al.* introduced a novel method of generating porous

poly(methylmethacrylate) (PMMA) membranes, to which they applied a TEOS/FAS/H_2O solution and later grew nanoparticles directly onto the PMMA surface and within the surface pores, using an ammonia vapour (see Fig. 1.33 a-c).[123] Particle hydrophobicity was attained simultaneously *via* the incorporation of FAS, as a modifier silane, into the sol-gel process, where a contact angle of 175° was observed for optimised coatings. In an alternative approach, Zhang *et al*. utilized high-performance polymer particles (polyethersulfone) as a textured structure to grow SiO_2 nanoparticles from – contrasting to the previous example which used porosity as its primary source of surface roughness.[124] Here, dopamine was self-polymerised onto the surface of the polyethersulfone particles to form polydopamine, to which SiO_2 nanoparticles were grown *in-situ* and covalently grafted onto, before being treated with FAS. Coatings inspired by the lychee fruit were produced, with an observed contact angle of 157.2 $\pm$ 1° and tilting angle of 3 $\pm$ 0.5° (see Fig. 1.33 d-f).

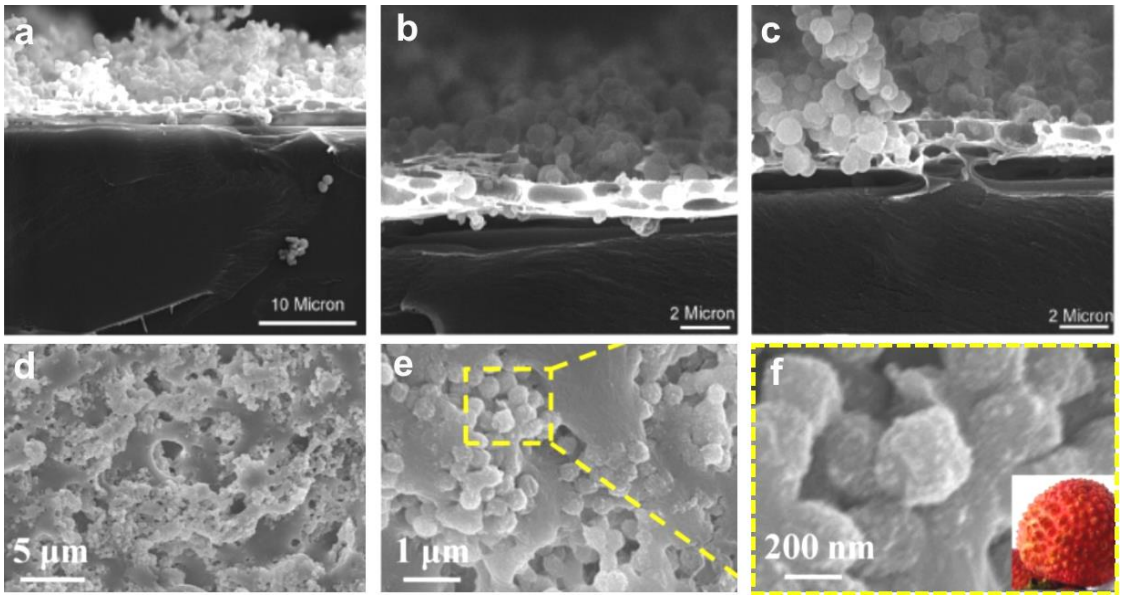

Figure 1.33: SEM micrographs highlighting; (**a-c**) the surface morphology of *in-situ* grown SiO_2 nanoparticles on porous PMMA films and (**d-f**) the surface morphology of polyethersulfone-polydopamine-SiO_2 composites, where SiO_2 nanoparticles were grown *in-situ*. Inset; lychee fruit. Scale bars are shown. Figures taken from refs.[123,124]

1.5.3.2 Covalently Linked Networks

The formation of nanoparticle-polymer networks *via* covalent linking of nanoparticles and polymers, is well documented (either *in-situ* synthesis or post-synthesised). This approach works on the basis that compatible functional groups, present on both the polymer and the particles, will react and subsequently form covalent bonds, resulting in a network that can be tethered to a substrate or exist as an independent structure.[125–127] Polymers can be specifically tailored by the use of monomers with desirable functional groups during the polymerisation

process, as reported by Mahadik *et al*., who fabricated a compressible silica-polyHIPE porous network with contact angles ranging 160-165° for oil-spill clean-up and recovery.[125] Initially, a polyHIPE – a porous polymer formed by mixing two immiscible liquids in the presence of an emulsifier, followed by the removal of one phase to generate a porous network – was synthesised from a pre-made polymer that was structured from hydrophobic pendant groups and the commercially available monomer 3-(trimethoxysilyl)propyl methacrylate. This monomer contains methoxy groups at the chain end, and hydrolysis of these groups can be carried out to facilitate bonding with silicates as seen in Figure 1.34), to form a composite network.[128]

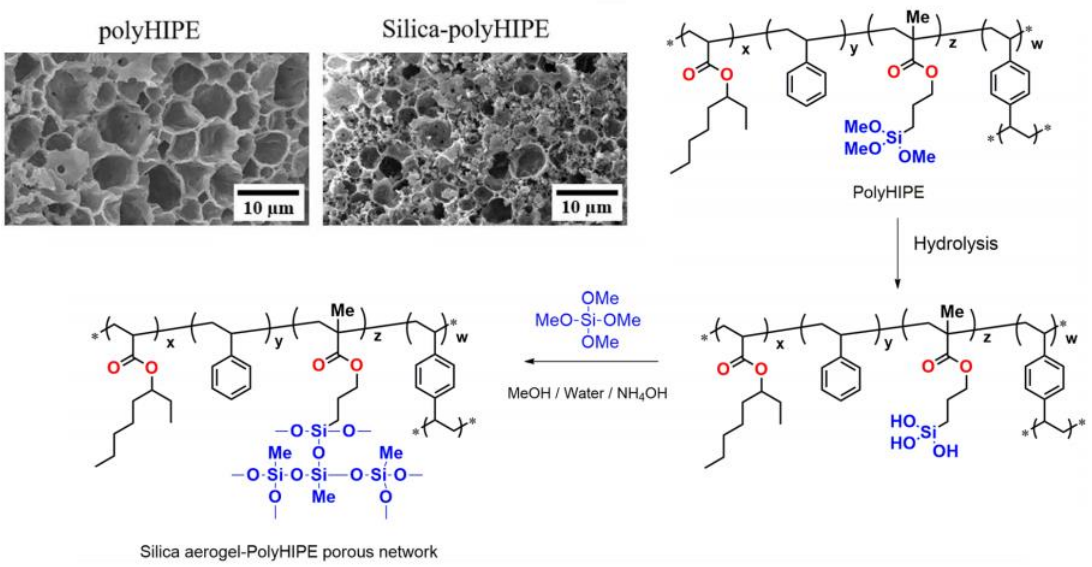

Figure 1.34: An outlined method for the synthesis of a covalently linked silica-polyHIPE porous network. Inset; SEM micrographs of an example polyHIPE and the composite silica-polyHIPE. Scale bars are shown. Figures taken from ref.[125]

Targeting a different application (UV-blocking textiles), Chen *et al*. formulated a novel crosslinked network, by crosslinking the hydroxyl groups of pre-synthesised TiO_2 nanoparticles with vinyl groups present on polymer, polyvinylsilsesquioxane.[126] This, in turn, was further crosslinked to hydroxyl groups which were present on the surface of cotton fabric, after a short heat treatment. Coatings survived several washes, showing contact angles > 150°, which was attributed to the strong 3D crosslinked structure. Naturally derived polymers, such as epoxidized soybean oil, have also been used to form networks between substrates and inorganic metal oxides particles. For example, Cheng *et al.* reported the crosslinking of epoxidized soybean oil, enabling polymers to act as an interlayer, in this case between cellulosic filter paper and ZnO nanoparticles.[127]

1.5.3.3 Non-Covalent Composites

The examples outlined so far, have mostly focused on the covalent bonding of nanoparticles and polymers to generate hierarchically roughened hydrophobic materials. However, significant research has also been carried out on polymer-nanoparticle composites that rely solely on intermolecular bonding between species. As a result, the range of polymers that can be incorporated into nanocoatings is extended, as the requirement for specific functional groups between particles and polymer is no longer necessary (except for ionic interactions).[129–132] Uniform mixing between components, primarily resulting from Van der Waals interactions (in non-polar solvents), is the basis for coating formation and the driving force within composites.[133] Hence, a wider variety of organic and inorganic polymers have been investigated for their use.

Simple composites such as polystyrene-SiO_2 have been fabricated, as reported by Baba *et al.*, where pre-hydrophobised SiO_2 nanoparticles were introduced into a solution of polystyrene/toluene, before being spin-coated onto glass substrates. Contact angles that ranged from 95-172° were observed as the weight percentage of SiO_2 nanoparticles was varied.[129] Although the fabrication process required only the facile mixing of components, polystyrene-SiO_2 has proved highly effective as a water repellent coating with excellent substrate versatility. For example, novel substrate materials such as, naturally dried *Tectona grandis* leaf meshes, as developed by Latthe *et al*. (see Fig. 1.35). Water droplets were observed to have a contact angle of 162 ± 2° and a tilting angle < 7 ± 1°, in contrast to oil which displayed a contact angle nearing 0°, resulting in a separation efficiency greater than 95% (18+ cycles) and providing eco-friendly solutions for oil-water separation.[134]

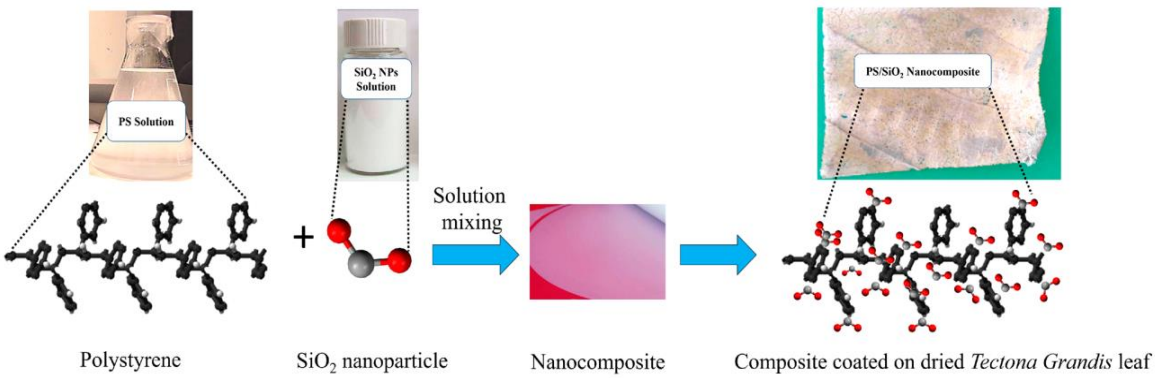

Figure 1.35: Illustration outlining the fabrication process of polystyrene-SiO_2 composite coatings on a *Tectona grandis* leaf mesh, that were later utilized for oil-water separation. Figure taken from ref.[134]

Other common polymers, such as; polyethylene, siloxanes, and epoxy resins, amongst many more, have been employed in a similar manner to obtain superhydrophobic surface coatings (i.e. *via* mixing with inorganic nanoparticles).[130–132] To ensure hydrophobic properties and effective blending of coating components, molecular functionalisation of nanoparticles and/or polar functional groups within polymer chains (if the polymer is not inherently hydrophobic) is often carried out. This was demonstrated by Liu *et al*. who modified commercially available epoxy resin with octadecylamine to increase its contact angle from $82 \pm 2°$ to $102 \pm 3°$, before blending with hydrophobic SiO_2 nanoparticles to achieve superhydrophobicity.[132] The compatibility of suspensions with conventional deposition techniques often allow for the incorporation of additives to impart additional functionalities into the resultant coatings; this will be further discussed in section 1.7. On the other hand, polymers with low solubility and/or extremely high melting points present more challenges but can be employed to form polymer-nanoparticle composites *via* other developed methods. PTFE, for example, is insoluble in all common solvents and dissolves only in perfluorinated solvents at high temperatures and pressures. In addition, it has an approximate melting point of 327℃ and a high viscosity, making it exceptionally difficult and expensive to process.[135,136] Nonetheless, PTFE has been heavily investigated for its use in separation membranes and meshes, which commonly involve electrospinning of PTFE-based suspensions, followed by sintering at high temperatures to fuse PFTE particles together, and decompose any additives that were used in the electrospinning process.[137]

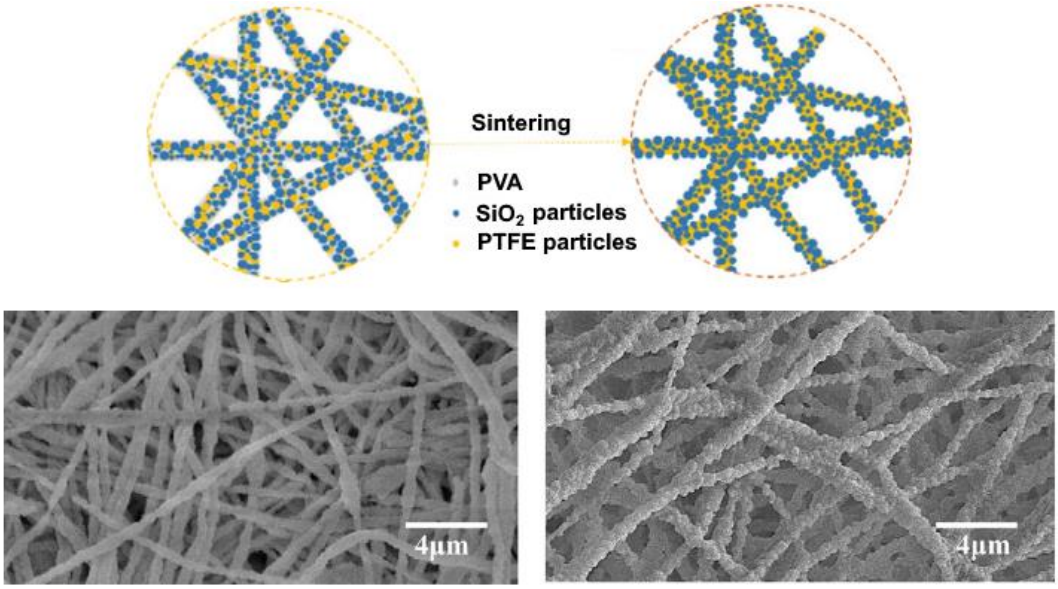

Figure 1.36: Illustration of the fibre sintering process (390 ℃ for 60 minutes) to decompose PVA and fuse PTFE particles together. In addition, the corresponding SEM micrographs of a 7.3 wt % SiO_2 composite, highlighting the fibre morphology before sintering (**left**) and after sintering (**right**). Figures taken from ref.[138]

Liang *et al.* generated self-cleaning nanofiber membranes for potential applications in waterproof and breathable clothing, which were spun from suspensions of PTFE particles and hydrophilic SiO_2 nanoparticles in aqueous solutions of PVA. After sintering at 390 ℃, coverage of SiO_2 nanoparticles with fused PTFE was reported, generating roughened nanofibers that displayed an advancing contact angle of 155° (see Fig. 1.36, pure PFTE membranes displayed an advancing contact angle of 138°).[138] Conversely, Zhu *et al*. carried out similar work, yet grafted FAS onto the surface of electrospun PTFE-SiO_2 membranes after detecting a peak corresponding to –OH groups during Fourier transform infrared (FTIR) analysis, highlighting some surface exposure of hydrophilic SiO_2. This gave rise to an increased contact angle of $173 \pm 4°$.[139]

1.6 Durability

As outlined by H.Y. Erbil in a recent publication (2020), the prospective application of superhydrophobic materials as long-term innovative solutions to many commercial and industrial issues does not come without challenges.[140]

1.6.1 Challenges

The problematic characteristics that are fundamental in preventing the widespread implementation of highly water repellent materials are grouped below:

Mechanical Durability

Lack of structural integrity, resulting from small-scale (often nano-scale) features, is well-known for inhibiting the use of superhydrophobic materials. In some cases, coatings have been fully removed with as little abrasion force as a finger wipe.[141] It has been suggested that two levels of physical degradation exist; initially, the air-layer is lost from within the surface structure, which can be regarded as recoverable degradation as regeneration is possible (see section 1.6.2.4). Secondly, perpetual degradation of the surface microstructure occurs, which then irreversibly reduces surface roughness.[6, 142]

Changes to Surface Wettability

Surface damage in the form of; strong acid/alkali solutions, plasma treatment, employment of photocatalytic particles, extreme heat treatment, or long-term surface fouling, amongst others, can all have detrimental effects on surface hydrophobicity. This can result in the complete removal of covalently-bound hydrophobic surface groups and/or the attachment/introduction of unwanted contaminants (biofilms, oxygen-containing groups etc.), both of which, result in surfaces with modified wettability.[143–145]

Plastron Lifetime

The retained air layer, also termed the plastron (initially coined within the biological community and used to describe the air pockets that aid the underwater respiration systems of aquatic insects), has been shown to be highly unstable during submersion in water. Hence, the rapid decay of the plastron is often observed *via* diffusion of gas into the surrounding aqueous environment. A change in the wetting state from the non-wetted Cassie-Baxter state to the wetted Wenzel state supports this and signifies the complete removal of any surface-bound air bubbles.[146–148]

1.6.2 Prospective Solutions

Over the years, numerous attempts to enhance the durability of superhydrophobic materials have been made by scientists. Although a superhydrophobic coating that shows universal resilience is yet to be developed, some innovative approaches have been reported to tackle durability-related issues.

1.6.2.1 Physical Reinforcement

Reinforcement can be an effective route to strengthening pre-existing materials and their resultant microstructures. Additives with exceptional mechanical strength, such as polymer fibres or carbon nanotubes, can be embedded directly within a superhydrophobic matrix to provide advanced resilience against physical deformation and abrasive wear.[149–151] In some cases, strengthening agents can be actively used in place of traditional nanofillers (e.g. inorganic nanoparticles) to impart additional durability, while creating a textured microstructure.[152] This was studied comprehensively by Hernández *et al.*, who used a nanoimprinting process to engineer arrays of reinforced polymer pillars (see Fig. 1.37).[151] Here, the employment of carbon nanotubes to physically aid imprinted polystyrene microstructures and somewhat enhance superhydrophobicity (polystyrene pillars; contact angle $172 \pm 2°$ / sliding angle $6 \pm 1°$ and composite pillars; contact angle $173 \pm 1°$ / sliding angle $3 \pm 2°$), was reported. While probing the mechanical properties *via* a series of nanoscratch and nanoindentation tests, the reinforced pillars demonstrated superior mechanical properties with respect to the pristine polymer arrays. Alternative forms of reinforcement which specifically target the intrinsically weak adhesion between coatings and substrate materials have also been documented; interconnecting layers in the form of commercial adhesives (multipurpose, double-sided tape, epoxy resins, etc.) or other polymer resins/molecular layers, that act as a covalently-linked bridge between the substrate and coating molecules, have been employed to anchor external coatings and provide additional physical support.[145, 157, 158]

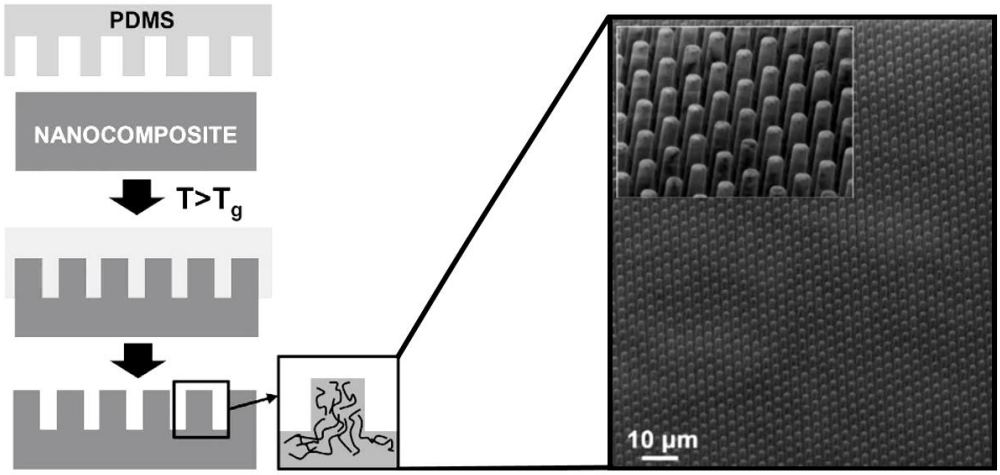

Figure 1.37: Illustration outlining the nanoimprinting process used to fabricate superhydrophobic polymer composite coatings (**left**) and a corresponding SEM micrograph of polystyrene/carbon nanotube 2 µm pillar arrays (**right**). Scale bar is shown. Figures taken from ref.[151]

1.6.2.2 Strategic Surface Designs

Optimised surface architectures have been proposed, to overcome the barriers of limited wear-resistance and rapid loss of entrapped air.

1.6.2.2.1 Wear-Resistance

Mechanical abrasion can facilitate the irreversible wear of surface features, or in some cases, the total destruction of the surface microstructure, depending upon the intrinsic resilience and design of the surface. Simple considerations can lead to more structurally sound microstructures, e.g. designing surfaces from bulk hydrophobic materials to eliminate the exposure of hydrophilic defect sites and reduce the effects of water pinning, that may arise from the physical removal of a hydrophobic coating (see Fig. 1.38).[155]

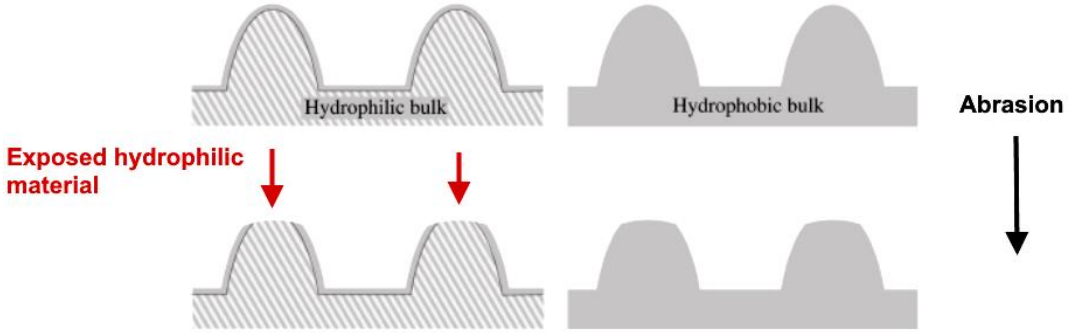

Figure 1.38: Abrasion effects on a hydrophilic microstructure coated with a hydrophobic material (**left**) vs a bulk hydrophobic microstructure (**right**), highlighting the exposed hydrophilic sites where material has been abraded. Figure taken from ref.[155]

Smart routes to generating hierarchical surface roughness, that manipulate the formation and geometry of micro/nano-structures to impart greater topological durability, have also been reported. Kondrashov *et al*. reported optimised surfaces, comprising micron-sized cones and nanograss while investigating the complex relationship between structural stability and surface design. It was found that large microstructures dispersed strategically throughout coatings (high density of cones) can act as contact points to protect smaller nano-sized features from abrasion, resulting only in the truncation of cones. However, cone size and density must be controlled in a way that balances structural durability with superhydrophobicity.[156] Other methods have focused on developing bulk superhydrophobic mesh-like materials, which pose internal and external superhydrophobic structures.[157]

1.6.2.2.2 Air Retention

Engineering systems and surface designs that promote the retention of air have received much attention in recent years. Those inspired by nature, generally replicate hair-like structures and satisfy other criteria to meet the morphological requirements that plants and insects use, to maintain a stable plastron.[158] Different bioinspired designs have been reported, from the hot stretching of polycarbonate to produce nanofur, to the creation of *Salvina*-inspired vertically aligned arrays of carbon nanotubes.[159,160] A common factor is the high aspect ratio surface features, that subsequently promote a large surface area for the entrapment of air, if features densely populated the surface (diluted features can lead to Wenzel wetting). Even so, external factors which exist within dynamic wetting environments, e.g. hydrostatic pressure, mechanical vibrations, etc., can present a prolifically challenging set of circumstances, in

which surface coatings must be able to show resilience. This has led to more complex systems being developed, for example, Vüllers *et al*. published work on the plastron pressurisation of nanofur using a pressure cell, in an attempt to counteract and balance external pressures.[161]

1.6.2.3 Self-Healing Mechanisms

Integrated self-healing mechanisms, i.e. internal species that are responsive to physical or chemical damage, have been established in a bid to bridge the gap between synthetic materials and those found in nature. SAMs of molecules, such as those reported in section 1.5.2.1, have been shown to display self-healing behaviour. Lee *et al*. reported that long-chain molecules can undergo self-reorganisation in the presence of heat treatment to restore any previous chemical degradation and re-establish surface hydrophobicity. It has been suggested that molecules can spontaneously migrate from within the coating to the surface *via* thermal motion.[115] Self-healing polymers have been studied in a similar manner, where polymers that contain groups (either on the polymer or within the crosslinked matrix) that are capable of forming new bonds, e.g. disulfide bonds (S-S) are utilized. These can be employed to repair large cracks within the surface of composite materials, subsequently eliminating defects.[162,163] In other work, researchers have uncovered mechanisms that can fully restore physically deformed morphological features, however, in some cases these mechanisms are still not fully understood.[164] A different approach has been to apply multilayers of superhydrophobic coatings, so in the event of surface damage, a new layer will be exposed that can effectively restore the surface properties of the native material.[165] Generally, mechanisms either show physical or chemical healing, although, the synergistic healing of both has been reported (see Fig. 1.39 for an example of physical restoration).[144, 166]

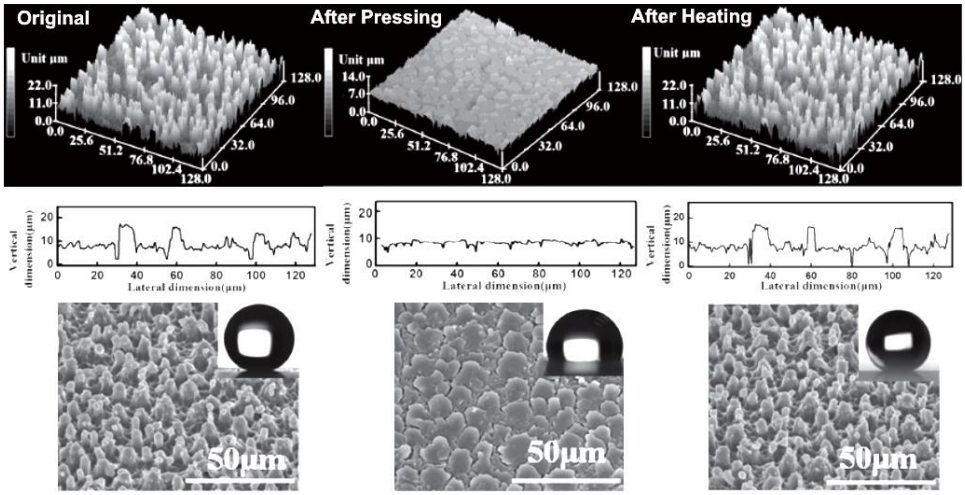

Figure 1.39: 3D confocal microscopy images, corresponding profiles, SEM micrographs and contact angle images of a healable superhydrophobic polymer in its original state, compressed state and finally after a heat treatment at 85℃ for 120 seconds. Scale bars are shown. Figures taken from ref.[144]

1.6.2.4 Plastron Regeneration

Research, primarily into the underwater stability of highly water repellent materials, has spurred the ongoing investigation into systems that can regenerate the plastron *in-situ*, at the interface of submerged materials, which otherwise, has been proven to rapidly decay.[167] Panchanathan *et al.* reported the employment of diluted hydrogen peroxide solution (3-4 wt %) into the surrounding aqueous environment, that could react with the now-exposed catalyst (previously deposited between surface microstructures) upon partial depletion of the air-layer, to decompose hydrogen peroxide. Subsequently, gas was produced and the plastron was replenished. By controlling surface texturing parameters, they were able to ensure plastron recovery.[168] This is undoubtedly an innovative approach to regeneration, however, the practicality and large-scale operation are somewhat questionable. In an alternative approach, Simovich *et al.* recently outlined thermoregeneration of plastrons, based on the reduced solubility of O_2 gas in water at increased temperatures. Raising the temperature of a substrate above that of the surrounding solution was proven to induce localised gas supersaturation, whereby the rough nature of the superhydrophobic surface provided nucleation sites for bubble/plastron formation. As predicted, this was only sustainable when there was a temperature differential, and began to decay when heating was suspended, following dissolution of O_2 back into the surrounding environment.[169] Other approaches have also been taken, including more complex approaches such as *in-situ* water splitting and alternatively, relatively straightforward techniques like the use of air-supersaturated aqueous environments.[146,170]

1.6.2.5 SLIPS

Slippery liquid-infused porous surfaces (SLIPS) are an emerging category of 'smart' materials, first reported by Wong *et al*. in 2011, where a lubricating liquid that is immiscible with water (often oils e.g. silicone oil) is infused within the surface porosity of a hydrophobic solid, resulting in coatings with very limited adhesion and large slippage (see Fig. 1.40).[171] Inspired by the *Nepenthes pitcher* plant, SLIPS have been widely investigated as an alternative to conventional superhydrophobic coatings – which lock air within surface microstructures – as plastron stability is no longer a limiting factor, governing the lifetime of coating properties.[172,173] Moreover, the smooth, homogenous layer of lubricant often displays excellent resistance against the infiltration of water, due to the favourable hydrophobic interactions between the lubricant and the solid surface.[174,171] Surfaces are very versatile and have been fabricated using the same methods as many conventional superhydrophobic materials, where the employment of various kinds of materials (metals, polymers, nanoparticles, SAM

composites, fibres etc.) have been seen to generate porous architectures.[172] SLIPS have been studied for their application within different areas, due to their stable protective lubricating layer (anti-corrosion, anti-fouling etc.).[175, 176] However, there has been a particularly large interest in their icephobic behaviour (ice repelling and prevention properties), due to limited condensation and adhesion of water droplets, owing to the lack of surface features that small droplets can adhere to – only comparable to superhydrophobic materials when they are in a stable Cassie-Baxter state.[172,177]

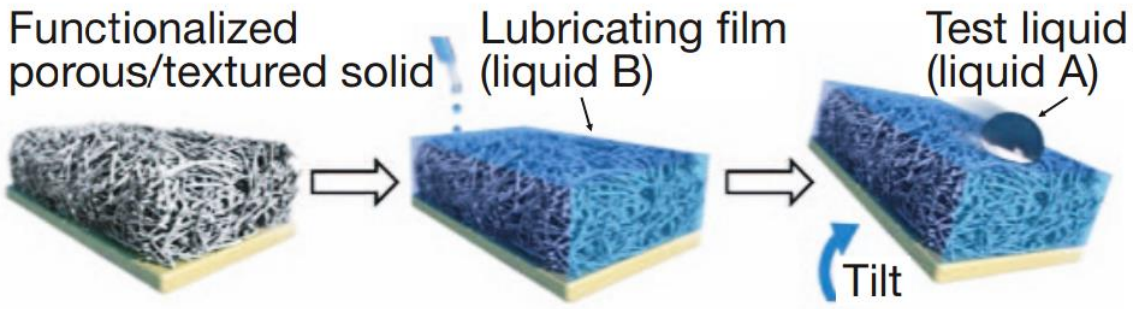

Figure 1.40: A schematic depicting the generalised fabrication process of SLIPS; liquid A being hydrophilic and liquid B being hydrophobic, in the case of water-repellent SLIPS. Figure taken from ref.[171]

1.7 Inherent Properties and Commercial Applicability

Superhydrophobic materials are of special interest when it comes to both, pioneering research and establishing valid commercial applications, owing to the emerging range of properties that they can display, some of which are featured in Figure 1.41. Superhydrophobic materials collectively cover an array of prospective commercial and industrial target markets, however, overlap exists between individual sectors, where specific properties could be mutually beneficial.

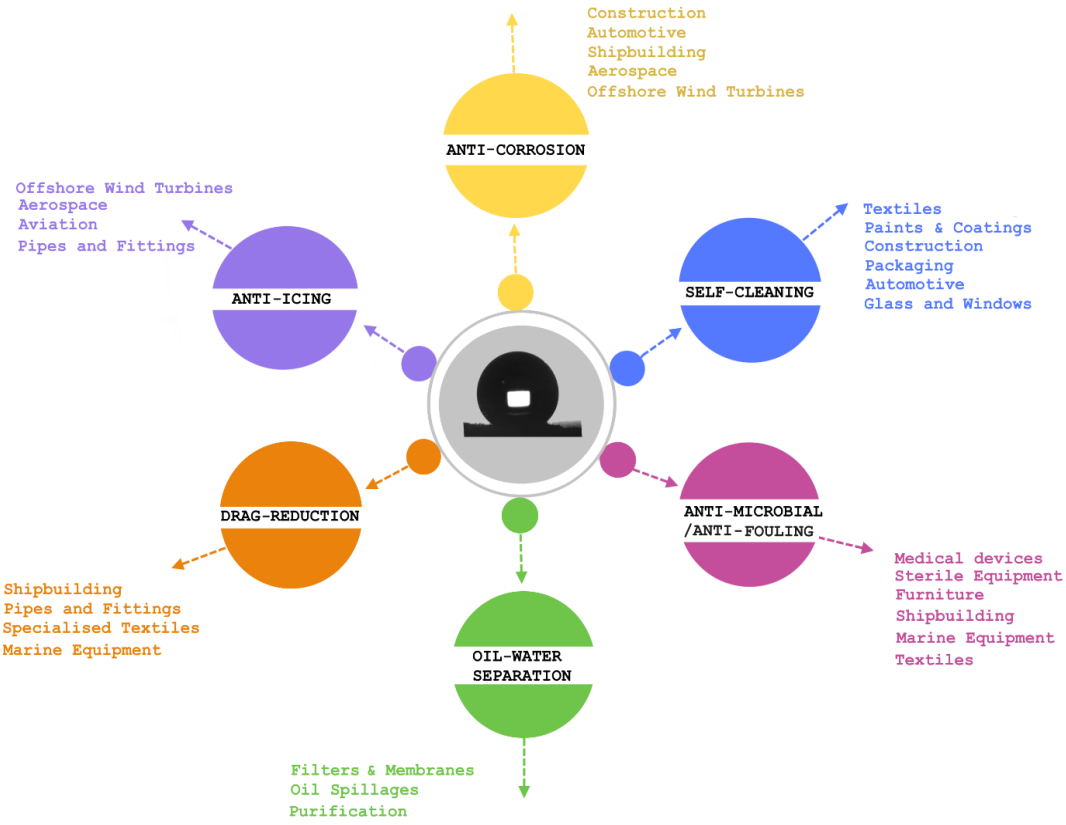

Figure 1.41: Map highlighting a selection of inherent properties that superhydrophobic materials possess and the corresponding commercial sectors that are relevant to each property.

1.7.1 Clean Surfaces

The primary selling point of superhydrophobic materials, that has received significant attention over the years, is the intrinsic self-cleaning mechanism (Lotus Effect) that has been successfully replicated from the Lotus leaf. A patent launched by Barthlott in 1998 first trademarked the Lotus-Effect® and fuelled the excitement for large-scale collaborations, focused on integrating self-cleaning nanotechnology within real-world applications.[158] Subsequently, this led to a commercial facade paint being developed by Sto in 1999, which

has now further evolved into an assortment of 'intelligent paints' (StoColor Lotusan®) that incorporate the patented Lotus-Effect® technology.[178] A second commercial product that utilizes the Lotus-Effect® technology is Aeroxide® LE – commercially available hydrophobic nanopowders – which are developed by Degussa.[179] Any application that requires clean surfaces is relevant, encouraging the expansion into several potential markets, where successful research has been carried out on materials from self-cleaning concrete and self-cleaning textiles for outdoor clothing and automotive upholstery, to anti-biofouling coatings for the marine industry, in addition to many more (glass for windows and other applications, paints, food and beverage containers/packaging etc.).[133,141,143,180–182] Superhydrophobicity can be integrated into materials either directly *via* the adaptation of materials (subject to compatibility), or as an applied external coating – which to date, has seemingly been the route taken by the handful of commercial superhydrophobic self-cleaning products which have been successfully launched onto the market. Generic coatings which can be directly applied (often sprayed) onto a range of different surfaces (fabric, outdoor surfaces, shoes etc.) are most common. For example, commercially available NeverWet, Ultra-Ever Dry and Supercoat (See Fig 1.42).[183–185]

Figure 1.42: Range of commercial NeverWet sprays, aimed at different application surfaces (**top**). Commercial marketing campaign of Ultra-Ever Dry, showing the protection of clothes against contaminating liquids (**bottom**).

Additives to enhance the anti-microbial properties of coatings have also been frequently studied, particularly photocatalytic TiO_2 and/or silver (Ag) nanoparticles.[87,155,156,186,187] In recent years, research has been further steered towards meeting consumer demands; Wu *et al.* produced superhydrophobic Ag nanoparticle-based coatings for cotton fabrics with integrated antimicrobial properties, while introducing tuneable fabric colours by controlling Ag nanoparticle synthesis parameters, leading to various nanoparticle sizes and shapes (see Fig.

1.43).[186] Producing textiles with intrinsically incorporated dyes, as opposed to synthetic dyes which are widely known to cause severe environmental pollution, likely generates more appeal to the modern-day textile industry.

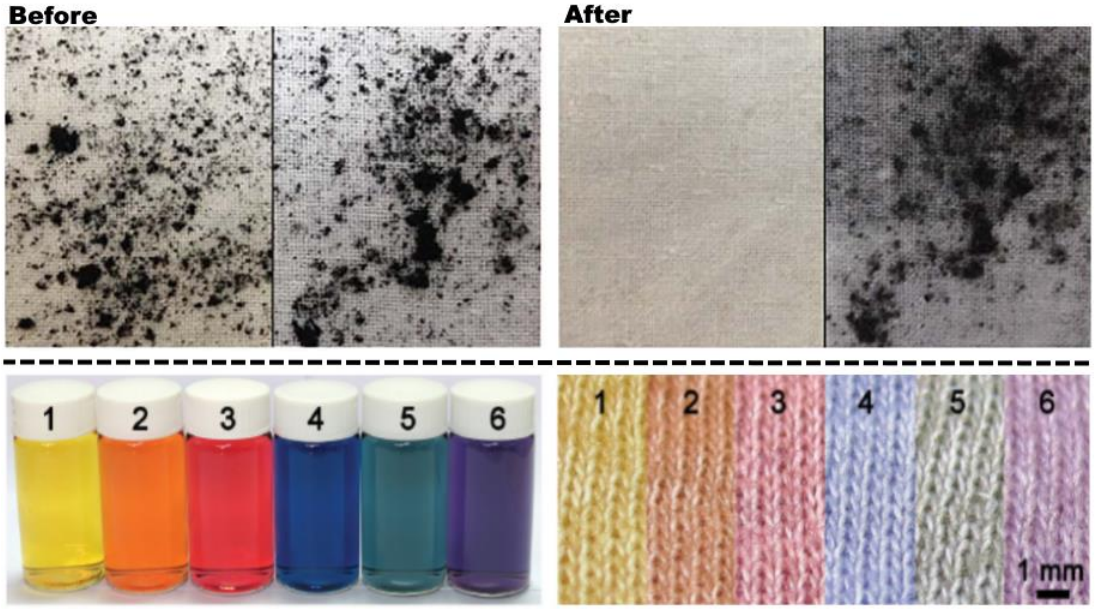

Figure 1.43: Optical images of pristine cotton fabric (**right**) *vs* treated cotton fabric (coating comprised TiO_2 nanoparticles functionalised with n-octyl triethoxysilane; **left**) with simulated dust particles (pencil shavings), before and after rinsing with water droplets to demonstrate the self-cleaning Lotus Effect on the treated fabric (**top**). Figures taken from ref.[188] Optical images of aqueous solutions of Ag nanoparticles (**left**) and the corresponding dyed cotton fabrics (**right**, **bottom**). Figures taken from ref.[186]

Other self-cleaning materials have capitalised on hydrophilic technology, which commonly involves the coating of surfaces in photoactive TiO_2 particles, to achieve the dual effect of photocatalysis and superhydrophilicity.[189,190] Commercial self-cleaning glass is a good example of this, first developed by NSG Co, who founded Pilkington Activ.[189] Yet, the commercial market is moving away from the use of biocides, due to the raising concerns related to health and safety and environmental toxicity. Therefore, competing biocide-free alternatives are currently more sought-after.[158]

1.7.2 Surface Protection

The use of highly water repellent coatings for the prevention of corrosion and icing has been demonstrated throughout the literature, and has shown great potential for limiting the degradation of infrastructure and icing of jet engines/wind turbines, subsequently avoiding

significant financial losses.[191,192] Hence, this area of research is particularly relevant to construction, offshore and aerospace industries, which must generate materials that can withstand extreme weathering and long-term usage. Superhydrophobic coatings minimise the substrate-water contact area due to the presence of air pockets, and therefore, can act as a barrier against corrosion and limit icing (water is instantly repelled, so limited time for it to freeze).[192,193] If commercially established, these coatings may show accelerated performance and sustainability, in comparison to commercial barrier coatings and de-icing liquids/icephobic coatings that are typically only generic hydrophobic polymers. To date, commercial superhydrophobic coatings for the above applications are scarce as they must provide long-term solutions to be financially viable. However, a US company, Synavax™, are currently marketing hydrophobic/icephobic coatings and claim to have trialled their products with Network Rail and the U.S Navy, following which, Network Rail now use Synavax™ icephobic coating technology to coat tunnels and bridges to increase rail safety.[194] In an effort to tackle aeronautic anti-icing, many researchers have worked with industry to trial products; one prospective coating involved oil-infused PDMS crosslinked coatings and was developed by Golovin *et al*. in a joint collaboration between the University of Michigan and Edwards Air Force Base in California.[195] However, the search for durable commercial anti-icing and anti-corrosion coatings is ongoing.

1.7.3 Drag Reduction

Objects moving through aqueous media can often experience large hydrodynamic drag forces, subsequently leading to multiple commercial and economic issues.[42] For example, the drag force exerted on operational ships can result in increased fuel consumption, imposing greater financial and environmental costs.[14] Additionally, the friction felt within pipes during liquid transportation can present significant energy efficiency challenges within the pipeline industry.[42] A possible solution that has been heavily investigated is the application of superhydrophobic coatings, as the entrapment of air within the solid surface acts to provide an environment with low frictional drag, on the condition that a stable Cassie-Baxter state is maintained. Current high-performance commercial coatings that act to reduce drag forces, often exist in the form of hull paints e.g. HullSpeed®, which has patented a two-part epoxy/silicone technology and claims to show up to 10% improvement in speed and up to 13% improvement in fuel economy.[196] Recent reports probing the drag reducing properties of superhydrophobic coatings have shown excellent results; Liu *et al*. reported up to 27.7% drag reduction when testing an epoxy-based resin with integrated fluorinated SiO_2 nanoparticles, displaying a contact angle of 168°.[162] Furthermore, Ayan *et al*. reported up to 67% drag

reduction for heated superhydrophobic surfaces, when compared to unheated and regular surfaces.[197] Although it is difficult to directly compare the drag reducing properties of reported coatings, as a result of the different conditions and use of alternative techniques. It can be said that superhydrophobic coatings unquestionably lower frictional drag and in some cases, current non-superhydrophobic commercial products have been proved to provide very little, if any, change to hydrodynamic drag.[198]

1.7.4 Oil-Water Separation

In the modern-day world, environmental pollution is a very real issue, so discovering innovative technologies to separate oil from water and aid water purification is crucial. The BP oil spill in 2010 was the biggest in US history, resulting in 200 million gallons of crude oil being deposited into the Gulf of Mexico, consequently having a detrimental impact on local wildlife populations.[199] Furthermore, treatment of wastewater and seawater desalination to remove any natural organic matter/organic contaminants is an area that has received great attention, due to global shortages in freshwater.[200] Oil and water have opposing chemistries, i.e. oil molecules are non-polar long-chain fatty acids. Hence, meshes coated with superhydrophobic materials often show superoleophilic properties, meaning that they will permit the passage of oils/non-polar solvents, with oil collection efficiencies of up to 99.5% in some cases, while efficiently blocking the transportation of water molecules (see Fig.1.44).[201] A contributing factor as to why superhydrophobic materials would be far superior to commercially available hydrophobic membranes/filters, is due to their intrinsic anti-fouling nature. As a result, applied superhydrophobic membranes and filters have been shown to reduce membrane fouling, aiding process sustainability.[202] Research into superhydrophobic sponges has also been widely investigated to treat independent liquid spillages, owing to the large absorption capacity/selectivity and often good recyclability of materials.[203]

Figure 1.44: Optical images of a weighted miniature boat, constructed from a superhydrophobic copper mesh (nanoneedle arrays coated with stearic acid), efficiently removing hexadecane (dyed with oil red) from water. Images taken from ref.[201]

1.8 Summary

As seen throughout chapter 1, the range of superhydrophobic fabrication routes and coating design is tremendously broad, and has been studied comprehensively over recent years. A large proportion of the reported surfaces utilizes hydrophobic polymers due to the wide range of properties and stability that they can impart into superhydrophobic materials. Furthermore, metal oxide nanoparticles are often preferably chosen as a roughening agent, as they can be easily integrated into materials and provide a blank canvas for tuneable surface hydrophobicity. However, the fundamental issue – that often prevents the widespread commercial use of superhydrophobic materials, as documented above – is their intrinsically weak durability and susceptibility to both chemical and physical degradation, in both atmospheric and underwater environments, severing limiting functional use.

This PhD thesis details methods of optimising and imparting resilience into superhydrophobic polymer-nanoparticle composite coatings, targeting both thermoset and thermoplastic polymers, in order to extend the real-world potential of synthetic materials. The first experimental chapter (**chapter 2**) investigates the optimisation of polymer-nanoparticle systems, and outlines how the composition of superhydrophobic formulations can impact the resultant structural and functional properties of coatings, with the use of an applied design principle. More specifically, highlighting differences between formulations that comprise common thermoset and thermoplastic polymers. Following this, the UV stability of pigmented superhydrophobic materials is investigated (**chapter 3**), when using photocatalytic metal oxide nanoparticles, titanium dioxide and cerium oxide. Here, molecular and polymeric composites are examined in parallel, and the relationship between composition and UV durability is assessed, with respect to both primary pigment and hydrophobic coating. In further work, the physical resilience and underwater instability issues that surround superhydrophobic materials is addressed, as self-cleaning coatings are applied to high-density polyethylene substrates (**chapter 4**). A deposition method capable of depositing dried formulations, and the addition of a high-strength additive, are explored as a combined solution to enhance mechanical strength and plastron stability. Before finally, polymers that are comprised of natural crosslinkers and waste by-products are examined for the first time, for their use as a more sustainable raw material for superhydrophobic materials design (**chapter 5**). The multi-functional properties of these coatings are investigated, to assess whether they can address some of the current challenges faced, when designing highly functional water repellent materials.

1.9 References

1 X.-Q. Feng, X. Gao, Z. Wu, L. Jiang and Q.-S. Zheng, *Langmuir*, 2007, **23**, 4892–4896.

2 W. Barthlott and C. Neinhuis, *Planta*, 1997, **202**, 1–8.

3 C.-T. Hsieh, F.-L. Wu and S.-Y. Yang, *Surf. Coatings Technol.*, 2008, **202**, 6103–6108.

4 P. Roach, N. J. Shirtcliffe and M. I. Newton, *Soft Matter*, 2008, **4**, 224–240.

5 Y.-L. Zhang, H. Xia, E. Kim and H.-B. Sun, *Soft Matter*, 2012, **8**, 11217–11231.

6 H. Xu, C. R. Crick and R. J. Poole, *J. Mater. Chem. A*, 2018, **6**, 4458–4465.

7 X. Tian, S. Shaw, K. R. Lind and L. Cademartiri, *Adv. Mater.*, 2016, **28**, 3677–3682.

8 A. Hooda, M. S. Goyat, J. K. Pandey, A. Kumar and R. Gupta, *Prog. Org. Coatings*, 2020, **142**, 105557.

9 C. Yu, S. Sasic, K. Liu, S. Salameh, R. H. A. Ras and J. R. van Ommen, *Chem. Eng. Res. Des.*, 2020, **155**, 48-65.

10 M. Ghasemlou, F. Daver, E. P. Ivanova and B. Adhikari, *J. Mater. Chem. A*, 2019, **7**, 16643–16670.

11 O. Tricinci, T. Terencio, B. Mazzolai, N. M. Pugno, F. Greco and V. Mattoli, *ACS Appl. Mater. Interfaces*, 2015, **7**, 25560–25567.

12 Y. Yang, X. Li, X. Zheng, Z. Chen, Q. Zhou and Y. Chen, *Adv. Mater.*, 2018, **30**, 1704912.

13 W. Barthlott, T. Schimmel, S. Wiersch, K. Koch, M. Brede, M. Barczewski, S. Walheim, A. Weis, A. Kaltenmaier and A. Leder, *Adv. Mater.*, 2010, **22**, 2325–2328.

14 J. Busch, W. Barthlott, M. Brede, W. Terlau and M. Mail, *Philos. Trans. R. Soc. A*, 2019, **377**, 20180263.

15 Y. Liu, H. Gu, Y. Jia, J. Liu, H. Zhang, R. Wang, B. Zhang, H. Zhang and Q. Zhang, *Chem. Eng. J.*, 2019, **356**, 318–328.

16 J. N. A. Matthews, *Phys. Today*, 2008, **61**, 32.

17 Z. Guo, W. Liu and B.-L. Su, *J. Colloid Interface Sci.*, 2011, **353**, 335–355.

18 M. Zhang, S. Feng, L. Wang and Y. Zheng, *Biotribology*, 2016, **5**, 31–43.

19 N. Verplanck, Y. Coffinier, V. Thomy and R. Boukherroub, *Nanoscale Res. Lett.*, 2007, **2**, 577.

20 J. Bico, U. Thiele and D. Quéré, *Colloids Surfaces A Physicochem. Eng. Asp.*, 2002, **206**, 41–46.

21 M. Miwa, A. Nakajima, A. Fujishima, K. Hashimoto and T. Watanabe, *Langmuir*, 2000, **16**, 5754–5760.

22 E. L. Decker and S. Garoff, *Langmuir*, 1997, **13**, 6321–6332.

23 M. P. Krafft and M. Goldmann, *Curr. Opin. Colloid Interface Sci.*, 2003, **8**, 243–250.

24 N. J. Shirtcliffe, G. McHale, S. Atherton and M. I. Newton, *Adv. Colloid Interface Sci.*, 2010, **161**, 124–138.

25 Y. Y. Yan, N. Gao and W. Barthlott, *Adv. Colloid Interface Sci.*, 2011, **169**, 80–105.

26 C. Dorrer and J. Ruhe, *Soft Matter*, 2009, **5**, 51–61.

27 M. Nosonovsky and B. Bhushan, *J. Phys. Condens. Matter*, 2008, **20**, 225009.

28 R. N. Wenzel, *J. Phys. Chem.*, 1949, **53**, 1466–1467.

29 R. N. Wenzel, *Ind. Eng. Chem.*, 1936, **28**, 988–994.

30 A. B. D. Cassie and S. Baxter, *Trans. Faraday Soc.*, 1944, **40**, 546–551.

31 A. J. B. Milne and A. Amirfazli, *Adv. Colloid Interface Sci.*, 2012, **170**, 48–55.

32 C. Ishino, K. Okumura and D. Quéré, *EPL (Europhysics Lett.*, 2004, **68**, 419.

33 D. Quéré, *Annu. Rev. Mater. Res.*, 2008, **38**, 71–99.

34 D. Quéré, A. Lafuma and J. Bico, *Nanotechnology*, 2003, **14**, 1109.

35 A. Lafuma and D. Quéré, *Nat. Mater.*, 2003, **2**, 457–460.

36 N. J. Shirtcliffe, S. Aqil, C. Evans, G. McHale, M. I. Newton, C. C. Perry and P. Roach, *J. Micromechanics Microengineering*, 2004, **14**, 1384.

37 L. Gao and T. J. McCarthy, *Langmuir*, 2006, **22**, 6234–6237.

38 G. B. Darband, M. Aliofkhazraei, S. Khorsand, S. Sokhanvar and A. Kaboli, *Arab. J. Chem.*, 2020, **13**, 1763–1802.

39 G. McHale, N. J. Shirtcliffe and M. I. Newton, *Langmuir*, 2004, **20**, 10146–10149.

40 H. B. Eral and J. M. Oh, *Colloid Polym. Sci.*, 2013, **291**, 247–260.

41 M. Jin, Q. Xing and Z. Chen, *J. Biomater. Nanobiotechnol.*, 2020, **11**, 110.

42 M. Liravi, H. Pakzad, A. Moosavi and A. Nouri-Borujerdi, *Prog. Org. Coatings*, 2020, **140**, 105537.

43 J. Jeevahan, M. Chandrasekaran, G. B. Joseph, R. B. Durairaj and G. Mageshwaran, *J. Coatings Technol. Res.*, 2018, **15**, 231–250.

44 D. Öner and T. J. McCarthy, *Langmuir*, 2000, **16**, 7777–7782.

45 H.-B. Jiang, Y.-Q. Liu, Y.-L. Zhang, Y. Liu, X.-Y. Fu, D.-D. Han, Y.-Y. Song, L. Ren and H.-B. Sun, *ACS Appl. Mater. Interfaces*, 2018, **10**, 18416–18425.

46 Y. Chen, H. Wang, Q. Yao, B. Fan, C. Wang, Y. Xiong, C. Jin and Q. Sun, *J. Mater. Sci.*, 2017, **52**, 7428–7438.

47 X. Gao, X. Yan, X. Yao, L. Xu, K. Zhang, J. Zhang, B. Yang and L. Jiang, *Adv. Mater.*, 2007, **19**, 2213–2217.

48 J. Yao, J. Wang, Y. Yu, H. Yang and Y. Xu, *Chinese Sci. Bull.*, 2012, **57**, 2631–2634.

49 F. Wang, S. Li and L. Wang, *Colloids Surfaces A Physicochem. Eng. Asp.*, 2017, **513**, 389–395.

50 S. Y. Chou, P. R. Krauss and P. J. Renstrom, *J. Vac. Sci. Technol. B Microelectron. Nanom. Struct. Process. Meas. Phenom.*, 1996, **14**, 4129–4133.

51 S. Y. Chou, P. R. Krauss and P. J. Renstrom, *Science (80-.).*, 1996, **272**, 85–87.

52 B. Kwon and J. H. Kim, *Importance of Molds for Nanoimprint Lithography: Hard, Soft, and Hybrid Molds*, Journal of Nanoscience, 2016.

53 H.-J. Choi, S. Choo, J.-H. Shin, K.-I. Kim and H. Lee, *J. Phys. Chem. C*, 2013, **117**, 24354–24359.

54 A. P. Nayak, M. S. Islam and V. J. Logeeswaran, ed. B. Bhushan, Springer Netherlands, Dordrecht, 2012, pp. 2829–2830.

55 A. Kumar and D. Nanda, in *Superhydrophobic Polymer Coatings*, Elsevier, 2019, pp. 43–75.

56 B. Qian and Z. Shen, *Langmuir*, 2005, **21**, 9007–9009.

57 J. Lomga, P. Varshney, D. Nanda, M. Satapathy, S. S. Mohapatra and A. Kumar, *J. Alloys Compd.*, 2017, **702**, 161–170.

58 R. Jafari, S. Asadollahi and M. Farzaneh, *Plasma Chem. Plasma Process.*, 2013, **33**, 177–200.

59 G. S. Oehrlein, *Mater. Sci. Eng. B*, 1989, **4**, 441–450.

60 W. Hou, Y. Shen, J. Tao, Y. Xu, J. Jiang, H. Chen and Z. Jia, *Colloids Surfaces A Physicochem. Eng. Asp.*, 2020, **586**, 124180.

61 K. Tsougeni, N. Vourdas, A. Tserepi, E. Gogolides and C. Cardinaud, *Langmuir*, 2009, **25**, 11748–11759.

62 H. C. Barshilia and N. Gupta, *Vacuum*, 2014, **99**, 42–48.

63 T. Takahashi, Y. Hirano, Y. Takasawa, T. Gowa, N. Fukutake, A. Oshima, S. Tagawa and M. Washio, *Radiat. Phys. Chem.*, 2011, **80**, 253–256.

64 B. Cortese and H. Morgan, *Langmuir*, 2012, **28**, 896–904.

65 R. Jafari, C. Cloutier, A. Allahdini and G. Momen, *Int. J. Adv. Manuf. Technol.*, 2019, **103**, 1225–1238.

66 Z. He, Y. Chen, J. Yang, C. Tang, J. Lv, Y. Liu, J. Mei, W. Lau and D. Hui, *Compos. Part B Eng.*, 2017, **129**, 58–65.

67 D. Lin, Q. Nian, B. Deng, S. Jin, Y. Hu, W. Wang and G. J. Cheng, *ACS Nano*, 2014, **8**, 9710–9715.

68 J. Lv, Z. Gong, Z. He, J. Yang, Y. Chen, C. Tang, Y. Liu, M. Fan and W.-M. Lau, *J. Mater. Chem. A*, 2017, **5**, 12435–12444.

69 Y. Zhang, M.-J. Yin, X. Ouyang, A. P. Zhang and H.-Y. Tam, *Appl. Mater. Today*, 2020, **19**, 100580.

70 E. Hosono, S. Fujihara, I. Honma and H. Zhou, *J. Am. Chem. Soc.*, 2005, **127**, 13458–13459.

71 I. Sas, R. E. Gorga, J. A. Joines and K. A. Thoney, *J. Polym. Sci. Part B Polym. Phys.*, 2012, **50**, 824–845.

72 T. Subbiah, G. S. Bhat, R. W. Tock, S. Parameswaran and S. S. Ramkumar, *J. Appl. Polym. Sci.*, 2005, **96**, 557–569.

73 M. W. Lee, S. An, S. S. Latthe, C. Lee, S. Hong and S. S. Yoon, *ACS Appl. Mater. Interfaces*, 2013, **5**, 10597–10604.

74 L.-F. Ren, F. Xia, J. Shao, X. Zhang and J. Li, *Desalination*, 2017, **404**, 155–166.

75 D. Cho, H. Zhou, Y. Cho, D. Audus and Y. L. Joo, *Polymer (Guildf).*, 2010, **51**, 6005–6012.

76 Z. Liu, H. Wang, E. Wang, X. Zhang, R. Yuan and Y. Zhu, *Polymer (Guildf).*, 2016, **82**, 105–113.

77 H. O. Pierson, *Handbook of chemical vapor deposition: principles, technology and applications*, William Andrew, 1999.

78 W. A. Bryant, *J. Mater. Sci.*, 1977, **12**, 1285–1306.

79 K. L. Choy, *Prog. Mater. Sci.*, 2003, **48**, 57–170.

80 C. Piccirillo, R. Binions and I. P. Parkin, *Thin Solid Films*, 2008, **516**, 1992–1997.

81 C. R. Crick, J. C. Bear, P. Southern and I. P. Parkin, *J. Mater. Chem. A*, 2013, **1**, 4336–4344.

82 C. R. Crick, Joseph. C. Bear, K. Andreas and I. P. Parkin, *Adv. Mater.*, **24**, 3505–3508.

83 C. R. Crick and I. P. Parkin, *J. Mater. Chem.*, 2009, **19**, 1074–1076.

84 R. H. Fernando, *Nanotechnol. Appl. Coatings*, 2009, **1008**, 2–21.

85 J. Lin, H. Chen, T. Fei and J. Zhang, *Colloids Surfaces A Physicochem. Eng. Asp.*, 2013, **421**, 51–62.

86 C. R. Crick and I. P. Parkin, *J. Mater. Chem.*, 2011, **21**, 9362–9366.

87 A. Tombesi, S. Li, S. Sathasivam, K. Page, F. L. Heale, C. Pettinari, C. J. Carmalt and I. P. Parkin, *Sci. Rep.*, 2019, **9**, 1–12.

88 X. Zhao, T. Hu and J. Zhang, *J. Colloid Interface Sci.*, 2018, **515**, 255–263.

89 J. M. Morrissette, P. J. Carroll, I. S. Bayer, J. Qin, D. Waldroup and C. M. Megaridis, *Green Chem.*, 2018, **20**, 5169–5178.

90 M. Long, S. Peng, W. Deng, X. Yang, K. Miao, N. Wen, X. Miao and W. Deng, *J. Colloid Interface Sci.*, 2017, **508**, 18–27.

91 H. Lei, J. Xiao, L. Zheng, M. Xiong, Y. Zhu, J. Qian, Q. Zhuang and Z. Han, *Polymer (Guildf).*, 2016, **86**, 22–31.

92 L. Chen, X. Sun, J. Hang, L. Jin, D. Shang and L. Shi, *Adv. Mater. Interfaces*, 2016, **3**, 1500718.

93 D. Zhi, Y. Lu, S. Sathasivam, I. P. Parkin and X. Zhang, *J. Mater. Chem. A*, 2017, **5**, 10622–10631.

94 V. Bounor-Legaré and P. Cassagnau, *Prog. Polym. Sci.*, 2014, **39**, 1473–1497.

95 X. Zhang, F. Zheng, L. Ye, P. Xiong, L. Yan, W. Yang and B. Jiang, *RSC Adv.*, 2014, **4**, 9838–9841.

96 I. A. Rahman, P. Vejayakumaran, C. S. Sipaut, J. Ismail, M. A. Bakar, R. Adnan and C. K. Chee, *Colloids Surfaces A Physicochem. Eng. Asp.*, 2007, **294**, 102–110.

97 I. A. Rahman and V. Padavettan, *Synthesis of Silica Nanoparticles by Sol-gel: Size-Dependent Properties, Surface Modification, and Applications in Silica-Polymer Nanocomposites—a review*, Journal of Nanomaterials, 2012.

98 S. S. Latthe, H. Imai, V. Ganesan and A. V. Rao, *Appl. Surf. Sci.*, 2009, **256**, 217–222.

99 J. Bravo, L. Zhai, Z. Wu, R. E. Cohen and M. F. Rubner, *Langmuir*, 2007, **23**, 7293–7298.

100 S. A. Mahadik, M. S. Kavale, S. K. Mukherjee and A. V. Rao, *Appl. Surf. Sci.*, 2010, **257**, 333–339.

101 Z. Duan, Z. Zhao, D. Luo, M. Zhao and G. Zhao, *Appl. Surf. Sci.*, 2016, **360**, 1030–1035.

102 B. Xu, J. Ding, L. Feng, Y. Ding, F. Ge and Z. Cai, *Surf. Coatings Technol.*, 2015, **262**, 70–76.

103 G. Qi, X. Liu, C. Li, C. Wang and Z. Yuan, *Angew. Chemie Int. Ed.*, 2019, **58**, 17406–17411.

104 X. Zhang, W. Su, M. Lin, X. Miao, L. Ye, W. Yang and B. Jiang, *J. Sol-Gel Sci. Technol.*, 2015, **74**, 594–602.

105 M. Manca, A. Cannavale, L. De Marco, A. S. Arico, R. Cingolani and G. Gigli, *Langmuir*, 2009, **25**, 6357–6362.

106 C. Hu, W. Chen, T. Li, Y. Ding, H. Yang, S. Zhao, E. A. Tsiwah, X. Zhao and Y. Xie, *Colloids Surfaces A Physicochem. Eng. Asp.*, 2018, **551**, 65–73.

107 A. Lazauskas, A. Guobienė, I. Prosyčevas, V. Baltrušaitis, V. Grigaliūnas, P. Narmontas and J. Baltrusaitis, *Mater. Charact.*, 2013, **82**, 9–16.

108 D. Lai, G. Kong and C. Che, *Surf. Coatings Technol.*, 2017, **315**, 509–518.

109 Y. Song, J. Yu, D. Dai, L. Song and N. Jiang, *Mater. Des.*, 2014, **64**, 687–693.

110 V. M. Gun'Ko, M. S. Vedamuthu, G. L. Henderson and J. P. Blitz, *J. Colloid Interface Sci.*,

2000, **228**, 157–170.

111 D. Goswami, S. K. Medda and G. De, *ACS Appl. Mater. Interfaces*, 2011, **3**, 3440–3447.

112 D. Nakajima, T. Kikuchi, S. Natsui and R. O. Suzuki, *Appl. Surf. Sci.*, 2018, **440**, 506–513.

113 S. Wang, L. Feng, H. Liu, T. Sun, X. Zhang, L. Jiang and D. Zhu, *ChemPhysChem*, 2005, **6**, 1475–1478.

114 S. M. R. Razavi, J. Oh, S. Sett, L. Feng, X. Yan, M. J. Hoque, A. Liu, R. T. Haasch, M. Masoomi and R. Bagheri, *ACS Sustain. Chem. Eng.*, 2017, **5**, 11362–11370.

115 Y. Lee, E.-A. You and Y.-G. Ha, *ACS Appl. Mater. Interfaces*, 2018, **10**, 9823–9831.

116 Z. Li, Y. Xing and J. Dai, *Appl. Surf. Sci.*, 2008, **254**, 2131–2135.

117 B. D. Key, R. D. Howell and C. S. Criddle, *Environ. Sci. Technol.*, 1997, **31**, 2445–2454.

118 D. Schondelmaier, S. Cramm, R. Klingeler, J. Morenzin, C. Zilkens and W. Eberhardt, *Langmuir*, 2002, **18**, 6242–6245.

119 S. Liu, X. Liu, S. S. Latthe, L. Gao, S. An, S. S. Yoon, B. Liu and R. Xing, *Appl. Surf. Sci.*, 2015, **351**, 897–903.

120 X. Ke, S. Guo, B. Gou, N. Wang, X. Zhou, L. Xiao, G. Hao and W. Jiang, *Adv. Mater. Interfaces*, 2019, **6**, 1901025.

121 X. Wang, J. Zeng, X. Yu, C. Liang and Y. Zhang, *Appl. Surf. Sci.*, 2019, **465**, 986–994.

122 N. Madireddi and P. A. Mahanwar, *Int. J. Mater. Metall. Eng.*, 2015, **10**, 34–41.

123 F. Farbod, B. Pourabbas and M. Sharif, *J. Polym. Sci. Part B Polym. Phys.*, 2013, **51**, 441–451.

124 X. Zhang, Z. Liu, X. Zhang, Y. Li, H. Wang, J. Wang and Y. Zhu, *Chem. Eng. J.*, 2018, **343**, 699–707.

125 D. B. Mahadik, K.-Y. Lee, R. V Ghorpade and H.-H. Park, *Sci. Rep.*, 2018, **8**, 1–9.

126 D. Chen, Z. Mai, X. Liu, D. Ye, H. Zhang, X. Yin, Y. Zhou, M. Liu and W. Xu, *Cellulose*, 2018, **25**, 3635–3647.

127 Q.-Y. Cheng, X.-P. An, Y.-D. Li, C.-L. Huang and J.-B. Zeng, *ACS Sustain. Chem. Eng.*, 2017, **5**, 11440–11450.

128 M. S. Silverstein and N. R. Cameron, *Encycl. Polym. Sci. Technol.*, 2010.

129 E. M. Baba, C. E. Cansoy and E. O. Zayim, *Prog. Org. Coatings*, 2016, **99**, 378–385.

130 M. Satapathy, P. Varshney, D. Nanda, S. S. Mohapatra, A. Behera and A. Kumar, *Surf. Coatings Technol.*, 2018, **341**, 31–39.

131 D. Aslanidou, I. Karapanagiotis and C. Panayiotou, *Mater. Des.*, 2016, **108**, 736–744.

132 H. Liu, H. Zhang, J. Pang, Y.-J. Ning, F. Jia, W.-F. Yuan, B. Gu and Q.-P. Zhang, *Mater. Lett.*, 2019, **247**, 204–207.

133 S. Martin and B. Bhushan, *J. Colloid Interface Sci.*, 2017, **488**, 118–126.

134 S. S. Latthe, R. S. Sutar, T. B. Shinde, S. B. Pawar, T. M. Khot, A. K. Bhosale, K. K. Sadasivuni, R. Xing, L. Mao and S. Liu, *ACS Appl. Nano Mater.*, 2019, **2**, 799–805.

135 W. H. Tuminello and G. T. Dee, *Macromolecules*, 1994, **27**, 669–676.

136 J. Blumm, A. Lindemann, M. Meyer and C. Strasser, *Int. J. Thermophys.*, 2010, **31**, 1919–1927.

137 W. Qing, X. Shi, Y. Deng, W. Zhang, J. Wang and C. Y. Tang, *J. Memb. Sci.*, 2017, **540**, 354–361.

138 Y. Liang, J. Ju, N. Deng, X. Zhou, J. Yan, W. Kang and B. Cheng, *Appl. Surf. Sci.*, 2018, **442**,

54–64.

139 X. Zhu, S. Feng, S. Zhao, F. Zhang, C. Xu, M. Hu, Z. Zhong and W. Xing, *J. Memb. Sci.*, 2020, **594**, 117473.

140 H. Y. Erbil, *Langmuir*, 2020, **36**, 2493–2509.

141 Y. Lu, S. Sathasivam, J. Song, C. R. Crick, C. J. Carmalt and I. P. Parkin, *Science (80-.).*, 2015, **347**, 1132–1135.

142 C. R. Crick, in *Superhydrophobic Surfaces-Fabrications to Practical Applications*, IntechOpen, 2018.

143 S. P. Dalawai, M. A. S. Aly, S. S. Latthe, R. Xing, R. S. Sutar, S. Nagappan, C.-S. Ha, K. K. Sadasivuni and S. Liu, *Prog. Org. Coatings*, 2020, **138**, 105381.

144 T. Lv, Z. Cheng, E. Zhang, H. Kang, Y. Liu and L. Jiang, *Small*, 2017, **13**, 1503402.

145 T. T. Isimjan, T. Wang and S. Rohani, *Chem. Eng. J.*, 2012, **210**, 182–187.

146 J. Lee and K. Yong, *NPG Asia Mater.*, 2015, **7**, e201–e201.

147 N. J. Shirtcliffe, G. McHale, M. I. Newton, C. C. Perry and F. B. Pyatt, *Appl. Phys. Lett.*, 2006, **89**, 104106.

148 P. Lv, Y. Xue, Y. Shi, H. Lin and H. Duan, *Phys. Rev. Lett.*, 2014, **112**, 196101.

149 M. Shi, C. Tang, X. Yang, J. Zhou, F. Jia, Y. Han and Z. Li, *RSC Adv.*, 2017, **7**, 4039–4045.

150 B. Wu, C. Peng, W. Li, Z. Yuan and L. Sheng, in *2016 International Conference on Innovative Material Science and Technology (IMST 2016)*, Atlantis Press, 2016.

151 J. J. Hernández, M. A. Monclús, I. Navarro-Baena, F. Viela, J. M. Molina-Aldareguia and I. Rodríguez, *Sci. Rep.*, 2017, **7**, 43450.

152 F. Zhang, H. Qian, L. Wang, Z. Wang, C. Du, X. Li and D. Zhang, *Surf. Coatings Technol.*, 2018, **341**, 15–23.

153 A. Cholewinski, J. Trinidad, B. McDonald and B. Zhao, *Surf. Coatings Technol.*, 2014, **254**, 230–237.

154 J. Zhi and L.-Z. Zhang, *Sci. Rep.*, 2017, **7**, 9946.

155 V. Tuukka, B. Chris, A. Piers, F. Sami, I. Olli and R. R. H. A., *Adv. Mater.*, **23**, 673–678.

156 V. Kondrashov and J. Rühe, *Langmuir*, 2014, **30**, 4342–4350.

157 S. T. Yohe, J. D. Freedman, E. J. Falde, Y. L. Colson and M. W. Grinstaff, *Adv. Funct. Mater.*, 2013, **23**, 3628–3637.

158 A. Solga, Z. Cerman, B. F. Striffler, M. Spaeth and W. Barthlott, *Bioinspir. Biomim.*, 2007, **2**, S126.

159 M. N. Kavalenka, F. Vüllers, S. Lischker, C. Zeiger, A. Hopf, M. Röhrig, B. E. Rapp, M. Worgull and H. Hölscher, *ACS Appl. Mater. Interfaces*, 2015, **7**, 10651–10655.

160 D. J. Babu, M. Mail, W. Barthlott and J. J. Schneider, *Adv. Mater. Interfaces*, 2017, **4**, 1700273.

161 F. Vüllers, Y. Germain, L. Petit, H. Hölscher and M. N. Kavalenka, *Adv. Mater. Interfaces*, 2018, **5**, 1800125.

162 Y. Liu, J. Liu, Y. Tian, H. Zhang, R. Wang, B. Zhang, H. Zhang and Q. Zhang, *Ind. Eng. Chem. Res.*, 2019, **58**, 4468–4478.

163 S. Kim, H. Jeon, S. Shin, S. Park, J. Jegal, S. Y. Hwang, D. X. Oh and J. Park, *Adv. Mater.*, 2018, **30**, 1705145.

164 U. Manna and D. M. Lynn, *Adv. Mater.*, 2013, **25**, 5104–5108.

165 Z. Chen, G. Li, L. Wang, Y. Lin and W. Zhou, *Mater. Des.*, 2018, **141**, 37–47.

166 K. Golovin, M. Boban, J. M. Mabry and A. Tuteja, *ACS Appl. Mater. Interfaces*, 2017, **9**, 11212–11223.

167 F. Vüllers, S. Peppou-Chapman, M. N. Kavalenka, H. Hölscher and C. Neto, *Phys. Fluids*, 2019, **31**, 12102.

168 D. Panchanathan, A. Rajappan, K. K. Varanasi and G. H. McKinley, *ACS Appl. Mater. Interfaces*, 2018, **10**, 33684–33692.

169 T. Simovich, A. Rosenhahn and R. N. Lamb, *Adv. Eng. Mater.*, 2020, **22**, 1900806.

170 I. U. Vakarelski, D. Y. C. Chan, J. O. Marston and S. T. Thoroddsen, *Langmuir*, 2013, **29**, 11074–11081.

171 T.-S. Wong, S. H. Kang, S. K. Y. Tang, E. J. Smythe, B. D. Hatton, A. Grinthal and J. Aizenberg, *Nature*, 2011, **477**, 443–447.

172 S. S. Latthe, R. S. Sutar, A. K. Bhosale, S. Nagappan, C.-S. Ha, K. K. Sadasivuni, S. Liu and R. Xing, *Prog. Org. Coatings*, 2019, **137**, 105373.

173 T. Xiang, M. Zhang, H. R. Sadig, Z. Li, M. Zhang, C. Dong, L. Yang, W. Chan and C. Li, *Chem. Eng. J.*, 2018, **345**, 147–155.

174 Y. Tuo, H. Zhang, W. Chen and X. Liu, *Appl. Surf. Sci.*, 2017, **423**, 365–374.

175 Z. Shi, Y. Ouyang, R. Qiu, S. Hu, Y. Zhang, M. Chen and P. Wang, *Prog. Org. Coatings*, 2019, **131**, 49–59.

176 C. S. Ware, T. Smith-Palmer, S. Peppou-Chapman, L. R. J. Scarratt, E. M. Humphries, D. Balzer and C. Neto, *ACS Appl. Mater. Interfaces*, 2018, **10**, 4173–4182.

177 M. J. Coady, M. Wood, G. Q. Wallace, K. E. Nielsen, A.-M. Kietzig, F. Lagugné-Labarthet and P. J. Ragogna, *ACS Appl. Mater. Interfaces*, 2018, **10**, 2890–2896.

178 G. Rouni and M. Kim, in *International Workshop on Energy Performance and Environmental Quality of Buildings, Milos island, Greece*, 2006.

179 R. J. Baumgart, S. Kanagasabapathy and F. E. Lockwood, *Water based hydrophobic self-cleaning coating compositions*, U.S. Patent Application No. 12/204,432., 2009.

180 J. Song, D. Zhao, Z. Han, W. Xu, Y. Lu, X. Liu, B. Liu, C. J. Carmalt, X. Deng and I. P. Parkin, *J. Mater. Chem. A*, 2017, **5**, 14542–14550.

181 W. Wang, K. Lockwood, L. M. Boyd, M. D. Davidson, S. Movafaghi, H. Vahabi, S. R. Khetani and A. K. Kota, *ACS Appl. Mater. Interfaces*, 2016, **8**, 18664–18668.

182 M. S. Selim, S. A. El-Safty, N. A. Fatthallah and M. A. Shenashen, *Prog. Org. Coatings*, 2018, **121**, 160–172.

183 R. Gupta, V. Vaikuntanathan and D. Sivakumar, *Colloids Surfaces A Physicochem. Eng. Asp.*, 2016, **500**, 45–53.

184 Z.-J. Yu, J. Yang, F. Wan, Q. Ge, L.-L. Yang, Z.-L. Ding, D.-Q. Yang, E. Sacher and T. T. Isimjan, *J. Mater. Chem. A*, 2014, **2**, 10639–10646.

185 L. Wang, J. Yang, Y. Zhu, Z. Li, T. Sheng, Y. M. Hu and D.-Q. Yang, *Colloids Surfaces A Physicochem. Eng. Asp.*, 2016, **497**, 16–27.

186 M. Wu, B. Ma, T. Pan, S. Chen and J. Sun, *Adv. Funct. Mater.*, 2016, **26**, 569–576.

187 L. Gao, W. Gan, S. Xiao, X. Zhan and J. Li, *Ceram. Int.*, 2016, **42**, 2170–2179.

188 S. Gao, J. Huang, S. Li, H. Liu, F. Li, Y. Li, G. Chen and Y. Lai, *Mater. Des.*, 2017, **128**, 1–8.

189 V. A. Maiorov, *Glas. Phys. Chem.*, 2019, **45**, 161–174.

190 A. Chabas, T. Lombardo, H. Cachier, M. H. Pertuisot, K. Oikonomou, R. Falcone, M. Verità and F. Geotti-Bianchini, *Build. Environ.*, 2008, **43**, 2124–2131.

191 X. Huang, N. Tepylo, V. Pommier-Budinger, M. Budinger, E. Bonaccurso, P. Villedieu and L. Bennani, *Prog. Aerosp. Sci.*, 2019, **105**, 74–97.

192 A. M. A. Mohamed, A. M. Abdullah and N. A. Younan, *Arab. J. Chem.*, 2015, **8**, 749–765.

193 C. Antonini, M. Innocenti, T. Horn, M. Marengo and A. Amirfazli, *Cold Reg. Sci. Technol.*, 2011, **67**, 58–67.

194 https://www.synavax.com/hydrophobic-coatings-icephobic-coatings/.

195 K. Golovin, S. P. R. Kobaku, D. H. Lee, E. T. DiLoreto, J. M. Mabry and A. Tuteja, *Sci. Adv.*, 2016, **2**, e1501496.

196 https://www.hullspeed.us/index.php/products#!/~/product/category=10282075&id=39268373.

197 M. S. Ayan, M. Entezari and S. F. Chini, *Int. J. Heat Mass Transf.*, 2019, **132**, 271–279.

198 A. J. Greidanus, R. Delfos and J. Westerweel, in *Journal of Physics: Conference Series*, IOP Publishing, 2011, vol. 318, p. 82016.

199 S. McCormick, *Ecol. Soc.*, 2012, **17**, 31.

200 X. Fan, Y. Liu, X. Quan, H. Zhao, S. Chen, G. Yi and L. Du, *J. Memb. Sci.*, 2016, **514**, 501–509.

201 G. Ren, Y. Song, X. Li, Y. Zhou, Z. Zhang and X. Zhu, *Appl. Surf. Sci.*, 2018, **428**, 520–525.

202 J. Guo, B. J. Deka, K.-J. Kim and A. K. An, *Desalination*, 2019, **468**, 114054.

203 L. Zhang, H. Li, X. Lai, X. Su, T. Liang and X. Zeng, *Chem. Eng. J.*, 2017, **316**, 736–743.

Chapter 2

Optimisation of Superhydrophobic Polymer-Nanoparticle Composite Systems

Publications:

A general formulation approach for the fabrication of water repellent materials: how composition can impact resilience and functionality. R. L. Upton, Z. Davies-Manifold, M. Marcello, K. Arnold and C. R. Crick. *Mol. Syst. Des. Eng.*, 2020, **5**, 477-483.

Contributions:

Focused-Ion Beam preparation and imaging was carried out by Dr. Keith Arnold (Materials Innovation Factory).

Confocal Fluorescence Microscopy imaging was carried out by Dr. Marco Marcello (Liverpool Centre for Cell Imaging).

Fluorescence Lifetime measurements were carried out by Dr. Krzysztof Pawlak (Materials Innovation Factory).

2.1 Introduction

The potential for self-cleaning technology has seen advanced growth in recent years, with many prospective target markets emerging, as outlined throughout chapter 1. When designing coatings for applied self-cleaning technologies [e.g. paints, external building materials and industrial processes], coating optimisation, scalability and adaptability are crucial factors to consider to ensure that coating are high performance and remain operative throughout their lifecycle.[1–3] Superhydrophobic coatings, designed from nanomaterials that have been coated with hydrophobic polymers, can be considered superior to molecular composites, due to having enhanced functional properties, improved resilience and being generally of lower cost.[4] In this chapter, a range of superhydrophobic polymer-nanoparticle composite (SPNC) coatings, fabricated from a range of hydrophobic polymers, will be methodically formulated and optimised, while comparisons are drawn between different SPNC systems (thermoset *vs* thermoplastic).

2.1.1 Polymers: Thermoset vs Thermoplastic

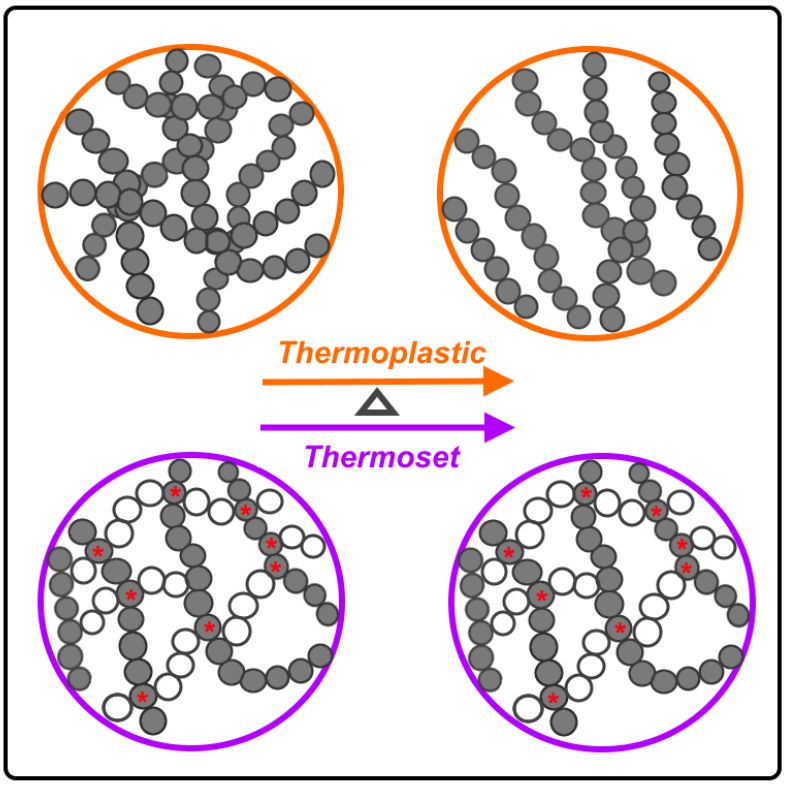

Figure 2.01: Illustration showing the structural differences between thermoplastic polymers and thermoset polymers upon heating; intermolecular interactions between thermoplastic polymer chains are disrupted and the polymer proceeds to melt, whereas thermoset polymers remain structurally intact, due to having a covalently bonded polymer network (crosslinks, marked by red *).

Polymers, both synthetic and naturally occurring, are fundamental in today's society, reflected by their extensive implementation across our everyday lives. Macromolecules built from shorter chained repeating units can be extremely versatile and display a range of unique properties, that are primarily governed by the chemical composition of the monomer(s) used and the subsequent bonding interactions.[5] Generally, when considering a polymers physical response to heat, they can be grouped into two classes; thermosetting and thermoplastic (see Fig. 2.01).[5] Thermosetting polymers can be categorised by their physical change into a solid during heating (from a liquid at room temperature), due to a series of crosslinking reactions, leading to a covalently bonded polymer network. Excessive heating beyond this point will initiate thermal degradation. Conversely, thermoplastic polymers will proceed to melt and enter a fluid state when heated, as the intermolecular forces between linear polymer chains become disrupted (i.e. interruption of relatively weak interactions; Van der Waals, dipole-dipole, hydrogen bonding). Solidification then takes place when the fluid polymer is cooled back to a temperature below its melting point.[6] In line with this, the solvation of thermoset and thermoplastic polymers also differs; thermosetting polymers will only swell in a compatible solvent, due to their highly crosslinked polymer network, whereas thermoplastics can be fully solvated if a suitable solvent and conditions are employed.[6] Hence, specific processing approaches may be needed when designing systems that incorporate different types of polymers. Nonetheless, hydrophobic thermoset and thermoplastic polymers have both been successfully integrated into synthetic highly water repellent materials.

2.1.2 SPNC Materials

As outlined in detail throughout the introductory chapter, extreme surface hydrophobicity can be attributed to the multifaceted surface design of a material, comprising of a combination of micro/nanostructures and intrinsically hydrophobic surface chemistry.[7] This hierarchical surface results in materials with remarkable functional properties, attracting attention in several fields, particularly, self-cleaning technology.[1,8–10] Significant research has shown that the selection of materials used to fabricate superhydrophobic coatings has a broad variety.[11–14] However, the wider functionality and applicability of coatings is often determined by the constituent components of the system. Two fundamental factors which must be considered when designing superhydrophobic coatings are the chemical stability (e.g. UV degradation) and physical resilience (e.g. abrasive wear) of the resultant materials.[15,16] Nanomaterials, in particular, have substantial physical resilience concerns, regarding particle-substrate and inter-particle adhesion, resulting from the small-length scales of materials (see Fig. 2.02).[17,18] Therefore, polymers are often chosen, in comparison to their molecular counterparts, as they

generally display greater resilience due to the presence of highly bonded networks (covalent crosslinks or secondary interactions).

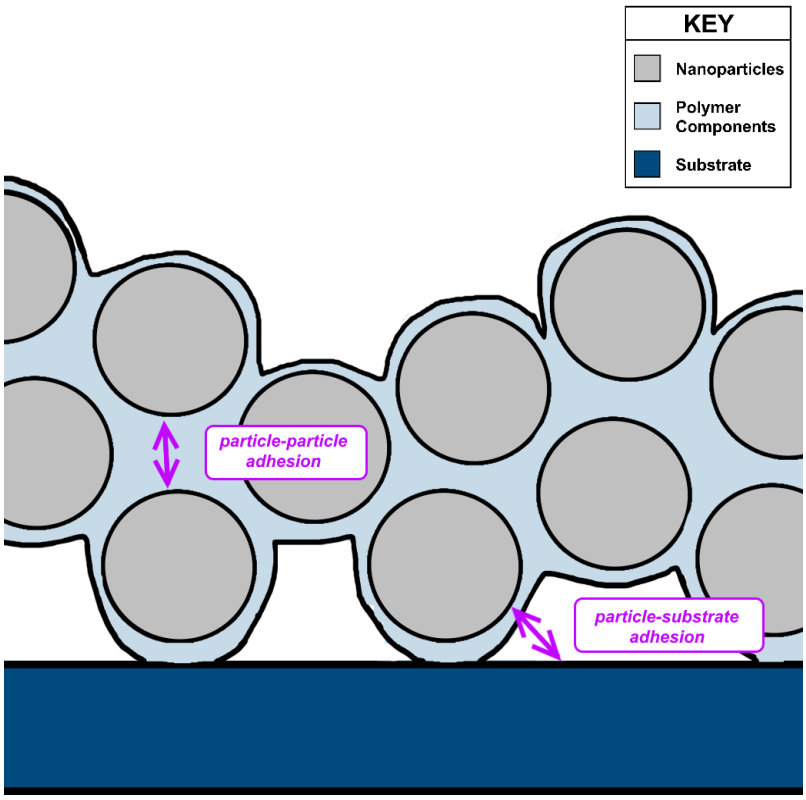

Figure 2.02: Illustration highlighting the inter-particle and particle-substrate adhesion within SPNC coatings.

The majority of reported surfaces are specifically engineered with the utilisation of dedicated techniques or sample preparation.[19] Hydrophobic polymers are regularly implemented in techniques such as moulding, or machining, as a relatively straightforward method of ensuring hydrophobic chemistry and surface roughness.[20–22] Moulding/machining are highly effective roughening techniques, however, are difficult to scale up in a versatile manner. Hence, incorporation of nanoparticles using a 'bottom-up' approach is often a more preferable route to providing high surface roughness, as seen in section 1.5.3, although chemical treatment of their surfaces is often required.[23] Molecular functionalisation of these nanomaterials, can however, increase the films susceptibility to chemical degradation over time.[24] Hence, the optimisation of superhydrophobic materials is not typically a straightforward consideration.

2.1.3 The Importance of Optimisation

As highlighted by Golovin *et al.*, optimisation of highly water repellent materials is essential in order to fabricate materials with enhanced properties and resilience.[25] The relationship between component miscibility and durability of superhydrophobic materials was reported,

where different hydrophobic fillers (small soluble molecules) and polymeric binders (polyurethane and epoxy resins) were combined. In this work, the resultant surface hydrophobicity of coatings was found to be based upon the chemical miscibility of species within a solution. By fine-tuning which components comprised each formulation, *via* the use of solubility parameters and miscibility spheres, and employing a generic spray-coating procedure, they were able to generate a spectrum of surface microtextures (from non-superhydrophobic and smooth, to superhydrophobic and mechanically fragile), while investigating the effects this has on the overall durability of the resultant coatings. Although small molecules were utilised within this work – instead of insoluble metal oxide nanoparticles that are employed within this chapter – and only a small selection of fillers/binders were studied, the same principle applies to both. In that, the mass ratio, inherent surface chemistry and chemical compatibility of formulation components are crucial to consider when designing any superhydrophobic composite system.

Highly water repellent coatings that comprise hydrophobic polymers and nanomaterials have been documented heavily throughout the literature, as seen throughout chapter 1. Although publications that optimise SPNC systems do exist, they do not provide a systematic and comprehensive study of various polymer systems. Furthermore, documented reports of synthetic superhydrophobic materials, engineered from two or more components, typically only vary the weight percentage of one component in the system, without carrying out any systematic analysis; examples of which, can be seen documented throughout sections 1.4 and 1.5. Hence, making it difficult to better deduce how system optimisation is related to the unique coating architecture of each system, which is likely dependent upon the hydrophobic polymer that is being used.

2.1.4 Chapter Aims

In this chapter, the primary aims were to generate an array of SPNC formulations, both solution-based and 'solvent-free', following a generalised fabrication approach that facilitated the comparison of different hydrophobic systems. In doing so, we aimed to identify common trends/discrepancies in relation to coating architectures, and the overall functionality/properties of materials when the polymer component of each system was varied; the theoretical polymer thickness ($\mathbf{r}_{poly}$) surrounding nanoparticles was used as a tool to systematically probe SPNC systems, and relied fundamentally on the polymer:nanoparticle ratio (see section 2.3.2 for full details). Here, alternative deposition techniques were employed, in line with formulation requirements, and readily available materials of low cost were utilised to promote scalable surface coatings. A common thermosetting silicone polymer

polydimethylsiloxane (PDMS) was used, alongside a range of generic thermoplastics [polyvinyl chloride (PVC), polyethylene and polypropylene], and the nanomaterial filler was consistently kept as hydrophobic silica (SiO_2) to ensure a constant component across all formulations. Commonly used polymers were selected for investigation, as these are most relatable to the current industrial and commercial processes. Furthermore, different scale systems were probed, to uncover any effects of varying nanoparticle size on the overall optimisation process.

To achieve this, the following objectives were met:

- Establishment of a systematic method that can be employed to successfully optimise SPNC formulations.
- The fabrication and optimisation of an array of SPNC formulations, incorporating both thermoset and thermoplastic polymers, across a wide range of theoretical polymer thickness values, probing both solution-based and 'solvent-free' formulations.
- Exploration of alternative deposition techniques and experimental conditions, tailored to each individual formulation (spray-coating, dip-coating and use of a parallel plate hot press).
- The scale-up of an SPNC system, replacing 15 nm SiO_2 particles with larger 250 nm particles, to govern any changes in optimisation and functionality.
- Direct comparison of thermoset and thermoplastic SPNC coating architectures, including, polymer curing behaviour and other factors, with the use of confocal fluorescence microscopy, to identify any differences that may affect surface hydrophobicity and/or physical resilience.

2.2 Materials and Methods

2.2.1 Materials

Sylgard-184 (Silicone elastomer) was purchased from Ellsworth Adhesive Ltd. High molecular weight polyvinylchloride (PVC, product number 81387), high-density polyethylene (product number 547999), polypropylene (Mw~340000), silicon dioxide nanopowder (SiO_2, 10-20 nm), fumed silica (SiO_2, 0.2-0.3 μm average particle size), silica gel spherical (SiO_2, 40-75 μm), hexamethyldisilazane (HMDS, reagent grade, ≥ 99 %), 1H, 1H, 2H, 2H-perfluorooctyltriethoxysilane (FAS, 98 %) and diisodecyl phthalate (DIDP) were purchased from Sigma Aldrich. Lucigenin (10,10'-Dimethyl-9,9'-biacridinium dinitrate) and Nile Red (9-(Diethylamino)-5*H*-benzo[*a*]phenoxazin-5-one) were purchased from Tokyo Chemical Industry UK Ltd. Hexane (HPLC grade), tetrahydrofuran (THF, 99+ %, extra pure, stabilized with BHT), xylene (analytical reagent grade), toluene (99.8+ %), chloroform ($CHCl_3$, 99.8%) and ethanol (analytical reagent grade) were purchased from Fisher Scientific Limited. 4-methyl-2-pentanone (99%) and n-butyl acetate (99+%) were purchased from Alfa Aesar. Plasticized PVC coated fabric was purchased from Amazon (Fabrics 2 Cover). Grade P120 aluminium oxide sandpaper was purchased from the hardware store B&Q.

2.2.2 Preparation of SPNC Formulations

2.2.2.1 Solution-Based Formulations

A known mass of polymer was dissolved in a set volume of a compatible solvent (see Table 2.01), with mechanical stirring. All formulations were prepared at ambient temperature, with the exception of polyethylene- and polypropylene-based formulations, which were prepared at 120℃ to encourage dissolution. When the polymer was visibly dissolved, marked by the formation of a clear, colourless solution, HMDS-functionalised SiO_2 nanoparticles were added and the suspension was continuously stirred for:

- Approximately 2 hours for suspensions at ambient temperature, followed by a short period of sonication prior to deposition, to facilitate complete mixing.
- Approximately 1 hour for heated suspensions.

Sonication was avoided and a shorter mixing time was employed for suspensions that required heating, in order to limit solvent evaporation and maintain a constant temperature range which was crucial for uniform depositions.

2.2.2.2 *Dried Formulations*

For dried formulations, plasticized PVC was dissolved from the bought-in plasticized PVC coated fabric by soaking 2 cm x 5 cm strips of material in a beaker of THF, followed by solvent removal, leaving behind blocks of plasticized PVC. 0.2 g of plasticized PVC was re-dissolved in 30 mL THF, before HMDS-functionalised SiO_2 nanoparticles (15 nm, 0.2353 g) were added in the same manner as described in section 2.2.2.1. The solvent was later removed with the use of moderate heating. A dried powder remained after solvent removal, which was then finely ground using a pestle and mortar before use. See Table 2.01 below, for the formulations summary and relevant quantities.

2.2.2.3 Formulation Summary

Table 2.01: SPNC formulation summary, detailing each formulation and their corresponding $\mathbf{r}_{poly}$ range and optimal $\mathbf{r}_{poly}$ value. The SPNC design principle was used to calculate nanoparticle/polymer quantities, based upon theoretical polymer thickness calculations. $\mathbf{r}_{poly}$ refers to the theoretical polymer thickness and $\mathbf{r}_{sphere}$ refers to the average radius of the nanoparticles used.

SPNC System	**#1**	**#2**	**#3**	**#4**	**#5**	**#6**
Nanoparticle	SiO_2	SiO_2	SiO_2	SiO_2	SiO_2	SiO_2
$\boldsymbol{r}_{sphere}$ *(nm)*	7.5	125	7.5	7.5	7.5	7.5
Polymer	PDMS	PDMS	PVC	Polyethylene	Polypropylene	Plasticized PVC
Solvent system	n-Hexane	n-Hexane	THF	Xylene	Xylene	THF
Deposition technique	Spray coat	Spray coat	Spray coat	Dip coat	Dip coat	Hot press
$\boldsymbol{r}_{poly}$ *range (nm)*	2-10	30-120	1.5-5	1.5-5	1.5-5	N/A
Optimal $\boldsymbol{r}_{poly}$ *value (nm)*	5	80	1.5	1.5	1.5	1.5
*Nanoparticle mass (g)**	0.2	0.4	0.2	Varied with r_{poly}	Varied with r_{poly}	0.2353
*Polymer mass (g)**	Varied with r_{poly}	Varied with r_{poly}	Varied with r_{poly}	0.1	0.1	0.2
Solvent volume (mL)	30	60	30	70	70	30
Deposition temperature (℃)	Ambient	Ambient	Ambient	83-87	68-72	180

*Formulations comprising thermoset polymer PDMS (10:1 mass ratio of elastomer and curing agent) and thermoplastic PVC used a constant starting mass of nanoparticles, and formulations comprising thermoplastics, polyethylene and polypropylene, used a constant starting mass of polymer. This was due to the difficulties associated with accurately weighing polyethylene and polypropylene pellets to 4 decimal places.

Table 2.02: Formulation #1 SiO_2-PDMS (r_{sphere} = 7.5 nm) – mass and mass ratio summary for $\mathbf{r}_{poly}$ value range 2-10 nm:

r_{poly}	*Mass ratio*	*Mass SiO_2 nanoparticles (g)*	*Total mass Sylgard-184 (g)*
2	0.413	0.2	0.0826
4	1.042	0.2	0.2084
5	1.452	0.2	0.2905
6	1.933	0.2	0.3870
7	2.491	0.2	0.4981
8	3.132	0.2	0.6263
10	4.682	0.2	0.9363

Table 2.03: Formulation #2 SiO_2-PDMS ($\mathbf{r}_{sphere}$ = 125 nm) – mass and mass ratio summary for $\mathbf{r}_{poly}$ value range 30-120 nm:

r_{poly}	*Mass ratio*	*Mass SiO_2 nanoparticles (g)*	*Total mass Sylgard-184 (g)*
30	0.365	0.4	0.1460
70	1.121	0.4	0.4482
80	1.367	0.4	0.5467
100	1.944	0.4	0.7776
120	2.616	0.4	1.0464

Table 2.04: Formulation #3 SiO_2-PVC ($\mathbf{r}_{sphere}$ = 7.5 nm) – mass and mass ratio summary for $\mathbf{r}_{poly}$ value range 1.5-5 nm:

r_{poly}	*Mass ratio*	*Mass SiO_2 nanoparticles (g)*	*Mass PVC (g)*
1.5	0.425	0.2	0.085
2	0.602	0.2	0.1204
3	1.017	0.2	0.2034
4	1.520	0.2	0.3040
5	2.117	0.2	0.4234

Table 2.05: Formulation #4 SiO_2-polyethylene ($\mathbf{r}_{sphere}$ = 7.5 nm) – mass and mass ratio summary for $\mathbf{r}_{poly}$ value range 1.5-5 nm:

$\boldsymbol{r}_{poly}$	*Mass ratio*	*Mass SiO_2 nanoparticles (g)*	*Mass Polyethylene (g)*
1.5	0.288	0.3472	0.1
2	0.408	0.2451	0.1
3	0.691	0.1447	0.1
4	1.031	0.0970	0.1
5	1.436	0.0696	0.1

Table 2.06: Formulation #5 SiO_2-polypropylene ($\mathbf{r}_{sphere}$ = 7.5 nm) – mass and mass ratio summary for $\mathbf{r}_{poly}$ value range 1.5-5 nm:

$\boldsymbol{r}_{poly}$	*Mass ratio*	*Mass SiO_2 nanoparticles (g)*	*Mass Polypropylene (g)*
1.5	0.273	0.3663	0.1
2	0.387	0.2584	0.1
3	0.654	0.1529	0.1
4	0.979	0.1024	0.1
5	1.361	0.0735	0.1

2.2.3 Hydrophobization of SiO_2 Particles

2.2.3.1 Functionalisation with HMDS

A solution of HMDS (1 mL) in toluene (100 mL) was added to a suspension of as received SiO_2 nanoparticles (10 g) in toluene (250 mL), and refluxed at 120°C for 24 hours with magnetic stirring. Functionalised nanoparticles were then centrifuged (2000 rpm for 10 minutes) and washed once with toluene and twice with ethanol, before being dried in the oven at 80°C overnight to remove any residual ethanol.

2.2.3.2 Functionalisation with FAS

SiO_2 nanoparticles (0.3 g) were suspended in ethanol (25 mL) with mechanical stirring. FAS was added *via* a syringe (0.16 mL), in addition to trimethylamine (0.1 mL) to encourage functionalisation, and the suspension was stirred for a further hour before deposition.

2.2.4 Preparation of Fluorescent Composites

2.2.4.1 Nile Red and SiO_2/PDMS

A stock solution of Nile Red dye in chloroform (1.96 mM, 10 mL) was made up. 30, 60 or 120 μL was pipetted into a pre-weighed PDMS solution (0.1895/0.0189 g in 30 mL $CHCl_3$) and allowed to mechanically stir for 30 minutes at ambient temperature. Following this, HMDS-functionalised SiO_2 (40-75 μm, 0.2 g) was added and the suspension was stirred for an additional 2 hours. Suspensions were then drop-cast onto cover glass substrates (Sigma Aldrich 24 mm x 60 mm, 0.13-0.17 mm) that were positioned on a hotplate that had been previously set to 120°C, for 30 minutes, to encourage solvent to evaporate and facilitate rapid polymer curing.

2.2.4.2 Lucigenin and SiO_2/PVC

A stock solution of Lucigenin dye in distilled water (1.96 mM, 10 mL) was made up. 120 μL was pipetted into a pre-weighed PVC solution (0.1 g in 30 mL tetrahydrofuran) and allowed to mechanically stir for 30 minutes at ambient temperature. Following this, HMDS-functionalised SiO_2 (40-75 μm, 0.2353 g) was added and the suspension was stirred for an additional 2 hours. Suspensions were drop-cast cover glass substrates (Sigma Aldrich 24 mm x 60 mm, 0.13-0.17 mm) at ambient temperature, where solvent evaporation was allowed to take place.

2.2.5 Deposition Techniques

2.2.5.1 Spray-coating

A compression pump and airbrush kit was purchased from Voilamart. The spraying nozzle, pressurised by air at 2 bar, was used at a distance of approximately 4 cm away from the substrate surface. The SiO_2-polymer suspensions, described in section 2.2.2.1, were spray-coated onto glass substrates (Thermo scientific 76 x 26 mm) in a diagonal motion, periodically

across the surface. This was repeated a total of three times for each sample, unless otherwise stated, to ensure even coverage. Coated substrates were left to dry at room temperature – overnight for thermoplastics or at least 48 hours for thermoset polymer coatings, to ensure full curing and limit surface cracking.

2.2.5.2 Dip-coating

An RDC 15 Bungard dip coater (280 x 470 x 960 mm) with manually programmed emersion and withdrawing times, emersion and withdrawing speeds and iteration cycles was used. Settings were programmed as follows: emersion rate of 1530 mm/min; emersion time of 10 seconds; withdrawing rate of 760 mm/min; drying time of 10 seconds; and 7 iterations. A glass substrate was suspended from a height of 30 cm and mechanically moved into the suspension that resided directly below (described in section 2.2.2.1). After all iterations were complete, the coated substrates were left to air dry for 10 minutes.

2.2.5.3 Hot pressing

A layer of composite powder, described in section 2.2.2.2, was manually deposited and spread across the surface of the bought-in plasticized PVC coated fabric substrate, before being pressed at 180℃ under a pressure of 0.1MPa for 30 seconds (30 x 24 cm heating element, bottom plate unheated). This was repeated a total of three times to achieve a near-homogenous surface coating. Following this, any excess powdered coating was removed by light mechanical abrasion and flowing nitrogen gas across the surface. See Figure 2.03 below.

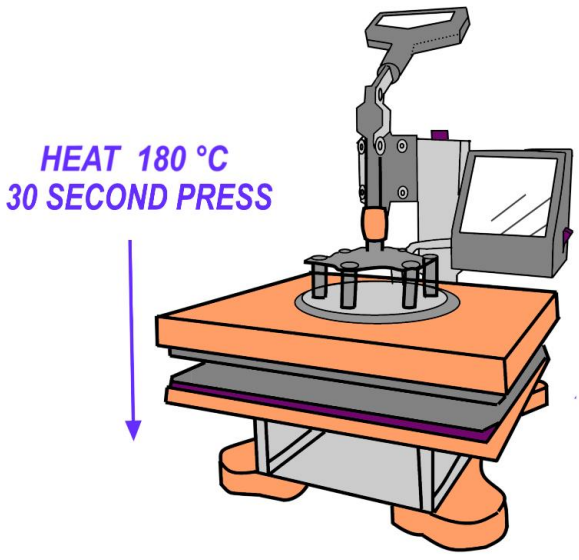

Figure 2.03: Schematic representation of the hot pressing instrument, described in section 2.2.5.3.

2.2.6 Plasticizing PVC with DIDP

High-density PVC and diisodecyl phthalate (DIDP) were manually mixed in a crucible, with the use of a metal spatula. A total mass of 1.00 g was used to determine different weight percentages, as seen below:

Table 2.07: DIDP-plasticized PVC mass summary for varying weight percentages:

Weight percent DIDP	*Total mass (g)*	*Mass PVC (g)*	*Mass DIDP (g)*
40	1.00	0.6	0.4
60	1.00	0.4	0.6
80	1.00	0.2	0.8

The hot plate was set to a temperature of 180 °C and the crucible was placed onto the surface, until PVC was visually observed to dissolve into the plasticizer – changing from a white powder to a clear liquid. Following this, the crucible was removed from the heat and set aside to reach ambient temperature.

2.2.7 Materials Characterisation

Surface morphologies of coatings were analysed using a scanning electron microscope (SEM, JEOL JSM-7001F/Tescan FIB SEM S8000G) operating at an acceleration voltage of 5-10 kV. Samples were vacuum sputter coated in a thin layer of chromium using a Quorum S150T ES sputter coater, to improve electrical conductivity. Fourier Transform Infrared (FTIR) measurements were taken using a Bruker Optics' Vertex 70 over a range of 500 to 4000 cm^{-1}. Confocal fluorescence microscopy was carried out by **Dr Marco Marcello** at the Liverpool Centre for Cell Imaging, using a Zeiss LSM710 on a Zeiss Observer Z1 (Zeiss, Jena, Germany) with a 40x /1.2 NA W Korr and a 63x/1.40 oil objectives. Samples were excited using an argon ion laser at 488 nm and a DPSS 561 nm laser. Data was captured using ZEN software (Zeiss, Jena, Germany). 3D volumetric data consisting of 57 z slices (SiO_2-PDMS) was processed with Imaris x64 8.4.2 (Bitplane A.G., Zurich, Switzerland). Segmentation of the data was performed with a grain size of 0.200 μm, and manual threshold and morphological parameters were measured. Images were stored and managed using OMERO software. Focused-ion beam preparation and imaging (Tescan S8000G) was carried out by **Dr Keith Arnold** at the Materials Innovation Factory. Cross-sections were prepared using a

gallium ion source. The ion beam was operated at between 30 kV and 5 kV, and beam currents ranged between 20 nA and 250 pA. A strap of platinum was deposited onto the surfaces of interest prior to milling, in order to minimise damage. Corresponding micrographs were imaged using the same microscope. Samples were measured using FLS 100 modular fluorescence spectrometer from Edinburgh Instruments. A 450 W xenon arc lamp that emits continuous radiation from 230 nm to >1000 nm was used. The light from the xenon arc was focused into the monochromator using a high-reflectivity off-axis ellipsoidal mirror, ensuring excellent focus at the entrance slit and completely uniform illumination of the monochromator grating. The monochromators in the FLS1000 are of Czerny-Turner configuration with 325 mm or 2 x 325 mm focal length. A photomultiplier tube detector with a wavelength coverage from 200-850 nm was operated at -21.8℃.

2.2.8 Contact Angle Measurements

Static contact angle measurements were taken using a DSA100 Expert Drop Shape Analyser (Kruss GmbH) in the sessile drop operating mode with Young-Laplace fitting and manual assignment of the baseline. 6 μL water droplets were dispensed from a Hamilton microliter syringe with a 30 gauge dispensing tip directly onto the surface and at least 5 contact angle measurements, from evenly distributed positions across the surface, were taken and averaged for every reported contact angle. Tilting angles were recorded manually by dispensing a water droplet on the surface and tilting the surface at 2°/s, recording the angle at which the droplet began to roll. At least 5 measurements, from evenly distributed positions across the surface, were taken and averaged for every reported tilting angle. Surface free energy values were calculated by the DSA100 Expert Drop Shape Analyser using the OWRK method. The OWRK method considers both polar and dispersive interactions within a material, and so uses two different solvents to record contact angles (6 μL droplets), where water was employed as the polar liquid and diiodomethane as the dispersive liquid. Here, 5 measurements were recorded using each solvent and used to compute surface free energy values. Statistical analysis was not performed (investigation of p-values) as clear trends were observed in wettability data when considering larger theoretical polymer thicknesses, and as smaller theoretical polymer thicknesses were reached, contact angle values generally plateaued with low standard deviation. Therefore, suggesting that values were statistically significant, as this fit with the evolving morphologies of surfaces and was consistent across different SPNC systems.

2.2.9 Abrasive Wear Testing

Weighted samples (100 g) were placed face down onto P120 grade aluminium oxide (Al_2O_3) sandpaper. The abrasion process saw samples moving anticlockwise around the square portion of sandpaper used. First, samples were propelled 10 cm horizontally across the sandpaper, before being rotated 90° (anticlockwise) and moved a further 10 cm in the vertical direction to complete one cycle (20 cm in total). Samples were rotated a further 90° to begin the second cycle (continuing anticlockwise, as above) so that substrates were abraded from all angles.

2.2.10 Self-Cleaning Test

Magnesium (IV) oxide (MnO_2) was randomly dispersed on the surface of a coated glass slide, held at an approximate angle of 45°, to simulate dirt particulates. Distilled water, dyed with methylene blue to aid visualisation, was pipetted onto the surface of the coated slide in a downward motion.

2.3 Results and Discussion

2.3.1 Approaching the SPNC Design Principle

Initially, a polymer-solvent system that was established by Crick *et al.* and used to fabricate superhydrophobic films *via* AACVD (see section 1.4.2.2), was used as a benchmark for a preliminary investigation into polymer systems.[26,27] Here, precursor solutions of Sylgard-184 in chloroform were employed to generate superhydrophobic coatings, comprising deposited polymer aggregates.

Although AACVD was successful in generating superhydrophobic materials, it is not readily scalable. To develop a methodology that is more applicable to real-world applications, an alternative deposition technique – spray coating – was used, that could facilitate depositions onto larger areas and over a wider range of substrate materials. The first formulation, that was trialled to gain a basic insight into the deposition of polymers, was Sylgard-184 in chloroform (the same polymer system as reported above). The solution-based formulation was spray-coated onto a heated glass substrate to encourage solvent evaporation and the platinum-catalysed curing of PDMS. Sylgard-184 is a two-part elastomer that consists of a base and a curing agent, mixed in a 10:1 ratio. A platinum catalyst is utilized to initiate bonding between terminal vinyl groups on dimethyl siloxane oligomers (base) and Si-H groups, present on the curing agent component, *via* a proposed hydrosilylation reaction (see Fig. 2.04).

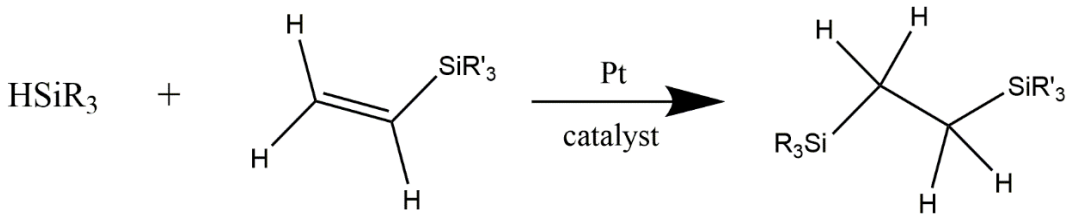

Figure 2.04: Generalised hydrosilylation mechanism between the base and curing agent components of Sylgard-184.

Subsequently, once fully cured at 120℃ for 30 minutes, a hydrophobic film with a contact angle of 104° ± 2 was obtained (Fig. 2.05). It became apparent that spray-coating was not a technique that could independently induce surface texturing, unlike the AACVD process, and that a roughening agent would be required in order to generate a sufficient level of surface texture.

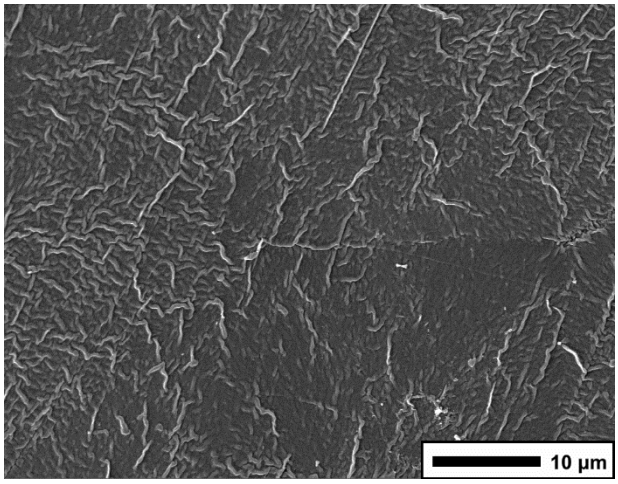

Figure 2.05: SEM micrograph of PDMS coating, deposited *via* spray-coating from a chloroform solution at 120℃. Scale bar is shown.

Hence, inorganic metal oxide nanoparticles (SiO_2 nanoparticles) were introduced into formulations as a support scaffold to enhance morphological texturing. Although inherently hydrophilic, the silanol groups present on the surface of SiO_2 particles can undergo functionalisation to reduce the surface energy and reverse the surface wettability of particles. Hexamethyldisilazane (HMDS) is a widely used hydrophobic molecule, owed to the two trimethylsilyl groups it possesses. Here, it was employed to functionalise SiO_2 nanoparticles, resulting in the covalent bonding of trimethylsilyl groups to the particle surface, *via* the formation of siloxane linkages and the release of ammonia. The proposed mechanism of this reaction is outlined in section 1.5.2.1, where the modification of nanoparticles is discussed. Particle hydrophobicity was corroborated by Fourier-transform infrared spectroscopy (FTIR, see Fig. 2.07) and a visual assessment, where functionalised particles could be seen to suspend in an aqueous solvent (see Fig. 2.06).

Figure 2.06: Image highlighting the dispersion of as received, unfunctionalised SiO_2 nanoparticles in aqueous solution (**left**) and HMDS-functionalised SiO_2 nanoparticles suspending above aqueous solution (**right**), suggesting a change in surface chemistry.

Hydrophilic SiO_2 displayed a signal at 3650 cm^{-1}, representative of surface -OH groups, and at 1100 cm^{-1} which is characteristic of Si-O-Si stretching, respectively.[28] A reduction in the intensity of the band representative of -OH can be observed, highlighting the displacement of surface silanol groups with trimethylsilyl groups, after the functionalisation process. Furthermore, a band observed at ~2980 cm^{-1} can be assigned to the stretching frequency of -CH_3 groups, in addition to bands at ~870 cm^{-1} and ~750 cm^{-1} corresponding to Si-C stretching.[29]

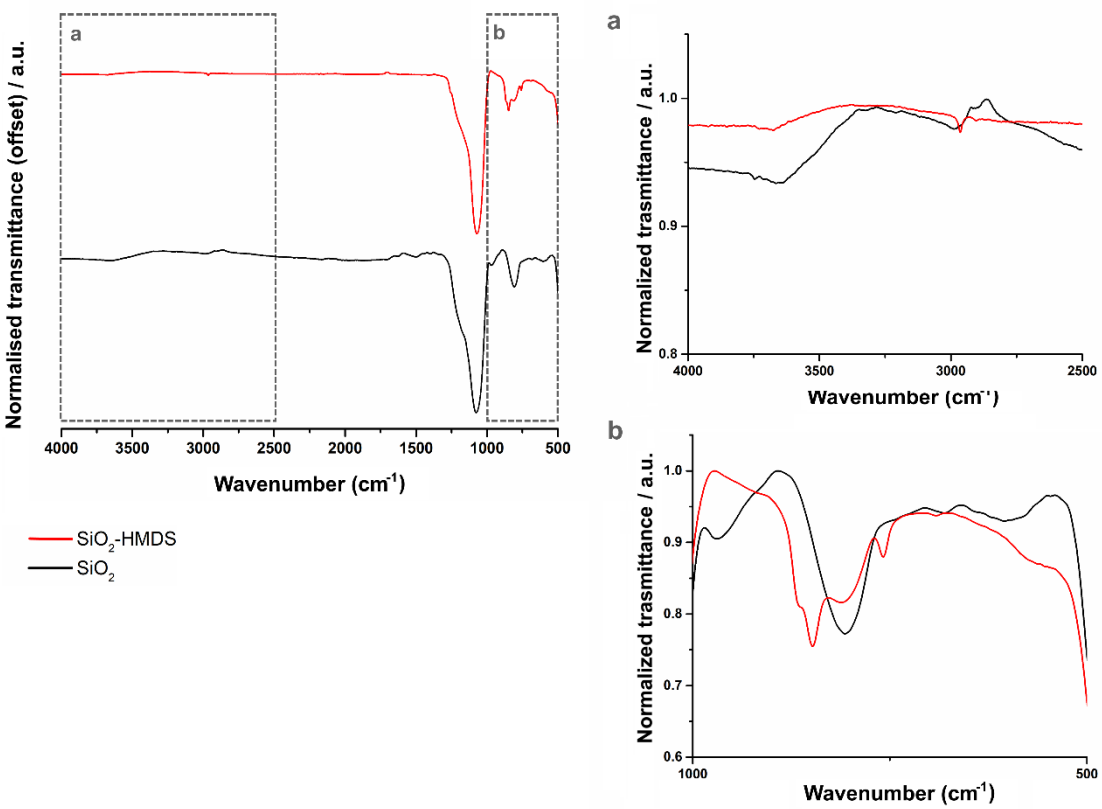

Figure 2.07: Stacked FTIR spectra of HMDS-functionalised SiO_2 nanoparticles (**r_{sphere}** = 7.5 nm, **red line**) and as-received SiO_2 nanoparticles (**r_{sphere}** = 7.5 nm, **black line**). Magnified regions of spectra between; (**a**) 4000-2500 cm^{-1} and (**b**) 1000-500 cm^{-1} for visual aid and accentuation of significant signals.

After hydrophobization, it was anticipated that SiO_2 particles would have enhanced compatibility with both components in the solution (the polymer and the solvent) and so, various formulations were made up. The mass of incorporated SiO_2 nanoparticles was periodically increased to probe any effect that this would have on the resultant surface hydrophobicity of coatings. It was quickly realised that the ratio of polymer:nanoparticle played a fundamental role in the surface structure of the coating; a lack of polymer appeared to provide poor inter-particle adhesion and a resultant SPNC coating with very low physical

resilience, verified arbitrarily with a finger-wipe. Therefore, very little force, such as increasing the size of the water droplet, subsequently enhancing the gravitational force acting on the droplet, or dispensing a droplet from an increased height onto the surface, could have detrimental effects on the integrity of the surface coating. Alternatively, an overabundance of polymer resulted in the filling of the porosity of the nanoparticle scaffold, causing a substantial reduction in surface roughness, and a subsequent decline in surface hydrophobicity (see section 2.3.3, see Fig. 2.08).

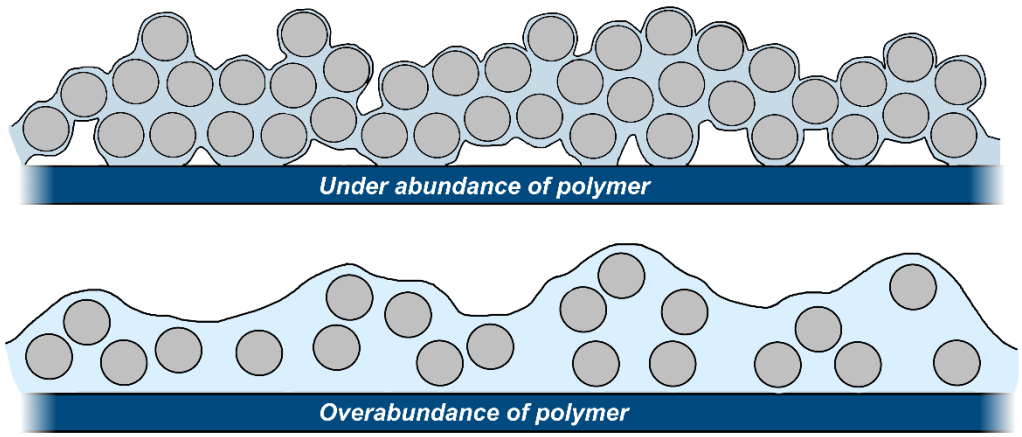

Figure 2.08: Illustration highlighting how an SPNC coating may form with an under abundance of polymer (**top**) or an overabundance of polymer (**bottom**).

Furthermore, it was noticed that rapid solvent removal encouraged the presence of surface cracking, subsequently inducing water pinning to the underlying glass substrate (see Fig. 2.09a). To overcome this, two alterations were made to the process:

(i) Chloroform was replaced with an alternate hydrophobic solvent, n-hexane, which also effectively solubilises Slygard-184, yet has a lower vapour pressure and a higher boiling point.

(ii) The deposition temperature of coatings was changed from 120℃ to room temperature. The platinum-catalysed curing of PDMS is reported to be temperature-dependent, so that time and temperature can be tuned to govern the extent of crosslinking. Hence, full crosslinking can be achieved either at room temperature for 48 hours or at elevated temperatures for shorter periods.

A combination of both appeared to successfully reduce the extent of cracking (see Fig. 2.09b), thus promoting greater coating homogeneity, and were therefore, implemented into the fabrication process from there onwards.

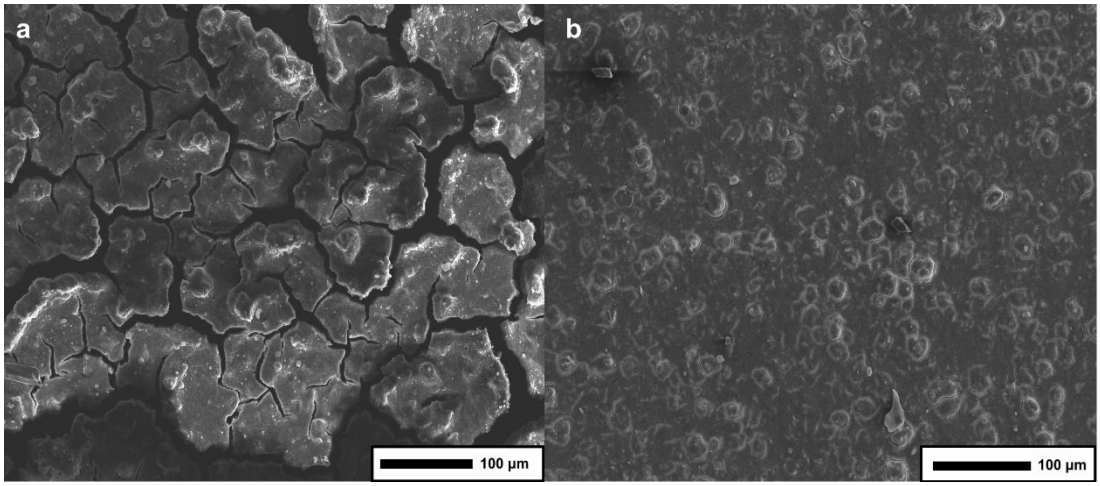

Figure 2.09: SEM micrographs of SiO_2-PDMS composite coatings, deposited *via* spray-coating from; (**a**) a chloroform solution with heat and (**b**) a hexane solution at ambient temperature. In all images, the nanoparticle diameter is 15 nm. Scale bars are shown.

2.3.2 The SPNC Design Principle

After briefly concluding that different factors, e.g. solvent effects, the mass of polymer etc., can impact the resultant surface hydrophobicity of coatings, it became apparent that finding a way to methodically investigate different polymer-nanoparticle systems would be useful and possibly shed more light on how to optimise coatings. Hence, after some preliminary work, we developed the SPNC design principle. This can be considered as a generalised fabrication approach, when adopting key formulation principles (summarised below), and can be extended to many nanomaterials and polymers, as outlined throughout this chapter.

Formulation principles:

- At least 3 components are required; solvent, nanoparticles and polymer.
- All components must satisfy a level of compatibility to ensure homogenous mixing, i.e. surface functionalisation may be required.
- The deposition technique must consider any experimental conditions required to maintain good polymer solubility.

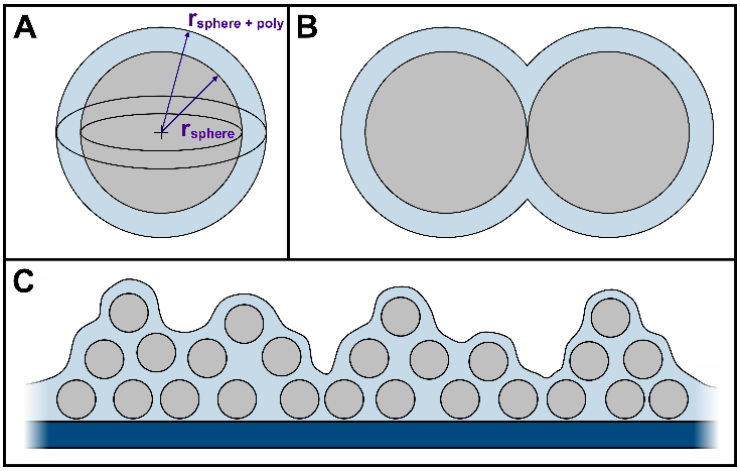

Figure 2.10: Illustration of the SPNC architecture. (**A**) Shows an idealised model of a polymer coating on individual nanoparticles, detailing $\mathbf{r}_{sphere}$ and $\mathbf{r}_{poly.}$ (**B**) The importance of considering the polymer:nanoparticle composition when two nanoparticles make contact. (**C**) Shows an SPNC coating on a substrate after drying has taken place.

The primary factor in the design of SPNC coatings is the polymer:nanoparticle composition. This governs the theoretical thickness of the external polymer coating ($\mathbf{r}_{poly}$, Fig. 2.10A) that surrounds the nanoparticle core ($\mathbf{r}_{sphere,}$ average particle radius), and the manner in which the polymer layer forms between multiple nanoparticles (Fig. 2.10B). To convert theoretical compositions into mass ratios, specific to each formulation, firstly, theoretical spherical volume ratios were calculated based on the average size of the nanoparticle core, and the core and polymer shell combined ($\mathbf{r}_{sphere+poly}$), as illustrated in Fig. 2.10A.

$$Theoretical\ Volume_{\ (sphere\ +\ poly)}: 4/3\pi*(\mathbf{r}_{sphere\ +\ poly\ *\ 10^{-9}})^3$$

$$Theoretical\ Volume_{\ (sphere)}: 4/3\pi*(\mathbf{r}_{sphere\ *\ 10^{-9}})^3$$

$$Theoretical\ Volume_{\ (poly)} = Volume_{\ (sphere\ +\ poly)} - Volume_{\ (sphere)}$$

The densities of the respective nanomaterials/polymer can then be incorporated to yield mass ratios for practical implementation. Although theoretical polymer thickness values are calculated with precision, it is important to stress that this is only a guideline for the comparative assessment of different polymer-nanoparticle systems. Varying from system to system, homogenous coating of particles with polymer may not be achieved and yet calculations are based upon this theory (idealised case). Hence, the SPNC design principle is primarily implemented as a systematic method to probe the coating formation of individual

systems and highlight any differences in the resultant properties of films, when subject to increasing theoretical polymer thickness and ultimately a reduction in surface texture.

2.3.3 SPNC Systems

SPNC formulation systems can range in complexity, from the facile combination of readily available components that are ideal for industrial scale-up, to the methodical development of compatible constituents. However, in this work, SiO_2 nanoparticles that required hydrophobic treatment prior to use (see section 2.3.1), were used to formulate composite suspensions, as they are robust metal oxide particles that show no photoactivity. Hence, short term photodegradation of polymer coatings, which is known to modify the surface chemistry of films over time, was not considered to be a concern, and coatings could be comparatively assessed.

Generally, three components are required to fabricate a working SPNC formulation; (**i**) a roughening agent to generate a textured surface architecture, in this case, SiO_2 (can be extended to other nanoparticles providing that they are compatible, see chapter 3); (**ii**) a hydrophobic polymer to generate surface hydrophobicity, while adhering particles together to form a more resilient coating, and finally (**iii**) a solvent that is compatible with both, nanoparticles and polymer, to provide a medium where homogenous mixing can take place without comprising or effecting the interactions between components. Throughout this work, solution-based and dried SPNC formulations were generated and different coating deposition approaches were taken (including; spray-coating, dip-coating and the use of a hot press), governed by the suitability of each individual coating formulation (see Fig. 2.11), which will be discussed in detail in the forthcoming sections.

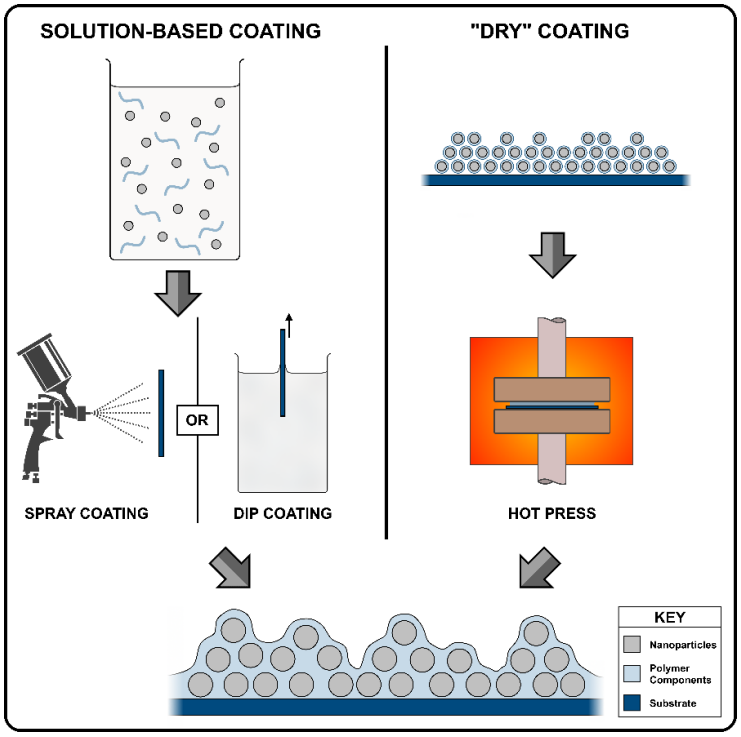

Figure 2.11: Schematic detailing the SPNC fabrication routes. Solution-based SPNCs require polymer dissolution and nanoparticle suspension in the same solvent, followed by coating onto a surface (**left**). The alternative approach of a "dried" coating, hot presses a 'solvent-free' composite to form a compacted SPNC coating – this method is only suitable for thermoplastic polymers (**right**). A key shows the respective coating components.

2.3.3.1 Solution-Based SPNC Formulations

Two main fabrication routes were chosen to generate an array of solution-based SPNC formulations. Formulations that required only facile mixing at room temperature were deposited *via* spray-coating, and to enable the use of polymers that required elevated temperatures to remain solvated, dip-coating was employed as an alternative technique.

2.3.3.1.1 Thermoset Systems

SiO_2-PDMS Formulation System

SiO_2 ($\mathbf{r}_{sphere}$ = 7.5 nm) coated with a thermoset polymer (PDMS), in hexane, was used as a model system for SPNC development, and is a principal example of a coating formulation that could be deposited at room temperature, *via* the aforementioned spray-coating technique. A wide range of polymer thicknesses were examined here ($\mathbf{r}_{poly}$ = 2-10 nm), to probe how increasing the mass of polymer can impact surface hydrophobicity. FTIR was employed to

confirm the coating of particles with PDMS (see Fig. 2.12), where a signal representative of CH_3 stretching in Si-CH_3 could be seen at 2962 cm^{-1}, a signal characteristic of the CH_3 symmetric deformation of Si-CH_3 at 1257 cm^{-1}, a signal arising from Si-O-Si stretching at 1057 cm^{-1}, and a band at 797 cm^{-1} due to the Si-C stretching vibration, respectively, in both pure PDMS and SiO_2-PDMS spectra (optimal $\mathbf{r}_{poly}$ coating, see later).[30,31]

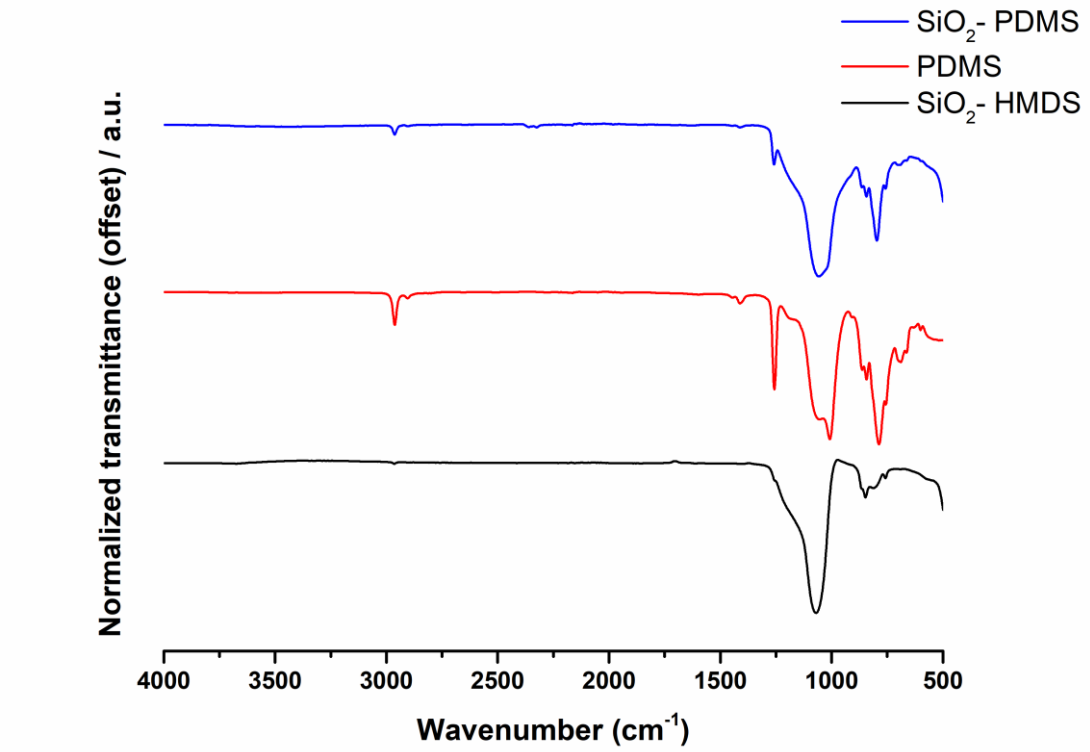

Figure 2.12: Stacked FTIR spectra of SiO_2-PDMS composite ($\mathbf{r}_{sphere}$ = 7.5 nm, $\mathbf{r}_{poly}$ = 5 nm **blue line**), PDMS (**red line**) and HMDS-functionalised SiO_2 nanoparticles ($\mathbf{r}_{sphere}$ = 7.5 nm, **black line**).

Table 2.08: Recorded contact angles and tilting angles for **Formulation #1** SiO_2-PDMS ($\mathbf{r}_{sphere}$ = 7.5 nm):

$\mathbf{r}_{poly}$	*Recorded static contact angle*	*Recorded tilting angle*
2	162° ± 2	5° ± 2
4	162° ± 2	6° ± 1
5	165° ± 2	5° ± 2
6	164° ± 1	6° ± 2
7	156° ± 8	7° ± 2
8	132° ± 15	>90°
10	107° ± 3	>90°

The SiO_2-PDMS system yielded an optimal $\mathbf{r}_{poly}$ value of 5 nm, displaying a contact angle of 167° ± 2 which is indicative of a highly roughened surface morphology. Samples were imaged *via* scanning electron microscopy (SEM) to confirm this. An excess of polymer was shown to dramatically reduce surface roughness, and subsequently, lower contact angles were observed, as seen in Table 2.08. This is reflected clearly in Fig. 2.13, where small aggregates of polymer-coated particles can be seen for the coating with an $\mathbf{r}_{poly}$ value of 6 nm. This is in direct contrast to the near-smooth polymer surface that was observed for an $\mathbf{r}_{poly}$ value of 10 nm, in which SiO_2 nanoparticles were embedded deep within the polymer coating, and almost all surface texture was lost. On the other hand, thinner coatings maintained superhydrophobicity, showing a minor decline in contact angle, as the theoretical polymer thickness value approached 2 nm. This reduction in contact angle, in line with smaller $\mathbf{r}_{poly}$ values, may be due to an incomplete encapsulation of nanoparticles by the polymer matrix. This, in turn, would expose the incoming droplet to different surface chemistries, and therefore, directly influence surface wettability. Additionally, a limited presence of polymer may limit inter-particle adhesion, potentially causing the droplet to penetrate somewhat into the surface coating. Nonetheless, PDMS coatings appeared to be relatively homogenous which was reflected by the low variation in contact angle for thinner polymer coatings; similarly, this was verified in chapter 3 for TiO_2-PDMS systems *via* scanning transmission electron microscopy (S-TEM), where a near-uniform polymeric coating can be observed surrounding aggregated particles.

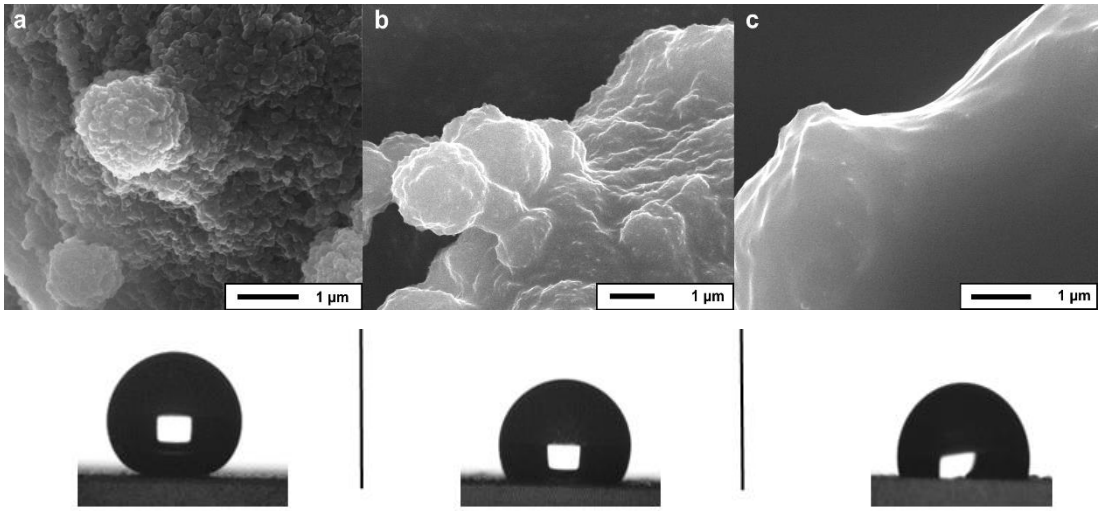

Figure 2.13: SEM micrographs of SiO_2-PDMS SPNCs at high magnification, deposited *via* spray-coating from a hexane solution. In all images the nanoparticle diameter is 15 nm, with polymer thicknesses of; (**a**) 6 nm; (**b**) 8 nm; and (**c**) 10 nm. Scale bars are shown. Additional images highlight the shape of a water droplet resting on the corresponding surface coating.

Tilting angles were recorded to shed more light on the interaction of water with these surfaces. It can be seen that tilting angles were <10° for coatings with an $\mathbf{r}_{poly}$ value of ≤ 7 nm, suggesting that a Cassie-Baxter wetting state is achieved. Air retained within the porosity of the surface coating provides a barrier against wetting and water rapidly moves across the surface with very little adhesion. However, as polymer coatings grow in thickness (8-10 nm), a combination of increasing pore volume and a reduction in pore number, induces water pinning to the tops of the surface microstructure. Hence, coatings undergo a wetting state transition to the 'sticky' Wenzel state, reflected here by a sharp reduction in contact angle and tilting angles that exceed 90°. When considering the 'real world' effects this could have on a surface coating, an excessive $\mathbf{r}_{poly}$ value not only increases water adhesion, but leads to a reduction in the efficiency of the self-cleaning phenomenon the Lotus Effect, as seen in Figure 2.14. For example, optimal SiO_2-PDMS coatings were employed in collaboration with Dr Darren Cook at the Liverpool School of Tropical Medicine, whereby superhydrophobic paper cones were designed in order to collect mosquito excretion for examination. Here, it was fundamental that low contact angle hysteresis was achieved, to prevent the adhesion of excretion droplets to the walls of the cone, and to facilitate the collection efficiency. Hence, highlighting the importance of considering polymer thickness when designing a functional SPNC system.

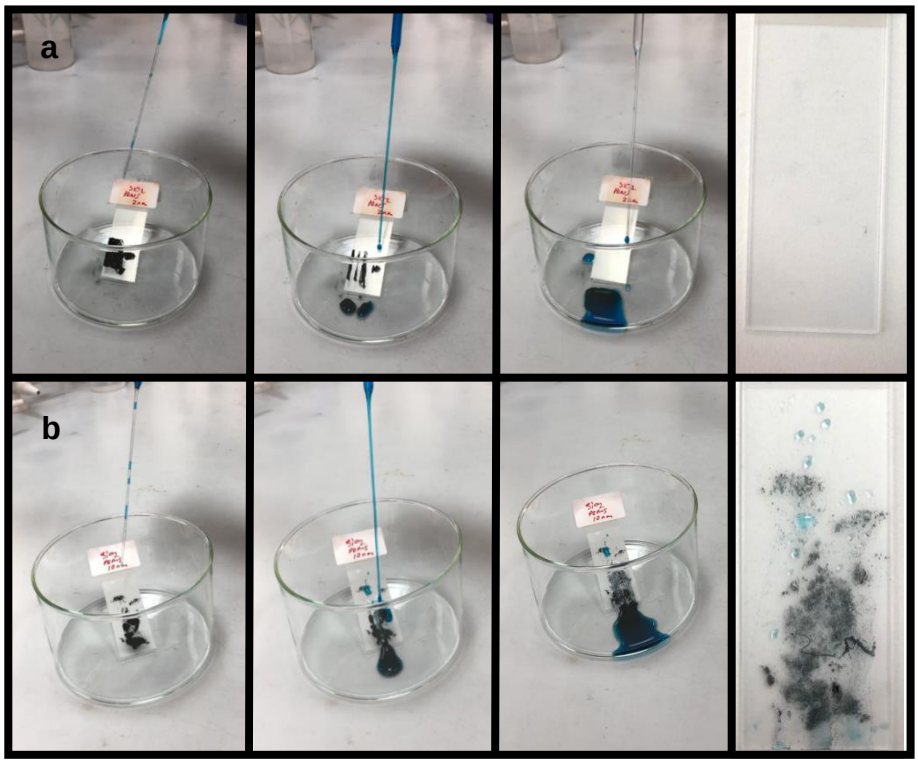

Figure 2.14: Self-cleaning tests before, during and after the removal of 'dirt' (MnO_2) from the coating surface by water *via* the Lotus Effect (dyed with methylene blue to aid visualisation); (**a**) SiO_2-PDMS ($\mathbf{r}_{sphere}$ = 7.5 nm, $\mathbf{r}_{poly}$ = 2 nm) and (**b**) SiO_2-PDMS ($\mathbf{r}_{sphere}$ = 7.5 nm, $\mathbf{r}_{poly}$ = 10 nm).

During further investigation, larger particles were introduced into an equivalent SPNC system (SiO_2-PDMS) to deduce any effects of increasing particle size on surface hydrophobicity and coating functionality. Here, duplicate formulations were made up. However, 250 nm fumed SiO_2 particles were now employed in place of 15 nm particles, and the reported polymer thickness values were scaled-up for an $\mathbf{r}_{poly}$ value range of 2-7 nm – which previously displayed the greatest surface hydrophobicity in the smaller scale system – as detailed below in Table 2.09:

Table 2.09: $\mathbf{r}_{poly}$ conversion table for SiO_2-PDMS formulations with an $\mathbf{r}_{sphere}$ value of 7.5 nm and 125 nm:

$\boldsymbol{r}_{poly}$ ($\boldsymbol{r}_{sphere}$ = 7.5 nm)	*Corresponding scaled-up* $\boldsymbol{r}_{poly}$ ($\boldsymbol{r}_{sphere}$ = 125 nm)
2	30
4	70
5	80
6	100
7	120

FTIR was used here also, to confirm the functionalisation of particles with PDMS, where the spectrum was near-identical to that of the 15 nm particle system (see appendix, Fig. A1). It was found that the optimal $\mathbf{r}_{poly}$ value for a 250 nm particle ($\mathbf{r}_{sphere}$ = 125 nm) was 80 nm, which interestingly, aligns well with the results obtained for smaller particles ($\mathbf{r}_{poly}$: particle size ≈ 1:3). Although it would be reasonable to predict that the surface features within this system would be marginally larger due to the use of larger particles, surface hydrophobicity was observed to be very similar [165° ± 1 for ($\mathbf{r}_{sphere}$ = 125 nm // $\mathbf{r}_{poly}$ = 80 nm,) compared to 165° ± 2 for ($\mathbf{r}_{sphere}$ = 7.5 nm // $\mathbf{r}_{poly}$ = 5 nm)]. Formulations are prone to unorganised aggregation during the deposition process and both systems comprised nano-scale particles, therefore, it is likely that overall aggregate size is comparable. Nonetheless, surface hydrophobicity was lost for polymer coatings that exceeded $\mathbf{r}_{poly}$ values of 80 nm, i.e. 100 nm and 120 nm, which translate to 6 nm and 7 nm in the smaller scale system, both of which, exhibited high water repellency. So it can therefore, be deduced that the range of $\mathbf{r}_{poly}$ values that gave rise to superhydrophobic coatings became increasingly limited as the particle size was increased.

Table 2.10: Recorded contact angles and tilting angles for **Formulation #2** SiO_2-PDMS ($\mathbf{r}_{sphere} = 125$ nm):

$\mathbf{r}_{poly}$	*Recorded static contact angle*	*Recorded tilting angle*
30	162° ± 2	6° ± 2
70	163° ± 2	5° ± 1
80	165° ± 1	5° ± 1
100	134° ± 8	>90°
120	123° ± 9	>90°

In line with this, the surface microstructure of coatings with lower $\mathbf{r}_{poly}$ values ($\leq$ 80 nm) appeared to have a comparable topography to that of the thinner polymer coatings ($\leq$ 6 nm) within the smaller scale system (Formulation #1, see appendix, Fig. A2), where polymer-particle agglomerates can be seen randomly dispersed, frequently throughout the surface. As the $\mathbf{r}_{poly}$ value began to increase, particularly for 100 nm and 120 nm, aggregates are still present but areas in between were noticeably flatter. Nonetheless, the change in surface microstructure was not as intense as the smaller scale SiO_2-PDMS SPNC system, where an obvious difference in surface roughness can be seen in the micrographs for coatings with a polymer thickness of 8 nm and 10 nm (see Fig. 2.13 *vs* Fig. 2.15). Titling angles revealed an almost-identical trend, in that, a Cassie-Baxter wetting state was adopted for coatings with smaller $\mathbf{r}_{poly}$ values, and as theoretical polymer thickness was enhanced, increased water pinning was observed, with reported tilting angles that exceed 90° for 100 nm and 120 nm polymer coatings.

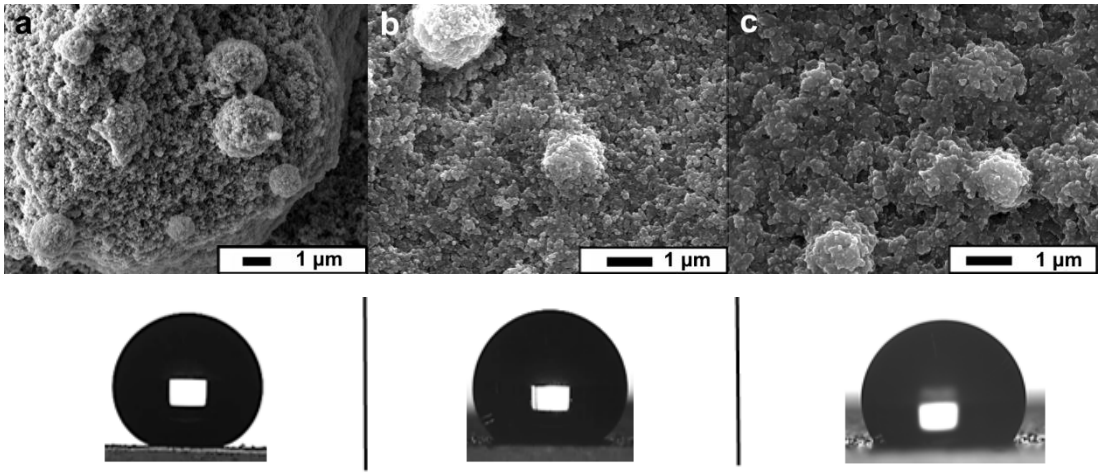

Figure 2.15: SEM micrographs of SiO_2-PDMS SPNCs at high magnification, deposited *via* spray-coating from a hexane solution. In all images the nanoparticle diameter is 250 nm, with polymer thicknesses of; (**a**) 80 nm; (**b**) 100 nm; and (**c**) 120 nm. Scale bars are shown. Additional images highlight the shape of a water droplet resting on the corresponding surface coating.

2.3.3.1.2 Thermoplastic Systems

SiO_2-PVC Formulation System

To draw comparisons between thermoset polymer systems, in which the polymer undergoes crosslinking in the presence of heat, and thermoplastic polymer systems, where ambient temperatures can be used to harden the polymer after solvent removal, common thermoplastic polymers were also studied. PVC was chosen as the initial thermoplastic polymer under investigation, as it can be fully solubilised in THF at ambient temperature. Hence, PVC-based formulations could be deposited in the same way, using the spray-coating technique that was employed for PDMS-based formulations, subsequently allowing any differences in coating formation to be accounted for (see section 2.3.4.2).

Formulations comprising SiO_2 ($\mathbf{r}_{sphere}$ = 7.5 nm), pre-functionalised with HMDS and coated with high-density PVC, in THF, were made up with theoretical polymer thicknesses spanning 1.5-5 nm. In line with thermoset systems, FTIR was employed to detect the polymer; characteristic vibrational stretches can be seen at 2800-3000 cm^{-1}, representative of aliphatic C-H stretches, at 2910 cm^{-1} owed to an asymmetric methylene C-H stretch, between 1425-1200 cm^{-1} which can be assigned to the C-H (H-C-Cl) stretch, at 1329 cm^{-1} typical of the in-plane CH deformation, and at 958 cm^{-1} which corresponds to C-H rocking vibrations, respectively.[32] Vibrational bands corresponding to characteristic PVC stretches could be seen in the SiO_2-PVC sample ($\mathbf{r}_{poly}$ value of 5 nm), as seen below in Figure 2.16.

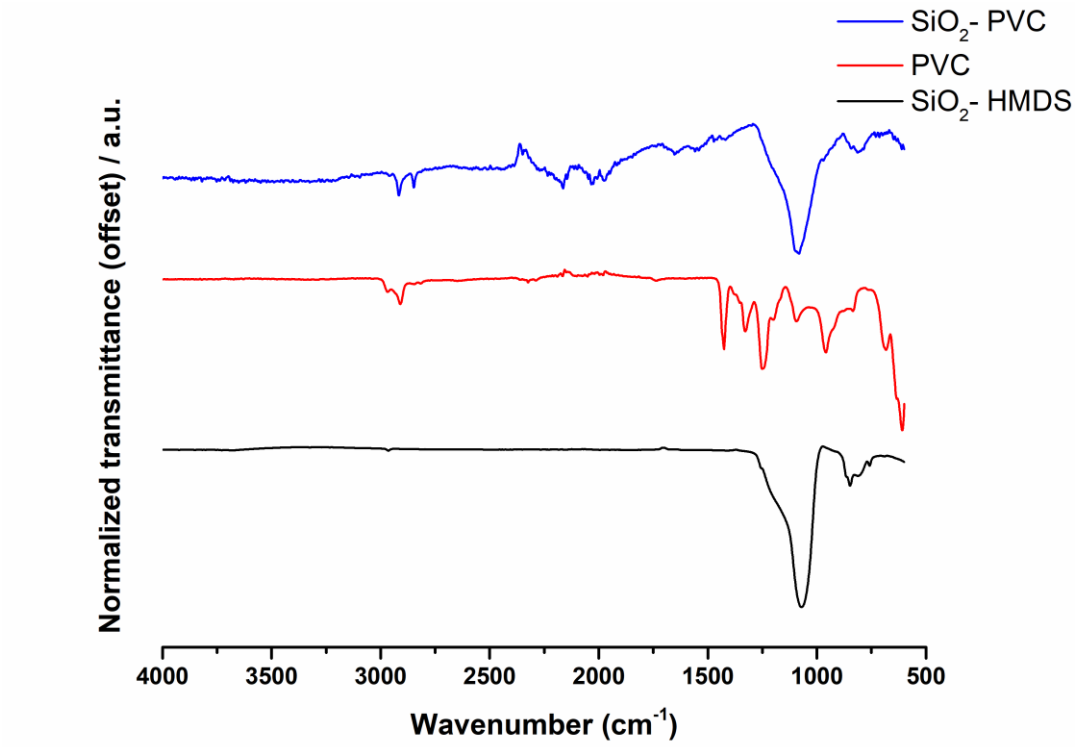

Figure 2.16: Stacked FTIR spectra of SiO_2-PVC composite ($\mathbf{r}_{sphere}$ = 7.5 nm, $\mathbf{r}_{poly}$ = 5 nm **blue line**), high density PVC (**red line**) and HMDS-functionalised SiO_2 nanoparticles ($\mathbf{r}_{sphere}$ = 7.5 nm, **black line**).

Table 2.11: Recorded contact angles and tilting angles for **Formulation #3** SiO_2-PVC ($\mathbf{r}_{sphere}$ = 7.5 nm):

$\mathbf{r}_{poly}$	*Recorded static contact angle*	*Recorded tilting angle*
1.5	165° ± 2	23° ± 18
2	156° ± 6	31° ± 33
3	149° ± 10	64 ° ± 35
4	119° ± 4	>90°
5	113° ± 9	>90°

In contrast to thermoset systems, which generally displayed an optimum $\mathbf{r}_{poly}$ value that was mid-range (Formulation #1/2, see section 2.3.3.1.1), SiO_2-PVC coatings exhibited an alternative trend, whereby surface hydrophobicity decreased in line with increasing polymer thickness; as seen in Table 2.11. The optimal $\mathbf{r}_{poly}$ value for this system was 1.5 nm ($\mathbf{r}_{poly}$: particle size ≈ 1:10) and superhydrophobicity was promptly lost for coatings when the $\mathbf{r}_{poly}$ value ≥ 3 nm. Despite employing nanoparticles of the same size (i.e. SiO_2 $\mathbf{r}_{sphere}$ = 7.5 nm), a

different relationship between the theoretical polymer thickness and surface wettability, highlights a change in coating formation/architecture for thermoplastic systems. Prospectively, this can be attributed to the variation in which different types of polymers form around the nanoparticle scaffold, which is subsequently dependent on several factors (see section 2.3.4.2 for a more detailed discussion), and is fundamental in governing the optimal nanoparticle:polymer ratio of any given system. It can be seen from SEM micrographs (see Fig. 2.17) that uniform polymer coverage around nanoparticles/nanoparticle aggregates is not achieved, unlike that of PDMS systems, giving rise to the reduced surface hydrophobicity as the $\mathbf{r}_{poly}$ value is increased. Alternatively, nanoparticles appeared to be protruding through a thickened polymer layer, where areas of exposed nanoparticles in the absence of polymer were visible. Additionally, flat regions of polymer that lacked any roughening agent could also be observed. As a result, different surface textures exist and alternate surface chemistries are exposed, consequently, inducing water pinning which is reflected in the rapidly increasing tilt angles. In comparison to thermoset systems, which displayed tilting angles <10° across a wide range of $\mathbf{r}_{poly}$ values (2-7 nm), all SiO_2-PVC coatings displayed tilting angles that could be considered atypical of a 'characteristic' superhydrophobic material i.e., those surfaces which adopt a Cassie-Baxter wetting state. Coatings with an $\mathbf{r}_{poly}$ value of 1.5 nm and 2 nm exhibited tilting angles of $23° \pm 18$ and $31° \pm 33$, suggesting that a form of intermediate wetting state exists i.e., a transitional state between stable Cassie-Baxter and Wenzel regimes, whereby water partially adheres to the surface microstructure and penetrates slightly into the porosity, before completely adopting a Wenzel wetting state – as seen for coatings with an $\mathbf{r}_{poly}$ value >3 nm. Due to the lack of homogeneity within PVC-based surface coatings, surface roughness becomes quickly compromised, in line with an increasing mass of polymer, and over a smaller $\mathbf{r}_{poly}$ range than what would be observed for a system with greater chemical compatibility, e.g. SiO_2-PDMS. Subsequently, reducing the liquid-vapour interfacial area and exposing larger solid fractions which facilitate water adhesion.

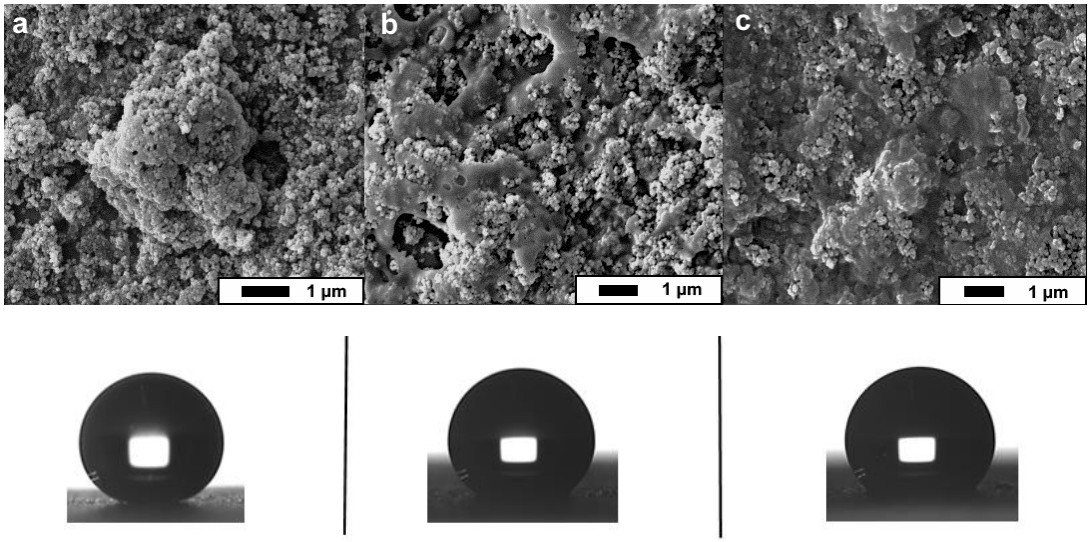

Figure 2.17: SEM micrographs of SiO_2-PVC SPNCs at high magnification, deposited *via* spray-coating from a THF solution. In all images the nanoparticle diameter is 15 nm, with polymer thicknesses of; (**a**) 1.5 nm; (**b**) 2 nm; and (**c**) 3 nm. Scale bars are shown. Additional images highlight the shape of a water droplet resting on the corresponding surface coating.

SiO_2-Polyethylene Formulation System

SiO_2-polyethylene was the first thermoplastic system that required the use of the dip coater. Optimal deposition parameters including; emersion rate, emersion time, withdrawing rate, drying time and the number of cycles (termed iterations) were established for SiO_2-polyethylene, and were used for both thermoplastic systems which required elevated solvation temperatures (see appendix, Table A1/A2). Individual deposition temperature ranges were experimentally determined for each formulation, in order to avoid premature precipitation and/or re-dissolution of polymer from the substrate. For SiO_2-polyethylene coatings, a deposition temperature range of 83-87 ℃ was chosen, where the polymer remained fully solubilised in xylene – verified by a clear and colourless precursor solution. In line with that of SiO_2-PVC, formulations with theoretical polymer thickness values ranging from 1.5-5 nm were investigated. The recorded FTIR spectrum of the composite coating ($\mathbf{r}_{poly}$ value of 5 nm) displayed peaks corresponding to both SiO_2 and polyethylene, as seen in Figure 2.18; vibrational bands at 2916 cm^{-1} and 2848 cm^{-1}, representative of C–H asymmetric and C–H symmetric stretching vibrations, could be seen. In addition to bands at 1471 cm^{-1} and 717 cm^{-1}, owing to the C–H deformation vibrations and C–C rocking vibrations in CH_2 groups.[33] Hence, it could be concluded that polymer was present within the composite coating.

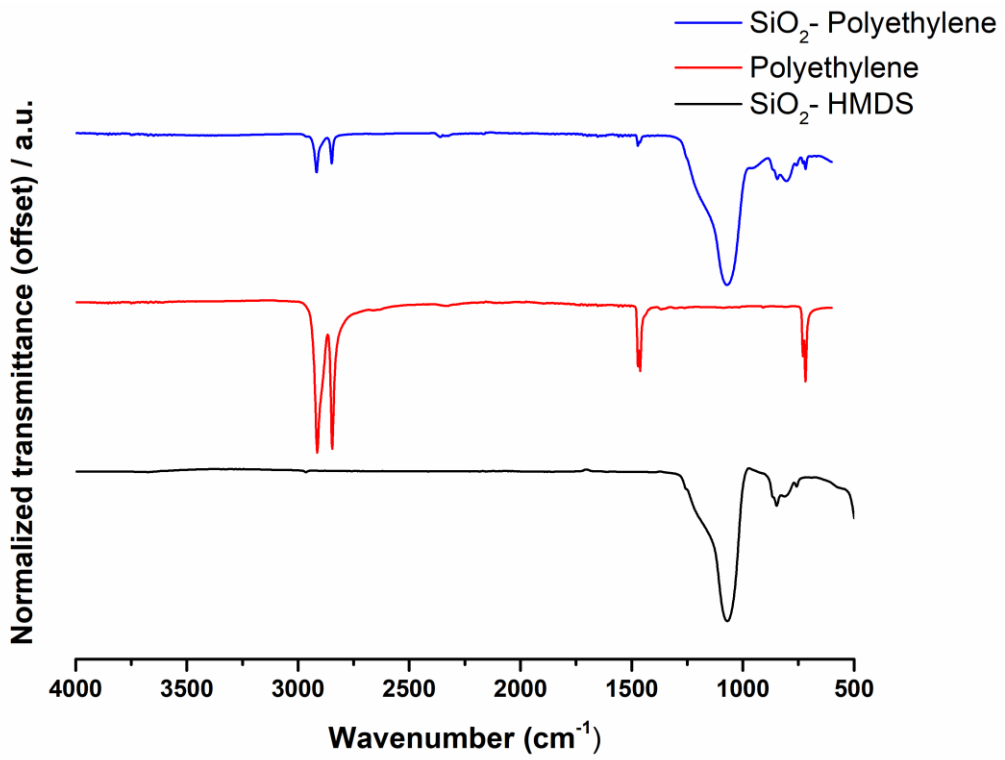

Figure 2.18: Stacked FTIR spectra of SiO_2-polytheylene composite ($\mathbf{r}_{sphere}$ = 7.5 nm, $\mathbf{r}_{poly}$ = 5 nm, **blue line**), polyethylene (**red line**) and HMDS-functionalised SiO_2 nanoparticles ($\mathbf{r}_{sphere}$ = 7.5 nm, **black line**).

Table 2.12: Recorded contact angles for **Formulation #4** SiO_2-polyethylene ($\mathbf{r}_{sphere}$ = 7.5 nm):

$\mathbf{r}_{poly}$	*Recorded static contact angle*
1.5	165° ± 2
2	162° ± 3
3	161° ± 2
4	154° ± 7
5	143° ± 6

SiO_2 ($\mathbf{r}_{sphere}$ = 7.5 nm) pre-functionalised with HMDS and coated with polyethylene, in xylene, yielded an optimal $\mathbf{r}_{poly}$ value of 1.5 nm, displaying a contact angle of 165° ± 2. Contact angles were determined to steadily decline, in line with increasing $\mathbf{r}_{poly}$ value, and coatings with an $\mathbf{r}_{poly}$ value that exceeded 4 nm, resulted in the loss of superhydrophobicity (see Table 2.12). This system displayed a similar trend to what was observed for the first examined thermoplastic system, SiO_2-PVC (Formulation #3), despite two different deposition techniques being employed. Likewise to this system, SiO_2-polyethylene coatings also had a

non-uniform surface morphology. From SEM micrographs, it became apparent that the homogenous coating of nanoparticles with polymer did not occur, but instead, the polymer adapted the role of a binder, adhering nanoparticle aggregates together (see Fig. 2.19). Therefore, as the mass of polymer began to increase, large regions of flat polymer began to form, subsequently, reducing the surface texture of the coating and promoting variations in surface wettability across the sample.

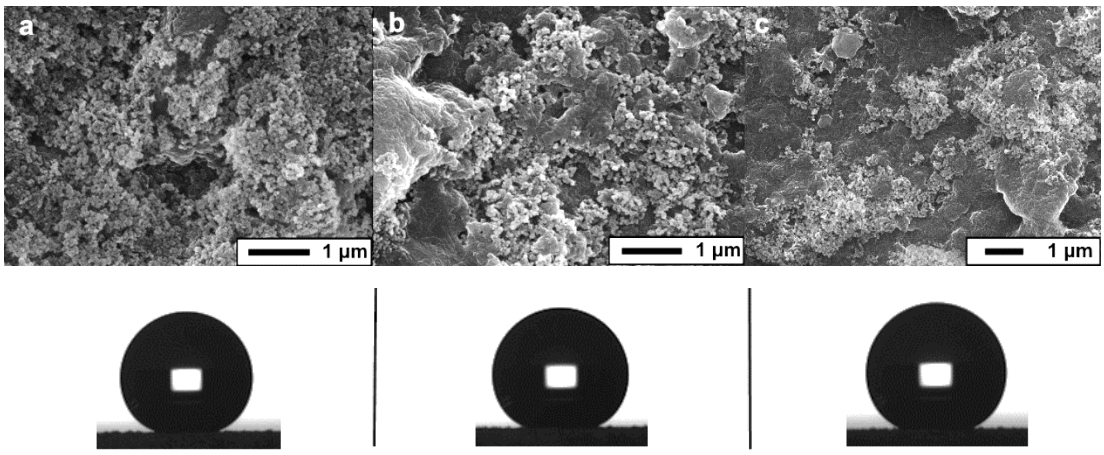

Figure 2.19: SEM micrographs of SiO_2-polyethylene SPNCs at high magnification, deposited *via* dip-coating from a xylene solution. In all images the nanoparticle diameter is 15 nm, with polymer thicknesses of; (**a**) 1.5 nm; (**b**) 2 nm; and (**c**) 3 nm. Scale bars are shown. Additional images highlight the shape of a water droplet resting on the corresponding surface coating.

One differentiating factor, however, was the extended range of polymer thicknesses over which superhydrophobicity was exhibited. This is likely attributed to the deposition technique, as it was noticed that during the drying process, solvent removal facilitated roughening of the polymer. This can be seen below in Figure 2.20, which depicts a micrograph of a dip-coated polyethylene surface from a xylene suspension, in the absence of any roughening agents.

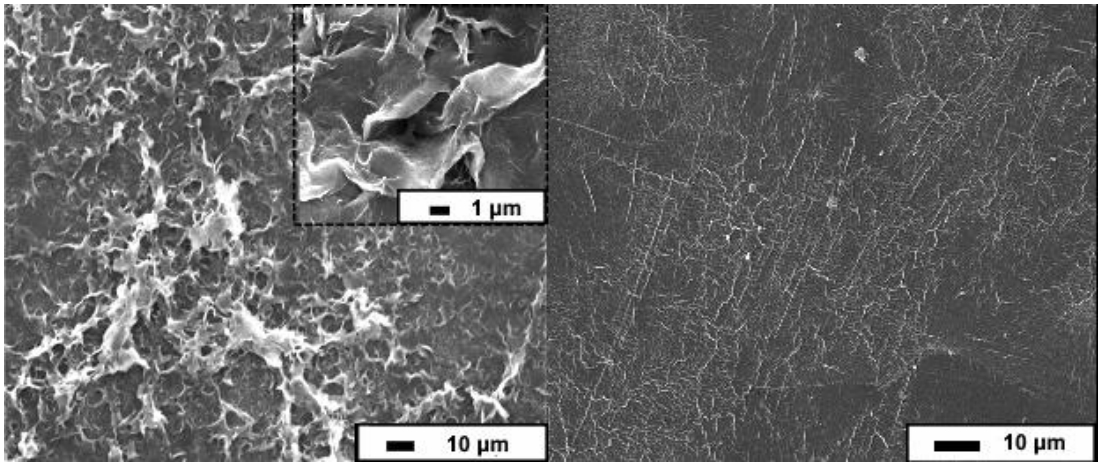

Figure 2.20: SEM micrograph of; (**a**) a polyethylene coating (in the absence of any roughening agents), deposited via dip-coating from a xylene solution and (**b**) a flat block of polyethylene. Inset; SEM micrograph of dip-coated polyethylene at high magnification. Scale bars are shown.

SiO_2-Polypropylene Formulation System

Similar to the two previously reported thermoplastic systems discussed above, SiO_2-polypropylene displayed a comparable relationship between surface hydrophobicity and theoretical polymer thickness. Polypropylene-based formulations were deposited *via* dip-coating (similar to polyethylene-based coatings), with an established deposition temperature range of 68-72℃. The solvation of polypropylene in xylene, was confirmed by the clear and colourless appearance of the solution, and formulations that spanned a theoretical polymer thickness range of 1.5-5 nm were investigated. FTIR was employed to confirm the presence of both components – polypropylene and HMDS-functionalised SiO_2 ($\mathbf{r}_{sphere}$ = 7.5 nm) – within the composite ($\mathbf{r}_{poly}$ value of 5 nm); four bands present in the region 3000-2800 cm^{-1} corresponded to asymmetric and symmetric alkyl C-H stretches, sharp signals at 1456 cm-1 and 1375 cm-1 can be attributed to asymmetric (1456 cm^{-1}) and symmetric (1375 cm^{-1}) CH_3-deformation vibrations, and additional signals at lower wavenumbers (1200-750 cm^{-1}) are representative of CH_3-/CH_2- rocking vibrations and C-C asymmetric/symmetric stretching vibrations (see Fig. 2.21).[34]

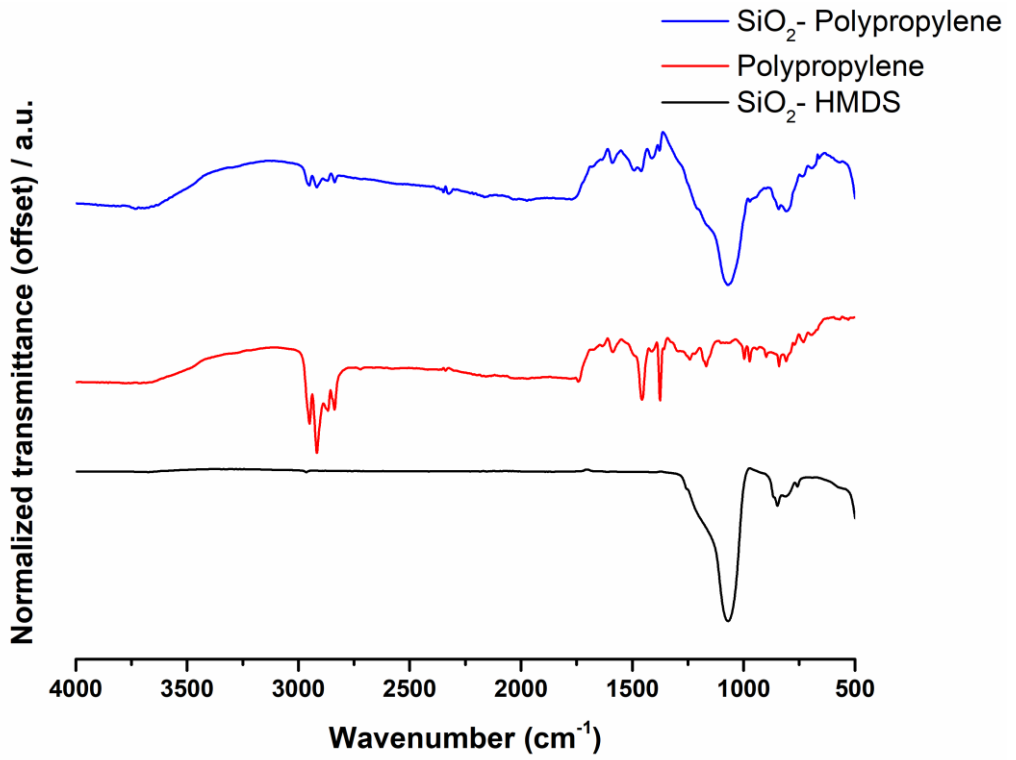

Figure 2.21: Stacked FTIR spectra of SiO_2-polypropylene composite ($\mathbf{r}_{sphere}$ = 7.5 nm, $\mathbf{r}_{poly}$ = 5 nm, **blue line**), polypropylene (**red line**) and HMDS-functionalised SiO_2 nanoparticles ($\mathbf{r}_{sphere}$ = 7.5 nm, **black line**).

Table 2.13: Recorded contact angles for **Formulation #5** SiO_2-polypropylene ($\mathbf{r}_{sphere}$ = 7.5 nm):

$\boldsymbol{r}_{poly}$	*Recorded static contact angle*
1.5	166° ± 1
2	164° ± 1
3	146° ± 6
4	137° ± 5
5	130° ± 13

In agreement, an optimal $\mathbf{r}_{poly}$ value of 1.5 nm was determined, where coatings exhibited a contact angle of 166° ± 1. Here, a rapid decrease in contact angle was observed with increasing theoretical polymer thickness, showing an intensified change in surface hydrophobicity when compared to the SiO_2-polyethylene system (Formulation #4), over the range of $\mathbf{r}_{poly}$ values analysed. Similar to SiO_2-PVC (Formulation #3), superhydrophobicity was lost for coatings with an $\mathbf{r}_{poly}$ value ≥ 3 nm. This is likely due to the drying behaviour of

the polymer; unlike polyethylene which appeared to adopt a roughened morphology during the dip-coating process (refer back to Fig. 2.20), polypropylene exhibited a more simplistic architecture with reduced surface roughness, where many regions appeared to be almost flat (see appendix, Fig. A3). During SEM assessment, SiO_2-polypropylene composites appeared to be marginally more uniform, in that the interactions between polymer and particles appeared to be more adhesive, when compared to the other investigated thermoplastic systems (see Fig. 2.22). Polypropylene was found to have the lowest surface free energy value of all examined thermoplastics, which may explain this observation (see appendix, Table A3). However, large regions of flat polymer were still present, preventing the entrapment of air at the interface and compromising surface superhydrophobicity, as larger $\mathbf{r}_{poly}$ values were reached.

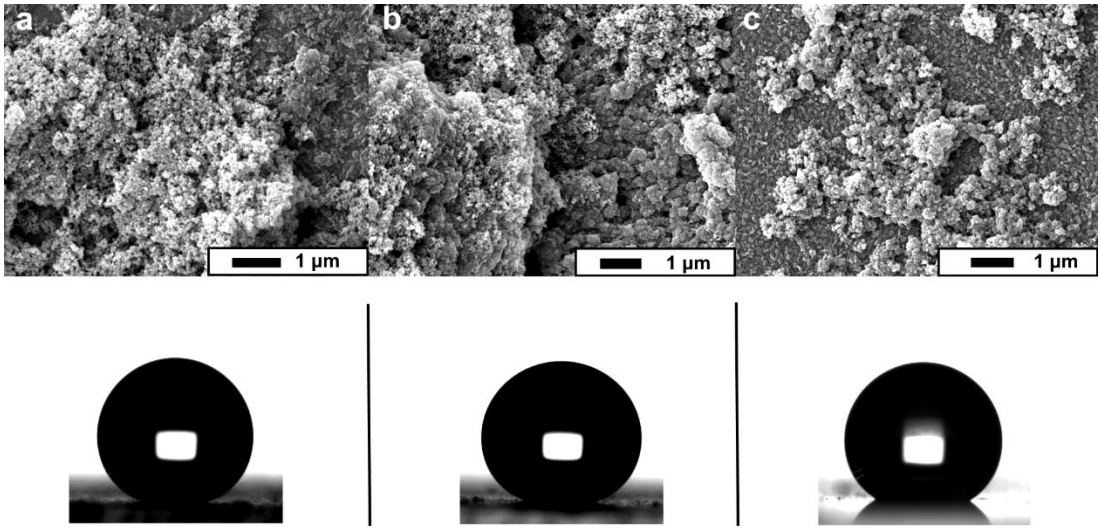

Figure 2.22: SEM micrographs of SiO_2-polypropylene SPNCs at high magnification, deposited *via* dip-coating from a xylene solution. In all images the nanoparticle diameter is 15 nm, with polymer thicknesses of; (**a**) 1.5 nm; (**b**) 2 nm; and (**c**) 3 nm. Scale bars are shown.

2.3.3.2 Solvent-Free SPNC Formulations

To target wider applications and examine the possibility of using alternative substrates, 'solvent-free' SPNC formulations were investigated. The work reported in this section led to the development of chapter 4, and was inspired by a collaboration with Croda and Uniroyal Global Limited, who aimed to uncover the feasibility of superhydrophobic polymer-nanoparticle coatings for fabrics, in particular, automotive seat upholstery. PVC was chosen as the polymer for this work, in order to provide a potential technology that could be directly

implemented into the current seat upholstery fabrication process. Bought-in plasticized PVC fabric was used as the substrate, in line with the products that Uniroyal Global manufacture.

2.3.3.2.1 Optimisation

The principle aim of this project was to investigate whether PVC fabrics could be successfully coated with an SPNC formulation and display relative resilience (i.e. couldn't be wiped off easily with as little force as a finger wipe). To do so, the formulation and deposition approach both required optimisation, to establish the most effective and environmentally conscious method of coating fabrics.

Initially, multiple attempts at spray-coating formulations that comprised a pre-determined ratio of high-density PVC and hydrophobic SiO_2 ($\mathbf{r}_{sphere}$ = 7.5 nm, pre-functionalised with HMDS for enhanced compatibility, $\mathbf{r}_{poly}$ = 1.5 nm, see section 2.3.3.1) were made. Here, more environmentally friendly solvents that were effective in solubilising high-density PVC were trialled in SPNC systems i.e., methylisobutylketone (MIBK) and butyl acetate, to avoid the use of THF due to environmental implications. However, introducing a new solvent into the system presented new challenges; both MIBK and butyl acetate have high boiling points and low vapour pressures, while being able to rapidly solubilize PVC. Hence, it was noticed that the underlying substrate endured partial solvation if the rate of solvent removal was too slow (50℃ deposition temperature), and excessive surface coatings (15+) had to be applied to reach partial superhydrophobicity, which was not practical or economical. Alternatively, increasing the deposition temperature to 80℃ then induced surface cracking, subsequently resulting in low reproducibility and induced water pinning. Despite making numerous changes to the deposition process (e.g. deposition conditions, concentration of SPNC formulations and introducing a mixed solvent system of MIBK/toluene, as toluene solvates PVC at a reduced rate), reproducible coating formation was unachievable. In light of this, THF was employed as the solvent within the SPNC system, and superhydrophobic coatings that were similar to those discussed in section 2.3.3.1.2 (Formulation #3) were successfully fabricated. Nonetheless, we wanted to avoid the use of this solvent as it is not environmentally friendly or safe to use within an industrial setting. Therefore, two alternative routes were purposed:

- **(i)** Introduction of plasticizers into SPNC formulations to eliminate or reduce solvent use.
- **(ii)** Investigation of a 'solvent-free' approach.

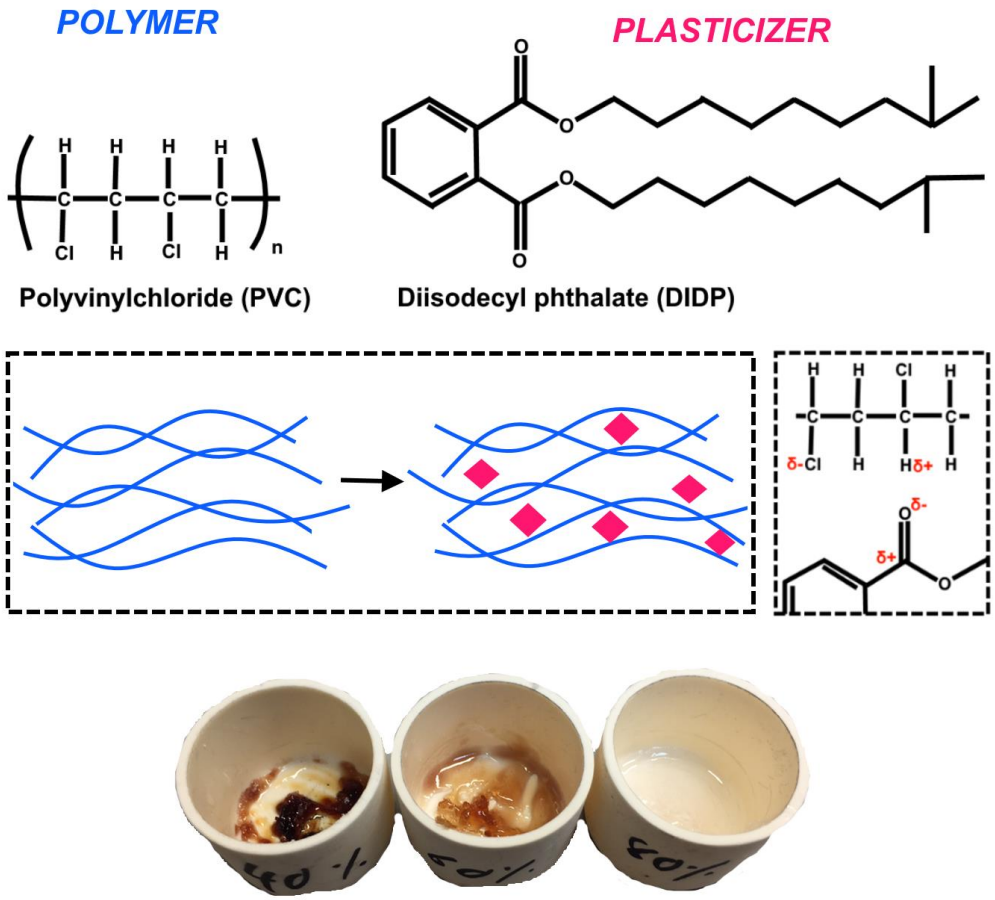

Figure 2.23: Illustration outlining the basic mechanism of polymer plasticization between PVC and DIDP; at high temperature, plasticizer molecules disrupt the intermolecular interactions between polymer chains, ultimately leading to softening of the polymer (**top**). Images of DIDP-plasticized PVC at (**left**) 40 wt % DIDP; (**middle**) 60 wt % DIDP; and (**right**) 80 wt % DIDP (**bottom**).

Diisodecyl phthalate (DIDP) – a long-chain hydrocarbon molecule, commonly used as a plasticizer within the PVC industry – was used to plasticize high-density PVC at different weight percentages (weight percentage of plasticizer/PVC can vary industrially). During the plasticizing process, intermolecular interactions between chlorine and hydrogen atoms on adjacent PVC chains are disrupted by plasticizer molecules, ultimately leading to the softening of the polymer, as plasticizer molecules remain positioned between polymer chains (see Fig. 2.23). Therefore, as the mass of plasticizer is increased, a reduction in the brittle nature of the polymer is expected. However, it must be noted that thermal degradation of PVC was initiated when plasticizing with lower weight percentages of DIDP, as seen in Figure 2.23. This can likely be explained by the reduced solvation of polymer chains by plasticizer, requiring high temperatures of >180 ℃.

Although the initial target was to apply plasticized coatings in the absence of solvent, it became quickly apparent that this would be extremely challenging and impractical, due to rapid polymer hardening/increased viscosity after plasticization had taken place (compared to liquid/molten PVC). Hence, the use of this method to eliminate solvent use was not viable, as there would be no effective route to generating SPNC formulations without using extreme temperatures or high weight percentages of DIDP – both of which have fundamental issues. Interestingly, superhydrophobic coatings could be achieved when employing pre-plasticized PVC within SPNC formulations as the polymeric component, in place of generic high-density PVC.

2.3.3.2.2 Parallel Plate Hot Press

Due to facing multiple challenges when attempting to formulate 'environmentally friendly' PVC formulations, a more suitable deposition process was designed. It was believed that this process can, in theory, eliminate the use of solvents and potentially enhance the chemical and physical interactions between the fabric surface coating and the underlying substrate, as a result of the high processing temperatures (refer back to section 2.2.5.3, Fig. 2.03 for illustration of apparatus).

It was initially discovered that simply combining dried powders (functionalised SiO_2 nanoparticles and high-density PVC), in the absence of any solvent, led to nanoparticles that were only partially encapsulated by the polymer. Hence, generating inconsistencies throughout the surface, due to irregular heating/melting of polymer within the coating blend. To overcome this, solution-based SPNC formulations were initially made up, followed by removal of the solvent, leaving behind a dried powder of greater homogeneity, that could later be implemented into the hot pressing process. It was anticipated that if carried out on a large scale, solvents could be collected and recycled during the process to limit solvent waste and exposure. To ensure a strong integration between the fabric substrate and SPNC coating, and demonstrate that pre-plasticized polymers can have dual functionality, the same material was used as both the substrate and polymeric component within the SPNC formulation. Hence, the pre-plasticized polymer was dissolved from the bought-in plasticized PVC coated fabric, and was used also to coat hydrophobic SiO_2 nanoparticles. As this material was purchased externally, it is important to note that we were not aware of the exact composition, but it was assumed that plasticization had been carried out with a phthalate ester (see appendix, Fig. A4). Successful SPNC coatings were fabricated using this approach; hydrophobic SiO_2 ($\mathbf{r}_{sphere}$ = 7.5 nm) nanoparticles, coated with plasticized PVC and pre-treated in THF, in a pre-determined ratio which corresponded to a theoretical polymer thickness value of 1.5 nm. The dried

formulation was manually applied and spread across the surface of the bought-in plasticized PVC coated fabric, before being pressed at 180 ℃ under a pressure of 0.1MPa, for 30 seconds, yielding a contact angle of 157° ± 1.

It was predicted that coatings fabricated *via* this method may display superior resilience to those deposited using a conventional spray-coating technique, due to (**i**) infiltration of nanomaterial into the surface of the substrate and (**ii**) the use of high processing temperatures, facilitating interactions between PVC-based components (surface coating and fabric substrate). Samples were subject to an arbitrary robustness test to assess their mechanical durability. The weighted sample (100 g) was attached to a glass support and placed coating down on the sandpaper (P120 grade, Al_2O_3), similar to the process reported by Lu *et al.*[1] Following this, the sample was propelled 10 cm across sandpaper, turned by 90° and pushed a further 10 cm to complete one cycle (total of 20 cm), as seen in Figure 2.24. Samples were then rotated a further 90° (in the same direction) to begin the second cycle so that substrates were abraded from all angles. See section 2.2.9 for full details.

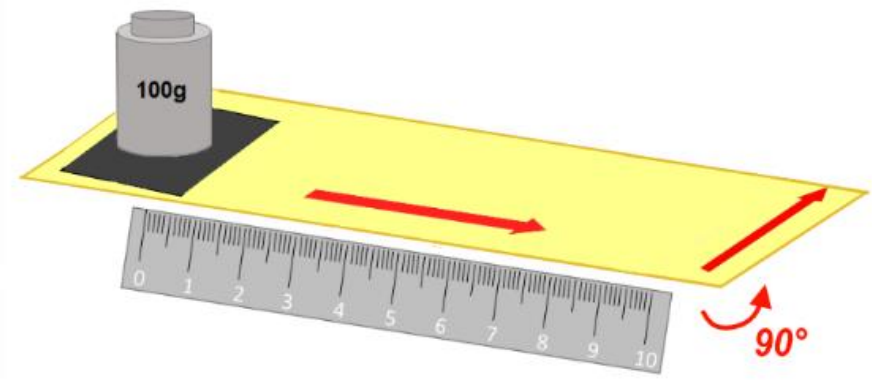

Figure 2.24: Illustration of the abrasive wear test, where the weighted sample was placed face down onto sandpaper (P120, Al_2O_3), propelled 10 cm in one direction, turned 90° and then propelled a further 10 cm.

Initially, water did not adhere to the surface, suggesting the presence of a large liquid-vapour interface, as water could be seen to bounce when deposited. Subsequently, indicating that a Cassie-Baxter wetting state was attained and facilitated by the extreme surface roughness, that could be observed on cross-sectional SEM micrographs (see Fig. 2.25). A total of 25 cycles was carried out, where a steady decline in contact angle was observed, showing a decrease to 150 ± 4° after the 25th cycle. Nonetheless, water droplets could be seen to readily bead up when in contact with the substrate, despite the partial removal of surface coating, as seen below in Figure 2.26. This is likely a result of the roughening agent being present not only at the surface interface, but also partially embedded within the surface of the plasticized PVC

coated fabric substrate. Hence, surface coatings fabricated *via* this approach appeared to display advanced resilience when compared to generic solution-based SPNC coatings.

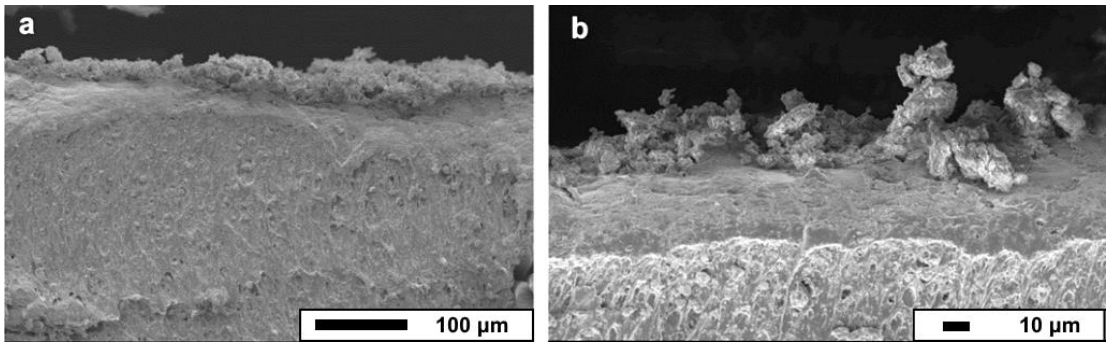

Figure 2.25: Cross-sectional SEM micrographs highlighting the surface morphology of SiO_2-PVC/plasticizer coatings on bought-in plasticized PVC fabric, obtained through cutting with a sharp blade, and fabricated using the hot pressing approach at; (**a**) low magnification and (**b**) high magnification. Scale bars are shown.

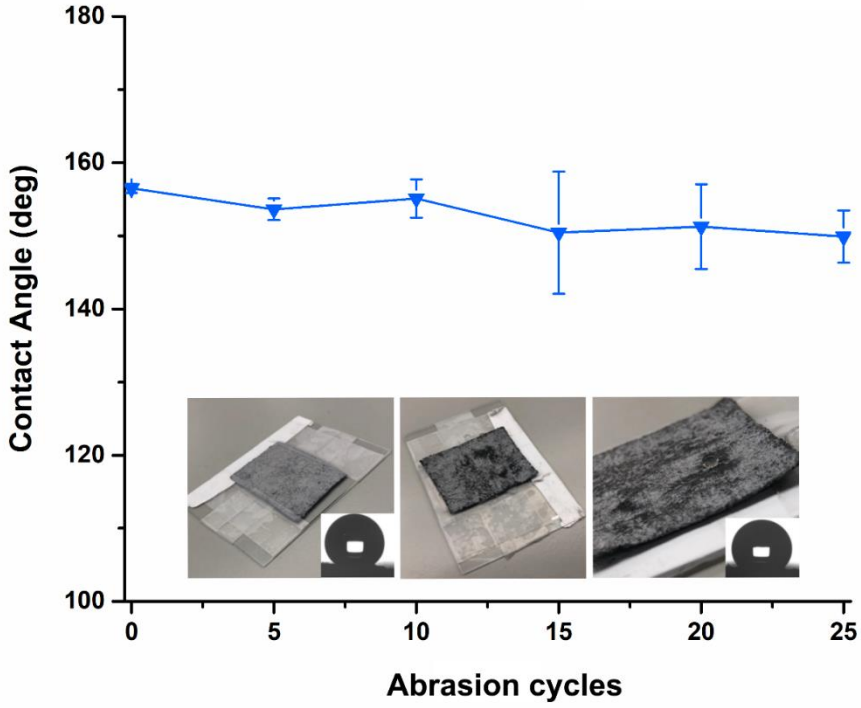

Figure 2.26: Abrasion testing of SiO_2-PVC/plasticizer coatings on bought-in plasticized PVC fabric, fabricated using the hot pressing approach (100 g weight, P120 Al_2O_3 sandpaper). Images of coatings before any physical abrasion (**left**), after 25 abrasion cycles (**middle**) and highlighting the superhydrophobicity of abraded areas (**right**). Insets; digital images of a water droplet resting on the surface before abrasion (**left**) and after 25 abrasion cycles (**right**).

2.3.4 Architecture of Polymer-Nanoparticle Composites

To better understand the architecture of different SPNC systems, and how these are related to the type of hydrophobic polymer that is being employed, more advanced microscopy techniques were utilised.

2.3.4.1 Focused Ion Beam (FIB)

In the first attempt, FIB was selected and carried out by Dr Keith Arnold, as it is a technique that can be employed to visualise the cross-section of a film, by milling into the surface with the use of an ion beam. A platinum strap is often applied to protect the external surface against the ion beam and give an accurate representation of the internal microstructure. SiO_2-PVC films of varying nanoparticle size ($\mathbf{r}_{sphere}$ = 7.5 nm and 125 nm, $\mathbf{r}_{poly}$ = 1.5 nm and its scaled-up equivalent) were cross-sectioned for study using SEM. A combination of FIB milling and SEM imaging provided a view of the internal structure of films, which appeared to have both meso- and macro-sized pores (see appendix, Fig. A5). However, the validity of these images as a true representation of the internal structure of the SPNC was considered to be unreliable, due to thermal effects and/or differences in the sputtering rates of the polymer and the nanoparticle materials. It was anticipated that the polymer would have undergone full thermal degradation under the ion beam, leaving only, the metal oxide frame intact. Hence, FIB milling was not carried out for the thermoset system and an alternative technique was sought to give a greater insight into the composite architectures.

2.3.4.2 Confocal Fluorescence Microscopy

In light of this, confocal fluorescence microscopy was identified as a technique able to characterise the internal structure in a non-destructive manner. Confocal fluorescence imaging is a useful tool that is frequently used to achieve good optical resolution, when imaging specimens. Briefly, through a series of filters and mirrors, light of a specific wavelength (specific to the excitation wavelength of the given fluorophore used) can hit a specimen and become absorbed, subsequently, causing the excitation of an electron within the fluorophore, followed by the quick relaxation of the electron back to the ground state. During this, photons of a higher wavelength than that which was initially used to excite the fluorophore, are emitted in the form of fluorescence, and can be detected and used to generate an image (lower energy as energy partially lost due to molecular vibrations – dissipated in the form of heat). Light from only one focal plane is detected due to the presence of a pinhole within the microscope,

which acts to cancel out any emitted light coming from above or below the specimen. In doing so, this allows high-resolution images, but also the generation of 3D models that involve taking images at different focal planes, using various z-heights, and compiling these with the use of the software.[35,36] This is a useful feature that we anticipated could be used to compliment the observed results so far, and enable a more sophisticated visualisation of the polymer-particle architectures within SPNC coatings. However, the general size of the nanomaterials used for SPNC formulations (15-250 nm) was below the optical limit for analysis using optical microscopy. As a result, two SPNC formulations were made up using larger particles (40-75 μm, 110 Å pore size) and polymers were stained with chemically compatible fluorescent dyes, allowing for visibility under the microscope. Larger particles were functionalised with HMDS, as seen previously for smaller scale systems, and imaged using electron microscopy to assess particle size distribution.

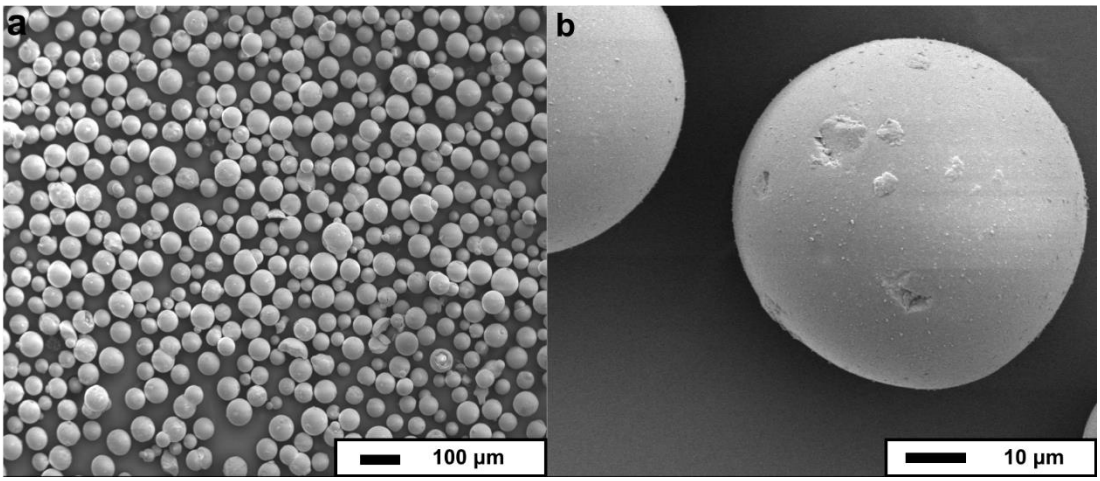

Figure 2.27: SEM micrographs showing as received SiO_2 microparticles (40-75 μm, 110 Å pore size) after functionalisation with HMDS at; **(a)** low magnification and **(b)** high magnification. Scale bars are shown.

As seen in Figure 2.27, the size distribution of particles is quite broad and appears to exceed the reported range of 40-75 μm; when measured using the Image J tool (a digital ruler calibrated against the SEM scale bar), the largest particle was measured to be in the region of ~80 μm and the smallest ~20 μm, with an average particle size of ~45 $\pm$ 16 μm for a sample of 50 particles. For these systems, a mass ratio of 1.042 was used, which corresponds to an $\mathbf{r}_{poly}$ value of 4 nm when considering smaller scale systems. As we were only attempting to visualise the polymer layer and compare systems, the $\mathbf{r}_{poly}$ value does not play such an important role here.

2.3.4.2.1 Thermoset SPNC System

The first SPNC system probed was SiO_2-PDMS. A stock solution of fluorescent dye in $CHCl_3$ (1.96 mM) was made up and added to a pre-weighed mass of PDMS, dissolved in $CHCl_3$ with mechanical stirring, before the addition of SiO_2 microparticles. Here, a hydrophobic dye was essential, in order to maintain compatibility within the SPNC system. Therefore, the commonly used fluorescent dye Nile Red, which has been previously reported in the literature for staining PDMS, was selected (see appendix, Fig. A11 for UV-Vis absorption spectrum).[37] Nonetheless, it was necessary to replace hexane as the solvent component within the system with $CHCl_3$, as it was apparent that the dye was not fully soluble in hexane. Prior to any confocal microscopy, SEM was used to probe the presence polymer on the external surface of the SiO_2 microparticles. From the SEM micrograph presented in Figure 2.28, polymer can be visually observed surrounding the particle core with full surface coverage, confirming the formation of composite particles within the scaled-up system.

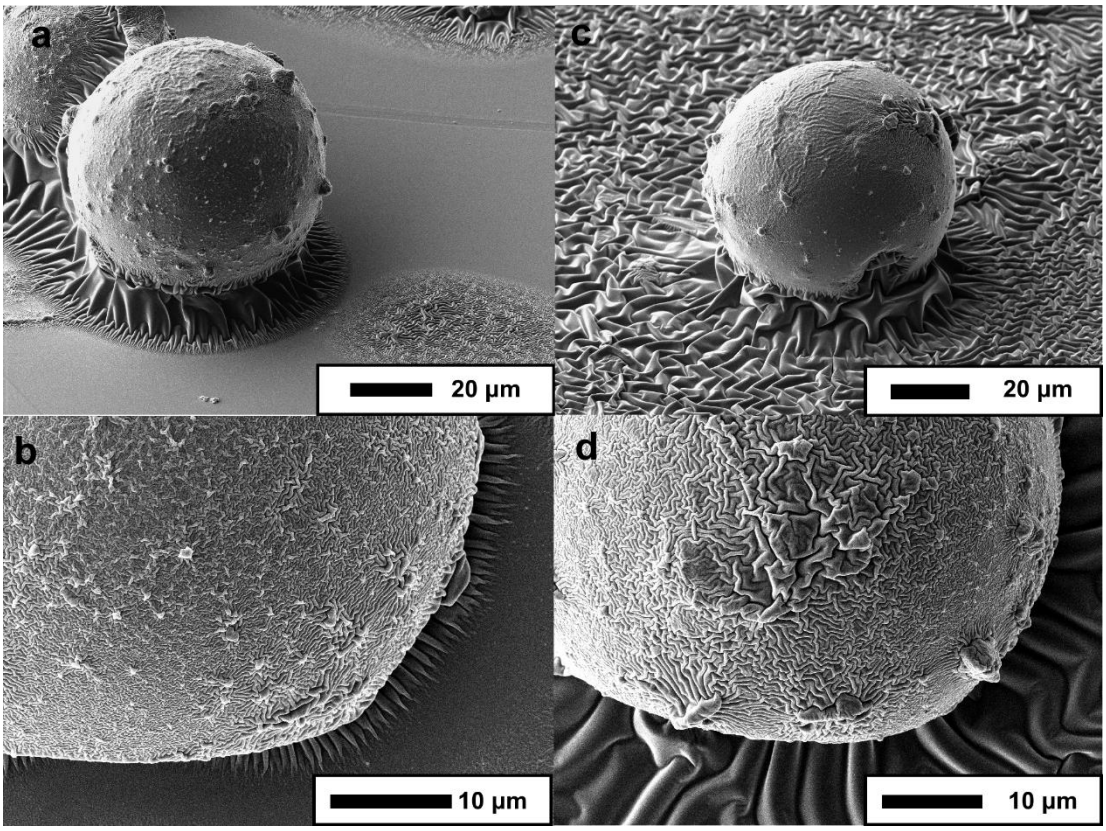

Figure 2.28: Top-down and side on SEM micrographs of the scaled-up SiO_2-PDMS thermoset SPNC system, deposited *via* drop-casting from a chloroform solution, with; (**a**-**b**) no dye incorporated and (**c**-**d**) Nile Red fluorescent dye (1.96 mM, 8 droplets stock solution). In all images, the particle diameter is 40-75 μm. Scale bars are shown.

To govern the concentration of dye required to stain PDMS, three solutions were initially made up using 2, 4 and 8 droplets of stock solution, which corresponded to 30, 60 or 120 μL (labelled PDMS-2, PDMS-4 and PDMS-8). Subsequently, these were then drop-cast onto cover glass substrates and cured, as stated in the experimental section 2.2.4. Confocal microscopy was initially carried out on these samples by Dr Marco Marcello using a laser beam with an excitation wavelength of 561 nm. PDMS-2 was found to be too weakly concentrated and displayed no fluorescence. However, PDMS-4 and PDMS-8 did fluoresce, where PDMS-8 was selected as the dye concentration for further analysis, as better quality images were attained that appeared less pixelated (see appendix, Fig. A6). The excitation wavelength of 561 nm was used as it was the closest wavelength available to that found in the literature, and can be seen in Figure 2.29 to excite Nile Red when probing PDMS-8 (in the absence of SiO_2 microparticles), resulting in the emission of fluorescence and confirming dye capture/polymer compatibility.[38]

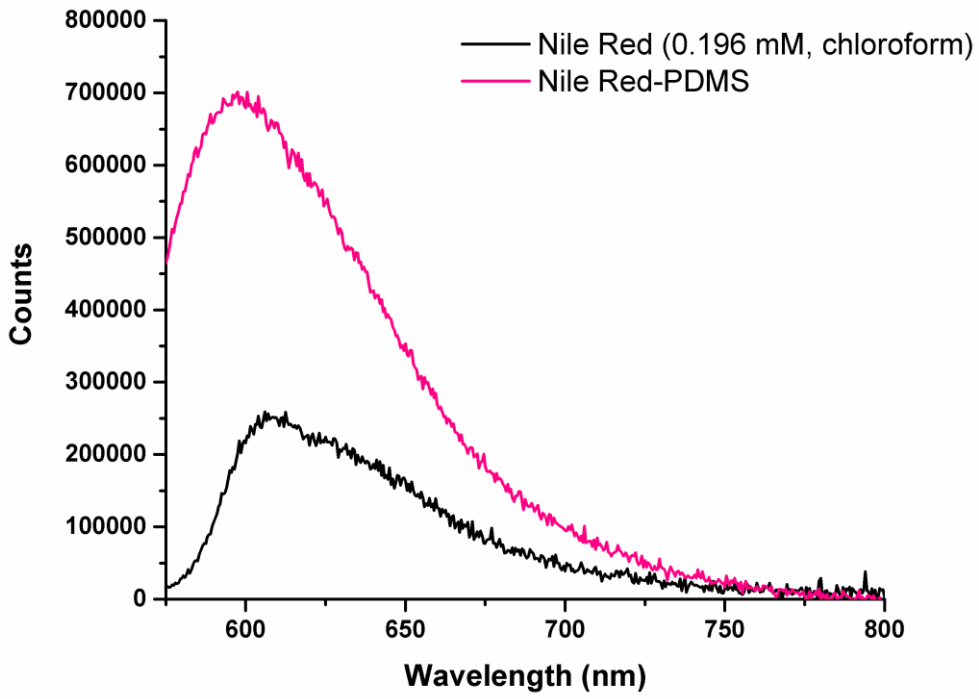

Figure 2.29: Fluorescence emission spectra using an excitation wavelength of 561 nm; Nile Red dye solution (0.196 mM, chloroform) and PDMS polymer stained with Nile Red dye [fabricated in the same way as PDMS-8 samples for confocal fluorescence, in the absence of SiO_2 microparticles].

Z-stack slices – images depicting the particle from a top-down view, beginning from the top of the particle and moving vertically throughout the particle until the substrate is reached – were taken in an attempt to observe the uniformity of the polymer coating and highlight any changes, both internally and externally. It can be seen from the z-stack images in Fig. 2.30 (A-C), taken at heights of 13, 24 and 35 μm, that (**i**) a near-conformal shell forms around the SiO_2 core, where dye is absent/less concentrated, and (**ii**) dye appeared more intensely towards the base of particles, indicating an abundance of polymer closest to the substrate. The 3D-model depicted in Fig. 2.30D displays the inner cavity and external PDMS shell of a single particle, which in agreement with the z-stack images and the SEM micrographs, accentuates this further. However, it must be noted that dye appears to diffuse into the particle core, likely as a result of using porous SiO_2, which makes it difficult to definitively identify discrete polymer and particle layers. Furthermore, after analysing samples using an excitation wavelength of 561 nm, it was realised that other excitation wavelengths gave rise to more intense emission peaks during fluorescence lifetime measurements, which were carried out by Dr Krzysztof Pawlak (see appendix, Fig. A7/A8). Hence, using an alternative excitation wavelength would have likely resulted in better resolution images. This was also true for PVC/Lucigenin samples, where the use of an excitation wavelength of 488 nm likely compromised image resolution (see section 2.3.4.2.2 and appendix, Fig. A9/A10).

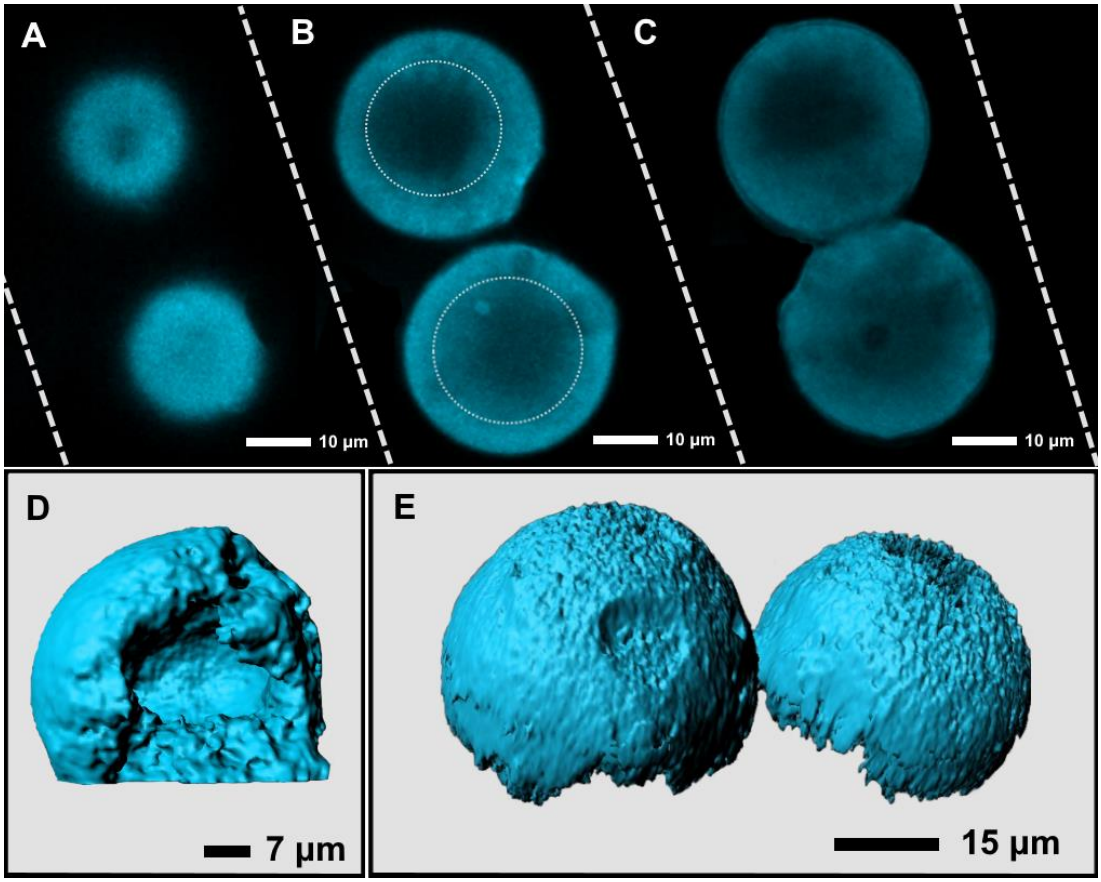

Figure 2.30: Confocal fluorescent microscopy images of SiO_2-PDMS SPNC (40-75 µm SiO_2 particles; PDMS stained with fluorescent dye Nile Red). (**A-C**) z-stack images of slices at the top of the particle (13 µm), middle (24 µm), and bottom (35 µm), with a circular dotted line added to represent the SiO_2 particle; (**D**) 3D construction of single coated particle, displaying inner cavity; and (**E**) 3D representation of two particles. Scale bars are shown.

Nonetheless, these images suggest that polymer coatings generate more physically resilient materials when compared to their molecular counterparts, by acting as a polymeric adhesive. Therefore, inducing stronger particle-particle interactions, in addition to enhancing the binding strength between the coating and underlying substrate. This was reflected during a light mechanical abrasion test (see appendix, Fig. A13), which revealed that SiO_2-PDMS ($\mathbf{r}_{sphere}$ = 7.5, $\mathbf{r}_{poly}$ = 5 nm) retained its superhydrophobicity after a finger wipe (water contact angle decreased from 167° ± 2 to 163° ± 1). Whereas, a molecularly functionalised SiO_2 composite coating ($\mathbf{r}_{sphere}$ = 7.5, SiO_2-FAS), synthesised by covalently grafting long-chain perfluorinated molecules onto the surface of particles (see chapter 3), was largely removed, showing limited adhesion and a dramatically reduced contact angle of 61° ± 3 (initially 159° ± 3).

2.3.4.2.2 Thermoplastic SPNC System

To highlight any differences between thermoset and thermoplastic SPNC systems, a second system was probed using confocal fluorescence microscopy. SiO_2-PVC formulations comprising SiO_2 microparticles and the polar fluorescent dye, Lucigenin, whose use has been reported as a fluorescence probe for PVC in THF solutions by Xia *et al.* (see appendix, Fig. A12 for UV-Vis absorption spectrum).[39] In a similar approach, a stock solution of the fluorescent dye in water (1.96 mM) was made up, which was then dispersed into a THF solution of pre-dissolved PVC, followed by the addition of HMDS functionalised SiO_2 microparticles. Here, 8 droplets of stock solution were used, in line with what was reported for the PDMS system and the water-soluble dye appeared to uniformly disperse, despite THF now being the primary solvent. Similarly, SEM imaging was employed to visualise interactions between the polymer and SiO_2 particles, where it was apparent that uniform coverage was not obtained, as seen for smaller-scale thermoplastic SPNC systems (see Fig. 2.31). Furthermore, microparticles appeared to undergo fracturing during the polymer solidification process as PVC is a hard and brittle thermoplastic, unlike silicone elastomer PDMS, where whole particles were predominantly observed during analysis (see appendix, Fig. A14).

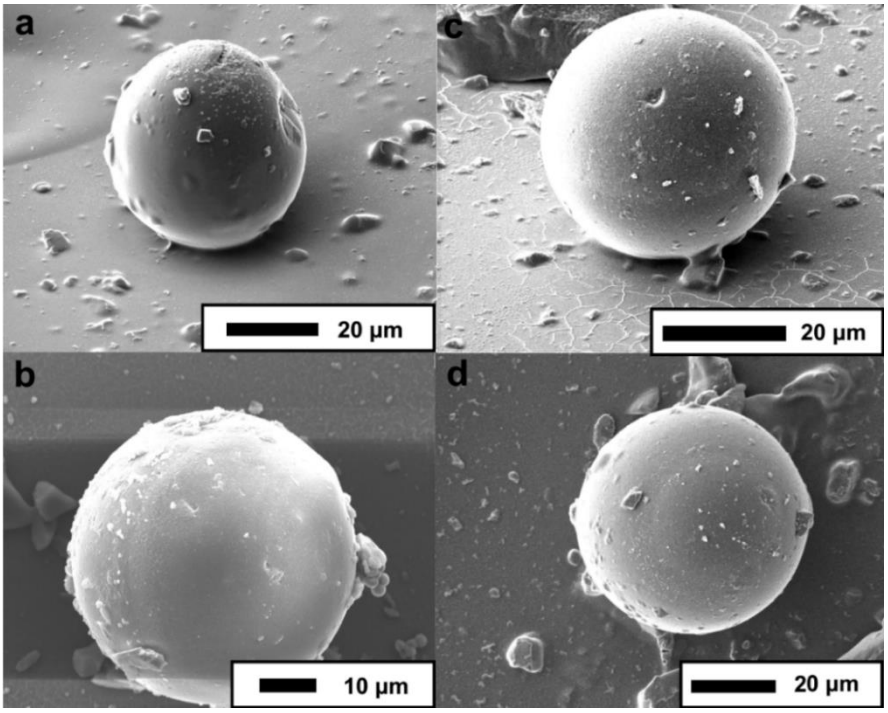

Figure 2.31: Top-down and side on SEM micrographs of the scaled-up SiO_2-PVC thermoplastic SPNC system, deposited *via* drop-casting from a THF/H_2O solution, with (**a-b**) no dye incorporated and (**c-d**) Lucigenin fluorescent dye (1.96 mM, 8 droplets stock solution). In all images, the particle diameter is 40-75 μm. Scale bars are shown.

This was further verified by confocal microscopy, where a non-conformal coating was also observed when recording a series of z-stack images, using an excitation wavelength of 488 nm. An excitation wavelength of 488 nm was employed here as it was closest to that found in the literature, as with Nile Red, and can be seen to excite Lucigenin when probing PVC stained with the dye (in the absence of SiO_2 microparticles, see Fig. 2.32).[39] However, due to the maximum excitation wavelength not being used, as discussed above, we were unable to obtain images with high enough resolution to compute a 3D-model.

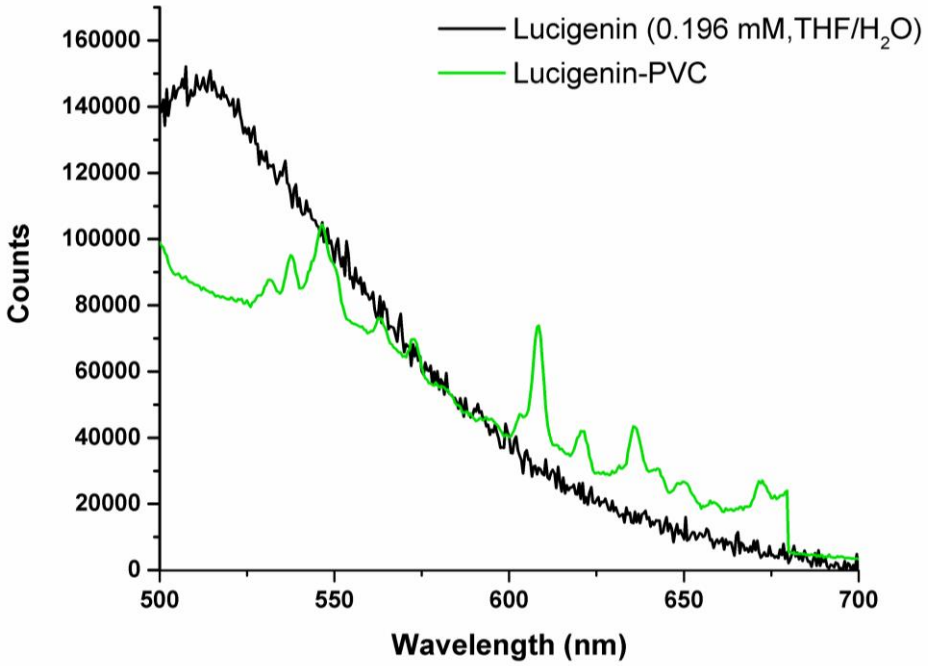

Figure 2.32: Fluorescence emission spectra using an excitation wavelength of 488 nm; Lucigenin dye solution (0.196 mM, THF/H_2O) and PVC polymer stained with Lucigenin dye [fabricated in the same way as PVC samples for confocal fluorescence, in the absence of SiO_2 microparticles].

Irrespective of this, it can be seen from z-stack images that the SiO_2 core was partially exposed due to incomplete coverage with polymer, as seen in Figure 2.33, which is suspected to be related to apparent differences in surface energy/tension between components within thermoplastic SPNC formulations. Variations in surface energy/tension for different components within a formulation can strongly influence the interaction between species, and predict whether phase separation is likely to occur.[25] Thermoplastic polymers were determined to have greater surface free energy values than the thermoset polymer, PDMS (19.98 $\pm$ 2 mN/m, see appendix, Table A3). Particularly PVC, which was found to have a surface free energy value of 42.97 $\pm$ 2 mN/m. Therefore, thermoplastic composites are likely to display greater chemical incompatibilities. Irrespective of this, thermoplastic polymers can still be

considered as an adhesive when compared to molecular composites, binding individual particles together throughout the coating, *via* the formation of polymer aggregates (see Fig. 2.34). However, the lack of uniformity may lead to reduced physical resilience, when compared to thermoset systems.

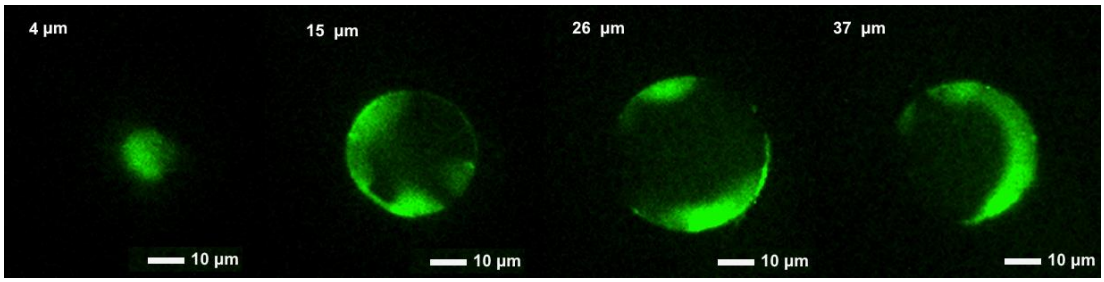

Figure 2.33: Confocal fluorescent microscopy images of SiO_2-PVC SPNC (40-75 μm SiO_2 particles; PVC stained with fluorescent dye Lucigenin); z-stack images of slices at 4, 15, 26 and 37 μm. Scale bars are shown.

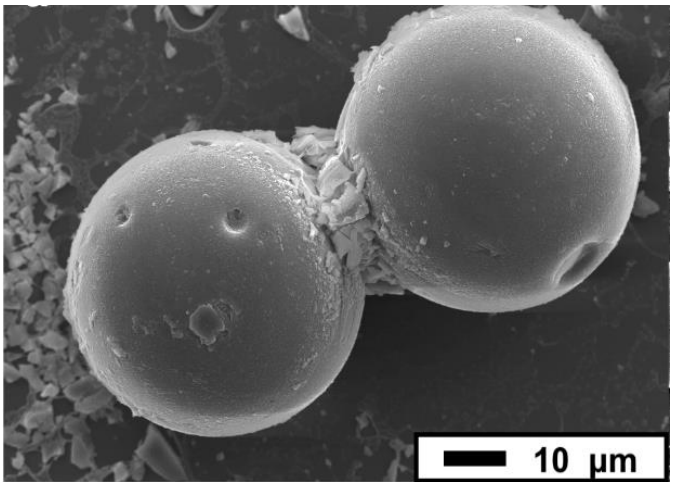

Figure 2.34: SEM micrographs of the scaled-up SiO_2-PVC thermoplastic SPNC system, deposited *via* drop-casting from a THF/H_2O solution, highlighting polymer adhering two particles together (particle diameter is 40-75 μm). Scale bars are shown.

2.4 Conclusions

Within this chapter, a series of SPNC formulations were generated, and structural and functional differences between formulations that comprised both, thermoset and thermoplastic polymers, were comparatively investigated using a series of techniques. The principal discoveries were as follows:

SPNC Design Principle – The SPNC design principle which uses parameters, $\mathbf{r}_{poly}$, $\mathbf{r}_{sphere}$ and $\mathbf{r}_{sphere+poly}$, has been used here to successfully fabricate a range of superhydrophobic coatings for alternative polymer-nanoparticle systems. This method can be employed as an effective route to systematically producing coatings, which is useful when looking to optimise a particular system. Furthermore, it is more precise than periodically increasing the weight percentage of one component – a practice that is commonly documented within the literature – as it allows for direct comparison between different systems, by utilising the theoretical polymer thickness value, which can be scaled up or down relative to particle size and/or nanoparticle density for formulations with different metal oxide nanoparticle systems. It is believed that this design principle is widely applicable and can be used to examine a wide selection of polymer-nanoparticle systems, providing that the polymer component can be solubilised, and that all components demonstrate a level of compatibility or can be modified to do so.

Theoretical Polymer Thickness and Surface Hydrophobicity – The relationship between theoretical polymer thickness and surface hydrophobicity has been demonstrated in this work. It was shown for thermoset systems, that the optimal $\mathbf{r}_{poly}$ value appeared to lie towards the middle (optimal $\mathbf{r}_{poly}$ value = 5 nm/80 nm), with too little or too much polymer subsequently reducing surface hydrophobicity. Alternatively, for thermoplastic systems, it was found that the optimal $\mathbf{r}_{poly}$ value was the lowest (optimal $\mathbf{r}_{poly}$ value = 1.5 nm), and further increases led to coatings with progressively reduced surface hydrophobicity. Furthermore, the self-cleaning performance of each coating appeared to be directly related to the surface hydrophobicity, due to changes in the adopted wetting state, and thus, could be anticipated over a range of $\mathbf{r}_{poly}$ values.

Thermoset vs Thermoplastic: Morphological Differences – Throughout this work, it has been demonstrated that there are clear differences between coatings which comprise either thermoset or thermoplastic polymers, as seen above. Ultimately, the functional differences between both (inherent hydrophobicity and self-cleaning ability) are affected by structural adaptations and changes in surface morphology. With the use of SEM imaging and confocal

fluorescence microscopy, it was deduced that thermoset polymers appeared to assemble rather uniformly around particles, with complete surface coverage apparent during imaging. Hence, the range of $\mathbf{r}_{poly}$ values which generate superhydrophobic coatings are generally larger for formulations that comprise thermoset polymers, as issues associated with reduced surface roughness, caused by polymer agglomeration, did not need to be taken into account. On the other hand, formulations that comprised thermoplastic polymers generally displayed a narrow range of $\mathbf{r}_{poly}$ values that were capable of generating superhydrophobic materials. This is owed to the incomplete coverage of particles with polymer, due to variations in surface energies between formulation components, resulting in partial polymer agglomeration. Furthermore, the fracturing of microparticles was apparent during the polymer solidification process of SiO_2-PVC; this may have been governed by the strong mechanical properties of the thermoplastic (opposed to the inherently flexible nature of PDMS), as this combined with the non-uniform surface deposition of polymer, likely induced fracturing points across the particle.

Use of Dried Formulations – Techniques other than spray-coating and dip-coating were investigated and alternative routes to depositing SPNC coatings were probed. 'Solvent-free' formulations were successfully developed for an example SPNC system (SiO_2-PVC), and fabricated with the use of a parallel plate hot press apparatus and a plasticized-PVC coated fabric substrate. In doing so, it became apparent that there was potential for generating SPNC coatings with enhanced physical resilience, during abrasive wear testing, due to the high processing temperatures used and strong integration between the dried coating and polymer-coated substrate. Furthermore, the use of plasticizers in place of a solvent within the SPNC system was investigated. However, this was impractical due to the requirement of extremely high temperatures and/or large weight percentages of plasticizer. Nonetheless, it was demonstrated that pre-plasticized polymer can be used in place of a conventional polymer to generate superhydrophobic materials, and promote coating-substrate integration.

Although a series of SPNC coatings were successfully generated and could be categorised based upon their $\mathbf{r}_{poly}$ value range, the realistic form of these systems almost certainly deviates from this idealised illustration shown in Fig. 2.10 (refer back to section 2.3.2). For example, gravitational effects of polymer layer formation, the differences in time required for polymer hardening (e.g. thermoset vs thermoplastic polymers) and the *in situ* agglomeration of nanoparticles. These deviations undoubtedly affect the apparent optimal $\mathbf{r}_{poly}$ value to an extent, especially as the morphologies of deposited films are known to be complex and differ between SPNC systems. Nonetheless, it can be concluded that comparative assessment of

different SPNC systems *via* the SPNC design principle was effective, and allowed for the fine-tuning of coating performance.

2.5 References

1 Y. Lu, S. Sathasivam, J. Song, C. R. Crick, C. J. Carmalt and I. P. Parkin, *Science (80-.).*, 2015, **347**, 1132–1135.

2 J. Song, D. Zhao, Z. Han, W. Xu, Y. Lu, X. Liu, B. Liu, C. J. Carmalt, X. Deng and I. P. Parkin, *J. Mater. Chem. A*, 2017, **5**, 14542–14550.

3 S. S. Latthe, R. S. Sutar, V. S. Kodag, A. K. Bhosale, A. M. Kumar, K. K. Sadasivuni, R. Xing and S. Liu, *Prog. Org. Coatings*, 2019, **128**, 52–58.

4 W. S. Y. Wong, Z. H. Stachurski, D. R. Nisbet and A. Tricoli, *ACS Appl. Mater. Interfaces*, 2016, **8**, 13615–13623.

5 H. F. Brinson and L. C. Brinson, *Polymer Engineering Science and Viscoelasticity*, An Introduction (Springer), 2008.

6 J.-P. Pascault, H. Sautereau, J. Verdu and R. J. J. Williams, *Thermosetting polymers*, CRC Press, 2002, vol. 64.

7 M. Ma and R. M. Hill, *Curr. Opin. Colloid Interface Sci.*, 2006, **11**, 193–202.

8 R. J. Daniello, N. E. Waterhouse and J. P. Rothstein, *Phys. Fluids*, 2009, **21**, 85103.

9 L. Feng, Z. Zhang, Z. Mai, Y. Ma, B. Liu, L. Jiang and D. Zhu, *Angew. Chemie*, 2004, **116**, 2046–2048.

10 B. J. Privett, J. Youn, S. A. Hong, J. Lee, J. Han, J. H. Shin and M. H. Schoenfisch, *Langmuir*, 2011, **27**, 9597–9601.

11 I. Karapanagiotis, P. N. Manoudis, A. Savva and C. Panayiotou, *Surf. Interface Anal.*, 2012, **44**, 870–875.

12 B. Liu, Y. He, Y. Fan and X. Wang, *Macromol. Rapid Commun.*, 2006, **27**, 1859–1864.

13 H. Y. Erbil, A. L. Demirel, Y. Avcı and O. Mert, *Science (80-.).*, 2003, **299**, 1377–1380.

14 Y. Qing, C. Yang, N. Yu, Y. Shang, Y. Sun, L. Wang and C. Liu, *Chem. Eng. J.*, 2016, **290**, 37–44.

15 X. Zhang, M. Jin, Z. Liu, D. A. Tryk, S. Nishimoto, T. Murakami and A. Fujishima, *J. Phys. Chem. C*, 2007, **111**, 14521–14529.

16 H. Xu, C. R. Crick and R. J. Poole, *J. Mater. Chem. A*, 2018, **6**, 4458–4465.

17 A. Milionis, E. Loth and I. S. Bayer, *Adv. Colloid Interface Sci.*, 2016, **229**, 57–79.

18 Y. Meng, T. Ma, F. J. Pavinatto and J. D. MacKenzie, *ACS Appl. Mater. Interfaces*, 2019, **11**, 9190–9196.

19 P. Roach, N. J. Shirtcliffe and M. I. Newton, *Soft Matter*, 2008, **4**, 224–240.

20 J. J. Victor, D. Facchini and U. Erb, *J. Mater. Sci.*, 2012, **47**, 3690–3697.

21 Y. Zhao, M. Li, Q. Lu and Z. Shi, *Langmuir*, 2008, **24**, 12651–12657.

22 F. Liang, J. Lehr, L. Danielczak, R. Leask and A.-M. Kietzig, *Int. J. Mol. Sci.*, 2014, **15**, 13681–13696.

23 H. Wang, J. Fang, T. Cheng, J. Ding, L. Qu, L. Dai, X. Wang and T. Lin, *Chem. Commun.*, 2008, 877–879.

24 A. Nakajima, K. Hashimoto, T. Watanabe, K. Takai, G. Yamauchi and A. Fujishima, *Langmuir*, 2000, **16**, 7044–7047.

25 K. Golovin, M. Boban, J. M. Mabry and A. Tuteja, *ACS Appl. Mater. Interfaces*, 2017, **9**, 11212–11223.

26 C. R. Crick and I. P. Parkin, *J. Mater. Chem.*, 2009, **19**, 1074–1076.

27 C. R. Crick, S. Ismail, J. Pratten and I. P. Parkin, *Thin Solid Films*, 2011, **519**, 3722–3727.

28 P. G. Pai, S. S. Chao, Y. Takagi and G. Lucovsky, *J. Vac. Sci. Technol. A Vacuum, Surfaces, Film.*, 1986, **4**, 689–694.

29 S. Haukka and A. Root, *J. Phys. Chem.*, 1994, **98**, 1695–1703.

30 X. Zhang, H. Ye, B. Xiao, L. Yan, H. Lv and B. Jiang, *J. Phys. Chem. C*, 2010, **114**, 19979–19983.

31 L. Johnson, L. Gao, C. Shields IV, M. Smith, K. Efimenko, K. Cushing, J. Genzer and G. P López, *J. Nanobiotechnology*, 2013, **11**, 22.

32 C.-Y. Loo, P. M. Young, W.-H. Lee, R. Cavaliere, C. B. Whitchurch and R. Rohanizadeh, *Acta Biomater.*, 2012, **8**, 1881–1890.

33 N. De Geyter, R. Morent and C. Leys, *Surf. Interface Anal. An Int. J. devoted to Dev. Appl. Tech. Anal. surfaces, interfaces thin Film.*, 2008, **40**, 608–611.

34 R. Morent, N. De Geyter, C. Leys, L. Gengembre and E. Payen, *Surf. Interface Anal. An Int. J. devoted to Dev. Appl. Tech. Anal. surfaces, interfaces thin Film.*, 2008, **40**, 597–600.

35 M. Muller, *Introduction to confocal fluorescence microscopy*, SPIE press, 2006, vol. 69.

36 W. G. Jerome and R. L. Price, *Basic confocal microscopy*, Springer, 2018.

37 S. Kalathimekkad, J. Missinne, D. Schaubroeck, R. Mandamparambil and G. Van Steenberge, *IEEE Sens. J.*, 2014, **15**, 76–81.

38 Thermo Fisher Scientific - Nile Red, https://www.thermofisher.com/order/catalog/product/N1142?uk&en#/N1142?uk&en.

39 H. Xia, T. Ueki and T. Hirai, *Langmuir*, 2011, **27**, 1207–1211.

40 T. Andjelković, D. Bogdanović, I. Kostić, G. Kocić, G. Nikolić and R. Pavlović, *Environ. Sci. Pollut. Res.*, 2021, 1–11.

Chapter 3

Investigating the UV Stability of Pigmented Water Repellent Coatings

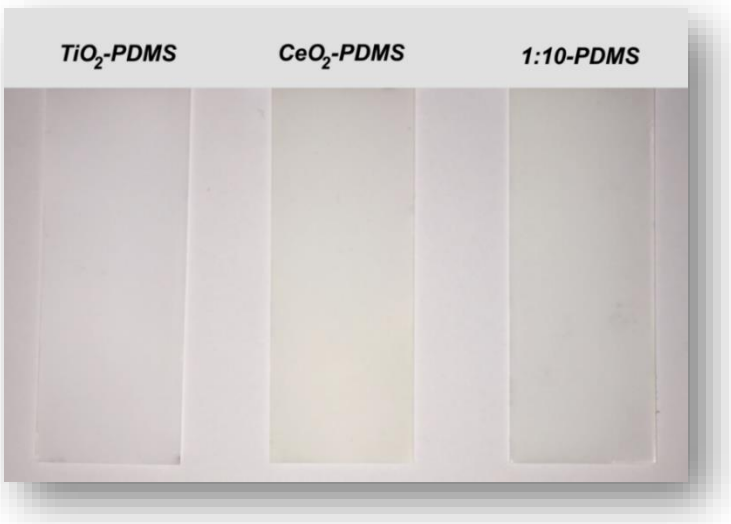

Publications: Pigmented self-cleaning coatings with enhanced UV resilience *via* the limitation of photocatalytic activity and its effects. R. L. Upton, C. R. Crick. *Mol. Syst. Des. Eng.*, 2020, **5** 876-881.

Contributions:

Transmission Electron Microscopy/Scanning-Transmission Electron Microscopy imaging was carried out under the supervision and aid of Dr Matt Bilton and Dr Karl Dawson (Imaging Centre at Liverpool).

EDX Mapping was carried out by Dr Karl Dawson (Imaging Centre at Liverpool).

3.1 Introduction

The development of aesthetically pleasing coatings is fundamental within the paints and coatings industries, which continually strive to provide their customers with the highest quality coatings. The market is vast and covers many commercial applications, however, over time the majority of surface coatings are exposed to multiple forms of contamination (dirt, biofilms etc.). Therefore, successfully integrating the intrinsic mechanisms of highly water repellent coatings to provide self-cleaning and anti-fouling abilities, would be extremely beneficial. As seen in section 1.7, intelligent paints that incorporate the patented Lotus-Effect® technology have been developed by Sto and are already commercially available.[1] However, this established technology is primarily aimed at the outdoor market, so may lack versatility in some respect. Hence, the requirement for further exploration is necessary. This chapter will investigate the potential of highly water repellent TiO_2-based coatings, and examine the feasibility of incorporating an alternative metal oxide pigment (CeO_2) to obtain a similar visual aesthetic with improved UV stability.

3.1.1 Titanium (IV) Dioxide

Although many formulations have been developed, inorganic nanoparticles are commonly employed (in the form of colloidal suspensions), due to their strong pigmentation and relative stability.[2] Titanium dioxide (TiO_2) is a wide bandgap semiconductor oxide (band gap: 3.2 eV) that is essential in commercial pigmented coatings, due to its high refractive index and known optical properties, which gives rise to high scattering of visible light in TiO_2-based nanomaterials. These factors make TiO_2 the brightest white pigment in common use and is therefore, a fundamental component within paint formulations.[3–5]

Employing TiO_2 nanoparticles, dually, as the primary pigment and as a roughening agent would be the most obvious route to fabricating TiO_2-based superhydrophobic materials. However, the presence of TiO_2 within superhydrophobic formulations is often detrimental, as wide bandgap semi-conducting oxide nanoparticles are inherently photocatalytic, degrading any organic/hydrophobic surface chemistry and inducing superhydrophilicity when exposed to UV radiation.[6] Incident radiation ($h\nu \geq$ bandgap energy) promotes the excitation of an electron from the valence band to the conduction band, inducing the formation of photo-generated holes (h^+) and electrons (e^-). Subsequently, successful charge carriers migrate to the surface of particles, where surface adsorbed species undergo oxidation reactions (electron donors) or reduction reactions (electron acceptors) to form active radicals (see Fig. 3.01). Competing mechanisms, such as the trapping of charge carriers or electron-hole

recombination (resulting in the release of energy) can limit photocatalysis by preventing charge carriers from reaching the particle surface to perform redox reactions. Despite a large recombination rate, TiO_2 shows high photocatalytic activity.[7,8] For this reason, environmentally induced change to surface wettability is a major concern for any highly water repellent materials that utilize TiO_2 nanoparticles, and has been shown to take place when exposing coatings to UV irradiation (mimicking solar radiation).[6,9–12] Subsequently, TiO_2 cannot be simply integrated into superhydrophobic materials and alternative measures must be taken to ensure the formation of chemically stable coatings.

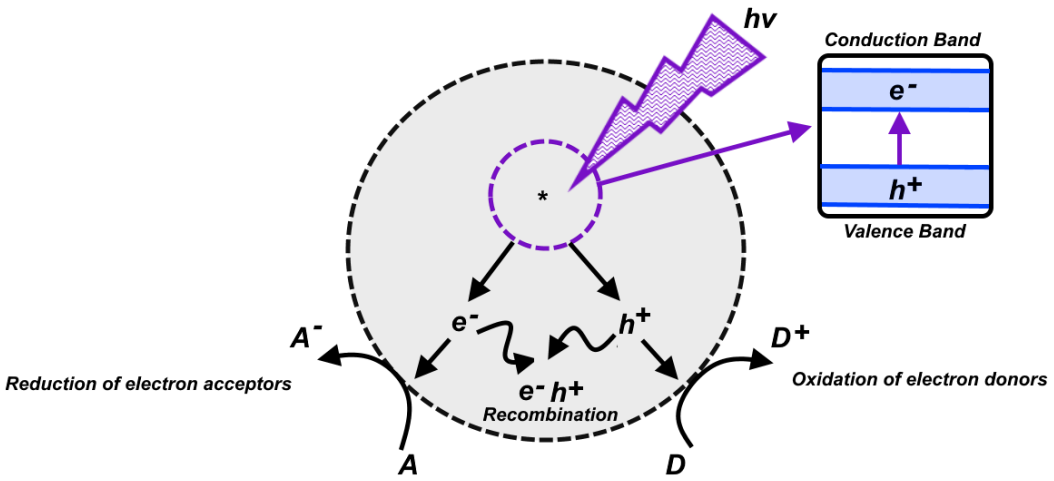

Figure 3.01: Schematic illustrating the photocatalysis process of TiO_2 particles, including; (**i**) the photoexcitation of electrons ($hv \geq$ bandgap energy) into the conduction band, generating holes in the valence band, (**ii**) recombination of charge carriers either in the bulk or at the surface of particles, and (**iii**) the redox processes of electron donors and acceptors with charge carriers which have successfully migrated to the surface of particles.[8]

3.1.2 UV Stability

Although pigmented superhydrophobic coatings have been successfully developed, fabricating TiO_2-based coatings with long term UV stability remains challenging. Nishimoto *et al.* reported TiO_2 modified with self-assembled monolayers of octadecylphosphonic acid, transforming from superhydrophobic (contact angle 173.6°) to superhydrophilic (near 0°) after just 10 minutes of irradiation (15 mW/cm^2).[13] Qing *et al.* reported a superhydrophobic thin film designed from polydimethylsiloxane (PDMS)/fluoroalkylsilane (FAS)/TiO_2 nanoparticles displaying a significant reduction in contact angle from 162.3° to 75.6° after 20 minutes UV irradiation (365 nm).[14] Two different fabrication approaches have been employed here, and though finding applications in superhydrophobic-superhydrophilic surface

patterning, both coatings provide minimal UV durability. This undoubtedly highlights the importance of chemical composition for long term resilience. Furthermore, Ding *et al.* reported a superhydrophobic self-cleaning coating fabricated by blending TiO_2 nanoparticles with fluorinated polysiloxane co-polymers. The direct blending of nanoparticles into the polymer results in a UV durable material. However, its practical application is limited by the inflexibility of the polymer casting technique and cost/regulatory issues relating to the commercial application of the fluorinated co-polymer system.[15] Generally, successful fabrication routes frequently involve the use of fluorinated chemicals, multi-step modification processes, or the requirement for specialised equipment, all of which, can be expensive and/or environmentally hazardous.

Many factors can have an impact on the stability of a molecular composite, including the inherent stability/resilience of the molecular coating – primarily governed by the bond strength – and the network of molecules that encapsulate particles.[16] As molecular coatings often form a self-assembled monolayer on the surface of particles, due to limitations relating to the number of available surface groups (outlined throughout section 1.5.2), little durability is provided.[13, 17] Additionally, the photocatalyst efficiency heavily contributes to the rate of photodegradation, as seen in the above examples, where coatings can be degraded in as little as 10 minutes.

3.1.3 Cerium (IV) Oxide

The strong oxidizing power of the TiO_2 photocatalyst is well-established, therefore, an alternative metal oxide could be better suited for employment as the primary pigment within highly water repellent coatings. Cerium oxide (CeO_2) is a rare earth metal oxide and similarly to TiO_2, is a wide bandgap semi-conductor (band gap: 3.0-3.4 eV) that has an intrinsic pale yellow pigmentation.[8] It has been reported to be inherently hydrophobic (advancing contact angle of ~ 100-110° on sintered CeO_2 pellets that had been polished), showing limited interaction with water as a result of its unique electronic structure (unfilled 4*f* orbitals are shielded by a full octet of electrons in $5s^2p^6$ orbitals). Consequently, hydrogen bonding between the surface and interfacial water molecules is somewhat disrupted, probing water molecules to orientate away from the surface, as proposed by Azimi *et al.*[18] In other studies, the interaction of water with the surface of CeO_2 has been predicted to be dependent on the crystal plane of the surface and the method of synthesis, which can result in quite significant variations in wettability (computed contact angles varying from 113° to 64° for different planes).[19] However, *Li et al.* reported the presence of surface hydroxyl groups for synthesised CeO_2 that predominantly existed in the preferred, lowest surface-energy crystal structure.

Hence, showing strong adhesion to water, which was found to increase when subject to a total of 24 hours of UV exposure (365 nm and 254 nm).[20] Contrary to this, other reports have employed low surface-energy molecules to functionalise the surface of CeO_2 structures, in order to generate/improve surface hydrophobicity.[21,22]

Work outlining the photocatalytic activity of CeO_2 has shown that CeO_2 nanoparticles often experience rapid electron/hole recombination, owing to their non-stoichiometric structure i.e. high concentration of oxygen defect sites, that stem from changes in chemical composition (Ce^{4+}/Ce^{3+} redox chemistry). Recombination can prevent mobile charge carriers from migrating to the particle surface and undergoing interfacial charge transfer, thus, reducing the efficiency of the photocatalyst.[23] Contrary to this, other researchers have purposed that the introduction of oxygen vacancies (by means of doping other semiconducting materials with CeO_2/Ce_2O_3) acts to separate holes and electrons, and reduce the extent of recombination, promoting photoactivity.[8, 24] Hence, the photocatalytic mechanism of CeO_2 appears to be somewhat more complex and may be system-specific.

Recent work published by Hu *et al.* investigated the use of hydrophobic black TiO_2/CeO_2 composites for visible light-activated self-cleaning coatings ($\lambda \geq 400$ nm).[25] Black TiO_2 is a defective form of TiO_2, usually synthesised *via* the inclusion of dopants or introduction of oxygen vacancies, which subsequently act to narrow the band gap (reported to be ~1.5-1.8 eV).[26, 25] Therefore, enabling photocatalytic activation by lower energy radiation i.e., light in the visible region of the spectrum. Coatings rich in CeO_2 (>60 wt %) were shown to have both high surface hydrophobicity and efficient self-cleaning properties, owing to the reported hydrophobic nature of CeO_2 and photodegradation of contaminants by black TiO_2. However, CeO_2 absorbs primarily in the UV region, so this work provided little insight into the long term UV stability of CeO_2-based coatings. In line with this, Li *et al*. reported the synthesis and use of CeO_2 nanotubes that were found to photodegrade contaminant oils, while retaining surface hydrophobicity.[27] Here, nanotubes were exposed to UV radiation (254 nm), however, the irradiation period was short and samples were only exposed for a maximum time period of 24 hours. Hence, the long-term UV stability of CeO_2 was not investigated within this work.

3.1.4 Chapter Aims

The principle aims of this chapter were to uncover the feasibility of employing photoactive metal oxide nanoparticles within superhydrophobic coatings, by studying their long-term stability towards UV radiation. Two pigmented metal oxides, that are both active as UV-light photocatalysts, were studied in parallel (TiO_2 *vs* CeO_2), while the UV resilience of molecular

and polymeric composites was examined. Here, molecular coatings were employed as a benchmark to evaluate the photocatalytic efficiencies of both metal oxides, as it was anticipated that self-assembled monolayers of FAS would be rapidly photodegraded, in line with what has been previously reported in the literature for TiO_2-based molecular composites. As discussed in chapter 2, polymeric composites allowed for greater coating optimisation, where tuning theoretical polymer thickness ($\mathbf{r}_{poly}$) was shown to impact the overall functionality of materials, respectively. Within this work, a silicone polymer (polydimethylsiloxane, PDMS) was appointed, owed to the near-homogeneous particle coverage and effective particle adhesion that had been demonstrated within the previous chapter – which was not observed when probing thermoplastic polymer-nanoparticle composites, as they behaved more so like adhesive binders [polyethylene, polyvinylchloride, polypropylene, see chapter 2]. Additionally, silicones are transparent (necessary for pigmented coatings) and have been reported to show moderate resistance to chemical attack, heat combustion and UV degradation, resulting from a combination of strong Si-O-Si bonds and an extensive crosslinked network.

To achieve this, the following objectives were met:

- The synthesis and characterisation of FAS molecular composite coatings, formulated with both metal oxide nanoparticles.
- The development of formulations that combine both metal oxide nanoparticles, to govern whether the visual pigmentation and photocatalyst efficiency/rate can be tuned.
- Optimisation of PDMS composite coatings, applying the superhydrophobic polymer-nanoparticle composite (SPNC) design principle, to uncover the effects of theoretical polymer thickness on the efficiency/rate of photodegradation for both metal oxide nanoparticle systems.
- The synthesis and characterisation of optimal PDMS composite coatings, formulated with both metal oxide nanoparticles.
- Perform UV degradation studies on both, molecular and optimal polymeric composites, formulated with both metal oxide nanoparticles (including a hybrid material) to draw comparisons on the performance and chemical stability when using:
  - Molecular *vs* polymeric coatings.
  - TiO_2 *vs* CeO_2 nanoparticles as the primary pigment.

3.2 Materials and Methods

3.2.1 Materials

Sylgard-184 (Silicone elastomer) was purchased from Ellsworth Adhesive Ltd. Multi-purpose adhesive was purchased from 3M. Titanium Dioxide (TiO_2, Aeroxide P25, 21 nm), cerium oxide (CeO_2, <25 nm), triethylamine (>99 %) and 1H, 1H, 2H, 2H-perfluorooctyltriethoxysilane (FAS, 98 %) were purchased from Sigma Aldrich. n-Hexane (HPLC grade) and ethanol (analytical reagent grade) were purchased from Fisher Scientific Limited.

3.2.2 Preparation of FAS Composite Coatings

Nanoparticles (2.91 mmol; total mass of 0.50 g for exclusive CeO_2/mixed coatings and a total mass of 0.23 g for exclusive TiO_2 coatings) were added to a solution of FAS (0.076 mL) in ethanol (12.5 mL), and left to mechanically stir overnight. A catalytic amount of triethylamine (1 mL) was added to CeO_2/mixed formulations to encourage the formation of the self-assembled monolayer. To aid composite-substrate binding, a commercial multi-purpose adhesive was utilized, similar to the procedure reported by Lu *et al*.[28] Hexane (4 mL) and multi-purpose adhesive (4 mL) were mixed in a glass vial using a vortex (Vortex-genie 2) for 2 minutes. One layer of this solution was drop cast *via* a pipette, evenly over the full surface of a glass substrate (Thermo scientific glass microscope slides, 76 x 26 mm), with tilting to remove any residual adhesive solution. The adhesive-coated substrate was left for 30 seconds before coating with FAS-based formulations. Coatings were deposited as stated in section 3.2.4.1.

3.2.3 Preparation of Sylgard-184 Composite Coatings

3.2.3.1 Initial Polymer Optimisation of TiO_2-PDMS Coatings

TiO_2 nanoparticles (0.25 g) were suspended in ethanol (10 mL). Following this, solutions of Sylgard-184 (10:1 mass ratio of elastomer and curing agent) in hexane (10 mL), that spanned theoretical polymer thicknesse values of 2-14 nm were made up:

Table 3.01: TiO_2-PDMS ($\mathbf{r}_{sphere}$ = 10.5 nm) mass and mass ratio summary for $\mathbf{r}_{poly}$ value range 2-14 nm:

$\boldsymbol{r}_{poly}$	*Mass ratio*	*Total mass Sylgard-184 (g)*
2	0.156	0.0390
4	0.371	0.0928
6	0.654	0.164
8	1.015	0.254
10	1.524	0.381
12	2.010	0.503
14	2.658	0.665

Once visibly dissolved with the use of mechanical stirring, Sylgard-184 solutions were added to nanoparticle suspensions and the formulations were mechanically stirred for a further 3 hours before deposition. Coatings were deposited as stated in section 3.2.4.2.

3.2.3.2 Optimal PDMS Composite Coatings

Nanoparticles (2.91 mmol; total mass of 0.50 g for exclusive CeO_2/mixed coatings and a total mass of 0.23 g for exclusive TiO_2 coatings) were suspended in ethanol (10 mL). Sylgard-184 solutions (10:1 mass ratio of elastomer and curing agent; 0.2 g elastomer and 0.02 g curing agent for CeO_2/mixed coatings and 0.15 g elastomer and 0.015 g curing agent for TiO_2 coatings) in hexane (10 mL) were made up. Once visibly dissolved with the use of mechanical stirring, Sylgard-184 solutions were added to the corresponding nanoparticle suspensions and the formulations were mechanically stirred for a further 3 hours, before deposition. Coatings were deposited as stated in section 3.2.4.2.

3.2.3.3 Investigating CeO_2-PDMS Coatings (section 3.3.5)

CeO_2 nanoparticles (0.5 g) were suspended in ethanol (10 mL). Solutions of Sylgard-184 (10:1 mass ratio of elastomer and curing agent) in hexane (10 mL), that spanned theoretical polymer thickness values of 2-8 nm were made up:

Table 3.02: CeO_2-PDMS ($\mathbf{r}_{sphere}$ = 12.5 nm) mass and mass ratio summary for $\mathbf{r}_{poly}$ value range 2-8 nm:

$\mathbf{r}_{poly}$	*Mass ratio*	*Total mass Sylgard-184 (g)*
2	0.0755	0.0377
4	0.175	0.0875
6	0.302	0.151
8	0.459	0.2295

Once visibly dissolved with the use of mechanical stirring, Sylgard-184 solutions were added to their corresponding nanoparticle suspensions and the formulations were mechanically stirred for a further 3 hours, before deposition. Coatings were deposited as stated in section 3.2.4.2.

3.2.4 Coating Deposition

A compression pump and airbrush kit was purchased from Voilamart. The spraying nozzle, pressurised by air at 2 bar, was used at a distance of approximately 4 cm away from the substrate surface. Precursor solutions, described in sections 3.2.2 and 3.2.3, were spray coated onto glass substrates (Thermo scientific glass microscope substrates (76 x 26 mm) in a diagonal motion, periodically across the surface.

3.2.4.1 FAS Composite Coatings

Three consecutive coatings of FAS composite formulations were applied to the adhesive-coated substrate at room temperature. Following this, coatings were left to dry under ambient conditions for 15 minutes.

3.2.4.2 PDMS Composite Coatings

To aid composite-substrate binding, a flat base layer of Sylgard-184 was deposited initially onto substrates, as follows; a temperature probe was set to 50℃ and a layer of Sylgard-184 solution (0.20 g elastomer/ 0.02 g curing agent in 10 mL hexane) was sprayed onto the moderately heated substrate. The base layer was left for 30 minutes to partially cure, before any further coating applications were carried out. Following this, the temperature probe was

increased to 125℃ and two consecutive layers of Sylgard-184 composite formulations were sprayed onto the heated substrates. Coatings were left for an additional 30 minutes, in order to facilitate the full curing of the polymer.

3.2.5 Materials Characterization

Surface morphologies of coatings were analysed using a scanning electron microscope (SEM, JEOL JSM-7001F/Tescan FIB SEM 58000G) operating at an acceleration voltage of 5-10 kV. The JEOL JSM-7001F SEM instrument had a built-in INCA X-act Energy Dispersive Spectroscopy (EDX) detector that was used to collect spectra. Cross-sectional samples were prepared by scoring the uncoated side of the glass substrate with a glass cutter and fracturing. All samples were vacuum sputter coated in a thin layer of chromium using a Quorum S150T ES sputter coater, to improve electrical conductivity, before imaging. A transmission electron microscope (TEM, JEOL 2100F) with built-in EDAX Octane T Optima windowless SDD EDX capabilities which was used to collect EDX maps, was operated at an acceleration voltage of 200 kV in both transmission (TEM) mode and scanning transmission (S-TEM) mode, using a CEOS GmbH "CESCOR" aberration correction system. TEM/S-TEM samples were prepared by scraping off a small quantity of surface coating or powder and sonicating it in 5 mL of ethanol. One drop of the suspension was pipetted onto a copper grid and left to air dry for 24 hours before imaging. TEM/S-TEM imaging was carried out under the supervision and guidance of **Dr Matt Bilton and Dr Karl Dawson** at the Imaging Centre at Liverpool. Corresponding EDX maps were carried out by **Dr Karl Dawson** at the Imaging Centre at Liverpool. Fourier Transform Infrared (FTIR) measurements were taken using a Bruker Optics' Vertex 70 over a range of 450 to 4000 cm^{-1}. UV-Vis diffuse reflectance spectra were obtained using a Cary 5000 UV-Vis-NIR Spectrometer in the range of 200-600 nm, using a pristine TiO_2 sample as the reference to set a 100% reflectance baseline.

3.2.6 Contact Angle Measurements

Static contact angle measurements were taken using a DSA100 Expert Drop Shape Analyser (Kruss GmbH) in the sessile drop operating mode with Young-Laplace fitting and manual assignment of the baseline. 6 μL water droplets were dispensed from a Hamilton microliter syringe with a 30 gauge dispensing tip directly onto the surface and at least 5 contact angle measurements, from evenly distributed positions across the surface, were taken and averaged for every reported contact angle. Tilting angles were recorded manually by dispensing a water droplet on the surface and tilting the surface at 2°/s, recording the angle at which the droplet

began to roll. At least 5 measurements, from evenly distributed positions across the surface, were taken and averaged for every reported tilting angle.

3.2.7 UV Lamp Set-up

Samples were positioned within a container, on top of which the UV lamp was situated (6.8 cm above coated slides), where it could emit radiation to the samples *via* a rectangular cut out in the container that was sized to fit the parameters of the lamp (20 x 5 cm). The Spectroline ENF-280c UV lamp was used with an emitted light of 365nm wavelength (8W power).

3.2.8 Water Bouncing Set-up

Water bouncing videos were recorded using a Sony Cyber-shot DSC-RX10 III digital camera (shooting at 1000 frames per second) and an average of 4 videos per coating was used to calculate bounces. 6 μL water droplets were dispensed from a 30 gauge dispensing tip which was positioned 20 mm above the substrate surface, similar to the set-up used by Crick *et al*.[29] Distilled water was dyed with methylene blue for visualisation purposes.

3.2.9 Self-Cleaning Test

See chapter 2, section 2.2.8 for the experimental procedure.

3.3 Results and Discussion

3.3.1 TiO_2-FAS Composite Coatings

Initial coatings were formulated using long-chain fluorinated silane molecules (FAS) due to their extremely low surface energy, straightforward functionalisation mechanism (*via* hydrolysis and condensation reactions), and wide recognition in the literature. TiO_2 nanoparticles were initially hydrophilic, due to the large presence of surface adsorbed hydroxyl groups. Therefore, functionalisation with molecular FAS was essential to alter the surface chemistry of particles and yield surface hydrophobicity. These treatments were carried out as ethanolic suspensions (99% ethanol, 1 % FAS), as metal oxide particles disperse well within this solvent – the intermolecular hydrogen bonding between ethanol molecules and hydroxyl groups on the surface of TiO_2 particles, stabilise the suspension – and ethanol facilitates the covalent grafting of FAS molecules onto the surface of nanoparticles. This has been reported previously in the literature by many research groups, as outlined throughout chapter 1, and has been utilized in chapter 2, where FAS was employed as a comparative SiO_2 molecular coating. See section 3.2 for full experimental details.

Coating suspensions were deposited *via* spray coating, which is a simplistic deposition technique that has few restrictions, as discussed in chapter 2. The resultant coatings appeared to be homogeneous and visually bright white. A strong white pigmentation was confirmed by UV-Vis spectroscopy, where coatings were observed to scatter ~ 75 % of visible light in diffuse reflectance measurements. This can be attributed to a combination of the high refractive index of TiO_2 (largely scatters visible light) and the light scattering capabilities of nanomaterials. Fourier-transform infrared (FTIR) spectroscopy was employed to confirm the presence of covalently bonded FAS molecules within surface coatings. Signals were relatively weak as the surface presence of FAS molecules is restricted by the number of surface groups on particles, available to undergo functionalisation (i.e., the formation of a self-assembled monolayer). However, expected vibrational bands that are representative of fluorinated groups ($-CF_2$, $-CF_3$) were observed, confirming the successful functionalisation of nanoparticles (see appendix for FTIR spectra, Fig. A1). An increase in surface hydrophobicity aligned well with the FTIR spectrum, showing an enhancement in contact angle from ~0° for as received TiO_2, to 162° ± 2 for TiO_2-FAS composite coatings.

Morphological assessment of TiO_2 nanoparticles was carried out *via* transmission electron microscopy (TEM) under the supervision and guidance of Dr Matt Bilton and Dr Karl Dawson, in order to better understand the average nanoparticle diameter and shape. Although the as received Aeroxide P25 TiO_2 particles were labelled as 21 nm ($\mathbf{r}_{sphere}$ = 10.5 nm), it appeared that particles were generally larger (24 ± 7 nm), when averaging a sample of 50

particle diameters using Image J and the calibrated ruler tool (see appendix, Table A1). Nanoparticles could be seen to be predominantly uniform in shape, during TEM imaging (see Fig. 3.02b). The surface microstructure of TiO_2-FAS was then examined using scanning electron microscopy (SEM), where a combination of randomly distributed nano- and micro-size particle aggregates could be observed throughout the coating, giving rise to a highly roughened surface architecture (see Fig. 3.02a). Subsequently, facilitating Cassie-Baxter wetting, whereby the formation of a new liquid-vapour interface gives rise to a 'slippery' surface. The general appearance could be described as fluffy, stemming from the lack of binder encapsulating and adhering particles together.

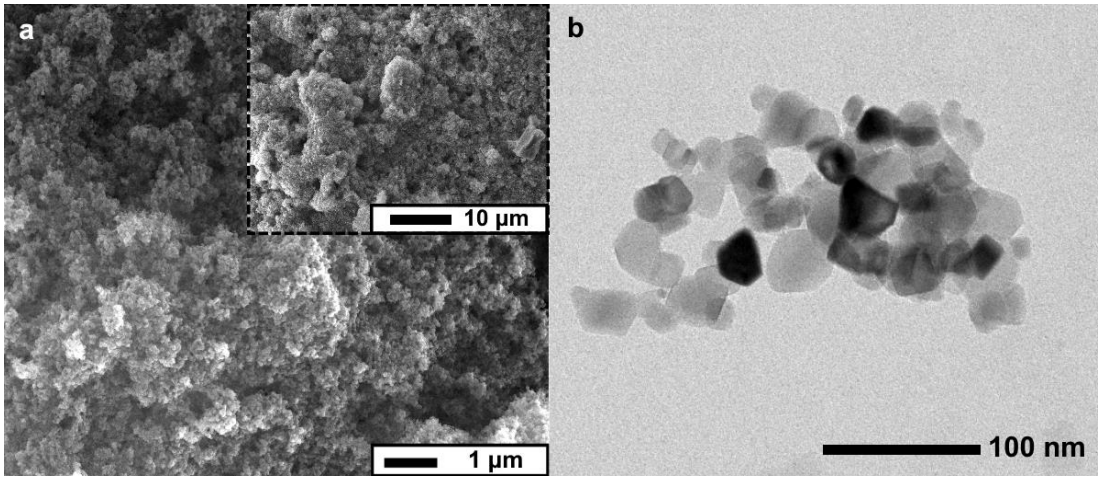

Figure 3.02: (**a**) SEM micrograph of TiO_2-FAS at high magnification, deposited *via* spray coating from an ethanolic suspension. Inset; micrograph at low magnification. (**b**) TEM image of as-received P25 TiO_2 nanoparticles (21 nm). Scale bars are shown.

Coatings were subject to intense periods of UV exposure, where any photo-induced loss in superhydrophobicity could be monitored by tracking a reduction in contact angle and enhancement in tilting angle. In order to generate an approximate comparison between the level of UV exposure we were subjecting coatings to, and that emitted by the sun on an average day outdoors, a solar equivalent was calculated. To do so, we used data published by Rafieepour *et al*., detailing the average monthly levels of detectable UVA radiation – UVB contributes very little to the solar radiation that reaches the earth, and UVC is completely blocked. Based on the average total UVA irradiance per day in a given year, being approximately 3.4 Wm^{-2}, it has been estimated that using a UVA source of this intensity (117.30 Wm^{-2}, 365 nm) has the solar equivalent of 35 days outdoor exposure.[30] Hence, 96 hours of irradiation under the lamp would be equivalent to approximately 139 days outdoor.

Initially, a contact angle of 162° ± 2 was observed for TiO_2-FAS films, which was seen to drastically reduce to 4° ± 6, after only 90 minutes of irradiation. This transition was also tracked using FTIR, where a reduction in the intensity of peaks representative of FAS could be seen, indicating the degradation of the chemisorbed fluoro-organosilane monolayer. During irradiation of a photocatalytic material, photo-generated holes (h^+) and electrons (e^-) are liberated within the bulk of the particles. Subsequently, charge carriers migrate to the surface to degrade surface adsorbed species in the presence of air, *via* the formation of active radicals (as discussed in section 3.1.2). Thus, it is expected that FAS molecules would undergo chemical degradation, resulting in an increase in surface-adsorbed hydroxyl groups, and ultimately restoring the hydrophilicity of the native TiO_2 surface. Hence, leading to a rapid loss in surface functionality.

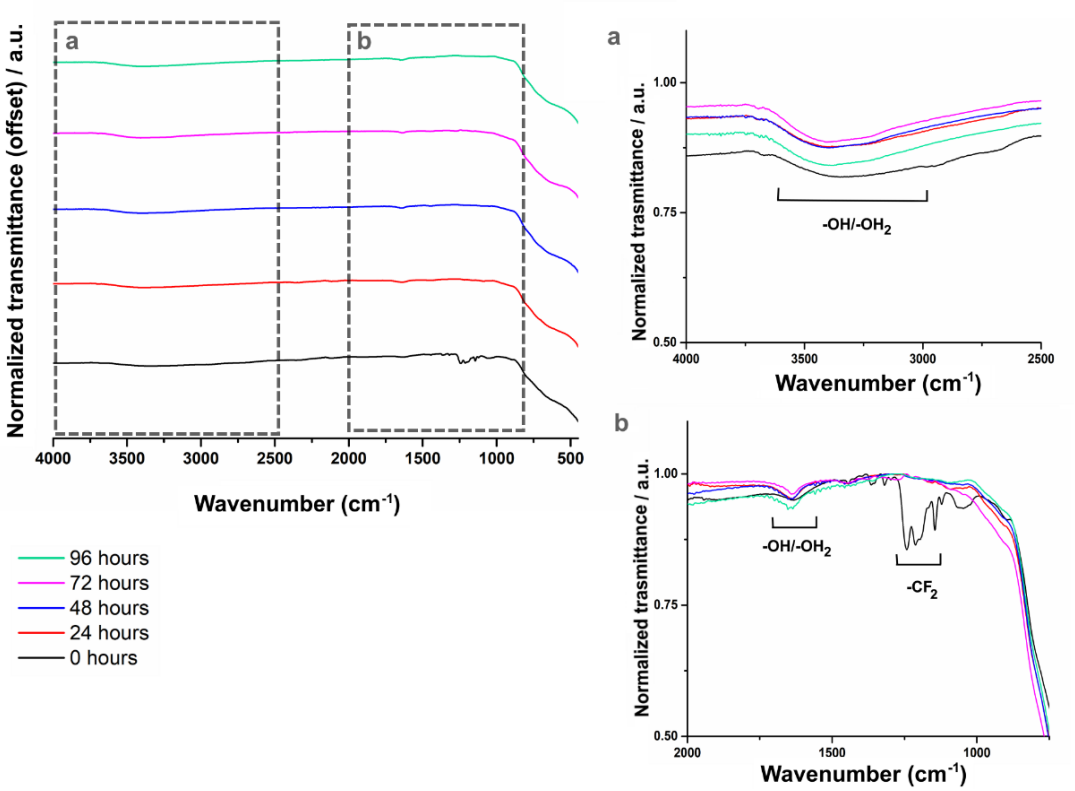

Figure 3.03 Stacked FTIR spectra of TiO_2-FAS composite coating at different UV exposure times (365 nm); spectra recorded at 24-hour time intervals. Magnified regions of spectra between; (**a**) 4000-2500 cm^{-1} and (**b**) 2000-750 cm^{-1} for visual aid and accentuation of significant signals.

Surface coating degradation can be identified by the disappearance of characteristic $–CF_2$ vibrational bands in the FTIR spectra over time, as seen in Figure 3.03. Furthermore, a vibrational band at ~1630 cm^{-1} is visible, which has been attributed in the literature to physically adsorbed water molecules (in addition to a broad peak at ~3400 cm^{-1}).[31,32] In line

with increasing UV irradiation time, the intensity of this peak is seen to slightly increase, further verifying UV-induced surface hydrophilicity and photodegradation of FAS molecules. However, it must be noted that this vibrational band was also present in the initial FTIR spectrum, suggesting that complete surface functionalisation may not have been achieved – although this was not reflected in the surface wettability of coatings, high static contact angles were attained. Similar findings have been reported in the literature; traits of unmodified particles were apparent in FTIR spectra of FAS-modified TiO_2 nanomaterials, within work carried out by Pazokifard *et al.* and Lee *et al*.[31,33] Hence, this may be a common occurrence.

3.3.2 CeO_2-FAS Composite Coatings

Analogous FAS composite coatings were fabricated (see section 3.2 for full experimental details). Experimental details were identical to that of TiO_2-FAS coatings, with the exception of using a larger initial mass of nanoparticles to form suspensions, to account for differences in metal oxide density, and use of a base to encourage molecular functionalisation. Coatings appeared to have a pale yellow pigmentation (scattered ~ 25 % visible light) and were visually similar in appearance to TiO_2-FAS coatings. As-received CeO_2 nanoparticles were pellet pressed to obtain a flat surface (a small mass of powder was inserted into the hydraulic press under a pressure of 2 ton, to obtain a 7 mm diameter pellet), to uncover the inherent surface wettability of particles, as mixed reports have been presented in the literature. However, due to the fragility of the pellet, only a rough contact angle of ~ 52° was recorded. Although some literature examples report synthesised/sintered CeO_2 materials to be intrinsically hydrophobic, as documented throughout section 3.1, the as-received particles from Sigma-Aldrich appeared to have a hydrophilic nature, and subsequently required surface functionalisation to achieve system compatibility. FTIR and surface wettability measurements were used to characterise coatings and confirm the functionalisation of particles with FAS molecules (see appendix for FTIR spectrum, Fig. A1). After functionalisation, an increase in contact angle was observed (166° $\pm$ 1, some intensification due to an enhancement in surface roughness), highlighting a change in surface chemistry, which was owed to the suspected covalent grafting of long-chain fluorinated molecules. A duplicate characterisation was carried out to assess the morphological structure of CeO_2-FAS coatings. Using the same technique (TEM and Image J), particles reported by the manufacturer to be < 25 nm ($\mathbf{r}_{sphere}$ = 12.5 nm) were determined to be ~27 $\pm$ 14 nm, showing a greater size distribution compared to that of TiO_2 (see appendix, Table A1). Additionally, TEM images showed CeO_2 nanoparticles to be highly non-uniform in shape, including; circular, square-like, and triangular structures, amongst other more irregular geometries (see Fig. 3.04b). SEM micrographs depicted a similar coating formation

to that of TiO_2-FAS, where aggregates of nanoparticles varied in size, resulting in a highly textured microstructure, as seen in Figure 3.04a.

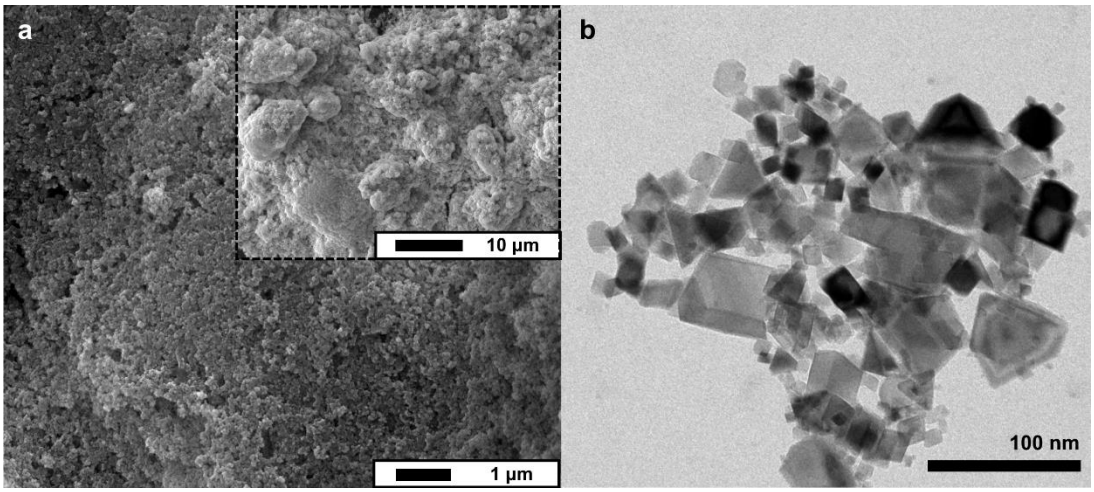

Figure 3.04: (**a**) SEM micrograph of CeO_2-FAS at high magnification, deposited *via* spray coating from an ethanolic suspension. Inset; micrograph at low magnification. (**b**) TEM image of as-received CeO_2 nanoparticles (< 25 nm). Scale bars are shown.

CeO_2-FAS coatings were subject to intense UV irradiation under the same conditions. Coatings were continually irradiated for a total of 96 hours, being paused only at the 24-hour mark to record any changes in surface wettability, following which, they were positioned back under the UV lamp for a further 24-hour cycle. It was anticipated that the inclusion of CeO_2 would actively extend the time it took for coatings to lose their functionality, as CeO_2 has been reported to be photocatalytically less efficient. CeO_2 nanostructured films withstood the full duration of 96 hours irradiation, showing a loss in superhydrophobicity only within the final 24 hours, where the contact angle decreased to $148° \pm 15$. During the final reading, non-homogeneity was apparent as contact angles recorded across different areas of the surface ranged from 158° to 122°. The sharp reduction in contact angle at specific surface points, combined with increased water pinning (apparent after 72 hours), alludes to a wetting state transition from the Cassie-Baxter to the Wenzel state. During repetition experiments, the extent of surface degradation appeared to be somewhat inconsistent, which could suggest the non-uniform bonding of FAS molecules to the surface of nanoceria. However, all samples were observed to be entirely superhydrophobic after 48 hours of irradiation. As irradiation continued, chemical degradation of FAS molecules on the surface of silane-treated particles likely occurred in parts, facilitating the partial loss of interfacial air, due to unfavourable interactions with newly introduced polar species. This is turn, leads to enhanced hydrogen

bonding between the surface coating and the deposited water droplet, as advanced pinning to the surface microstructure is observed.

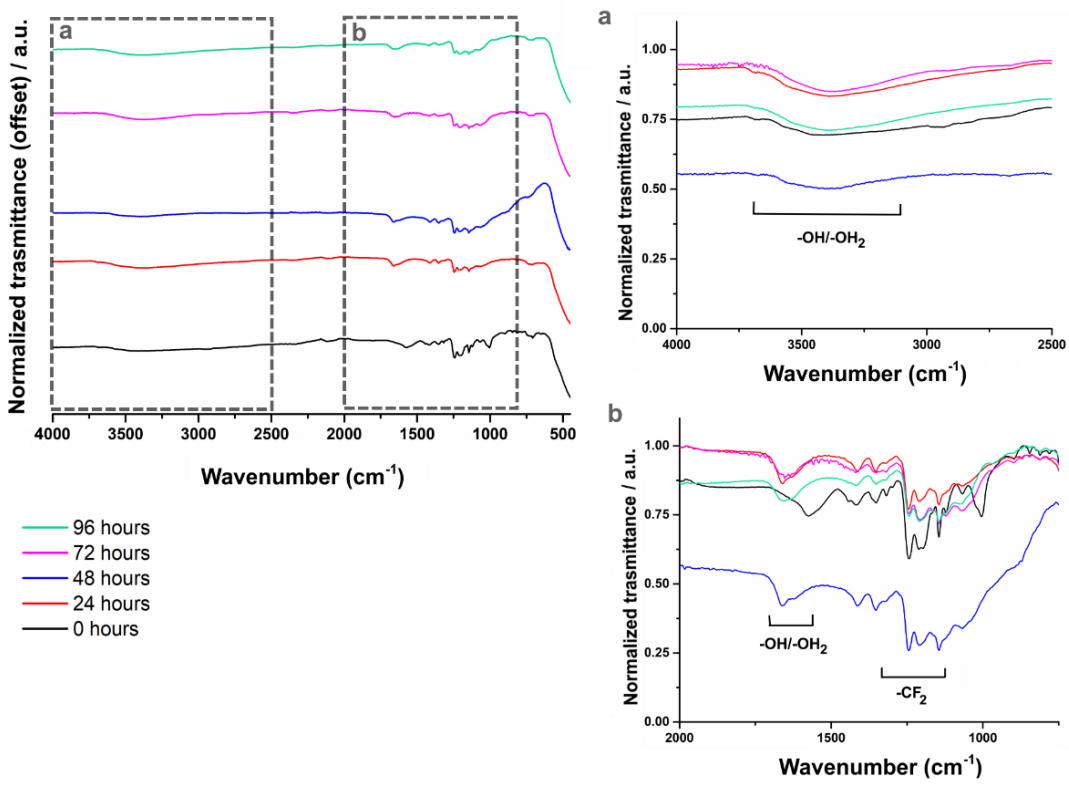

Figure 3.05: Stacked FTIR spectra of CeO_2-FAS composite coating at different UV exposure times (365 nm); spectra recorded at 24-hour time intervals. Magnified regions of spectra between; (**a**) 4000-2500 cm^{-1} and (**b**) 2000-750 cm^{-1} for visual aid and accentuation of significant signals.

FTIR was employed to track the presence of FAS-related vibrational bands during the course of the experiment, as seen in Figure 3.05. Bands representative of $–CF_2$ stretches could be observed after 96 hours of irradiation, confirming the reduced rate of degradation of FAS molecules, which aligns well with the reported contact angles. It must be noted that a band characteristic of physically adsorbed water molecules could be seen in all spectra (inclusive of the initial surface coating that was not exposed to UV light), as seen for TiO_2-FAS, suggesting that complete surface modification was not achieved and that alternate surface chemistries may have been present (see section 3.2.5 for further discussion). However, the presence of physisorbed water molecules is contrary to the reported static contact angles during UV testing, as CeO_2-FAS appeared to be relatively stable with respect to photodegradation.

CeO_2 nanoparticles appeared to be remarkably less efficient as a photocatalyst when employed as the primary pigment, which could be attributed to a combination of factors; (**i**) the slower

migration of charge carriers to the surface of particles, due to the presence of oxygen vacancies which act to trap carriers, (**ii**) larger rates of recombination for charge carrier that are not trapped and/or (**iii**) FAS molecules are more weakly bonded to the nanoceria surface. It is well documented in the literature that the adsorption behaviour of molecules can affect the photocatalytic activity of semiconductors.[24] Hence, as the exact surface conformation of the as-received CeO_2 nanoparticles was unknown, it may be reasonable to suggest that FAS molecules are more weakly adsorbed onto the surface of CeO_2, promoting a slower rate of photodegradation.

3.3.3 TiO_2 and CeO_2 Hybrid Coatings

Preliminary studies were conducted to probe the effects of blending both particles (TiO_2/CeO_2) on the resultant durability and pigmentation of coatings (see Fig. 3.06). Coatings were fabricated from precursor suspensions that comprised a systemically increased weight percentage of CeO_2 nanoparticles, and were then exposed to UV irradiation, to govern the formulation with the greatest UV stability.

Figure 3.06: Images highlighting the visual pigmentation of blended TiO_2/CeO_2-FAS ethanolic suspensions (**left to right**: 9 wt%, 17 wt%, 33 wt%, 50 wt%, 67 wt%, 83 wt% and 91 wt% CeO_2).

Table 3.03: Recorded static contact angles for coatings that comprised a systematically increased weight percentage of CeO_2, deposited *via* spray coating from ethanolic suspensions, before and after 18 hours of UV irradiation (365 nm, 8W power). Suspensions were briefly stirred for approximately 2 hours before coating deposition, to obtain preliminary results and give an indication of the best performing composites.

TiO_2:CeO_2 mass ratio	*Corresponding weight percentage of CeO_2 (total 0.5 g, w/w)*	*Initial static contact angle*	*Static contact angle after 18 hours of UV irradiation (365 nm)*
10:1	9 wt%	165° ± 2	0°
5:1	17 wt%	164° ± 3	0°
2:1	33 wt%	164° ± 2	0°
1:1	50 wt%	165 ° ± 3	0°
1:2	67 wt%	163° ± 2	0°
1:5	83 wt%	164° ± 1	135° ± 4
1:10	91 wt%	166° ± 2	143° ± 7

Formulations that comprised ≤ 67 wt % CeO_2 showed rapid photodegradation, reflected by a photo-induced change in surface wettability from superhydrophobic to superhydrophilic, yielding a water contact angle of ~0° as water visibly spread across the surface. When assessing exclusive coatings in sections 3.2.1 and 3.2.2, formulations were mechanically stirred overnight. However, in the interest of time, the suspensions studied here were mechanically mixed for only 2 hours, prior to deposition. Hence, superhydrophobicity was lost within 18 hours in all cases, likely due to incomplete surface modification. Nonetheless, the formulation that comprised 91 wt % CeO_2 (mass ratio 1:10 TiO_2:CeO_2, labelled 1:10-FAS) appeared to display the greatest UV resilience, and was therefore, selected for further examination. The same UV protocol that was used to examine exclusive molecular composite coatings was used for comparative studies (total 96 hours with 24-hour measurements), and coatings were mechanically stirred overnight, in line with the initially reported systems. Initially, a contact angle of 167° ± 1 was observed, which is marginally greater than that of both exclusive coatings. This is likely attributed to a combination of nanoparticles with different reported diameters and shapes (TiO_2 24 ± 7 nm and CeO_2 27 ± 14 nm), enhancing the level of surface texturing. Films withstood 48 hours of UV exposure while retaining their superhydrophobicity, surpassing the UV stability of exclusive TiO_2-FAS. However, a decline in contact angle was observed at the 72-hour mark (88° ± 4), that decreased further to 69° ± 7 after 96 hours. Diffuse reflectance spectra were recorded to draw comparisons between the

pigmentation of TiO_2-FAS, CeO_2-FAS and 1:10-FAS. For TiO_2-FAS films, reflectance began to increase at 328 nm and showed a steep rise at 351 nm, highlighting that TiO_2 absorbs very little light in the visible region (380-750 nm), with an absorption edge wavelength of 400 nm. Generally, lower reflectance was observed for CeO_2 containing films (scatters ~ 30 % visible light for 1:10 and ~ 25 % for CeO_2), suggesting CeO_2 nanostructured coatings either absorb more visible light, in line with coatings having a pale yellow pigmentation, or light is being transmitted through the coating. Reflectance began to increase at 361 nm for CeO_2-FAS (absorption edge wavelength 411 nm) and at 354 nm for 1:10-FAS (absorption edge wavelength 409 nm), marking a fractional shift in the edge of the absorption band towards the UV region for 1:10-FAS, which could suggest a slight reduction in the pale yellow pigmentation of the blended coating (see Fig. 3.07).

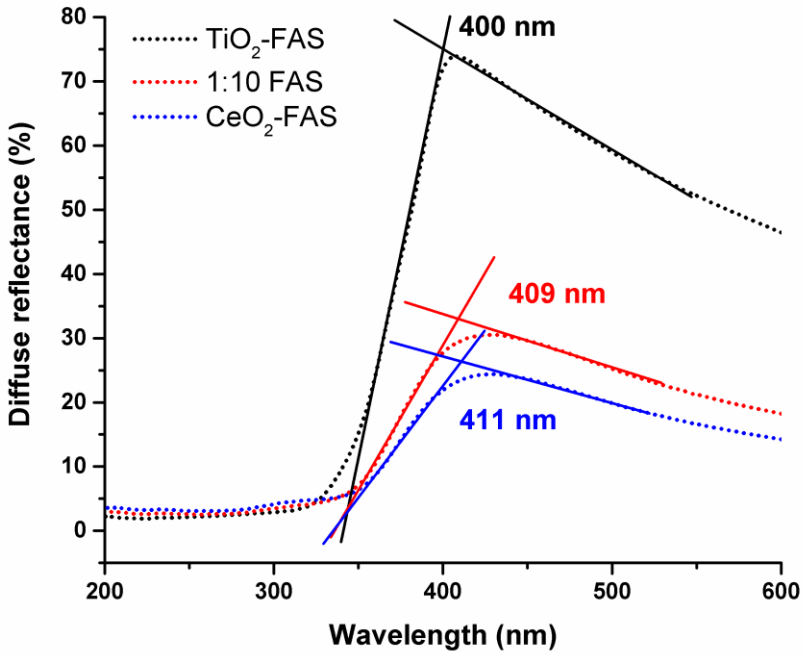

Figure 3.07: Overlaid diffuse reflectance spectra of TiO_2-FAS, CeO_2-FAS and 1:10-FAS, highlighting the absorption edge wavelength for each surface coating.

Bandgap energies (E_g) were calculated using the absorption edge wavelength and equation (**1**) below:

$$E = \frac{hc}{\lambda} \qquad (1)$$

where E is energy (J), h is planks constant (6.626 x 10^{-34} m^2kgs^{-1}), c is the speed of light constant (2.998 x 10^8 ms^{-1}) and λ is the absorption edge wavelength (x 10^{-9} m). Energy can then be converted from J into eV using a conversion factor of 6.242 x 10^8, respectively. TiO_2-

FAS was calculated to have an E_g value of 3.10 eV, CeO_2-FAS an E_g value of 3.02 eV and 1:10-FAS an E_g value of 3.03 eV. Furthermore, E_g values were calculated using the Kubelka-Munk theory (see appendix, Fig. A2), where values appeared to be significantly larger, yet still followed the same trend.[34] The surface coating that comprised a blend of both metal oxide nanoparticles appeared to have a slightly increased E_g value when using both methods (compared to exclusive CeO_2-FAS), suggesting that a small weight percentage of TiO_2 may affect not only the coating pigmentation, but also the electronic band structure.

3.3.4 Sylgard-184 Composite Coatings

A thermoset silicone elastomer was introduced to coat nanoparticles, for reasons discussed in section 3.1.4 (near-uniform coatings of particles, good adhesive binding of particles, general stability of silicones, etc.). Furthermore, the polymer employed within these SPNC systems required optical transparency, so that the coating pigmentation would not be impacted in any way. It can be seen from Figure 3.08 that PDMS was highly stable towards photodegradation, as expected, and therefore, any photodegradation is believed to be due to the photoactive pigments within coatings.

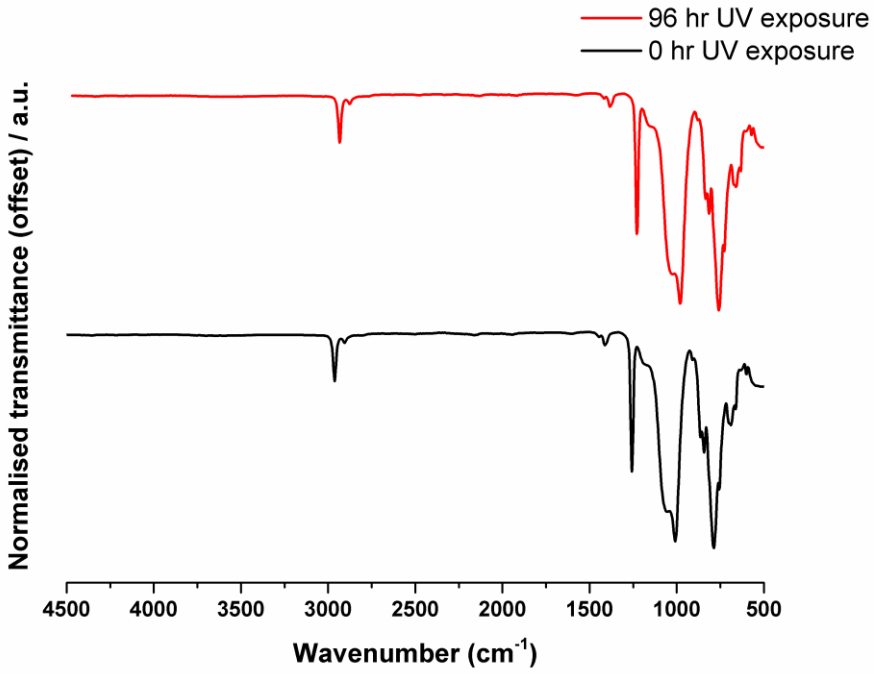

Figure 3.08: Stacked FTIR spectra comparing flat PDMS initially, after no exposure to UV (black line), and after 96 hours of continuous exposure to UV (365 nm, red line).

3.3.4.1 Polymer Optimisation

Prior to fabricating composite coatings for comparative UV testing, formulations were developed using the SPNC design principle to study the UV stability of TiO_2-PDMS coatings, over a range of theoretical polymer thickness values (see chapter 2). Coatings with initial $\mathbf{r}_{poly}$ values ranging 2-8 nm were irradiated for a total of 96 hours, and static contact angle measurements were taken at 24-hour intervals, in line with the testing of molecular composite systems.

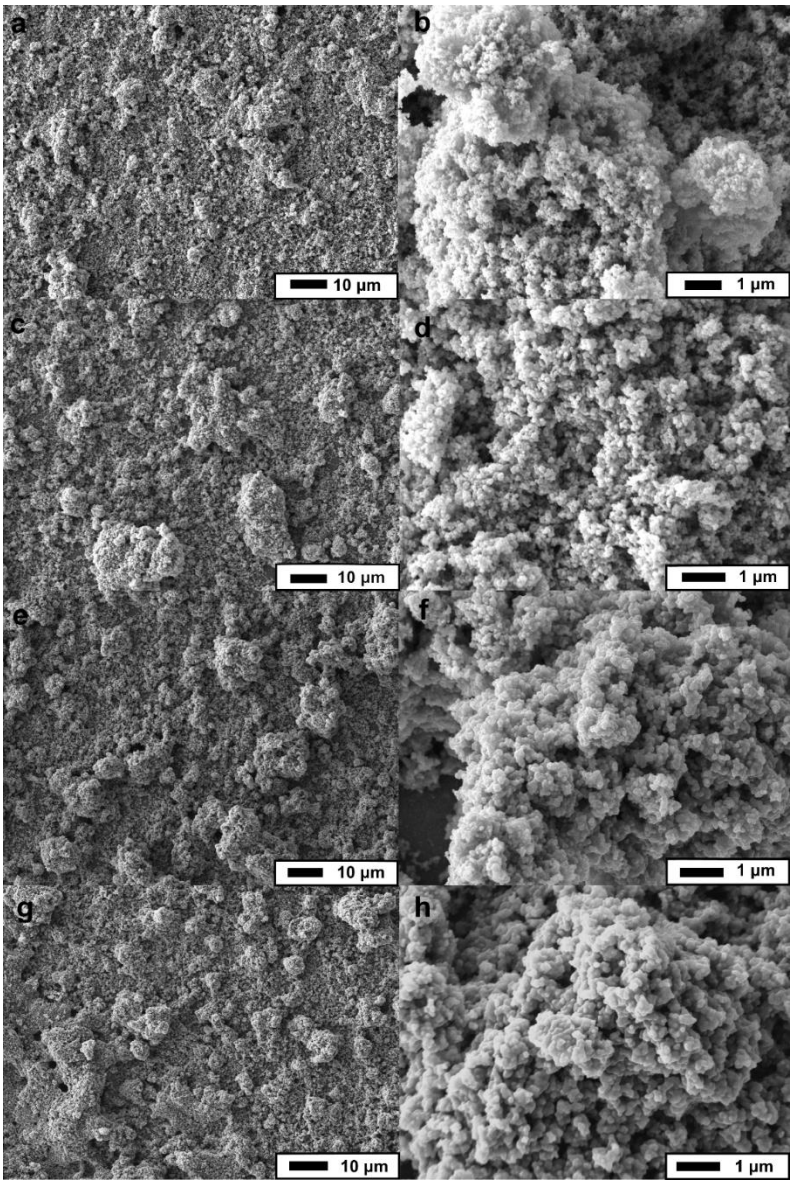

Figure 3.09: SEM micrographs highlighting the surface morphology of TiO_2-PDMS coatings, deposited *via* spray coating from ethanol/hexane suspensions (50:50 v/v). In all images the nanoparticle diameter is 21 nm, with theoretical polymer thicknesses of; (**a, b**) 2 nm, (**c, d**) 4 nm, (**e, f**) 6 nm and (**g, h**) 8 nm at low and high magnification. Scale bars are shown.

Initially, the surface hydrophobicity of all PDMS-based coatings did not differ significantly, suggesting that the range of $\mathbf{r}_{poly}$ values studied were not extreme enough to dramatically alter the surface morphology of coatings. This is confirmed in Figure 3.09, where the low magnification images highlight similarities in the morphology of each coating, despite a

visible increase in the thickness of the polymer layer surrounding particle aggregates (high magnification images, see Fig. 3.09b/d/f/h). This may be attributed to TiO_2 particles having a diameter that marginally exceeded the reported particle size, for which theoretical polymer thickness values were calculated. Furthermore, tilting angles for all coatings were low (<10°), suggesting a Cassie-Baxter wetting state and low water adhesion to the surface.

Table 3.04: Recorded static contact angles for TiO_2-PDMS coatings with theoretical polymer thickness values ($\mathbf{r}_{poly}$) ranging 2-8 nm, deposited *via* spray coating from ethanol/hexane suspensions (50:50 v/v), before and after 96 hours of irradiation (365 nm, 8W power).

$\mathbf{r}_{poly}$ *(nm)*	*Initial static contact angle*	*Static contact angle after 96 hours of UV irradiation (365 nm)*
2	165° ± 2	0°
4	166° ± 2	160° ± 5
6	165° ± 1	165° ± 2
8	163° ± 2	166° ± 3

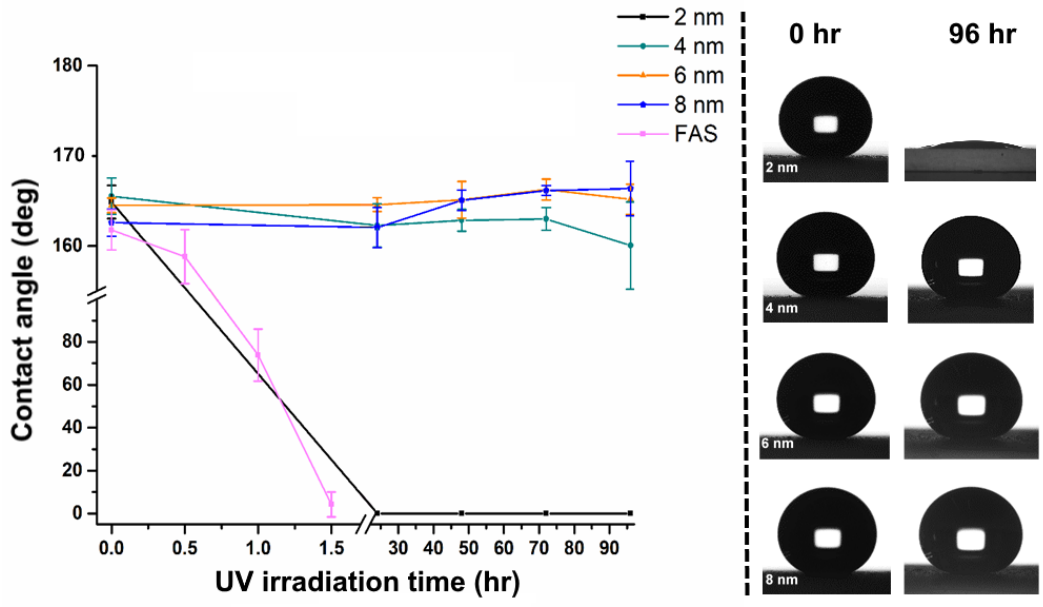

Figure 3.10: The change in static contact angle with UV irradiation time (365 nm, 8W power) for TiO_2-PDMS coatings with theoretical polymer thicknesses ranging 2-8 nm and TiO_2-FAS for comparative purposes (**left**). Corresponding digital images of a water droplet on the surface of PDMS-based coatings at labelled time intervals (**right**).

Coatings with an $\mathbf{r}_{poly}$ value of 2 nm turned superhydrophilic within 24 hours of UV exposure, highlighting that a thin layer of polymer can leave coatings susceptible to rapid photodegradation, and that a critical mass of PDMS is required to provide long-term stability. This was comparable to molecularly coated TiO_2 (TiO_2-FAS) which was shown to withstand only 90 minutes of irradiation. Conversely, films with theoretical polymer thickness values of 4 nm, 6 nm and 8 nm withstood the full 96 hours of irradiation, while showing a negligible change in contact angle, and retained surface functionality (see Fig. 3.10). TiO_2-PDMS with an $\mathbf{r}_{poly}$ value of 4 nm initially displayed the greatest surface hydrophobicity, however, also showed the largest decrease in contact angle, as documented in Table 3.04 (excluding the coating with an $\mathbf{r}_{poly}$ value of 2 nm). Hence, reiterating the importance of considering the specific requirements of the resultant material before designing SPNC coatings, so that coatings are best suited to their targeted application. Interestingly, TiO_2-PDMS coatings that comprised thicker polymer coatings i.e, an $\mathbf{r}_{poly}$ value of 8 nm, exhibited a static contact angle that was seen to increase with UV exposure time. To shed more light on this, TiO_2-PDMS coatings with theoretical polymer thickness values of 10 nm, 12 nm and 14 nm were fabricated and subject to UV testing.

Table 3.05: Recorded static contact angles for TiO_2-PDMS coatings with theoretical polymer thickness values ($\mathbf{r}_{poly}$) ranging 10-14 nm, deposited *via* spray coating from ethanol/hexane suspensions (50:50 v/v), before and after 96 hours of irradiation (365 nm, 8W power).

r_{poly} *(nm)*	*Initial static contact angle*	*Static contact after 96 hours of UV irradiation (365 nm)*
10	$163° \pm 2$	$161° \pm 3$
12	$159° \pm 1$	$162° \pm 3$
14	$146° \pm 15$	$162° \pm 3$

It appeared that coatings that comprised greater PDMS loadings experienced enhancements in surface hydrophobicity, in line with prolonged UV exposure, when examined. Although the exact reasoning for this is not clear, it is suspected to be related to; (**i**) partial surface degradation/crackin.g of the polymer during exposure, leading to enhanced surface texturing and/or (**ii**) changes in surface chemistry. However, when considering the contact angle values and standard deviation ranges, further work would be required to definitively confirm this. Nonetheless, the surface hydrophobicity of films with an $\mathbf{r}_{poly}$ value of 6 nm remained virtually constant throughout the irradiation period, demonstrating a strong stability towards

photodegradation. Therefore, moving forward, an optimal $\mathbf{r}_{poly}$ value of 6 nm was used for comparative studies between SPNC systems.

3.3.4.2 Fabrication

Similar to FAS-based coatings, exclusive TiO_2 (TiO_2-PDMS), exclusive CeO_2 (CeO_2-PDMS) and blended composite coatings (1:10-PDMS) were fabricated (see Fig. 3.11). Sylgard-184 is a two-part elastomer that consists of a base and a curing agent that are mixed in a 10:1 ratio and cured upon heating in the presence of a platinum catalyst, as discussed in chapter 2 (see section 2.3.1).

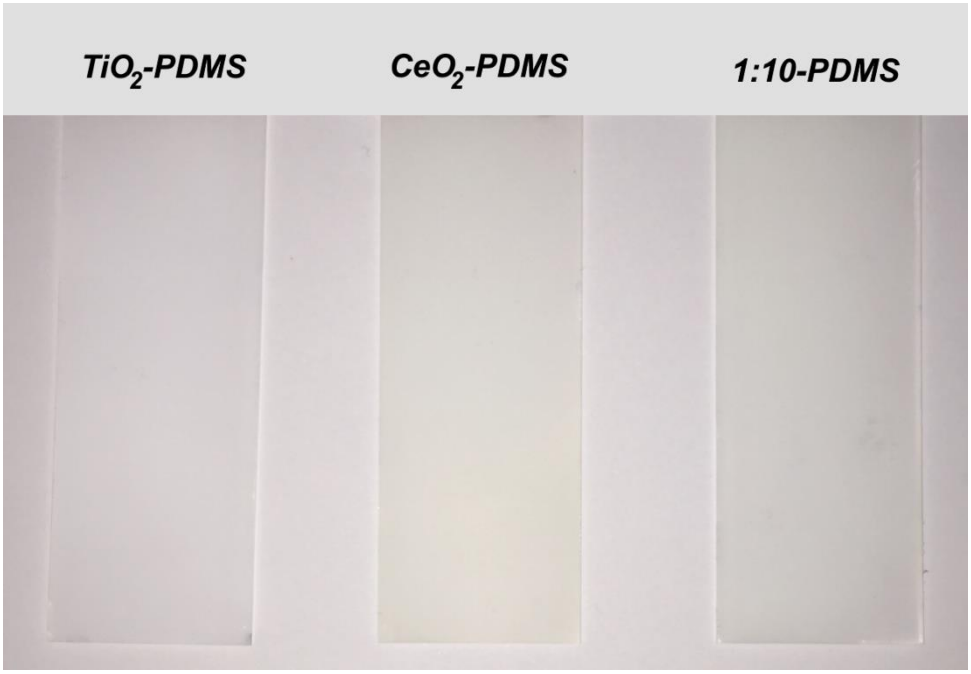

Figure 3.11: Image highlighting the physical appearance of PDMS composite coatings (**left to right:** TiO_2-PDMS, CeO_2-PDMS and 1:10-PDMS).

As stated above, the optimal thickness of TiO_2-PDMS was chosen to be 6 nm which correlated to a mass ratio of 0.654, when using the SPNC design principle. To simplify the weighing process, 0.23 g TiO_2 and 0.165 g PDMS (0.15 g base and 0.015 g curing agent) were used to make precursor formulations. Subsequently, this resulted in a marginally larger mass ratio of 0.717, leading to a projected coating thickness of 6.4 nm, for 21 nm particles. In order to fabricate comparative CeO_2-based coatings, the same mass ratio cannot be applied due to differences in density and particle size. However, the theoretical polymer thickness can be determined relative to nanoparticle size:

$$\textbf{TiO}_2\textbf{:}\ \frac{6.4\ nm}{21\ nm} = 0.305$$

$$\textbf{CeO}_2\textbf{:}\ 0.305 \times 25\ nm = 7.6\ nm \approx 8\ nm$$

Again, to simplify quantities for weighing, CeO_2-PDMS and 1:10-PDMS coatings were formulated using 0.5 g of particles (combined total for 1:10-PDMS) and 0.22 g PDMS (0.2 g base and 0.020 g curing agent). This yielded a mass ratio of 0.440 which corresponded to a theoretical polymer thickness of 7.8 nm for CeO_2-PDMS, and 7.5 nm for 1:10-PDMS; these can be regarded as 8 nm for simplicity.

Initially, the functionalisation of nanoparticles with oleic acid (a long-chain hydrocarbon molecule with intrinsic hydrophobicity) was attempted. It was anticipated that functionalisation was necessary to ensure a hydrophobic surface chemistry on the exterior of particles, and therefore, induce better component compatibility. Functionalisation of TiO_2 nanoparticles using a procedure previously reported in the literature by Crick *et al*. was carried out, and particles were found to be hydrophobic.[35] However, when repeating this for CeO_2 nanoparticles using the same experimental method, coatings comprising the 'functionalised' particles were found to show variable surface chemistry. This can likely be attributed to the complex redox chemistry between CeO_2 (Ce^{4+}) and Ce_2O_3 (Ce^{3+}), preventing straightforward surface functionalisation from taking place. After many unsuccessful attempts to alter the experimental procedure for ceria, it was decided that the use of unfunctionalized particles in a mixed solvent system of two miscible solvents that had different polarities, could be an alternative solution. The solvent selected to suspend nanoparticles was ethanol as metal oxides were seen to suspend reasonably well when fabricating FAS-based coatings, in addition to ethanol having physical properties that could aid the deposition process i.e., high vapour pressure. Alternatively, n-hexane – a non-polar solvent that facilitates the dissolution of PDMS precursor components (marked by their visual disappearance) – was used to soluble PDMS, and was then deposited into a vial containing ethanolic suspensions of metal oxide nanoparticles. Both solvents appeared to mix homogenously and particle agglomerates appeared to disperse well in the mixed solvent system, despite receiving no pre-treatment with hydrophobic molecules. Prior to coating depositions, the substrate was first spray coated with a layer of PDMS that was partially cured to provide a water repellent base. This was aimed at

increased hydrophobicity and physical durability, and was later fully crosslinked during the full curing process of deposited coatings.

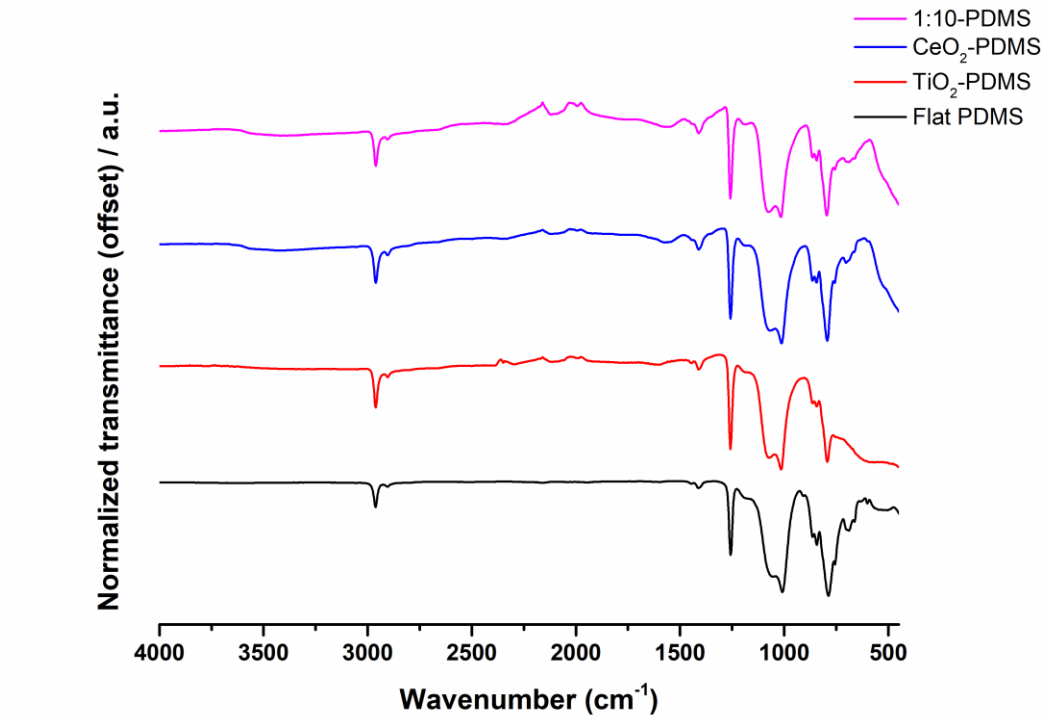

Figure 3.12: Stacked FTIR spectra of pure PDMS and PDMS composite coatings, prior to any UV exposure.

FTIR was used as a technique to detect the encapsulation of particles with PDMS, as seen in Figure 3.12. Vibrational bands representative of PDMS can be seen in all spectra; 2962 cm^{-1} and 2904 cm^{-1} owed to asymmetric -CH_3 stretching in Si-CH_3, 1257 cm^{-1} representative of symmetric -CH_3 deformation of Si-CH_3, 1060 cm^{-1} and 1010 cm^{-1} characteristic of the Si-O-Si stretching mode and at 790 cm^{-1} corresponding to –CH_3 rocking and Si-C stretching in Si-CH_3, respectively.[36] Additional peaks can be seen, characteristic of the metal oxide component; TiO_2-PDMS showed a peak at ~800-450 cm^{-1} which is characteristic of Ti-O/Ti-O-Ti stretching vibrations, and CeO_2-PDMS/1:10-PDMS spectra included a peak at ~560-450 cm^{-1} that can be owed to O-Ce-O stretching.[31,37] Furthermore, as seen in molecular composite coatings, a signal at ~1630 cm^{-1} was apparent – suggesting that physically adsorbed water molecules may have been present. However, it is difficult to deduce between chemisorbed (i.e., surface hydroxyl groups) and physisorbed water molecules, so this is not surprising for polymeric composites, due to metal oxide nanoparticles receiving no pre-treatment prior to encapsulation with PDMS. It must be noted that impurity peaks at ~ 2400

cm^{-1}, representing CO_2, can be seen in some spectra. Furthermore, high static contact angles were observed for polymeric composites – 164° ± 1 for TiO_2-PDMS, 165° ± 1 for CeO_2-PDMS and 168° ± 2 for 1:10-PDMS – resulting from a combination of surface roughness and the presence of hydrophobic methyl groups (covalently grafted onto the siloxane backbone), further confirming particle encapsulation with PDMS. All coatings were found to have low tilt angles (<10°), suggesting Cassie-Baxter surface wetting. Diffuse reflectance was used to confirm a shift in the absorption edge wavelength of 1:10-PDMS coatings (from 429 nm for exclusive CeO_2-PDMS to 420 nm for 1:10-PDMS), as seen in Figure 3.13, suggesting a possible reduction in the yellow pigmentation of coatings. These results align well with what was observed in molecular systems, however, the shift in absorption edge wavelength seemed to be more intense for polymeric systems. E_g values were calculated for all coatings using equation (**1**), where TiO_2-PDMS was found to have an E_g value of 3.14 eV, CeO_2-PDMS was found to have an E_g value of 2.89 eV and 1:10-PDMS was found to have an E_g value of 2.95 eV. Again, reiterating that particle blends can result in materials that can have tuneable pigmentation and electronic band structures.

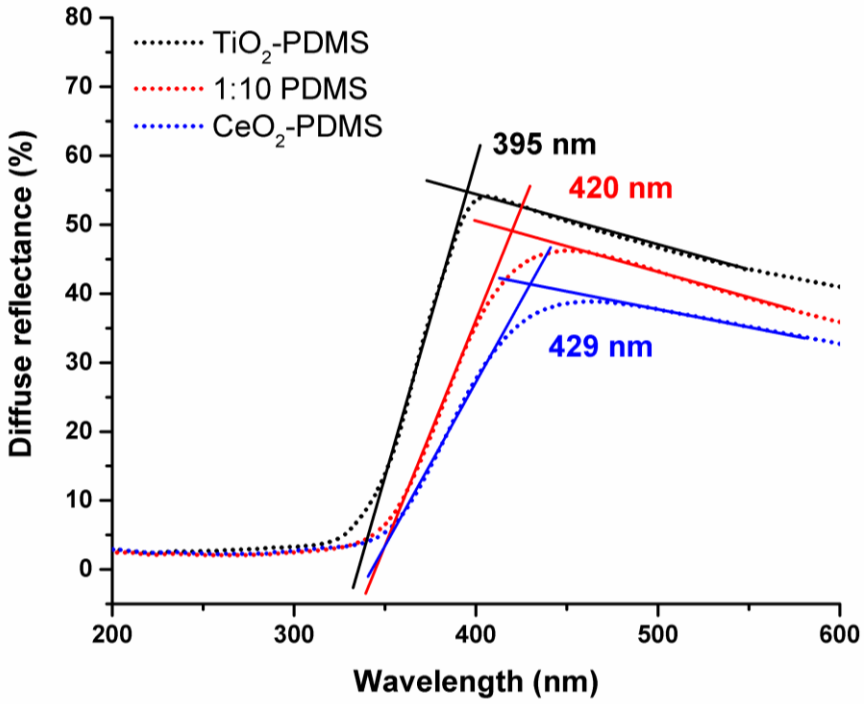

Figure 3.13: Overlaid diffuse reflectance spectra of TiO_2-PDMS, CeO_2-PDMS and 1:10-PDMS, highlighting the absorption edge wavelength for each surface coating.

3.3.4.3 Morphology

Similar to molecular composite coatings, surfaces displayed a highly roughened surface topography due to the partial agglomeration of particles during the spray coating process. An amorphous layer of polymer could be observed on the surface of particles, effectively encapsulating and adhering agglomerates together. Irregular microstructures ranging up to 43 μm could be observed from cross-sectional SEM micrographs, and an average film thickness was estimated to be between ~12-16 μm for TiO_2-PDMS – structured from a ~4 μm PDMS base layer and composite coating which was measured to be between ~8-12 μm, as seen in Figure 3.14. EDX confirmed the composition of coatings, as all suspected elements (C, O, Si, Ti and/or Ce) were present (see appendix, Table A2).

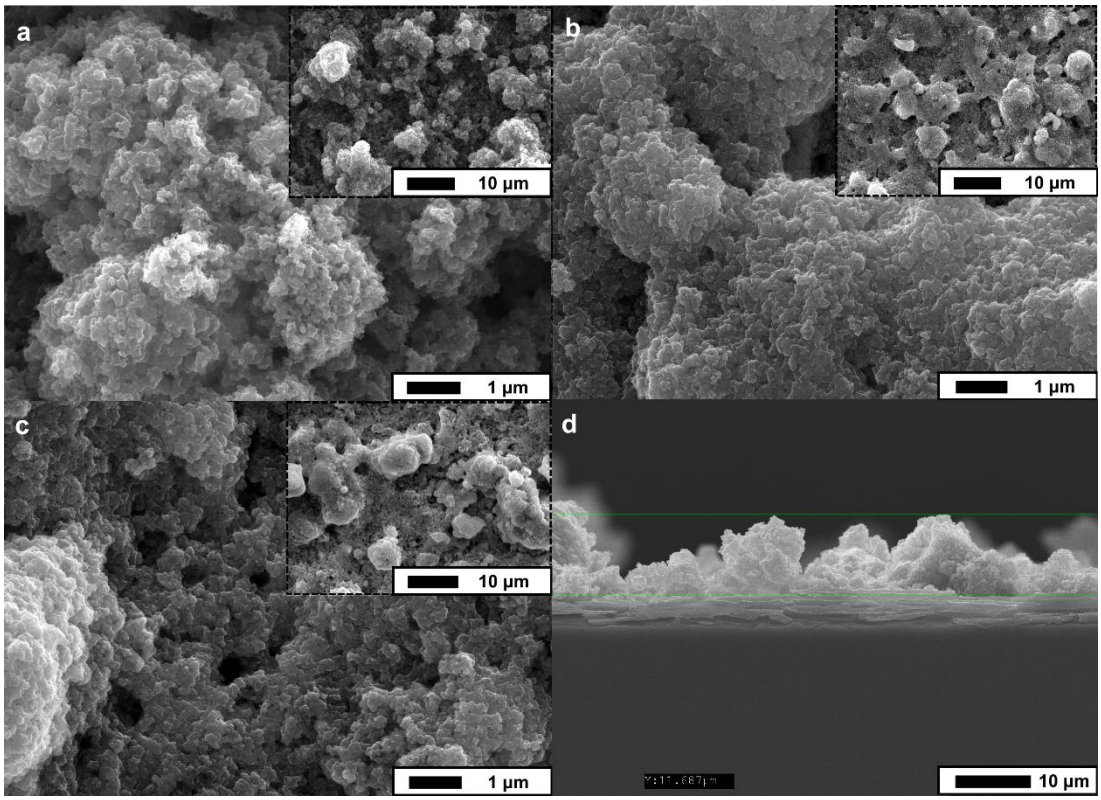

Figure 3.14: Top-down SEM micrographs depicting the morphological structure of; (**a**) TiO_2-PDMS, (**b**) CeO_2-PDMS and (**c**) 1:10-PDMS at high magnification, deposited *via* spray coating from ethanol/hexane suspensions (50:50 v/v). Insets; micrographs at low magnification. (**d**) Cross-sectional micrograph of TiO_2-PDMS, highlighting the PDMS base layer (~4 μm) and the approximate coating thickness (~8-12 μm). Scale bars are shown.

To further investigate how coatings naturally assemble and probe the accuracy of the SPNC design principle, TiO_2-PDMS was employed for further investigation. An amorphous layer surrounding TiO_2 particles was detected *via* scanning transmission electron microscopy (S-

TEM) after coating with PDMS, as seen in Figure 3.15. S-TEM is a microscopy technique that combines the principles of both TEM and SEM, as it generates high resolution images and detects transmitted electrons similar to TEM, yet employs a finely focused electron beam to scan over the surface in a raster pattern, which is characteristic of SEM. The external amorphous coating was measured to be of approximately 7 ± 2 nm thickness (average of 25 measurements using image J and the calibrated ruler tool), which aligned well with the predicted theoretical polymeric coating of 6.4 nm. It is important to note that theoretical polymer thickness values are only a guideline for the comparison of different SPNC systems, as these values do not take into account human error, inconsistencies in particle size or the chemical interactions between polymer and particles. EDX mapping was carried out by Dr Karl Dawson to visualise the elemental positioning, by highlighting titanium, silicon and oxygen atoms in areas where particles resided. However, there was no distinct layer of silicon/oxygen atoms surrounding TiO_2 nanoparticles. This could be attributed to partial/complete degradation of the polymer during exposure to the electron beam, and therefore, the generation of organic pollutants that may have subsequently contaminated the area (giving rise to an amorphous layer on S-TEM images).

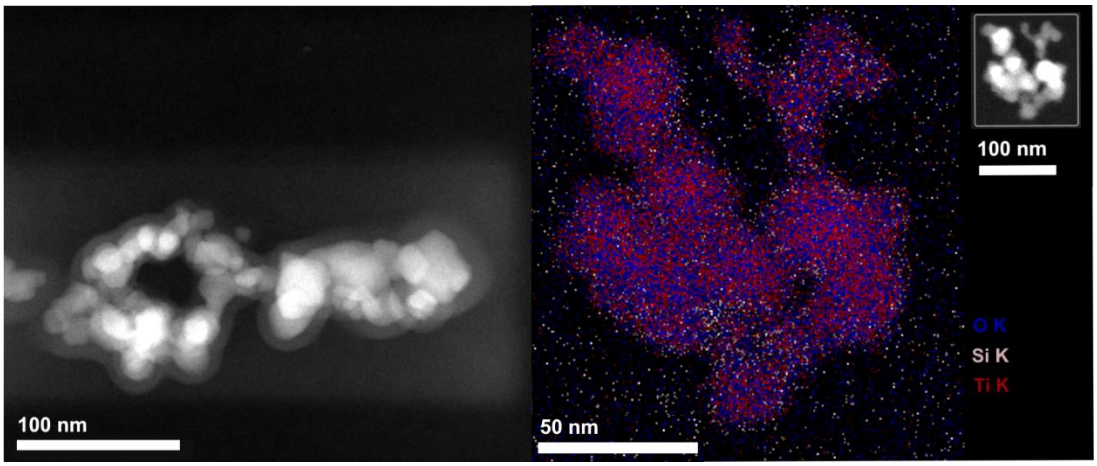

Figure 3.15: Darkfield S-TEM image of TiO_2-PDMS with a theoretical polymer thickness value of 6 nm and measured amorphous layer of 7 ± 2 nm (**left**) and the corresponding EDX map (O K blue, Si K pink and Ti K red, **right**). Inset S-TEM image of TiO_2-PDMS used for mapping. Scale bars are shown.

3.3.4.4 UV Degradation Studies

Optimal PDMS-based coatings were subject to analogous UV studies. TiO_2-PDMS initially displayed a contact angle of 164° ± 1, where a negligible decrease to 163° ± 2 was observed after 96 hours of irradiation, as seen in Figure 3.16. When compared to molecular TiO_2 coatings, which turned superhydrophilic after 90 minutes of irradiation, a significant

enhancement in UV stability was clear. The primary interaction between TiO_2 and PDMS has been speculated to be hydrogen bonding between the surface adsorbed hydroxyl groups of metal oxide particles and the backbone siloxane oxygen atoms of PDMS.[38] Siloxanes are a class of polymers that have highly flexible backbones (i.e., large bond angles and bond lengths compared to carbon-based polymers which aid the rotation of methyl groups about the Si-O-Si backbone). Furthermore, they exhibit high stability towards oxidative degradation, due to polymers being highly crosslinked and having strong siloxane linkages (Si-O has an average bond energy of 452 kJ/mol *vs* C-O which has an average bond energy of 358 kJ/mol).[39] Therefore, it is anticipated that a complex combination of high surface coverage through extensive intermolecular interactions, excellent backbone flexibility, the inherent resistance of silicones towards oxidative degradation, and the use of an optimal polymer:nanoparticle mass ratio, enabled PDMS to suppress photodegradation upon exposure to UV light. When probing CeO_2-PDMS and 1:10-PDMS coatings, excellent UV durability was also observed after 96 hours of UV exposure; contact angles were seen to negligibly decrease from 165° ± 1 to 164° ± 2 for CeO_2-PDMS and from 168° ± 2 to 164° ± 2 for 1:10-PDMS (see Fig. 3.16). This underlines the positive impact of using optically transparent thermoset coatings when designing UV durable superhydrophobic pigmented coatings.

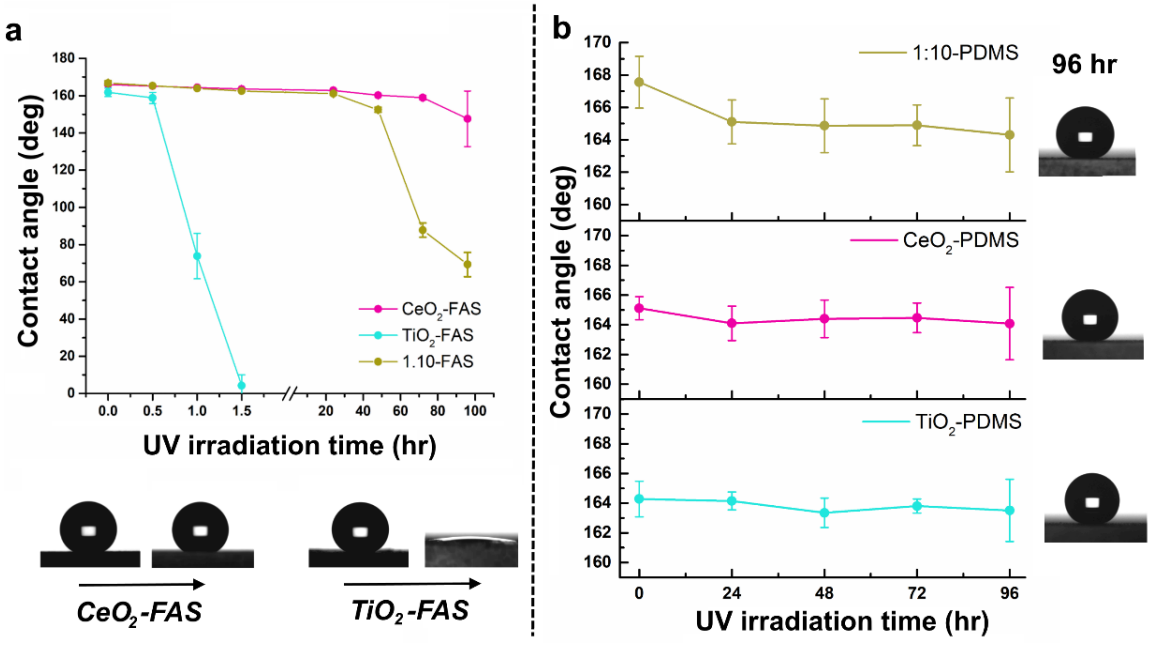

Figure 3.16: Plots to compare the variation in UV stability (static contact angle) of (**a**) molecular composite coatings and (**b**) polymeric composite coatings, when subject to 96 hours of UV irradiation (365 nm, 8W power). Inset; digital images highlighting a water droplet on the surface of each coating, initially and after 96 hours of irradiation.

To confirm that pigmented coatings were functional after irradiation, artificial dirt (MnO_2) was randomly dispersed onto the external surface of coatings. Deposited water droplets were employed to remove the simulated contaminant, where droplets could be seen to bead up, collecting particles and removing them from the surface, *via* the Lotus Effect (see Fig. 3.17). Furthermore, extended UV stability studies were carried out where coatings were exposed to a maximum of 250 hours UV irradiation, which resulted in static contact angles of ~160° and ~162° for TiO_2-PDMS and CeO_2-PDMS, respectively. Additionally, coatings were observed to remain superhydrophobic after 100 days of storage under ambient conditions, accentuating the real-world potential of these superhydrophobic pigmented coatings.

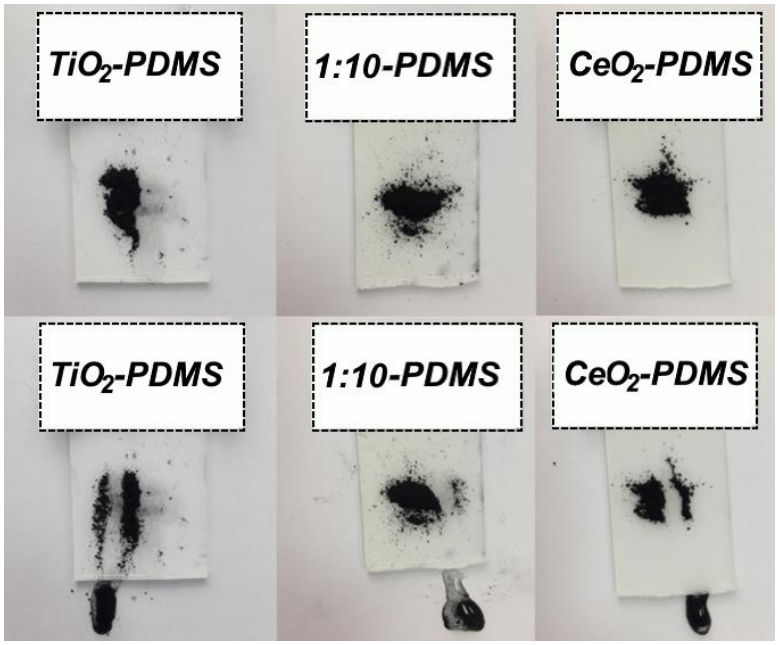

Figure 3.17: Images showing the self-cleaning performance of surfaces after 96 hours of UV irradiation (365 nm, 8W power, **left to right**: TiO_2-PDMS, 1:10-PDMS and CeO_2-PDMS). All surfaces were able to remove simulated dirt (MnO_2) *via* water droplets deposited directly onto the surface.

3.3.4.5 Water Bouncing

Water bouncing can be employed as a supporting characterisation technique to investigate the surface wettability/wetting regime of a surface. The use of this technique to characterise superhydrophobicity was firstly defined in the literature by Crick *et al*., where the 'ideal' set-up to perform water bouncing measurements, without observing droplet fragmentation during impact, was reported.[29] In a similar approach, 6 μL water droplets dyed with methylene blue for visualisation purposes, were dispensed from a 30 gauge dispensing tip that was positioned 20 mm above the coating surface (see section 3.2.8 for full details). A high-speed camera was employed to capture images (see Fig. 3.18).

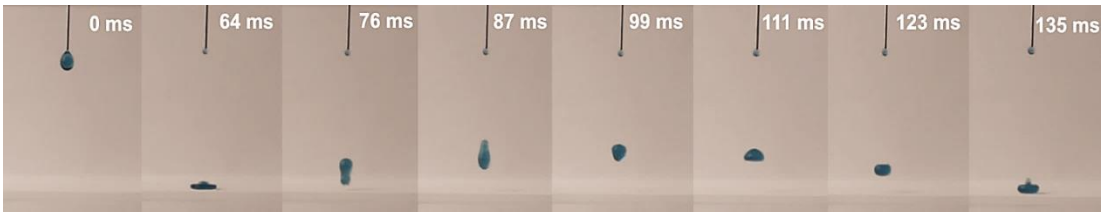

Figure 3.18: Images highlighting the dynamic wetting behaviour of 1:10-PDMS upon impact with a dispensed water droplet (6 μL droplet dispensed from 20 mm above the surface). Methylene blue dye was used to aid visualisation.

If a surface has an extensive liquid-vapour interface, water will bounce several times during impact and avoid penetrating the surface microstructure, due to a large presence of interfacial air pockets. However, if Wenzel wetting occurs or a form of intermediate wetting state – which shares both Cassie-Baxter and Wenzel attributes (see section 1.3.3) – deposited droplets will quickly pin to the surface and bounces will be limited. Hence, this technique can be used to shed light on the interfacial areas beneath the impacting droplet, as a form of dynamic wettability measurement. The average number of bounces appeared to generally increase, in line with the static contact angle of each surface coating. On average, TiO_2-PDMS displayed on ~11/12 bounces, CeO_2-PDMS displayed ~12 bounces and ~13/14 bounces were observed for 1:10-PDMS. A higher number of bounces were likely observed for CeO_2-based coatings due to larger inconsistencies in the uniformity of CeO_2 nanoparticles, and the introduction of dual-size particles for 1:10-PDMS, enhancing the architectural roughness of coatings and thus promoting the entrapment of air within the voids of the surface. A high number of bounces was expected, as this aligns well with the high static contact angles and predicted Cassie-Baxter wetting state of coatings, in addition to the research reported by *Crick et al.*, which stated that up to 12-14 bounces could be seen for coatings that displayed extreme superhydrophobicity (dependent on droplet size, static contact angle and surface morphology).[29]

3.3.5 Investigating CeO_2-Based Coatings Further

Throughout this work, it was assumed that CeO_2 would behave in a similar manner to TiO_2, with regards to molecular functionalisation and polymer encapsulation, due to both being semiconducting metal oxide nanoparticles. However, during the examination of molecular CeO_2 composite coatings, it became apparent that there were some inconsistencies between repeat experiments, as previously mentioned. Furthermore, within the literature, there are

mixed reviews regarding the intrinsic surface chemistry of nanoceria, as outlined throughout section 3.1.3. Hence, the functionalisation mechanism may not be as straightforward as other inorganic nanoparticles (e.g. TiO_2 or SiO_2), and it is likely that the surface structure of CeO_2 is highly complex and contains a combination of both, hydrophobic moieties and polar surface groups. In order to draw comparisons between TiO_2 systems and CeO_2 systems, CeO_2-PDMS coatings with different theoretical polymer thickness values (2-8 nm) were fabricated and subject to UV stability testing. All coating morphologies were similar in appearance to TiO_2-PDMS systems ($\mathbf{r}_{poly}$ values 2-8 nm), in that a highly roughened surface structure could be seen which evolved from a 'fluffy' appearance, where it was difficult to visualise any polymer ($\mathbf{r}_{poly}$ = 2 and 4 nm), to the visible presence of polymer-coated particle aggregates ($\mathbf{r}_{poly}$ = 6 and 8 nm), in line with increasing theoretical polymer thickness (see Fig. 3.19).

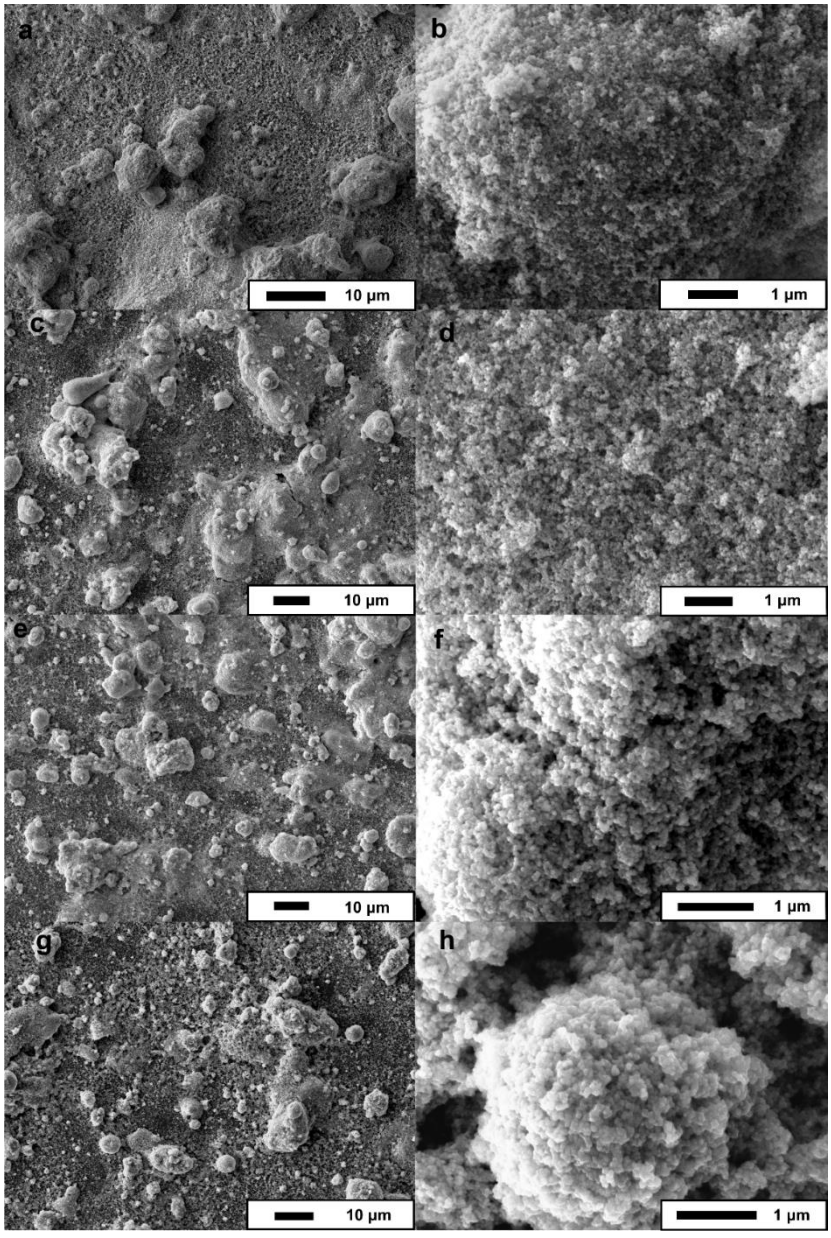

Figure 3.19: SEM micrographs highlighting the surface morphology of CeO_2-PDMS coatings, deposited *via* spray coating from ethanol/hexane (50:50 v/v) suspensions. In all images, the nanoparticle diameter is 25 nm, with theoretical polymer thickness values ranging (**a, b**) 2 nm, (**c, d**) 4 nm, (**e, f**) 6 nm and (**g, h**) 8 nm at low and high magnification. Scale bars are shown.

Table 3.06: Recorded static contact angles and tilting angles for CeO_2-PDMS coatings with theoretical polymer thickness values ($\mathbf{r}_{poly}$) ranging 2-8 nm, deposited *via* spray coating from ethanol/hexane suspensions, before and after 96 hours of irradiation (365 nm, 8W power).

r_{poly} *(nm)*	*Initial static contact angle*	*Initial tilting angle*	*Static contact angle after 96 hours of UV irradiation (365 nm)*	*Tilting angle after 96 hours of UV irradiation (365 nm)*
2	167° ± 1	>90°	0°	-
4	165° ± 2	4° ± 1	0°	-
6	165° ± 2	5° ± 1	129° ± 9	>90°
8	166° ± 3	7° ± 2	163° ± 3	5° ± 1

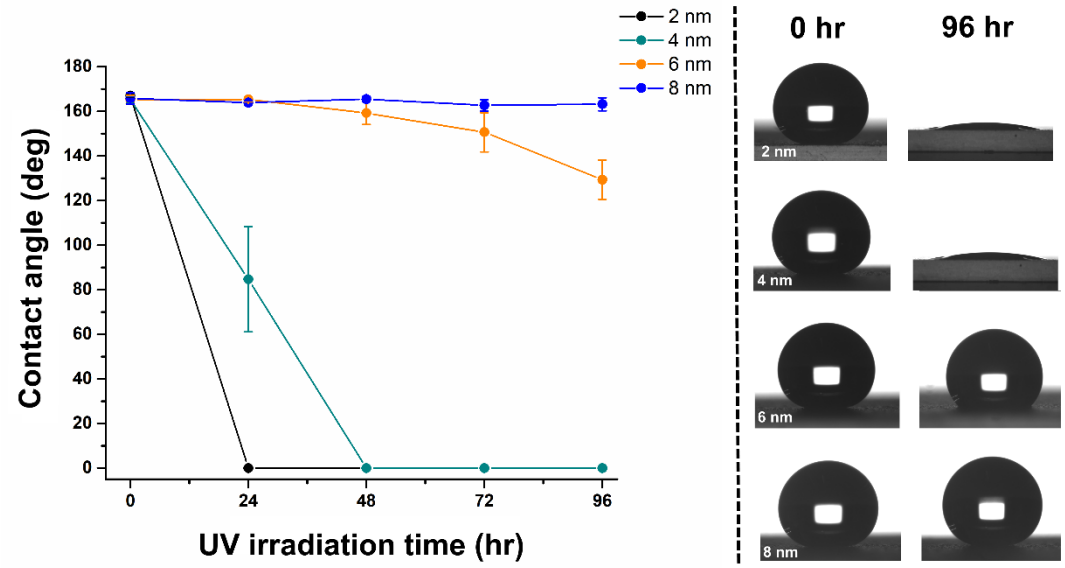

Figure 3.20: The change in static contact angle over the UV irradiation period (365 nm, 8W power) for CeO_2-PDMS coatings with theoretical polymer thickness values ranging 2-8 nm (**left**). Corresponding optical images of a water droplet on the surface of PDMS-based coatings at labelled time intervals (**right**).

From Table 3.06/Figure 3.20, all samples were initially superhydrophobic, displaying high contact angles (≥ 165°). After 24 hours of UV exposure, the CeO_2-PDMS coating with an $\mathbf{r}_{poly}$ value of 2 nm appeared to be completely hydrophilic, similar to the TiO_2-PDMS system, which can likely be attributed to a lack of polymer coating surrounding nanoparticles/incomplete coverage. Subsequently, resulting in photodegradation of the thin

PDMS coating, and promoting an enhancement in surface hydroxyl groups. However, unlike the TiO_2-PDMS system, large tilting angles were observed initially for the coating with an $\mathbf{r}_{poly}$ value of 2 nm (>90°), before any exposure to UV irradiation, which further highlights inconsistencies within CeO_2-based surface coatings. Nonetheless, high initial static contact angles were likely observed due to the presence of interfacial air, beneath the droplet. Interestingly, the CeO_2-PDMS coating with an increased $\mathbf{r}_{poly}$ value of 4 nm showed full coating degradation after 48 hours, and the coating with an $\mathbf{r}_{poly}$ value of 6 nm appeared to lose its superhydrophobicity after 96 hours, exhibiting a reduced contact angle of $129 ° \pm 9$. These results are contrasting to what was observed with TiO_2-based systems, as coatings with theoretical polymer thickness values that exceeded 2 nm, retained their superhydrophobicity after the full exposure period. After studying the molecular systems in parallel (TiO_2-FAS *vs* CeO_2-FAS), it was concluded that CeO_2 nanoparticles were less efficient photocatalysts than TiO_2. Hence, it is unlikely that any loss in superhydrophobicity is a direct result of strong photocatalysis and oxidative degradation of the siloxane coating (except for coatings with $\mathbf{r}_{poly}$ values of 2 nm).

Although the above results are not fully understood, possible justifications can be made;

(i) **Complex surface chemistry** – As mentioned throughout, it is predicted that the surface chemistry of the rare earth oxide, CeO_2, is complex. Due to the presence of both Ce^{3+} and Ce^{4+}, and subsequently, the occurrence of defect oxygen vacancies within the crystal lattice, a combination of hydrophobic and hydrophilic surface chemistries likely exist (dependent on synthesis method, storage conditions, etc.). During the photocatalysis process, active radicals can migrate to the surface of ceria and undergo redox reactions with oxygen or adsorbed water molecules, and as stated by Li *et al.*, these could form peroxide intermediates that could then go on to reconvert Ce^{3+} defects back to Ce^{4+}.[20] In doing so, this could result in a greater presence of surface hydroxyl groups, located in areas where defects initially resided. Which in turn, could promote hydrophilic pinning points throughout the surface which is reflected in the high tilting angles. However, as high UV stability was observed during the initial 48 hours of UV exposure in molecular systems, this may not be a significant factor, or this may occur in combination with (**ii**) and/or (**iii**), particularly when probing polymeric systems.

(ii) **Reduced interactions with FAS/PDMS** – as CeO_2 particles were initially established to lower intrinsic hydrophilicity than TiO_2 nanoparticles, it is anticipated that there is a reduced presence of hydroxyl groups on the nanoceria

surface (compared to TiO_2, prior to irradiation). Hence, inconsistencies in molecular functionalisation/polymeric encapsulation of particles may stem from the reduced/varied intermolecular interactions between the surface of metal oxide particles and the siloxane backbone (i.e. hydrogen bonding network and Van Der Waals interactions), or covalent bonding in the case of molecular functionalisation. Subsequently, leading to functionalisation in parts, but partially exposing the surface of CeO_2 which was determined to have a more hydrophilic surface chemistry. This theory aligns well with the consistently low tilting angles observed for PDMS-based coatings with much greater $\mathbf{r}_{poly}$ values (i.e. 8 nm), even after the full exposure period, as the probability of achieving full surface coverage increases, alongside polymer mass.

(iii) **Solvent system** – As with (**ii**), where it was predicted that an inconsistent surface coating may have occurred due to variations in the surface chemistry of CeO_2, here it is anticipated that these variations may lead to an unstable suspension of particles. It was suspected that by employing a polar solvent (ethanol) as the solvent, or co-solvent to suspend metal oxide nanoparticles, the complete dispersion and functionalisation/encapsulation of particles within the suspension may have been inhibited. Consequently, this would likely act to produce non-conformal surface coatings due to particle aggregation and instability, and may have been a contributing factor.

A combination of the above has likely given rise to the unique wettability and UV stability/instability of CeO_2-based coatings. However, in order to address point (**iii**) and deduce whether the solvent system played a significant role when fabricating PDMS-based coatings (as this was the most feasible point to address), a solvent screen was set up that included a range of solvents that covered a spectrum of different polarities, to probe the stability of as-received CeO_2 particles (see Fig. 3.21).

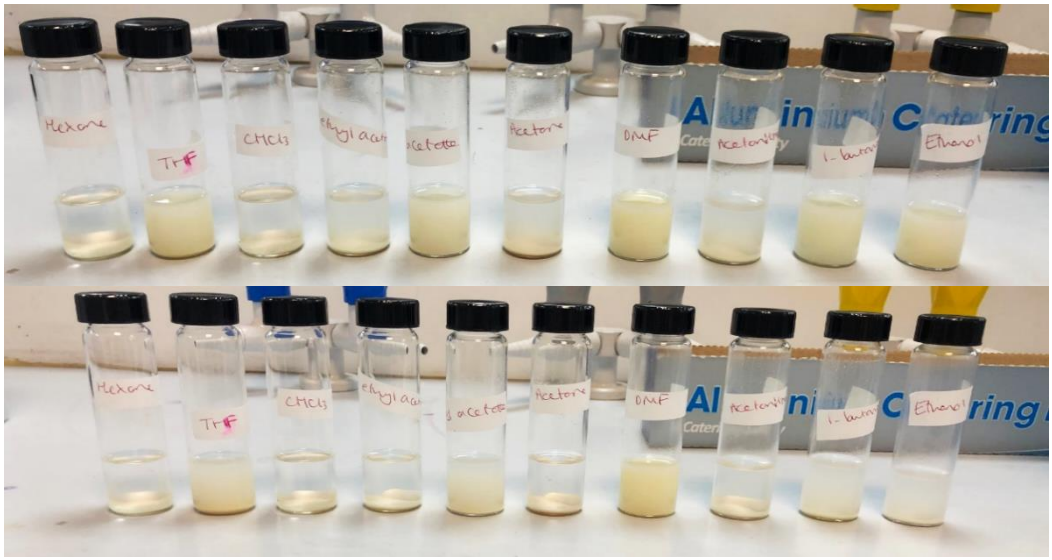

Figure 3.21: Solvent screen showing the stability of as-received CeO_2 particles immediately after 2 hours of mechanical stirring (**top**) and after a further 2 hours of standing under ambient conditions (**bottom**). Solvents (**left to right**): hexane, THF, chloroform, ethyl acetate, n-butyl acetate, acetone, dimethylformamide, acetonitrile, 1-butanol and ethanol.

After samples were left to stand under ambient conditions for 2 hours, it was apparent that as-received CeO_2 nanoparticles sediment in the majority of tested solvents, including ethanol. Particles only appeared to form one stable suspension in dimethylformamide (DMF), which has a relative polarity that is less than ethanol (see Table 3.07), and therefore, likely more compatible with the native surface chemistry of CeO_2 nanoparticles. Hence, a co-solvent system of DMF/chloroform ($CHCl_3$) was used to replace the original co-solvents of ethanol and hexane for polymeric systems (DMF and hexane are not miscible solvents and PDMS precursors are also readily soluble in $CHCl_3$). DMF/$CHCl_3$ formulations successfully yielded superhydrophobic coatings, for an $\mathbf{r}_{poly}$ value range of 2-6 nm.

Table 3.07: Solvent properties comparison table (boiling point, vapour pressure and relative polarity).[40,41]

Solvent	*Boiling point (℃)*	*Vapour pressure (hPa, 20℃)*	*Relative polarity (relative to water)*
n-Hexane	69.0	160.0	0.009
Ethanol	78.0	59.0	0.654
DMF	153.0	3.5	0.386
$CHCl_3$	60.5-61.5	210.0	0.259

Table 3.08: Recorded static contact angles for CeO_2-PDMS coatings with theoretical polymer thickness values ($\mathbf{r}_{poly}$) ranging 2-8 nm, deposited *via* spray coating from DMF/$CHCl_3$ suspensions, before and after 24 hours of irradiation (365 nm, 8W power).

$\mathbf{r}_{poly}$ *(nm)*	*Initial static contact*	*Initial tilting angle*	*Static contact angle after 24 hours of UV irradiation (365 nm)*
2	168° ± 2	5° ± 1	0°
4	168 ° ± 1	4 ° ± 1	0°
6	157 ° ± 4	90°	0°

Although initial contact angles were >150° for all coatings, an opposite trend in tilting angles was observed for coatings fabricated using this solvent system (compared to the ethanol/hexane co-solvent system), where the tiling angle was seen to increase, in line with the $\mathbf{r}_{poly}$ value. Furthermore, all coatings underwent a UV-induced wetting transition from superhydrophobic to superhydrophilic within 24 hours of UV exposure. Though DMF worked to suspend CeO_2 particles more effectively, it appeared to disrupt the coating process further. It is suspected that high initial contact angles may be a direct consequence of the solvent removal process, due to the use of co-solvents with very different boiling points/vapour pressures; subsequently, individual solvents are evaporated at different rates, resulting in a porous-type network that directly enhances the hierarchical surface roughness and facilitates the trapping of interfacial air (see Fig. 3.22). Therefore, giving rise to coatings that display extreme surface hydrophobicity, but likely no improvement in the uniformity of polymer-encapsulated particles for systems that have low $\mathbf{r}_{poly}$ values ($\leq$ 6 nm).

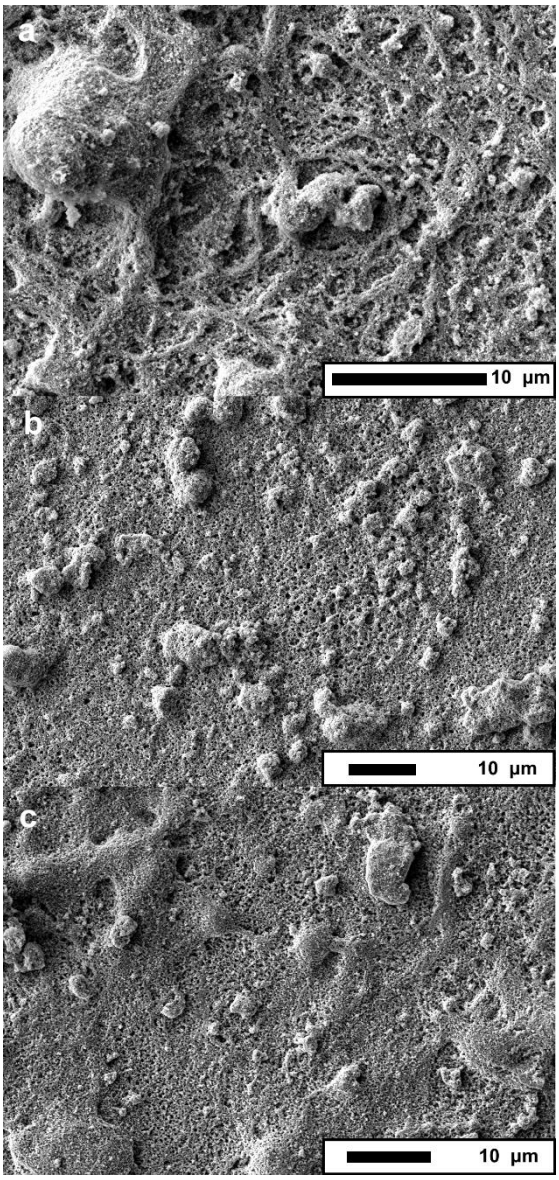

Figure 3.22: SEM micrographs highlighting the surface morphology of CeO_2-PDMS coatings, deposited via spray coating from $CHCl_3$/DMF (50:50 v/v) suspensions. In all images, the nanoparticle diameter is 25 nm, with polymer thickness values ranging (**a**) 2 nm, (**b**) 4 nm, (**c**) 6 nm. Scale bars are shown.

To shed light on this, the effects of DMF and ethanol on the solubility of pre-dissolved PDMS in $CHCl_3$ (1.1 g PDMS in 10 mL) were probed. It became apparent that an increasing volume of DMF promoted the precipitation of polymer into solution, and acted as an anti-solvent – which was not the case for ethanol (see Fig. 3.23). Therefore, increasingly inhibiting the mass of solubilised polymer as the $\mathbf{r}_{poly}$ value is increased. This suggests that less polymer coverage may be attained for coatings with larger theoretical polymer thicknesses, which aligns well with the increased tilting angle, observed when assessing coatings with an $\mathbf{r}_{poly}$ value of 6 nm. Unfortunately, a co-solvent system that facilitated the stable suspension of CeO_2 particles, while fully solvating PDMS was unable to be identified. Nonetheless, this highlights the importance of using a compatible solvent system when designing SPNC coatings, as discussed throughout chapter 2, as coating formation has been seen to drastically change.

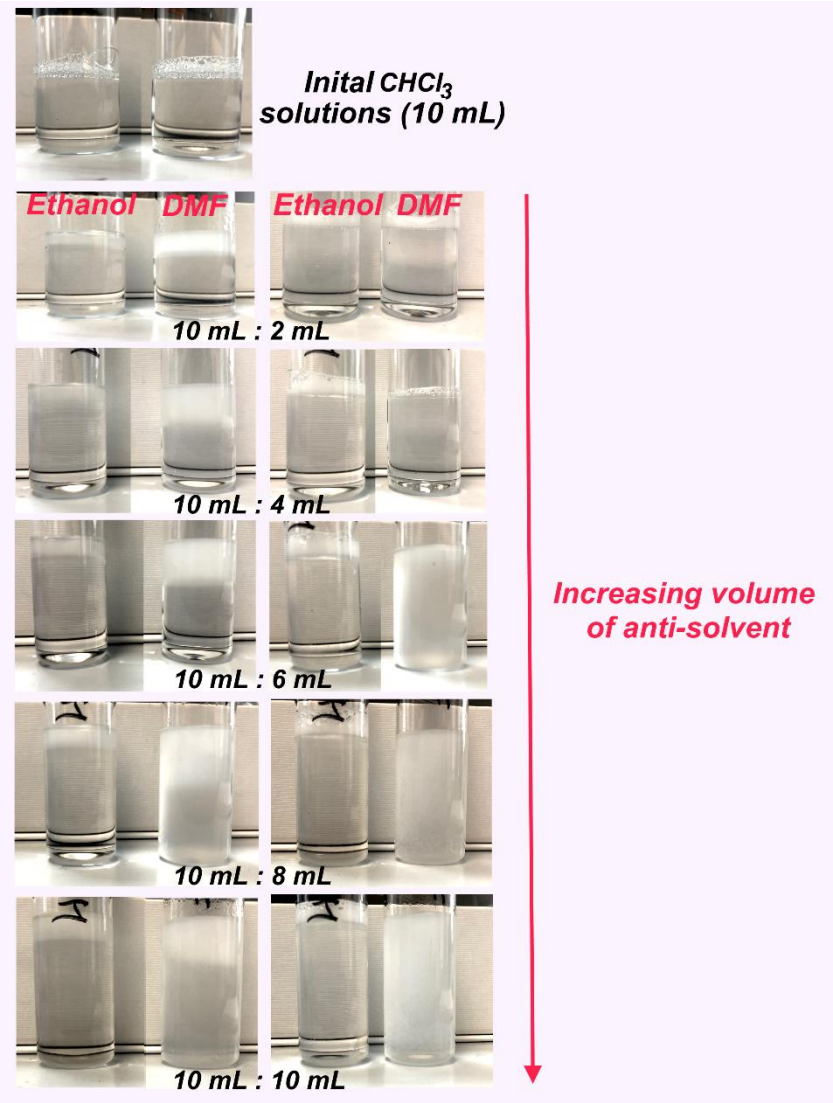

Figure 3.23: Images highlighting the anti-solvent effects of DMF, in comparison to that of ethanol, on solubilised PDMS in $CHCl_3$ (1.1 g PDMS in 10 mL); increasing volume of ethanol and DMF until 50:50 (v/v) is reached (**from top to bottom**), showing the visual appearance immediately after addition (**left images**) and after a short period of sonication (**right images**).

3.4 Conclusions

In this work, we probed the feasibility/realistic use of photoactive metal oxide nanoparticles within pigmented superhydrophobic surface coatings. In doing so, comparisons were drawn between the UV stability of molecular composite coatings and polymeric composite coatings. The key findings are discussed below:

Cerium Oxide as A Photocatalyst – Upon subjecting molecular composite coatings to UV testing (TiO_2-FAS and CeO_2-FAS), it was discovered that CeO_2-based coatings displayed significantly greater UV stability. It was found that CeO_2 is photocatalytically less efficient than TiO_2, which was seen to undergo a complete UV-induced wetting transition from superhydrophobic to superhydrophilic within 90 minutes of UV exposure, likely due to a combination of electronic and chemical factors. Molecular CeO_2-based coatings were found to continually maintain superhydrophobicity for 48 hours. After which, mixed results were obtained during repeat testing, underlining inconsistencies in the stability of the liquid-vapour interface at the surface of CeO_2-FAS coatings. Nonetheless, this work has highlighted how the inclusion of CeO_2 nanoparticles within superhydrophobic formulations can be hugely beneficial in extending the lifetime and performance of self-cleaning pigmented coatings, when compared to coatings that comprised the pigment TiO_2 (highly efficient photocatalyst).

Hybrid Coatings – It was determined that blends of TiO_2/CeO_2 could be used, in order to tune the UV stability and pigmentation of superhydrophobic surface coatings. A series of particle blends were made up, and when probing the UV stability, the formulation termed 1:10 (TiO_2:CeO_2 mass ratio) was found to be the most stable. This applied to both, molecular and polymeric composites. Furthermore, diffuse reflectance spectra revealed a slight shift in the absorption edge wavelength for blended coatings, suggesting that a change in pigmentation and the electronic band structure of the material may occur.

Molecular Coatings *vs* Polymeric Coatings: UV Stability – The use of polymeric coatings was shown within this work to dramatically enhance the UV stability of SPNC coatings, that comprised photoactive nanoparticles. By employing a siloxane polymer to coat particles, it is anticipated that a complex combination of factors, including; high surface coverage *via* extensive intermolecular interactions, the inherent stability of silicones towards oxidative degradation, the high flexibility of the siloxane backbone and determination of the optimal polymer:nanoparticle ratio, act to suppress/slow the extent of photo-degradation. This was particularly apparent in TiO_2-PDMS coatings (optimal coating, $\mathbf{r}_{poly}$ value of 6 nm), which were observed to survive over 250 hours of UV exposure, while retaining superhydrophobicity – a significant improvement from that of molecular TiO_2-FAS (90 minutes).

Cerium Oxide-Based Coatings: Properties and Stability – As pre-synthesized particles were utilized within this work (to enhance real-world applicability), the exact surface chemistry was unknown. Through investigating the optimal $\mathbf{r}_{poly}$ value of CeO_2-PDMS, it was realised that CeO_2-based materials appeared to degrade significantly quicker than TiO_2-based materials, during exposure to UV. Although several suggestions were made (complex surface chemistry, reduced interactions with molecules/polymer, etc.), investigation of different solvent systems led to CeO_2-PDMS coatings that displayed different physical properties, surface microstructures and UV stabilities. Thus, highlighting the importance of system compatibility and optimisation, and underlining factors that may need to be considered before designing an SPNC material for employment within a specific application.

It can be concluded that CeO_2 nanoparticles can be successfully employed in place of TiO_2 nanoparticles as the primary pigment within pigmented superhydrophobic coatings, to fabricate materials with enhanced UV durability – which is relevant to industries where aesthetics is an important factor. Furthermore, all materials were used 'as-received' without the need for particle synthesis or extensive functionalisation processes, enhancing real-world applicability. Despite challenges surrounding the inherent surface chemistry of 'as-received' CeO_2, and hence, its compatibility within SPNC formulations, it was proven that by using a compatible solvent system, establishing an optimal theoretical polymer thickness, and employing a polymer that is capable of suppressing photodegradation, that UV-stable pigmented superhydrophobic coatings can be fabricated.

3.5 References

1 G. Rouni and M. Kim, in *International Workshop on Energy Performance and Environmental Quality of Buildings, Milos island, Greece*, 2006.

2 W. A. Henson, D. A. Taber and E. B. Bradford, *Ind. Eng. Chem.*, 1953, **45**, 735–739.

3 J. H. Braun, A. Baidins and R. E. Marganski, *Prog. Org. coatings*, 1992, **20**, 105–138.

4 G. E. Morris, W. A. Skinner, P. G. Self and R. S. C. Smart, *Colloids Surfaces A Physicochem. Eng. Asp.*, 1999, **155**, 27–41.

5 M. Pelaez, N. T. Nolan, S. C. Pillai, M. K. Seery, P. Falaras, A. G. Kontos, P. S. M. Dunlop, J. W. J. Hamilton, J. A. Byrne, K. O'Shea, M. H. Entezari and D. D. Dionysiou, *Appl. Catal. B Environ.*, 2012, **125**, 331–349.

6 X. Zhang, M. Jin, Z. Liu, D. A. Tryk, S. Nishimoto, T. Murakami and A. Fujishima, *J. Phys. Chem. C*, 2007, **111**, 14521–14529.

7 R. Qian, H. Zong, J. Schneider, G. Zhou, T. Zhao, Y. Li, J. Yang, D. W. Bahnemann and J. H. Pan, *Catal. Today*, 2019, **335**, 78–90.

8 M. Bellardita, R. Fiorenza, L. Palmisano and S. Scirè, in *Cerium Oxide (CeO_2): Synthesis, Properties and Applications*, Elsevier, 2020, pp. 109–167.

9 B. Jalvo, M. Faraldos, A. Bahamonde and R. Rosal, *J. Hazard. Mater.*, 2017, **340**, 160–170.

10 Y. Qing, C. Yang, N. Yu, Y. Shang, Y. Sun, L. Wang and C. Liu, *Chem. Eng. J.*, 2016, **290**, 37–44.

11 Q. F. Xu, Y. Liu, F.-J. Lin, B. Mondal and A. M. Lyons, *ACS Appl. Mater. Interfaces*, 2013, **5**, 8915–8924.

12 S. Nishimoto, A. Kubo, K. Nohara, X. Zhang, N. Taneichi, T. Okui, Z. Liu, K. Nakata, H. Sakai and T. Murakami, *Appl. Surf. Sci.*, 2009, **255**, 6221–6225.

13 S. Nishimoto, M. Becchaku, Y. Kameshima, Y. Shirosaki, S. Hayakawa, A. Osaka and M. Miyake, *Thin Solid Films*, 2014, **558**, 221–226.

14 Y. Qing, C. Yang, Y. Sun, Y. Zheng, X. Wang, Y. Shang, L. Wang and C. Liu, *Colloids Surfaces A Physicochem. Eng. Asp.*, 2015, **484**, 471–477.

15 X. Ding, S. Zhou, G. Gu and L. Wu, *J. Mater. Chem.*, 2011, **21**, 6161–6164.

16 M. Xing, D. Qi, J. Zhang, F. Chen, B. Tian, S. Bagwas and M. Anpo, *J. Catal.*, 2012, **294**, 37–46.

17 Z. Duan, Z. Zhao, D. Luo, M. Zhao and G. Zhao, *Appl. Surf. Sci.*, 2016, **360**, 1030–1035.

18 G. Azimi, R. Dhiman, H.-M. Kwon, A. T. Paxson and K. K. Varanasi, *Nat. Mater.*, 2013, **12**, 315.

19 M. Fronzi, M. H. N. Assadi and D. A. H. Hanaor, *Appl. Surf. Sci.*, 2019, **478**, 68–74.

20 X. Li, Y. Sun, Y. Xu and Z. Chao, *Small*, 2018, **14**, 1801040.

21 T. Ishizaki, Y. Masuda and M. Sakamoto, *Langmuir*, 2011, **27**, 4780–4788.

22 S. Sanders and T. D. Golden, *Langmuir*, 2019, **35**, 5841–5847.

23 N. M. Zholobak, V. K. Ivanov, A. B. Shcherbakov, A. S. Shaporev, O. S. Polezhaeva, A. Y. Baranchikov, N. Y. Spivak and Y. D. Tretyakov, *J. Photochem. Photobiol. B Biol.*, 2011, **102**, 32–38.

24 F. B. Li, X. Z. Li, M. F. Hou, K. W. Cheah and W. C. H. Choy, *Appl. Catal. A Gen.*, 2005, **285**, 181–189.

25 L. Hu, X. Song, X. Shan, X. Zhao, F. Guo and P. Xiao, *ACS Appl. Mater. Interfaces*, 2019,

11, 37209–37215.

26 A. Naldoni, M. Allieta, S. Santangelo, M. Marelli, F. Fabbri, S. Cappelli, C. L. Bianchi, R. Psaro and V. Dal Santo, *J. Am. Chem. Soc.*, 2012, **134**, 7600–7603.

27 X.-P. Li, Y.-L. Sun, C.-W. Luo and Z.-S. Chao, *Ceram. Int.*, 2018, **44**, 13439–13443.

28 Y. Lu, S. Sathasivam, J. Song, C. R. Crick, C. J. Carmalt and I. P. Parkin, *Science (80-.).*, 2015, **347**, 1132–1135.

29 C. R. Crick and I. P. Parkin, *Chem. Commun.*, 2011, **47**, 12059–12061.

30 A. Rafieepour, F. Ghamari, A. Mohammadbeigi and M. Asghari, *Ann. Med. Health Sci. Res.*, 2015, **5**, 129–133.

31 S. Pazokifard, S. M. Mirabedini, M. Esfandeh and S. Farrokhpay, *Adv. Powder Technol.*, 2012, **23**, 428–436.

32 S. Pazokifard, S. M. Mirabedini, M. Esfandeh, M. Mohseni and Z. Ranjbar, *Surf. interface Anal.*, 2012, **44**, 41–47.

33 E.-J. Lee, A. K. An, T. He, Y. C. Woo and H. K. Shon, *J. Memb. Sci.*, 2016, **520**, 145–154.

34 S. S. Abdullahi, S. Güner, Y. Musa, B. I. Adamu and M. I. Abdulhamid, *NAMP J*, 2016, **35**, 241–246.

35 C. R. Crick, Joseph. C. Bear, K. Andreas and I. P. Parkin, *Adv. Mater.*, **24**, 3505–3508.

36 L. Johnson, L. Gao, C. Shields IV, M. Smith, K. Efimenko, K. Cushing, J. Genzer and G. P López, *J. Nanobiotechnology*, 2013, **11**, 22.

37 M. M. Ali, H. S. Mahdi, A. Parveen and A. Azam, in *AIP Conference Proceedings*, AIP Publishing LLC, 2018, vol. 1953, p. 30044.

38 P. Klonos, G. Dapei, I. Y. Sulym, S. Zidropoulos, D. Sternik, A. Deryło-Marczewska, M. V Borysenko, V. M. Gun'ko, A. Kyritsis and P. Pissis, *Eur. Polym. J.*, 2016, **74**, 64–80.

39 J. E. Huheey, E. A. Keiter, and R. L. Keiter, *Inorganic Chemistry: Principles of Structure and Reactivity, 4th ed*, Harper Collins, 1993.

40 Properties of Solvents Chart - Merck (Sigma Aldrich), https://www.sigmaaldrich.com/chemistry/stockroom-reagents/learning-center/technical-library/solvent-properties.html.

41 Properties of Solvents Used in Organic Chemistry, http://murov.info/orgsolvents.htm.

Chapter 4

Mechanically Resilient and Submersible Water Repellent Coatings for Polymeric Substrates

Publications:

Carbon nanofiber/SiO_2 nanoparticle/HDPE composites as physically resillient and submersible water-repellent coatings on HDPE substrates. R. L. Upton, A. Fedosyuk, J. B. Edel and C. R. Crick, *ACS Appl. Nano Mater.*, 2021, **4**, 10090-10102.

Contributions:

Reflectivity Measurements were carried out by Aleksandra Fedosyuk (Molecular Sciences Research Hub, Imperial College London).

X-ray Photoelectron Spectroscopy data collection was performed at the EPSRC National Facility for XPS (HarwellXPS) by Dr Mark Isaacs.

4.1 Introduction

As seen throughout chapter 1, superhydrophobic coatings have found countless applications to date. The research carried out in chapters 2 and 3 has led to the development of highly functional superhydrophobic coatings, however, fabricated materials thus far have displayed very limited resilience (excluding UV stability). As a result, the prospective of employing current coatings in a practical setting seems unlikely, due to the rate at which physical degradation and plastron decay would take place (when subject to abrasive wear or underwater submersion), often rendering the material almost immediately inoperable. In this chapter, we establish an approach for designing truly resilient materials, through demonstrating how conventional superhydrophobic polymer-nanoparticle composite (SPNC) coatings can enhance their application potential and work towards solving real-life problems, *via* the combined use of a high-strength additive and utilization of 'solvent-free' SPNC formulations.

4.1.1 A Global Problem: Polymer Waste and Contamination

Thermoplastic polymers are implemented extensively throughout our lives, in many different industrial and commercial areas.[1] Commonly used thermoplastics (e.g. polyethylene, polypropylene, polyvinylchloride (PVC), polycarbonate, polyamides and polyurethane) are currently employed heavily within a range of applications, including; pipes and fittings, automotive and biomedical industries.[2–4] A combination of consistently high demand and the ongoing desire to lower overall plastic production, due to rising concerns surrounding plastic waste and pollution, has created an emphasis on optimising these polymeric materials so that they can provide long-term usage.

A tremendous amount of research has been directed towards improving the properties of bulk polymeric materials (see section 4.1.3).[5–7] However, when considering the wider applications of many thermoplastic polymers, surface-related factors can impact heavily on a polymers overall performance. Outwardly exposed surfaces are subject to many environmental challenges, for example, severe weathering or intense fluid flow conditions (e.g. within water transport pipes), where surface defects can easily lead to stress fracturing.[8,9] This issue is magnified for surfaces with contamination in the form of biofilms, dirt or food contaminants.[10,11] Heavy contamination predominantly impacts the surface of materials and can be subsequently detrimental to the performance and integrity of the bulk polymer, creating a need for replacements and/or repeat surface treatments to temporarily enhance performance (which usually involve further polymer usage). Therefore, to fully extend the lifetime of thermoplastic materials, external surface coatings that can provide long-term environmental protection must also be considered.

4.1.2 Superhydrophobic Polymer Coatings and Their Challenges

Highly water repellent materials are widely known for their use as functional coatings as they can integrate long-lasting protective mechanisms into the underlying substrate material. Subsequently, minimising immediate surface contamination, and providing other desirable properties (e.g. reduced fluidic drag, anti-icing abilities, etc…) addressing many of the concerns stated in section 4.1.1.[12–14] The use of hydrophobic polymers to fabricate superhydrophobic coatings (directly or as exterior coatings of roughened substrates) has been widely investigated within the literature. One of the initial reports by Erbil *et al.,* detailed the transformation of a simple plastic, polypropylene, into a superhydrophobic surface by varying deposition conditions and employing an anti-solvent to produce different porous structures.[15] Furthermore, a common method has been the use of a hot moulding/embossing technique to pattern polymers and induce surface roughness.[16] Although successful as a nanofabrication technique, complex surface structures are typically more difficult to obtain without the inclusion of a nanomaterial (particles, fibres, etc.).[17] Issues associated with the viscosity of the molten polymer (when considering hot moulding techniques) can limit materials selection, and/or pose challenges when fabricating intricate microstructures, often requiring complex and/or multi-step fabrication processes.[18,19] The physical resilience of these polymer nano-architectures, fabricated *via* methods such as the 'pulling' technique, whereby molten polymer is stretched to generate fibre-like features, or the use of anodized moulds, still need to be validated under real-world conditions.[18–23]

A more simplistic route to generating high surface superhydrophobicity that typically involves little processing, is the use of polymer-nanoparticle composites as external surface coatings. However, as outlined throughout chapters 1 and 2, there are fundamental challenges relating to the implementation of SPNC coatings (chemical and physical stability).[24,25] As a result, commercially applicable superhydrophobic coatings are currently limited.[26] This limitation extends further if the application requires underwater submersion – which a significant amount of applied thermoplastics do, e.g. applications within the marine sector – due to the high instability of entrapped air within the surface porosity of the coating, termed; plastron decay.[27–29] Once the liquid-vapour interface is depleted, complete wetting of the solid surface takes place, rending the coating ineffective.[30] Therefore, new approaches to design SPNC coatings are required in order to heighten the inherent resilience of conventional superhydrophobic surface coatings, and extend their applicability.

4.1.3 Fibre Reinforced Superhydrophobic Materials

Reinforcement of materials, particularly thermoplastics, is not a new concept. Although different additives can be employed to improve the inherent properties of the host polymer, fibre reinforcement of thermoplastics has been widely studied, using both synthetic and natural fibres which include; vegetable fibres, glass fibres, carbon fibres and Kevlar, in addition to many more.[31] Carbon nanofibers (CNFs) are one of the strongest man-made fibres known to exist; they have exceptional mechanical strength and have been principally investigated for improving the tensile strength of thermoplastics, while providing other desirable properties.[32,33] With the exception of mechanical properties enhancement, research into CNF-reinforced thermoplastics has mainly been directed towards introducing new functionalities into the polymer matrix.[34,35] This work has spurred the use of fibres in alternative application areas also, including functional superhydrophobic materials fabrication, where CNF composites have been reported to show enhanced durability and/or advanced functionalities.

CNF-reinforced superhydrophobic materials that target enhanced durability, typically aim to enhance the physical resilience of free-standing objects i.e., not attached to an external substrate or support, *via* the use of a mould or the natural formation of a monolith (e.g. for use in oil-water separation).[36,37] Although the native material may have heightened mechanical properties, this is not extended to the coating adhesion strength (substrate-coating bonding). On the other hand, research that has focused on integrating functional properties into superhydrophobic materials *via* the introduction of CNFs (e.g. high thermal conductivity for anti-condensing coatings, enhanced electrical conductivity for wearable sensors, etc.), often perform application-specific testing, without providing any substantial report on the generic durability/adhesion strength of materials.[37–39] If coating adhesion is studied, often pre-treatments are used and enhancements in adhesion strength are not as a direct result of CNF integration.[38,40] In addition to using CNFs as a composite formulation, as seen above, CNFs have also been solely employed to fabricate highly water repellent coatings, due to their unique surface chemistry and ability to form highly porous structures.[41] Overall, there has been a large scope for the implementation of CNFs when designing superhydrophobic materials. Yet, facile nanofabrication methods that are capable of generating both resilient and stable superhydrophobic coatings on polymeric substrates, through the utilization of fibres, require further investigation.

4.1.4 Chapter Aims

Within this chapter, the main purpose was to establish a unique deposition/design approach, that combined the principles of using a high strength additive and maintaining robust air-layer stability, with a simplistic approach that avoided the use of complex fabrication protocols/techniques, to impart resilience into a conventional SPNC surface coating (i.e., a solution-based SPNC formulation with limited physical resilience). Here, resilient SPNC coatings were designed to be deposited directly onto bulk polymeric substrates, in order to address the rising concerns surrounding plastic waste and pollution, and to integrate long-lasting self-cleaning mechanisms into the surface of the polymer that shows resistance against physical degradation and underwater submersion. To ensure this, coatings were subject to both physical resilience testing (stability against abrasive wear) and submersion testing (short-term and long-term at two different hydrostatic pressures). The project focused on two principle aspects, that were fundamental in elevating the resilience of SPNC coatings:

- **Deposition Approach** – we aimed to optimise and develop the deposition approach preliminarily investigated in chapter 2 – 'solvent free' SPNCs that were deposited using a parallel plate hot press – as this approach initially displayed promising potential as a route to developing truly resilient microstructures (see section 2.3.3.2.2 for further details).
- **Novel Coating Design** – by integrating unmodified CNFs as a high-strength additive into an existing SPNC formulation, we anticipated that variances in surface chemistries between multiple formulation components would allow for partial control over the bulk positioning of fibres, subsequently enabling the design of highly versatile and resilient materials.

To achieve this, the following objectives were met:

- Selection of a model SPNC/thermoplastic system that exhibits compatibility with the deposition process and 'solvent-free' formulation approach.
- Optimisation of the parallel plate hot press deposition technique, and establishment of an effective method to deposit dried formulations.
- Complete optimisation of all systems, leading up to the ternary system of polymer, nanoparticles and fibres i.e., nanoparticles and polymer (establishing the optimal polymer:nanoparticle theoretical ratio for dried coatings) and CNFs and polymer, to ensure the requirement of all three components.

- The development of a series of CNF-based formulations, including surface coatings with different CNF loadings, and surface coatings fabricated from slurries with different dried formulation contents, in order to identify the most resilient materials.
- Characterisation of all fabricated coatings.
- Abrasive wear testing to evaluate the physical resilience of CNF-containing coatings, and to deduce any enhancement when compared to coatings that do not include fibres.
- Underwater submersion testing at two different hydrostatic pressures with the aid of both, wettability measurements and reflectivity measurements, to unveil the stability of the liquid-vapour interface under varying conditions.

4.2 Materials and Methods

4.2.1 Materials

High-density polyethylene (HDPE), silicon dioxide nanopowder (SiO_2, 10-20 nm), hexamethyldisilazane (HMDS, reagent grade, ≥99%), 1H, 1H, 2H, 2H-perfluorooctyltriethoxylsilane (FAS, 98%) and carbon nanofibers (graphitized, iron-free, composed of conical platelets, D × L 100 nm × 20-200 μm] were purchased from Sigma Aldrich. Xylene (analytical reagent grade) and ethanol (analytical reagent grade) were purchased from Fisher Scientific Limited. Hydrogen peroxide (35% w/w aq. solution) was purchased from Alfa Aesar. Grade P120 aluminium oxide sandpaper (Al_2O_3) was purchased from the hardware store B&Q.

4.2.2 Formation of HDPE Substrates

To form solid polyethylene substrates, 6.0 g of HDPE pellets were transferred into a silicone mould (3.5 x 3.5 x 3.5 cm) and heated at 200 ℃ in the oven for approximately two hours, as this was an effective route to repeatedly generating solid substrates of specific size measurements. The molten polymer was then allowed to solidify at room temperature, before being utilized as in the fabrication process.

4.2.3 Hydrophobization of SiO_2 Nanoparticles

This was carried out as described in earlier chapters. See ‘Functionalisation with HMDS’ in chapter 2, section 2.2.3.1 for the experimental procedure.

4.2.4 Fabrication of Precursor Powders

HDPE was dissolved in xylene (100 mL) by heating to 110°C with the aid of mechanical stirring. Once fully dissolved, pre-functionalised SiO_2 nanoparticles (where applicable) and as-received CNFs (where applicable) were added, with continual heating for a further two hours. The resultant suspension was immediately combined with 200 mL ethanol to encourage the precipitation of the polymer, which was performed with uniform mixing. Following this, the suspension was filtered by gravity and dried overnight at room temperature, to retrieve a solidified composite material. The resultant material was ground using a pestle and mortar to yield a fine powder/break up large fibre aggregates, and then applied to the substrate as detailed in section 4.2.5. See Table 4.01 for formulation details.

Table 4.01: Formulation summary detailing all fabricated binary and ternary precursor powders (SiO_2-HDPE, CNF-HDPE and SiO_2-HDPE-CNF):

Formulation	r_{poly}	*Mass ratio (SiO_2:HDPE)*	*Mass SiO_2 nanoparticles (g)*	*Mass CNF (g)*	*Total mass HDPE (g)*
SiO_2-HDPE	2	0.408	2.4500	-	1.00
SiO_2-HDPE	4	1.031	0.9700	-	1.00
SiO_2-HDPE	6	1.893	0.5283	-	1.00
CNF-HDPE	-	-	-	0.25	0.50
CNF-HDPE	-	-	-	0.50	0.50
CNF-HDPE	-	-	-	1.00	0.50
0.1-SiO_2-HDPE	2	0.408	2.450	0.10	1.00
0.3-SiO_2-HDPE	2	0.408	2.450	0.30	1.00
0.5-SiO_2-HDPE	2	0.408	2.450	0.50	1.00

4.2.5 Slurry Preparation and Coating Deposition (see Fig. 4.01)

Pre-made HDPE substrates were pressed at 180°C and 0.1MPa for 30 seconds, using a parallel plate hot press apparatus, to ensure a level surface before any coating application. Slurries were made up using a dried formulation content of 0.30 g per 4 mL solvent (xylene for SiO_2-HDPE and SiO_2-HDPE-CNF coatings, and chloroform for CNF-HDPE and sole CNF coatings), and used for the application of three separate coating layers – with the exception of coatings fabricated solely from as-received CNFs, whose slurry comprised 0.15 g CNF per 6 mL solvent, due to the low density of fibres. For each layer, the slurry was sonicated for 10 seconds, before being drop-cast onto the substrate and evenly spread across the surface (*via* a tilting motion), where the solvent was removed at approximately 80-100°C using the heated top plate of the hot press (30 x 24 cm heating element, bottom plate unheated), leaving behind a near-uniform coating of dried powder. This was then pressed at 180°C 0.1MPa for 30 seconds, and the process was repeated an additional two times. Any excess coating was removed by a series of light mechanical abrasion and flowing nitrogen across the surface before testing was carried out, to avoid the presence of loose powder. Slurries with a dried formulation content between 0.20-0.40 g per 4 mL xylene were investigated for SiO_2-HDPE-CNF coatings, to establish the optimal mass of precursor powder, as seen in Table 4.02 below:

Table 4.02: Summary of slurries that were formulated using different dried formulation contents, for **0.1**-SiO_2-HDPE-CNF, **0.3**-SiO_2-HDPE-CNF and **0.5**-SiO_2-HDPE-CNF:

Formulation	*Dried formulation content (g)*	*Xylene (mL)*
0.1/0.3/0.5-SiO_2-HDPE-CNF	0.20	4
0.1/0.3/0.5-SiO_2-HDPE-CNF	0.30	4
0.1/0.3/0.5-SiO_2-HDPE-CNF	0.40	4

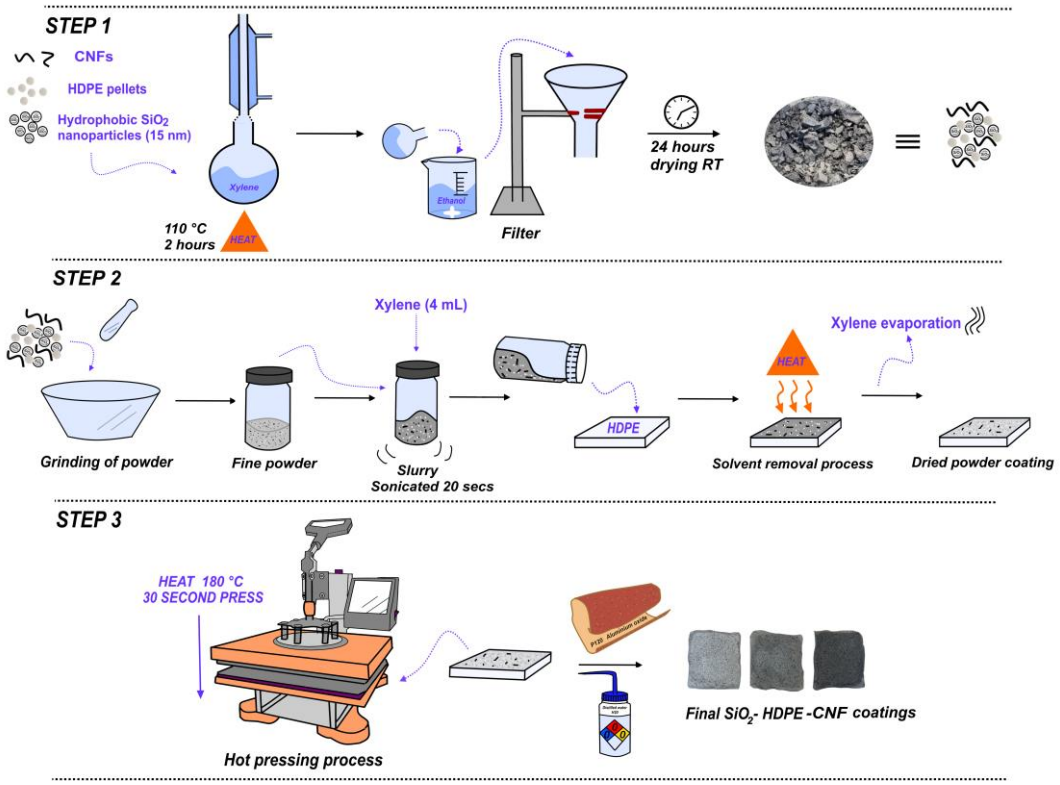

Figure 4.01: Ilustration detailing the formulation and fabrication processes of HDPE-SiO_2-CNF coatings; (**step 1**) formulation of the precursor powders; (**step 2**) formulation and **[**deposition of the slurry onto a HDPE substrate, followed by a solvent removal process, resulting in a dried powdered coating; and finally (**step 3**) use of the parallel plate hot press for coating depositon (30 second press at 180℃).] **Process in brackets repeated three times per sample.**

4.2.6 Fluorination of CNFs

As-received CNFs (0.8 g) were added to hydrogen peroxide (35% w/w aq. solution, 400 mL) and left at 65℃ for 4 days, with continuous mechanical stirring. Following this, fibres were vacuum filtered, washed with distilled water and re-dispersed into fresh distilled water to

repeat the cleaning process (until pH ~ 7). The material was then dried in the oven overnight at 110℃ to yield fibres with an increased surface concentration of hydroxyl groups. Hydroxyl-functionalised fibres (0.6 g) were suspended in ethanol (60 mL), and FAS (0.6 mL) was added. This suspension was mechanically stirred at 65℃ for a further 5 days. Fibres were then vacuum filtered and washed with ethanol, before drying in the oven overnight at 110℃, resulting in fluorinated CNFs.

4.2.7 Materials Characterization

Surface morphologies of coatings were analysed using a scanning electron microscope (SEM, JEOL JSM-7001F/Tescan FIB SEM S8000G) operating at an acceleration voltage of 5-10 kV. Cross-sectional samples were prepared by submersion in liquid nitrogen, followed by fracturing. Samples were vacuum sputter coated in a thin layer of chromium using a Quorum S150T ES sputter coater, to improve electrical conductivity. Fourier Transform Infrared (FTIR) measurements were taken using a Bruker Optics' Vertex 70 over a range of 450 to 4000 cm^{-1}. Brunauer-Emmett-Teller (BET) surface area analysis was conducted using a Micrometric 3-Flex 3500 Gas Sorption Analyser. X-ray photoelectron (XPS) data collection was performed at the EPSRC National Facility for XPS by **Dr Mark Issacs**. Data was acquired using a Kratos Axis SUPRA using monochromated Al kα (1486.69 eV) X-rays at 12 mA emission and 15 kV HT (180W) and a spot size/analysis area of 700 x 300 µm. Spectra have been charge corrected to the main line of the carbon 1s spectrum (adventitious carbon) set to 284.8 eV. All data was recorded at a base pressure of below 9 x 10^{-9} Torr and a room temperature of 294 K. Data was analysed using CasaXPS v2.3.19PR1.0. Peaks were fit with a Shirley background prior to component analysis and data analysis, was assisted by **Dr Mark Issacs**.

4.2.8 Contact Angle Measurements

Static contact angle measurements were taken using a DSA100 Expert Drop Shape Analyser (Kruss GmbH) in the sessile drop operating mode with Young-Laplace fitting and manual assignment of the baseline. 6 μL water droplets were dispensed from a Hamilton microliter syringe with a 30 gauge dispensing tip directly onto the surface and at least 5 contact angle measurements (3 for abrasion testing results when varying dried formulation content), from evenly distributed positions across the surface, were taken and averaged for every reported contact angle. Tilting angles were recorded manually by dispensing a water droplet on the surface and tilting the surface at 2°/s, recording the angle at which the droplet began to roll. At least 3 measurements (5 for long-term submersion testing at 7.85 kPa), from evenly

distributed positions across the surface, were taken and averaged for every reported tilting angle. Statistical analysis was not performed as experimental trends that fit coating composition were observed repeatedly within the wettability data, suggesting that the data was statistically significant.

4.2.9 Abrasive Wear Testing

Weighted samples (100 g or 200 g, ~1 x 1.5 cm) were placed face down onto aluminium oxide sandpaper (Al_2O_3, grade P120) and propelled 10 cm horizontally across the sandpaper, before being rotated 90° and moved a further 10 cm in the vertical direction. Samples were rotated a further 90° (in the same direction) to begin the second cycle so that substrates were abraded from all angles, similar to what was reported in section 2.2.9. For preliminary abrasion testing, 50 abrasion cycles were carried out on each sample and contact angles were recorded at 10 cycle intervals. During extended abrasive testing, a total of 100 abrasion cycles was carried out on each sample and contact angles/tilting angles were taken at 20 cycle intervals.

4.2.10 Submersion Testing

4.2.10.1 Testing at Low Hydrostatic Pressure (0.196 kPa)

Samples (3 x 2 cm) were immersed in individual beakers of deionised water (2 cm in depth) that were kept at room temperature and sealed to avoid evaporation. Samples were submerged for a total of 96 hours, being removed only for a short period of time (~ 15 minutes) to immediately record contact angles and tilting angles at each 24-hour interval.

4.2.10.2 Testing at Increased Hydrostatic Pressure (7.85 kPa)

Samples (3 x 2 cm) were adhered to a weighted support and immersed into a cylinder of deionised water (80 cm in depth) that was kept at room temperature, and sealed to avoid evaporation. Samples were submerged for a total of 96 hours, being removed only for a short period of time (~ 15 minutes) to immediately record contact angles and tilting angles at each 24-hour interval. For extended testing, smaller samples (~1 x 1.5 cm) – to ensure all samples fit – were adhered to individual weighted supports and lowered into the cylinder, that was kept under identical environmental conditions. Samples were only removed after the full submersion period, being continuously submerged for 1, 2 or 4 weeks, after which contact angles and tilting angles were immediately recorded.

4.2.11 Reflectivity Measurements

The reflectivity measurements were performed using a UV spectrometer (UV-2600, Shimadzu, Japan), equipped with an integrating sphere attachment. For that, the sample (1 x 1.5 cm) was adhered to the wall of a 1 cm plastic cuvette, *via* the use of adhesive, and then filled with distilled water to simulate shallow submersion (water layer approximately of 1.2-1.3 mm between the sample surface and the cuvette wall). Following this, the sample cuvette was placed at the exit on the reference side of the integrating sphere and the total reflectance (diffuse and specular), with an 8-degree incident angle to the integrating sphere was measured. The stability of the surface in water was examined over 7 weeks, by acquiring repeat reflectance measurements at different time intervals (average of 5 per interval). Baseline correction was performed using an aluminium mirror as a reference, prior to recording reflectivity spectra. Reflectivity measurements were carried out by **Aleksandra Fedosyuk** at the Molecular Sciences Research Hub, Imperial College London.

4.2.12 Water Bouncing Set-Up

This was carried out as described in earlier chapters. See ‘Water Bouncing Set-Up’ in chapter 3, section 3.2.8 for the experimental procedure.

4.3 Results and Discussion

Expanding on section 2.3.3.2 – where the preliminary investigation into 'solvent-free' SPNC formulations was initially carried out – an optimised deposition approach that involved the same hot pressing apparatus was explored within this chapter, as it was identified as a potential route for designing truly resilient micro-scale materials.

Initially, a suitable SPNC system that would be compatible with high processing temperatures needed to be established. Due to the nature of the hot-pressing deposition process, it was deduced that a thermoplastic polymer would be most appropriate. Furthermore, this polymer needed to be employed as both, the substrate material and the hydrophobic polymeric component within the formulation, in order to target strong compatibility between the surface coating and underlying substrate. For this the synthetic polymer, high-density polyethylene (HDPE), was chosen as it is a polymer of relatively high strength, and considered to be highly versatile due to being extremely workable (can be moulded at moderately high temperatures, without undergoing significant thermal degradation), showing wide compatibility with a range of processing methods, and can easily undergo modification to tune or impart additional functionalities.[42] Additionally, in chapter 2 it was shown that solution-based SPNC formulations that comprised HDPE and hexamethyldisilazane (HMDS)-functionalised silica nanoparticles (SiO_2, $\mathbf{r}_{sphere}$ = 7.5 nm), could generate superhydrophobic coatings when the theoretical polymer thickness value remained below 4 nm. Hence, this SPNC system was selected as the initial platform for developing high-performance SPNC materials.

4.3.1 Fabrication & Design: Optimisation

4.3.1.1 SiO_2-HDPE Coatings

Similar to chapter 2, 'solvent-free' formulations were initially made up with the use of a solvent (xylene), followed by its removal. Dried precursor formulations that comprised fine powders of HDPE and HMDS-functionalised SiO_2 nanoparticles were made *via* a series of steps ($\mathbf{r}_{poly}$ = 2, 4 and 6 nm, see experimental section 4.2.4, see chapter 2 for analysis of HMDS-functionalised SiO_2). It was deduced that the most effective method of generating near-uniform coatings on HDPE substrates was to employ highly concentrated dispersions, termed slurries, to avoid coating inconsistencies which were observed when applying the coating directly in its dried form (more apparent in CNF-based coatings, see section 4.3.2, Fig. 4.04b/c). Hence, dried precursor formulations of SiO_2-HDPE blends were suspended in solutions of xylene, after a short period of sonication. Once evenly deposited and spread across the substrate surface, the solvent was removed using the heated plate of the press, resulting in

a dried layer of composite powder. Three applications were required to limit the exposure of surface-bound cracks. Each layer was pressed into the surface of the HDPE substrate at 180℃ and 0.1 MPa, for 30 seconds, followed by a series of light mechanical abrasion and flowing nitrogen across the surface to remove any excess coating.

The polymer:nanoparticle ratio was initially investigated to probe links between the mass ratio, and both, surface hydrophobicity and composite-substrate binding. The ratio between polymer and nanoparticle plays a critical role in determining the morphological architecture of the coating, and therefore, the resultant hydrophobicity – as outlined throughout this thesis thus far. For this case, obtaining the optimal ratio was particularly crucial as the deposition was performed at high temperatures, and could easily result in the complete coverage of the surface roughening agent (SiO_2 nanoparticles) with excess molten polymer. Here, we estimated polymer thickness values using theoretical calculations and the SPCN design principle, as detailed in section 2.3.2. However, in this system, a conformal polymer coating is not achieved, as it was found previously that thermoplastic polymers adopt the role of adhesives, binding nanoparticle aggregates together, without uniformly coating individual particles (see section 2.3.4.2.2 for a more detailed discussion). Nonetheless, theoretical polymer:nanoparticle ratios and their corresponding polymer thickness values were used as a way to systematically increase the polymer content within SiO_2-HDPE dried formulations.

It was found that a theoretical polymer thickness value of 2 nm was optimal, yielding a contact angle of 159° ± 2 (on areas where the coating was present), when probing $\mathbf{r}_{poly}$ values of 2, 4 and 6 nm for SiO_2-HDPE systems. At increased $\mathbf{r}_{poly}$ values, surface roughness was seen to dramatically decrease, which was reflected in the resultant static contact angles presented in Table 4.03. The incorporation of excess polymer led to an increasingly reduced presence of nanoparticle filler within the coating formulations. Therefore, as the polymer proceeded to melt during the high temperature deposition (T = 180℃), the presence of nanofiller at the surface of the substrate fell below the critical mass required to generate hierarchical surface roughness. Instead, particles were observed to deeply penetrate the substrate surface, facilitated by the movement of molten polymer, resulting in a surface that was comparable to flat HDPE. This was reflected in scanning electron microscopy (SEM) micrographs, where a progressively flat morphology can be observed, in line with increasing theoretical polymer thickness (see Fig. 4.02). Conversely, a lack of polymer promotes superhydrophobicity, yet coatings tend to be more mechanically fragile, and display extreme morphological variability due to exposure of the underlying substrate in parts (affecting the consistency in surface hydrophobicity).

Table 4.03: Recorded static contact angles and tilting angles for SiO_2-HDPE coatings, fabricated *via* the hot pressing method from a xylene suspension, with $\mathbf{r}_{poly}$ values ranging 2-6 nm:

r_{poly}	*Recorded static contact angle*	*Tilting angles*
2 nm	159° ± 2	17° ± 1
4 nm	125° ± 8	90°
6 nm	84° ± 10	90°
Flat polymer (no nanoparticles)	87° ± 6	90°

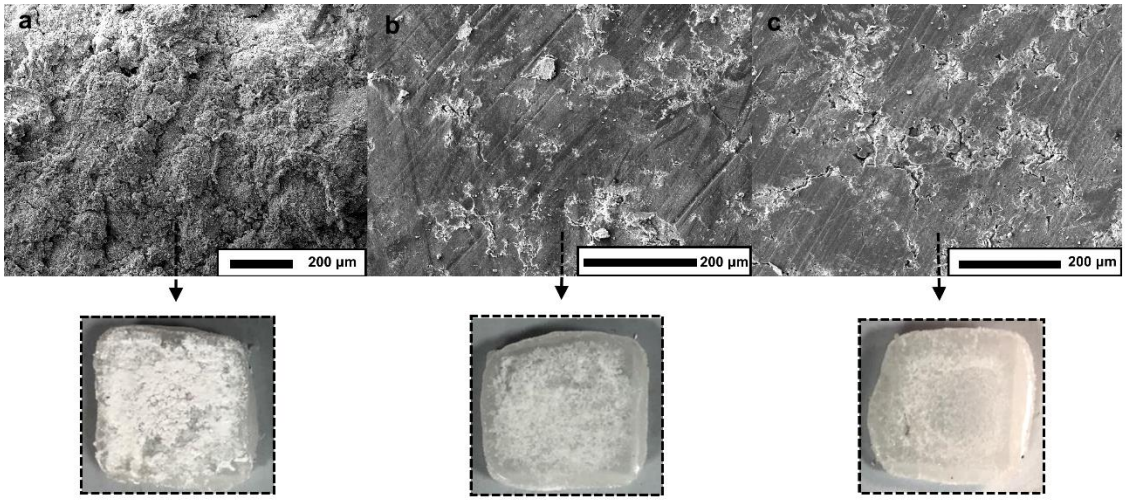

Figure 4.02: SEM micrographs showing the surface morphology of SiO_2-HDPE coatings with a theoretical polymer thickness of; (**a**) 2nm, (**b**) 4 nm and (**c**) 6 nm (**top**). Corresponding images of SiO_2-HDPE coatings, highlighting the physical appearance (**bottom**).

4.3.1.2 CNF-HDPE Coatings

To ensure full system optimisation and confirm the need for a three-component system to achieve the highest level of resilience, CNF-HDPE coatings were also fabricated in the absence of SiO_2 nanoparticles, using a chloroform solvent system. Precursor powders that comprised between 0.25-1.00 g of as-received CNFs (to 0.50 g HDPE) were used to formulate slurries and were deposited in the same way as SiO_2-HDPE coatings, as described above in section 4.3.1.1. For coatings that comprised a smaller CNF loading (0.25 g and 0.50 g), it was noted *via* SEM imaging that the bulk of fibres appeared to penetrate deeply into the surface of the substrate, limiting surface roughness and generating smooth morphologies – comparable to SiO_2-HDPE coatings with theoretical polymer thickness values of 4 nm and 6 nm (see Fig.

4.02 *vs* Fig. 4.03). However, as the CNF loading was increased to [1.00 g CNF / 0.50 g HDPE], superhydrophobicity was attained with coatings displaying a static contact angle of 152° ± 5. Although a roughened morphology was achieved, extensive regions of flat HDPE and areas where fibres had formed flattened aggregates, due to the nature of the deposition process, were apparent. Consequently, this led to a tilting angle that exceeded 90° and full water droplet adhesion, severely limiting the self-cleaning performance of materials.

To overcome the presence of flat polymer regions which acted as adhesion points for water droplets, a coating solely comprised from as-received CNFs was fabricated, where a contact angle of 154° ± 4 and a tilting angle of 18° ± 7 was recorded. Although this surface was functional as a self-cleaning coating, it was believed that due to a number of reasons; large voids within the surface coating due to severe aggregation during the deposition process, easy removal of highly concentrated surface fibres, and the intrinsic hydrophilicity of fibres (see section 4.3.3), that binary composite coatings would be inferior to the tertiary system, particularly during underwater submersion testing. Similarly, this has been previously documented by Peng *et al.*, who partially embedded CNFs into the surface of polymer matrices, and reported that superhydrophobicity was lost after only 10 minutes of immersion in deionised water, unless nanotubes were fluorinated.[41]

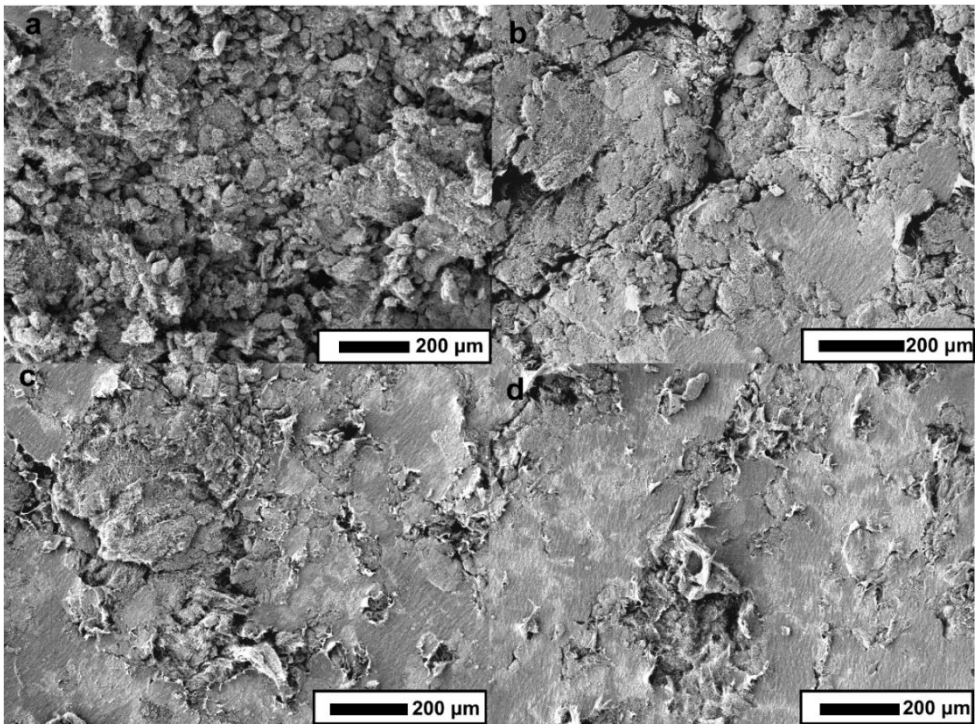

Figure 4.03: SEM micrographs showing the surface morphology of CNF-HDPE coatings with an initial CNF loading of; (**a**) CNFs (no polymer), (**b**) [1.00 g CNF / 0.50 g HDPE] and (**c**) [0.50 g CNF / 0.50 g HDPE] and (**d**) [0.25 g CNF / 0.50 g HDPE] (**top**). Coatings were fabricated using a dried formulation content of [0.15 g/6 mL] for CNFs (no polymer) and [0.30 g/4 mL] for HDPE-containing formulations. Scale bars are shown.

Table 4.04: Recorded static contact angles and tilting angles for CNF-HDPE coatings, fabricated *via* the hot pressing method from a chloroform suspension:

Fibre content	*Recorded static contact angle*	*Tilting angles*
CNFs (no polymer)	154° ± 4	18° ± 7
1.00 g	152° ± 5	90°
0.50 g	137° ± 9	90°
0.25 g	123° ± 11	90°

4.3.2 Fabrication & Design: Reinforcement

As-received CNFs were incorporated directly into the established SiO_2-HDPE fabrication process, as illustrated in Figure 4.01. Hydrophobic SiO_2 nanoparticle/HDPE/CNF blends were formulated while varying the mass of CNFs; 0.10g (**0.1**-SiO_2-HDPE), 0.30g (**0.3**-SiO_2-HDPE) or 0.50g (**0.5**-SiO_2-HDPE), to determine any effects of increased fibre content on the overall performance of the resultant coatings. An identical mass of polymer and nanoparticles was used for all CNF-based formulations (1.00 g HDPE and 2.42 g SiO_2; mass ratio which corresponded to a theoretical polymer thickness value of 2 nm), which were then made into slurries and deposited in the same manner onto HDPE substrates. During deposition, **i**t was key that the solvent was removed prior to hot pressing, to generate a near-uniform coating from dried composite material, and avoid unusable and irreproducible surfaces (see Fig. 4.04b *vs* Fig. 4.04c).

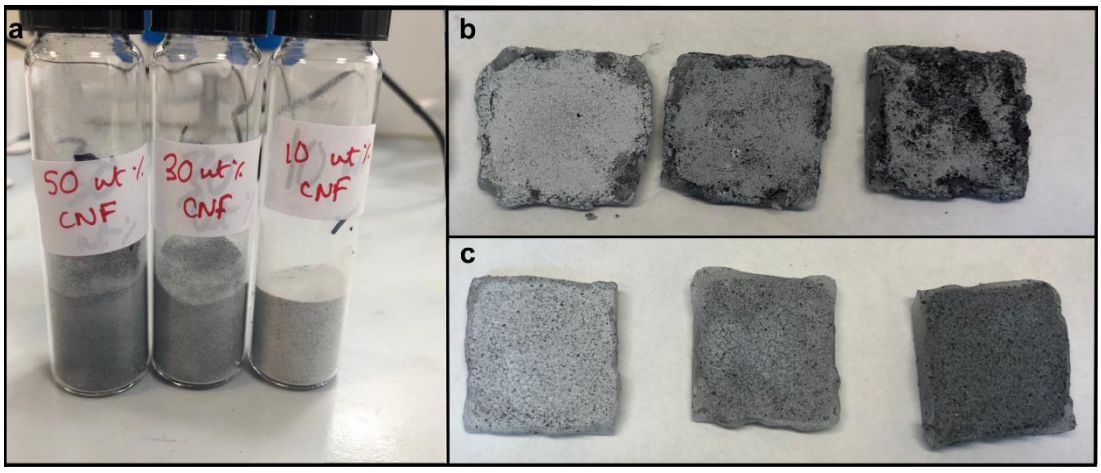

Figure 4.04: Images showing the physical appearance of; (**a**) **0.1**-SiO_2-HDPE, **0.3**-SiO_2-HDPE and **0.5**-SiO_2-HDPE dried precursor formulations after fine grinding; (**b**) surface coatings fabricated without solvent removal, and (**c**) surface coatings fabricated when incorporating a solvent removal step.

All coatings displayed initial surface superhydrophobicity, however, it must be noted that due to the nature of the deposition technique used, it was extremely challenging to consistently obtain replica surface coatings, despite controlling operational parameters and experimental conditions. This was countered by taking multiple measurements from across the surface of each coating. In addition, the tendency of water droplets to settle in the least hydrophobic positions, resulting in a wide range of initial contact angles, and tilting angles that differed. However, CNF-based coatings always upheld static contact angles which exceeded 150° (tilting angles ≤ 20°), and therefore, can be categorised as superhydrophobic materials. Water bouncing was used as an additional characterisation tool, to assess the dynamic wettability of coatings by directly depositing a water droplet onto the surface from a height of 20 mm. **0.5**-SiO_2-HDPE displayed >8 bounces before the droplet was seen to come to rest on the surface. Thus, indicating the presence of a large liquid-vapour interfacial area, and Cassie-Baxter wetting behaviour (see Fig. 4.05).

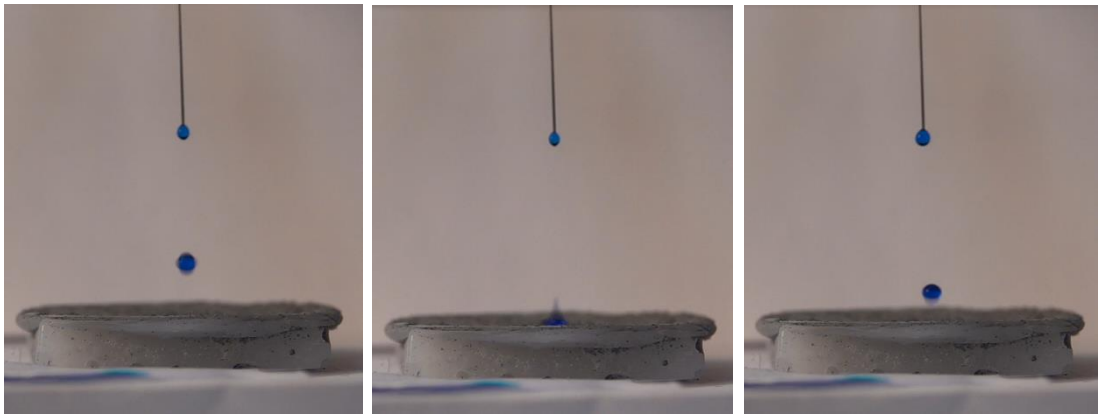

Figure 4.05: Images highlighting the dynamic wetting behaviour of **0.5**-SiO_2-HDPE upon impact with a dispensed water droplet (6 μL droplet dispensed from 20 mm above the surface). Methylene blue dye was used to aid visualisation.

4.3.3 Fabrication & Design: Morphology

SEM imaging enabled the assessment of coating architectures and shed light on the positioning/dispersion of fibres throughout the surface of coatings. Irregular microstructures of partially agglomerated hydrophobic SiO_2 nanoparticles served as a platform for generating hierarchical surface roughness, and could be seen regularly distributed throughout the surface of all coatings, *via* top-down SEM micrographs (inclusive of SiO_2-HDPE, $\mathbf{r}_{poly}$ value of 2 nm, see appendix, Fig. A1). Here, a large presence of roughening agent on the external surface layer of coatings was maintained, due to a low $\mathbf{r}_{poly}$ value of 2 nm. Furthermore, small regions concentrated with HDPE could be seen, highlighting some order of phase separation during

the fabrication process (see Fig. 4.06a/c); this aligns well with chapter 2, in that HDPE does not uniformly coat individual nanoparticles – arguably, a desirable feature when using a technique that involves high processing temperatures (T > melting point of polymer), so that a sufficient degree of surface texturing is upheld. As a result, surface roughness was not compromised, which is a frequent concern/challenge when processing thermoplastics at high temperatures for superhydrophobic applications (see section 4.1.2). Additional roughness was also provided by CNFs as they could be seen protruding through the surface in areas (see Fig. 4.06b/d), increasing in line with CNF loading, as the relative amount of fibre dispersion throughout the deposited coating became greater.

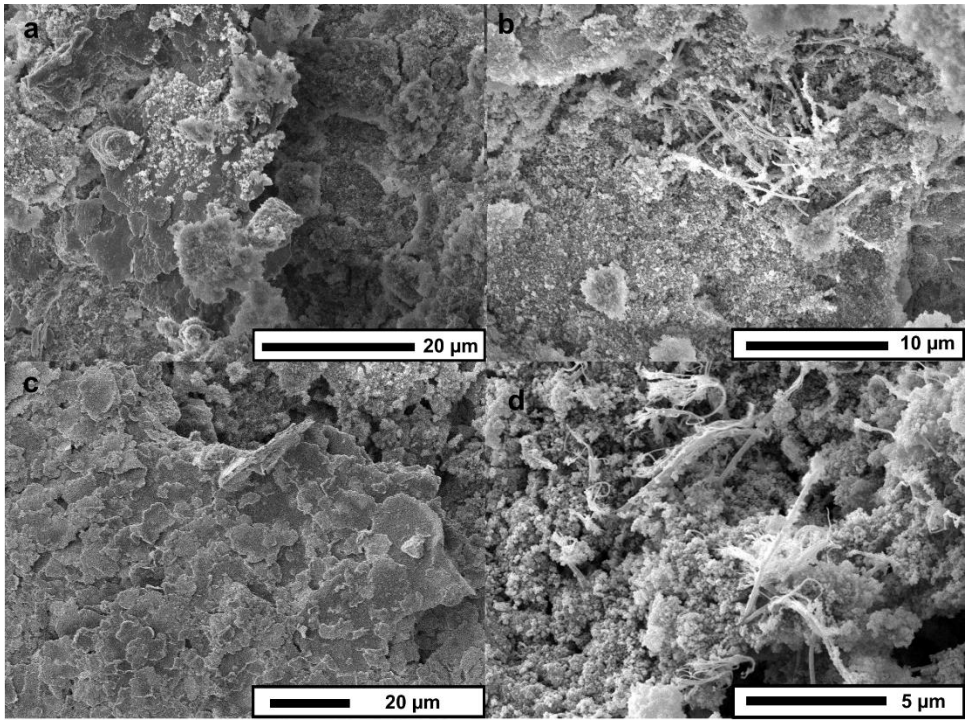

Figure 4.06: Top-down SEM micrographs highlighting regions of HDPE on the surface and areas where CNFs could be seen protruding through the surface of (**a/b**) **0.3-** SiO_2-HDPE and (**c/d**) **0.5-** SiO_2-HDPE. Scale bars are shown.

Cross-sectional samples, prepared *via* immersion into liquid nitrogen and physical fracturing, gave a greater insight into the distribution of CNFs. The bulk of fibres appeared to reside away from the surface of the coatings (see Fig. 4.07 and Fig. 4.08), however, a small number of fibres could be seen to extend toward and even penetrating the surface, mirroring what could be seen on top-down SEM micrographs. This is likely due to the CNF dispersion stability and respective interfacial tensions with other components within the slurry.[43] When left to stand at room temperature, slurries were seen to undergo partial phase separation (see appendix, Fig. A2).

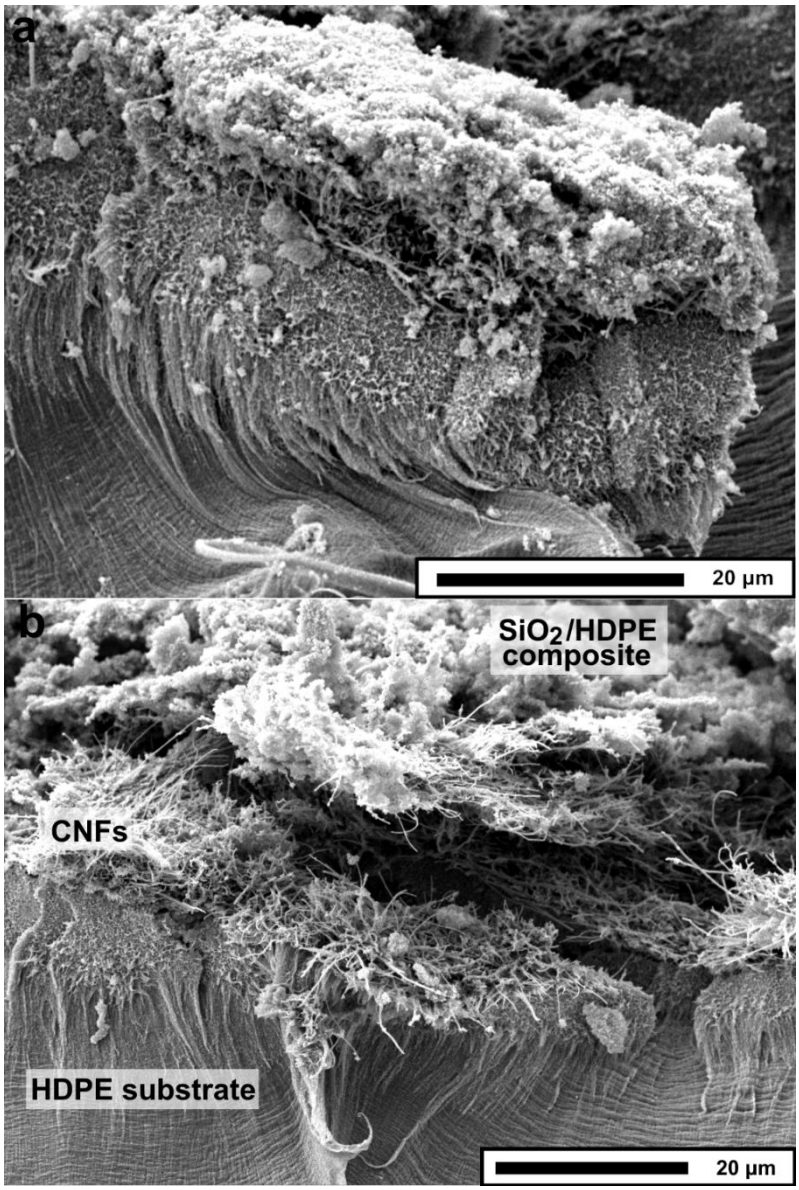

Figure 4.07: Cross-sectional SEM micrographs of **0.3**-SiO_2-HDPE, highlighting the bulk of CNFs positioned deeper within the surface coating, and underlining the strong substrate-coating binding (obtained by fracturing samples after immersion in liquid nitrogen). Scale bars are shown.

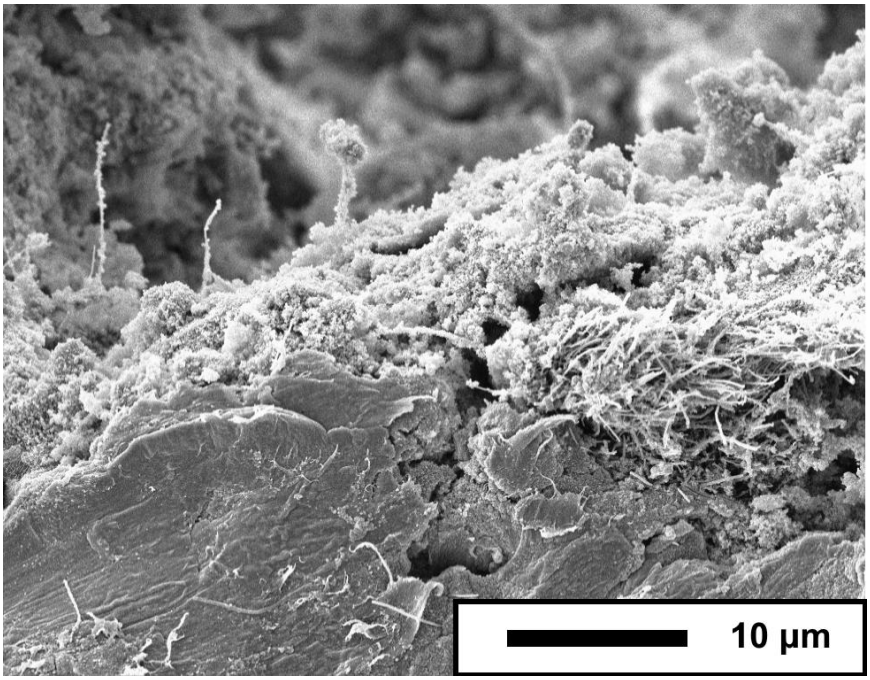

Figure 4.08: Cross-sectional SEM micrograph of **0.5**-SiO_2-HDPE, highlighting the bulk of CNFs positioned deeper within the surface coating, with few fibres protruding through the surface (obtained by fracturing samples after immersion in liquid nitrogen). Scale bar is shown.

CNFs are generally chemically inert and nonpolar, however, for some CNFs a small proportion of polar surface groups are known to be present.[44] XPS analysis was employed to deduce the chemical nature of the as-received fibres. The C1s XPS spectrum, shown in Figure 4.09a, indicated that fibres have two oxygen-containing groups at 285.2 eV and 287.6 eV, that subsequently correspond to hydroxyl (C-O) and carbonyl (C=O) surface groups. Additional fitted peaks at 284.4 eV and 291.4 eV were apparent and representative of sp^2 hybridised graphitic carbon (C=C) and a π-π^* shake-up satellite peak. The atomic percentage of oxygen-containing groups was found to be <2%, hence, confirming the presence of a small percentage of polar surface groups. Two oxygen-containing groups were present in the O1s XPS spectrum that gave rise to peaks at 531.6 eV (C=O) and 533.4 eV (C-O), as seen in Figure 4.09b. To further understand the intrinsic wettability of as-received fibres, fibres were pressed into small pellets to achieve a near-flat surface and directly compared to fibres that had been modified with fluoroalkylsilane (FAS) molecules (FAS-CNFs were prepared for comparative purposes only, see Figure 4.10 and see appendix, Fig. A3 for FAS-CNF XPS). The FAS-modified fibres demonstrated extreme hydrophobicity with a contact angle of 140° $\pm$ 5 on a near-flat surface (contact angle higher than expected due to some degree of unavoidable roughness). Conversely, when water droplets were dispensed onto the as-received CNF pellet they were observed to penetrate through the surface; this full wetting suggests the fibres are

inherently hydrophilic. The use of FAS-CNFs was subsequently avoided in order to encourage partial phase separation during the solvent removal process, and as a result, it was anticipated that the bulk of CNFs would settle primarily towards the interface between the substrate and surface coating. Thus, enhancing the interaction between the substrate and surface coating, with the aim of generating a robust intrinsic structure.

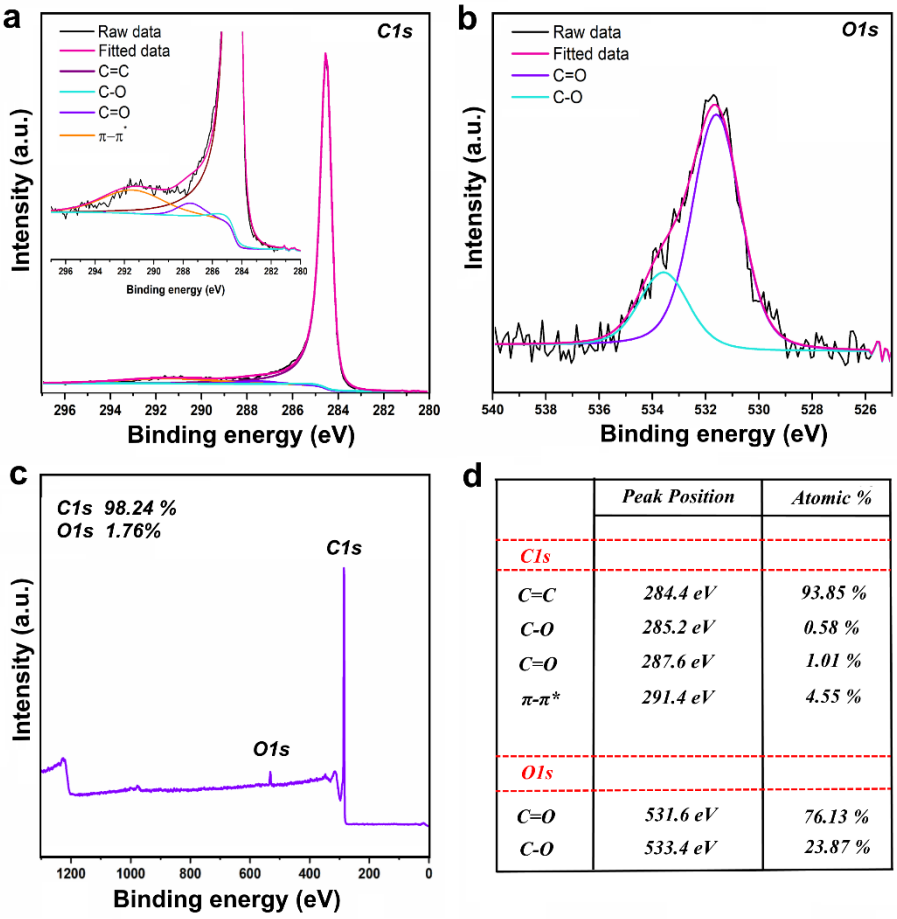

	Peak Position	Atomic %
C1s		
C=C	284.4 eV	93.85 %
C-O	285.2 eV	0.58 %
C=O	287.6 eV	1.01 %
π-π*	291.4 eV	4.55 %
O1s		
C=O	531.6 eV	76.13 %
C-O	533.4 eV	23.87 %

Figure 4.09: (**a**) C1s XPS spectrum, (**b**) O1s XPS spectrum, and (**c**) wide scan of as-received CNFs. (**d**) XPS C1s and O1s elemental composition for as-received CNFs.

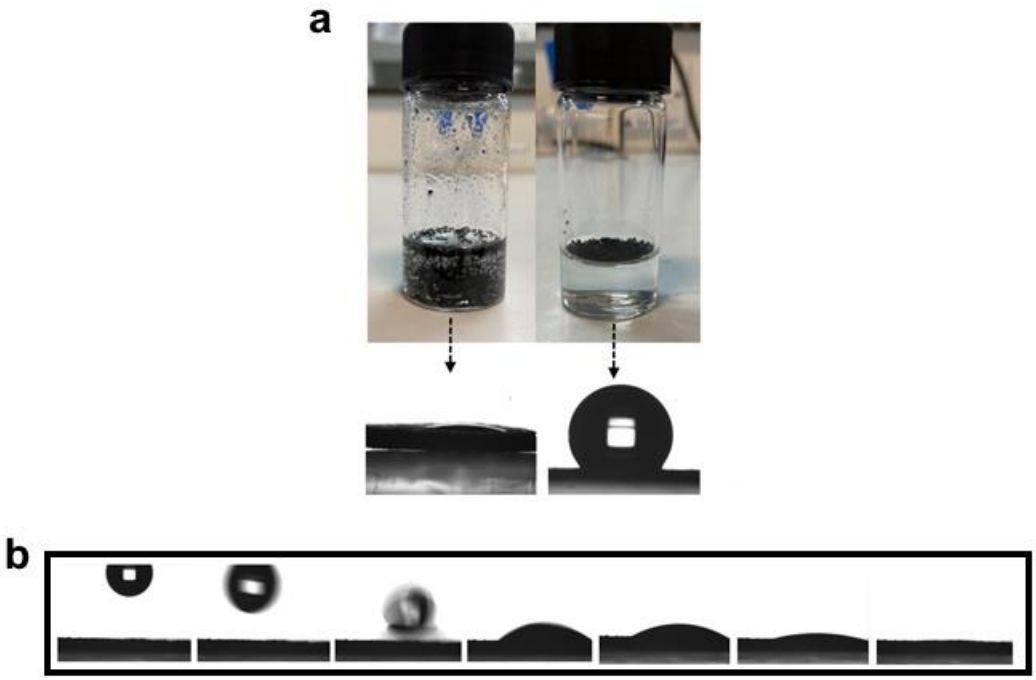

Figure 4.10: (**a**) Images showing the behaviour of as-received CNFs (**left**) and fluorinated CNFs (**right**) in water, and corresponding images showing the interaction of a water droplet with each CNF pellet. (**b**) Images showing the interaction of a water droplet, dispersed onto the surface of the as-received CNF pellet.

SEM micrographs show a comprehensive integration of the tertiary coating into the HDPE substrate, which included the infiltration of fibres into the substrate material and no observation of a distinct substrate-coating interface. Coatings were noted to be generally between 100-200 µm in thickness, varying throughout the sample due to the nature of the deposition technique used. Although, this was challenging to accurately determine as no clear boundary could be established (see appendix, Fig. A4).

4.3.4 Susceptibility to Degradation

When considering the practicality of highly water repellent coatings, many external factors could render coatings almost immediately inoperable. Unfortunately, superhydrophobic materials must face many of these on a day-to-day basis (e.g. extreme environmental conditions, human interaction, contamination etc.), and demonstrate a level of resilience, to be regarded as commercially viable functional coatings. Two of the primary concerns are the coating's susceptibility to physical abrasion and loss of entrapped air during underwater submersion, as outlined throughout chapter 1 and section 4.1. Hence, these are the two experimental parameters probed within this section.

4.3.4.1 Abrasive Wear Testing

To assess the expected real-life performance of coatings and investigate any enhancement in physical resilience (for CNF-containing coatings), mechanical wear was simulated *via* a series of sandpaper abrasion tests (grade P120 Al_2O_3 sandpaper). See section 4.2.9 for further details regarding the abrasion testing process.

4.3.4.1.1 Varying the Dried Formulation Content of Slurries

To optimise the coating process (i.e., ensure total substrate coverage and high surface hydrophobicity), as well as maximise the physical strength of the internal microstructure, the dried formulation content of slurries was varied between 0.20-0.40 g for all CNF-based coatings ([0.20 g composite/4 mL xylene], [0.30 g composite/4 mL xylene], and [0.40 g composite/4 mL xylene]). Abrasion tests were conducted for all samples using a 200 g weight, as a lower mass of 100 g was found to have limited impact on surface superhydrophobicity during the preliminary testing of samples to determine experimental parameters (see appendix, Fig. A5).

Slurries with an intermediate dried formulation content [0.30 g composite/4 mL xylene] appeared to generate the most resilient surface coatings. Coatings made with this solid proportion showed the following wettability changes after 50 abrasion cycles; a decrease in static contact angle of 15° (from 160° ± 2) for **0.1**-SiO_2-HDPE, a decrease of 5° (from 159° ± 3) for **0.3**-SiO_2-HDPE, and an increase of 1° (from 157° ± 2) for **0.5**-SiO_2-HDPE. This highlights the immediate benefit of including CNFs, as those with high CNF inclusion were shown to resist reductions in contact angle, and in some cases, display enhanced surface hydrophobicity (re-positioning of fibres/roughened polymer surface, see Fig. 4.11). Slurry formulations with a high amount of dried content [0.40 g composite/4mL xylene] resulted in decreasing resilience. The overabundance of coating components is thought to increase the proportion of solids that are not physically interacting with the substrate surface, and therefore, are unable to integrate successfully into the substrate material. This, in turn, encouraged a greater removal of the coating when subjected to repeat abrasive wear, which was principally apparent in **0.1**-SiO_2-HDPE, as it exhibited the largest decrease in contact angle of 24° (from 162° ± 2). This can likely be attributed to the **0.1**-SiO_2-HDPE material having the lowest CNF content, and so the least overall structural reinforcement. This, somewhat validates that the embedded CNF framework acts to support the coating at the substrate-coating interface, while also securing the internal integrity of the coating layer.

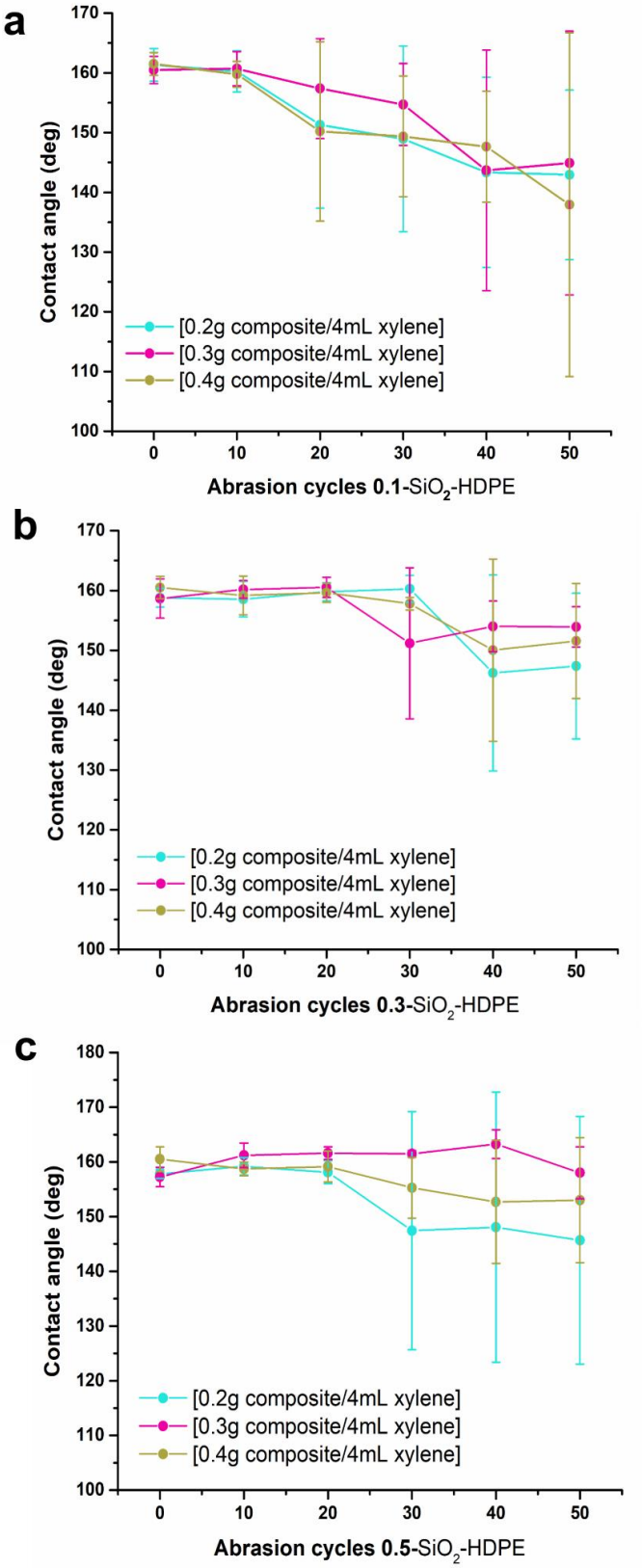

Figure 4.11: Abrasion testing results for all CNF-containing coatings, fabricated from slurries with dried formulation contents ranging 0.2-0.4 g per 4mL xylene (P120 Al_2O_3 sandpaper); (**a**) **0.1**-SiO_2-HDPE; (**b**) **0.3**-SiO_2-HDPE; and (**c**) **0.5**-SiO_2-HDPE.

Similarly, slurries with a reduced dried formulation content [0.20 g composite/4mL xylene] exhibited a significant decrease in surface hydrophobicity. This was rationalised through an

overall reduction in the mass of coating applied to surfaces, and as such, a less substantial layer is present to provide abrasion resistance, leading to a decrease in contact angle of 12° (from 159° ± 2) for **0.3**-SiO_2-HDPE and 12° (from 158° ± 1) for **0.5**-SiO_2-HDPE. However, **0.1**-SiO_2-HDPE was an exception to this, as a comparable change in contact to samples fabricated using the optimal dried formulation content was observed (decrease of 18° from 161° ± 3). See appendix for data table of contact angles, Table A1.

4.3.4.1.2 Extended Abrasion Testing

Extended abrasive testing (>50 cycles) was carried out on samples, fabricated from slurries that were made up using an optimal dried formulation content of [0.30 g composite/4 mL xylene], with aims of better establishing the link between wear resistance and CNF content, while shedding light on the interaction of water at the coating surface during repeat cycles. The initial contact angles and tilting angles of samples are displayed below:

Table 4.05: Recorded static contact angles and tilting angles for all coatings fabricated from slurries with a dried formulation content of [0.30 g composite/4 mL xylene], before and after 100 abrasive wear cycles (200 g weight, P120 Al_2O_3 sandpaper):

CNF content	*Initial static contact angle*	*Recorded static contact angle after100 abrasive wear cycles*	*Initial tilting angle*	*Recorded tilting angle after 100 abrasive wear cycles*
SiO_2-HDPE	148° ± 5	131° ± 11	17° ± 1	90° ± 0
0.1-SiO_2-HDPE	153° ± 2	151° ± 7	18° ± 5	59° ± 30
0.3-SiO_2-HDPE	153° ± 4	152° ± 7	9° ± 2	69° ± 26
0.5-SiO_2-HDPE	153° ± 2	151° ± 12	12° ± 2	48° ± 9

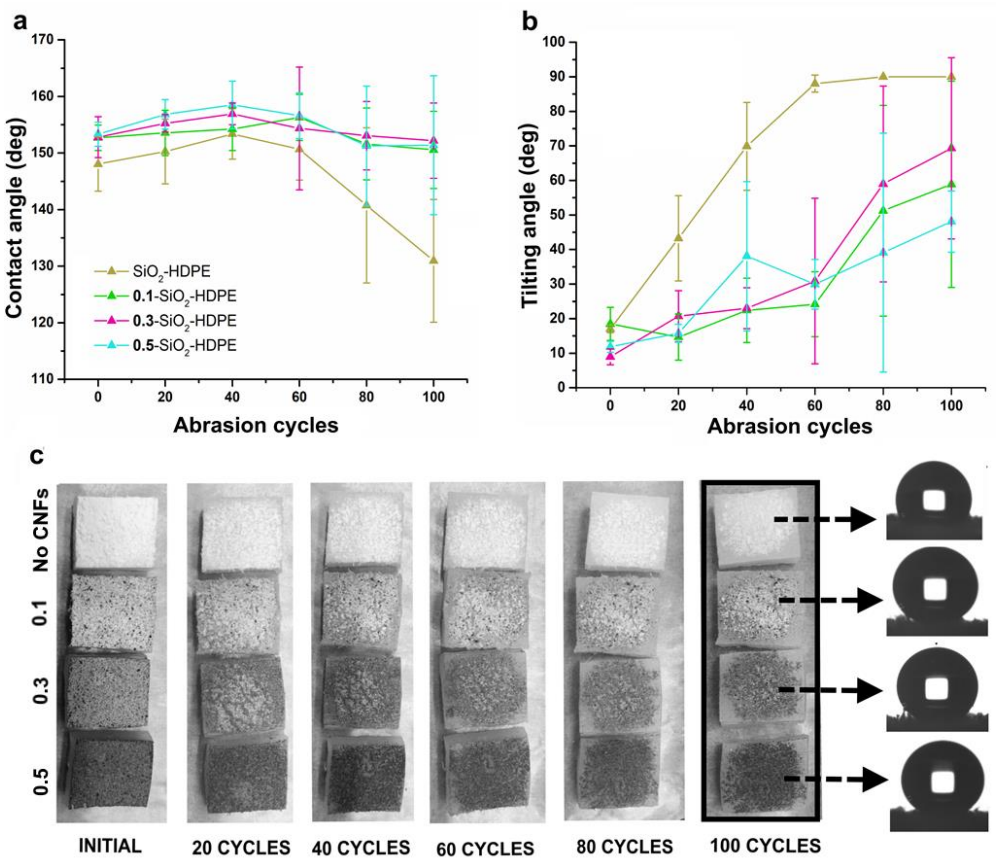

Figure 4.12: Extended abrasion testing of coatings, highlighting; (**a**) the change in static contact angle and (**b**) the change in tilting angle, of each coating during 100 successive abrasion cycles (200 g weight, P120 Al_2O_3 sandpaper). (**c**) Images displaying the visual appearance of all coatings at each 20 cycle interval and corresponding images of a water droplet resting on the surface after the 100th cycle.

Interestingly, all surface coatings displayed an initial enhancement in surface hydrophobicity during the first 40 cycles, as seen in Fig. 4.12, including those with no CNFs. Micrographs of abraded materials suggested that abrasive wear, could in fact, intensify surface roughness in the early stages of abrasion *via* two possible mechanisms; (**i**) direct roughening of the HDPE substrate, in addition to roughening of the surface coating, and (**ii**) greater surface exposure of CNFs in a non-aligned orientation (for those that contain CNFs). During abrasion, CNFs are orientated randomly throughout the coating material, which is predicted to aid the retention of air at the surface interface, due to the greater entrapment of interfacial air. This was primarily observed for **0.5**-SiO_2-HDPE, which displayed the lowest post-abrasion tilting angle. It was demonstrated that CNFs, therefore, not only strengthen and enhance the physical resilience of small-scale superhydrophobic materials, but can also facilitate the free movement of water droplets across the surface, strengthening the self-cleaning performance of materials.

However, after 100 abrasion cycles, SiO_2-HDPE suffered heavy wear and displayed a reduced contact angle of 131° ± 11, with a tilting angle that exceeded 90°. As a result, water droplets fully adhered to the surface coating, demonstrating Wenzel wetting behaviour, where the liquid-vapour interface beneath the droplet had been fully depleted through a change in surface architecture, primarily through a loss/flattening of nano-features. As hierarchical surface roughness is reduced and larger cavities are generated between surface microstructures, entrapped air can easily be replaced as water breaches the liquid-vapour interface and flows into surface apertures. Furthermore, it is visible from the micrographs in Figure 4.13a, that in particular areas, nanomaterial has been fully removed and the flat polymer is exposed.

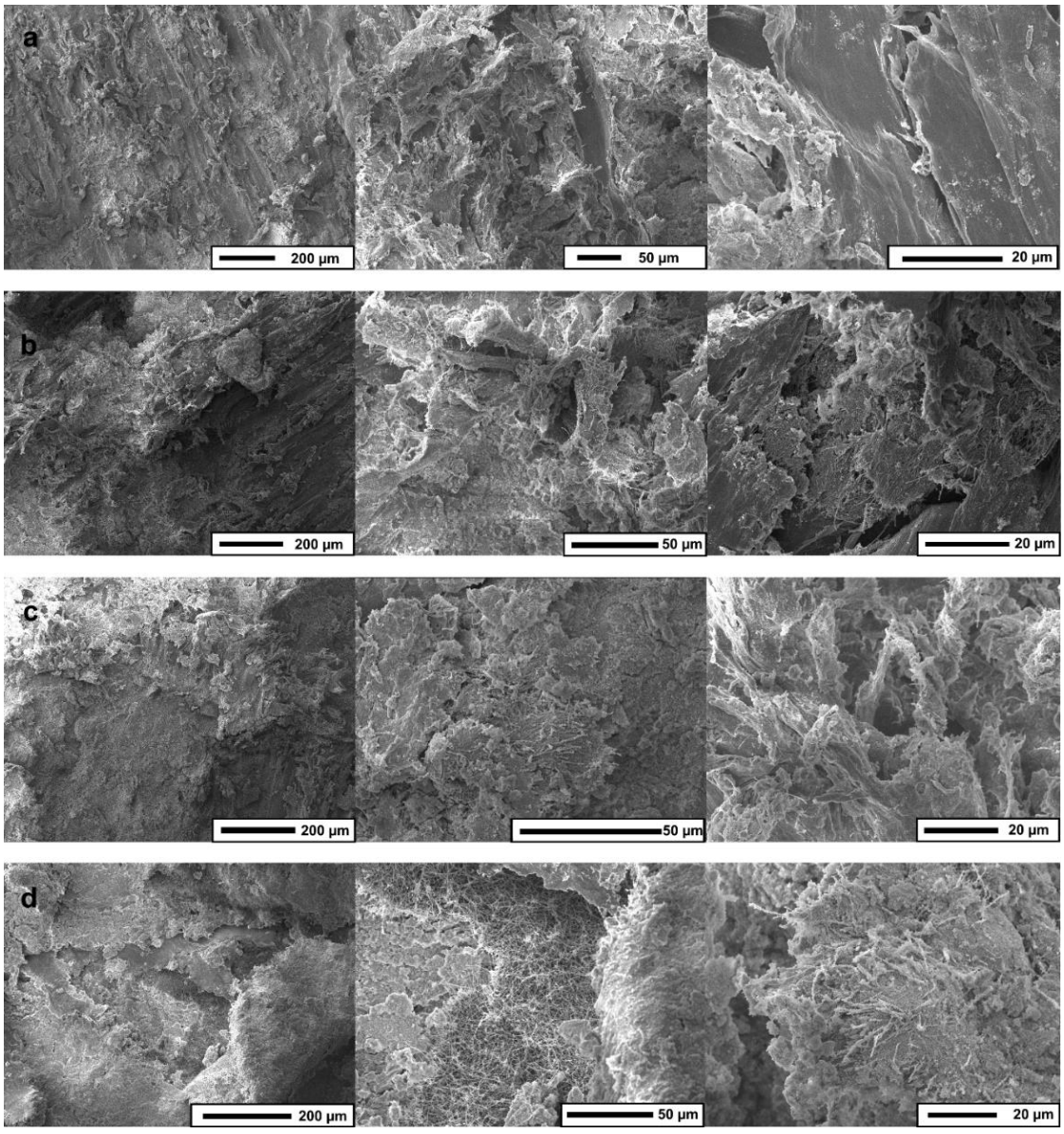

Figure 4.13: Top-down SEM micrographs displaying the surface morphology of coatings at different magnifications after 100 abrasion cycles (P120 Al_2O_3 sandpaper, 200 g weight); (**a**) SiO_2-HDPE; (**b**) **0.1-** SiO_2-HDPE; (**c**) **0.3-** SiO_2-HDPE; and (**d**) **0.5-** SiO_2-HDPE. Scale bars shown.

All CNF-based coatings retained a high level of water repellency after 100 abrasion cycles (see Fig. 4.12). This material loss particularly affected areas surrounding the substrate edges, as these were the leading edge of the material during abrasion. These areas, although heavily degraded were not completely flat (an artefact of the abrasive material), and so maintained relatively high static contact angles – equivalent to those expected for roughened HDPE. However, significant changes in tilting angles were apparent, as a Wenzel wetting mode was adopted and enhanced water pinning was observed (**0.1**-SiO_2-HDPE 59° ± 30, **0.3**-SiO_2-HDPE 69° ± 26 and **0.5**-SiO_2-HDPE 48° ± 9).

4.3.4.2 Underwater Plastron Stability

As stated throughout chapter 1, superhydrophobic coatings present a large liquid-vapour interfacial area (90-95%) when a certain level of hierarchical surface roughness is attained. The interfacial air layer (air pockets between surface structures) is termed the plastron, and is often studied in relation to the stability of superhydrophobic coatings during submersion in water. Generally, if the material has little underwater stability, a transition in wetting state from Cassie-Baxter to Wenzel is frequently seen in the early stages of submersion, as water droplets are observed to pin to the surface coating and functionality is rapidly lost (a similar process to that of chemical and physical degradation). The tertiary system (modified SiO_2/HDPE/unmodified CNFs) was studied to gauge the underwater stability of coatings by monitoring this wetting transition, while under various conditions i.e., short-term and long-term submersion periods and different hydrostatic pressures.

$$P = \rho g h \quad (1)$$

Using equation 1 – where P is the calculated hydrostatic pressure, ρ is the density of the liquid (water, 1000 kg/m^3), g is the acceleration of gravity (9.81 m/s^2) and h is the height of the cylinder (i.e., depth of water) – the coatings were subject to hydrostatic pressures that were computed to be 0.196 kPa and 7.85 kPa, relating to depths of 2 cm and 80 cm.

4.3.4.2.1 Plastron Stability at 0.196 kPa

When testing at low hydrostatic pressure, samples were submerged in beakers of distilled water and measurements were taken at 24-hour intervals, *via* the removal and re-submersion of each sample (for a 96-hour period, see Fig. 4.14 for set-up). Following this, the same samples were continuously submerged for a further 27 days (a total of 31 days, including the initial 96 hours), as detailed in section 4.2.10.1.

Figure 4.14: Testing set-up – side view of samples submerged in beakers of distilled water at 0.196 kPa (2 cm depth), sealed with parafilm to avoid water evaporation; **0.5**-SiO_2-HDPE (**left**); **0.3**-SiO_2-HDPE (**middle left**); **0.1**-SiO_2-HDPE (**middle right**); and SiO_2-HDPE (**right**).

Table 4.06: Recorded static contact angles and tilting angles for all coatings, fabricated from slurries with a dried formulation content of [0.30 g composite/4 mL xylene], before and after submersion at a hydrostatic pressure of 0.196 kPa for a time period of 96 hours:

CNF content	*Initial static contact angles*	*Recorded static contact angle after 96 hours of underwater submersion*	*Initial tilting angles*	*Recorded tilting angle after 96 hours of underwater submersion*
SiO_2-HDPE	159° ± 3	158° ± 2	6° ± 1	13° ± 2
0.1-SiO_2-HDPE	159° ± 2	158° ± 3	9° ± 2	10° ± 2
0.3-SiO_2-HDPE	158° ± 3	157° ± 2	5° ± 1	9° ± 2
0.5-SiO_2-HDPE	158° ± 2	155° ± 2	6° ± 1	20° ± 7

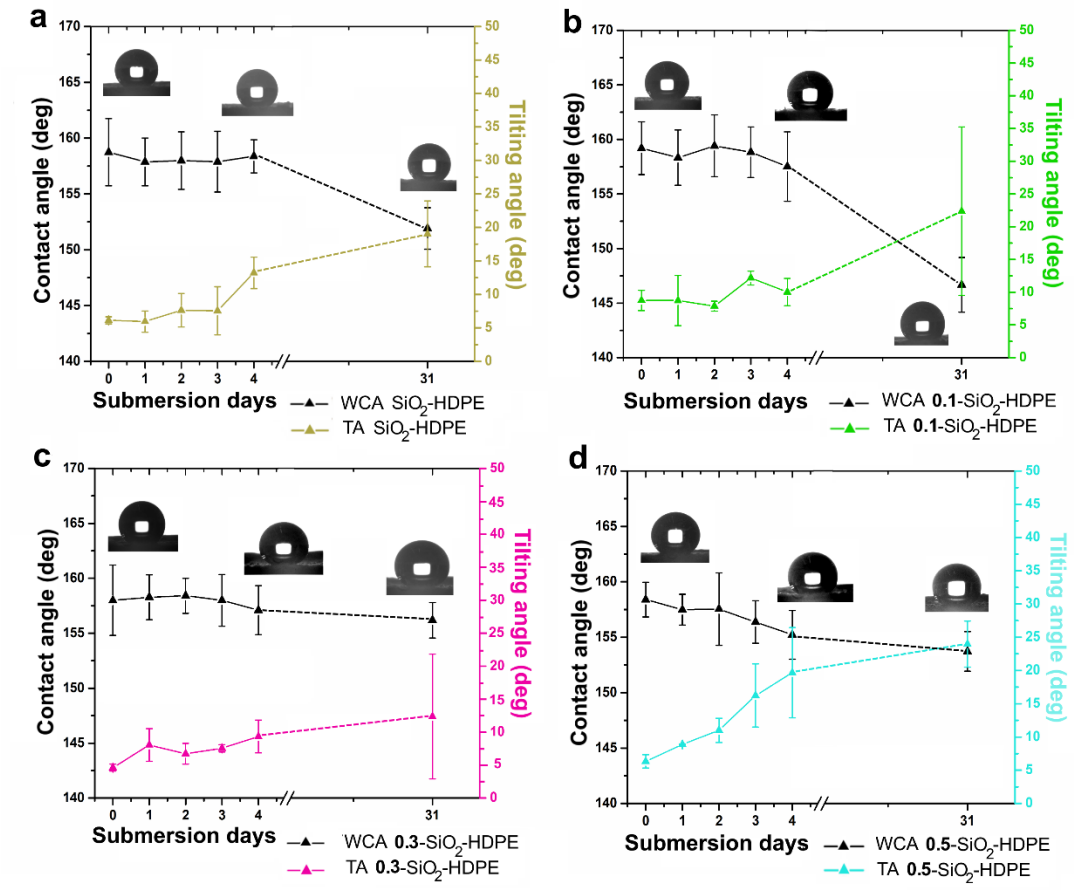

Figure 4.15: Static underwater plastron stability of all coatings submerged in distilled water at low hydrostatic pressure (0.196 kPa, 2 cm depth), monitored periodically for 96 hours, followed by a further 27 days continuous submersion (31 days total); (**a**) SiO_2-HDPE, (**b**) **0.1**-SiO_2-HDPE, (**c**) **0.3**-SiO_2-HDPE and (**d**) **0.5**-SiO_2-HDPE. Insets; digital images of a water droplet resting on the surface of highlighted coatings; initially, after 96 hours submersion and after 31 days submersion.

During short-term submersion (initial 96 hours), all coatings appeared to be relatively stable with the greatest loss in surface hydrophobicity of just 3°, occurring in **0.5**-SiO_2-HDPE coatings, as seen in Figure 4.15/Table 4.06. Furthermore, tilting angles remained moderately low (≤ 15°) for all coatings, except for **0.5**-SiO_2-HDPE, which showed a comparatively rapid short-term increase in the tilt angle of 14°. The porosity of dried formulations was measured *via* Brunauer-Emmett-Teller (BET) gas sorption analysis, where precursor powders were found to be mesoporous (2-50 nm pores, see Table 4.07), suggesting that nano-scale pores are likely to exist within the bulk of the surface coatings – preferably analysis would have been carried out on the end material (substrate and surface coating included), however, fully accounting for the weight of substrate would have been difficult and may have produced inaccurate measurements. This aligns well with the highly porous, intrinsic structure of the

thermoplastic-based SPNC system that comprised SiO_2 nanoparticles of the same size and was probed *via* FIB-SEM imaging in chapter 2. Although deposition techniques differed and coatings did not comprise fibres here, it was anticipated that thermoplastic composites would assemble similarly. In the absence of any regenerative mechanism (mechanical or chemical), the longevity of the plastron may be explained through the intrinsic porosity within the dense layer of composite material on the surface of substrates, acting to stabilise the plastron. It is anticipated that the transfer of air, from pockets deep within the bulk surface coating, may act to prevent rapid plastron depletion. As a result, over the conditions used, plastron decay may be limited to the uppermost layers of the coating over short-term submersion. The presence of CNFs is shown to play more of a pivotal role when the liquid-vapour interface is under greater pressure (see section 4.3.4.2.3), due to the internal support they provide for the cavies within the coating.[45] However, the exposure of polar groups on the surface of coatings, and morphological changes expected when incorporating different CNF loadings, may compromise the potential benefits of integrating fibres into coatings if droplet pinning is induced. Hence, surface polarity through the exposure of unmodified fibres, is likely a contributing factor to the initial enlargement in tilting angle for **0.5**-SiO_2-HDPE as the hydrostatic pressure was extremely low, and samples were kept under static conditions. Therefore, external factors are likely to play a limited role.

Table 4.07: BET surface area analysis and average adsorption pore size for CNF-containing precursor powders:

CNF content	*BET surface area (m^2/g)*	*Average adsorption pore size (nm)*
0.1-SiO_2-HDPE	191.9	11.4
0.3-SiO_2-HDPE	183.5	12.1
0.5-SiO_2-HDPE	173.8	11.5

To assess the long-term stability of coatings and further reveal any impact that CNFs may have, samples were left continually submerged for an extended period of time, as detailed above. High water repellency was retained for all surface coatings, with the exception of **0.1**-SiO_2-HDPE, which displayed a contact angle of 147° $\pm$ 3 and a significant increase in tilting angle of 12°. Samples with higher CNF compositions showed the greatest preservation of surface hydrophobicity across the additional 27-day submersion period (see Fig. 4.16). It was anticipated that a lower CNF content may be detrimental towards the long-term stability of the plastron, despite showing initial stability, due to facilitating interactions with water in

concentrated areas (fibres sparsely located throughout the surface), over time, aiding its infiltration. Conversely, a larger CNF content may have a long-term stabilising effect on the liquid-vapour interface if unmodified fibres are present in a large enough quantity, and therefore, protrude more uniformly throughout the surface (see Fig. 4.17). This is similar to the *Salvinia* effect, whereby fibres can pin to the liquid-vapour interface in regions where they are exposed, providing extra stabilisation and prevention from the infiltration of water.[46,47] A similar phenomenon was reported by Babu *et al.,* where superhydrophobic surfaces, fabricated from vertically aligned carbon nanotubes, were studied for their biomimetic air retention under water.[47]

Table 4.08: Recorded static contact angles and tilting angles for all coatings, fabricated from slurries with a dried formulation content of [0.30 g composite/4 mL xylene], before and after submersion at a hydrostatic pressure of 0.196 kPa for a time period of 31 days:

CNF content	*Initial static contact angles*	*Recorded static contact angle after 31 days of underwater submersion*	*Initial tilting angles*	*Recorded tilting angle after 31 days of underwater submersion*
SiO_2-HDPE	$159° \pm 3$	$152° \pm 2$	$6° \pm 1$	$19° \pm 5$
0.1-SiO_2-HDPE	$159° \pm 2$	$147° \pm 3$	$9° \pm 2$	$22° \pm 13$
0.3-SiO_2-HDPE	$158° \pm 3$	$156° \pm 2$	$5° \pm 1$	$12° \pm 9$
0.5-SiO_2-HDPE	$158° \pm 2$	$154° \pm 2$	$6° \pm 1$	$24° \pm 3$

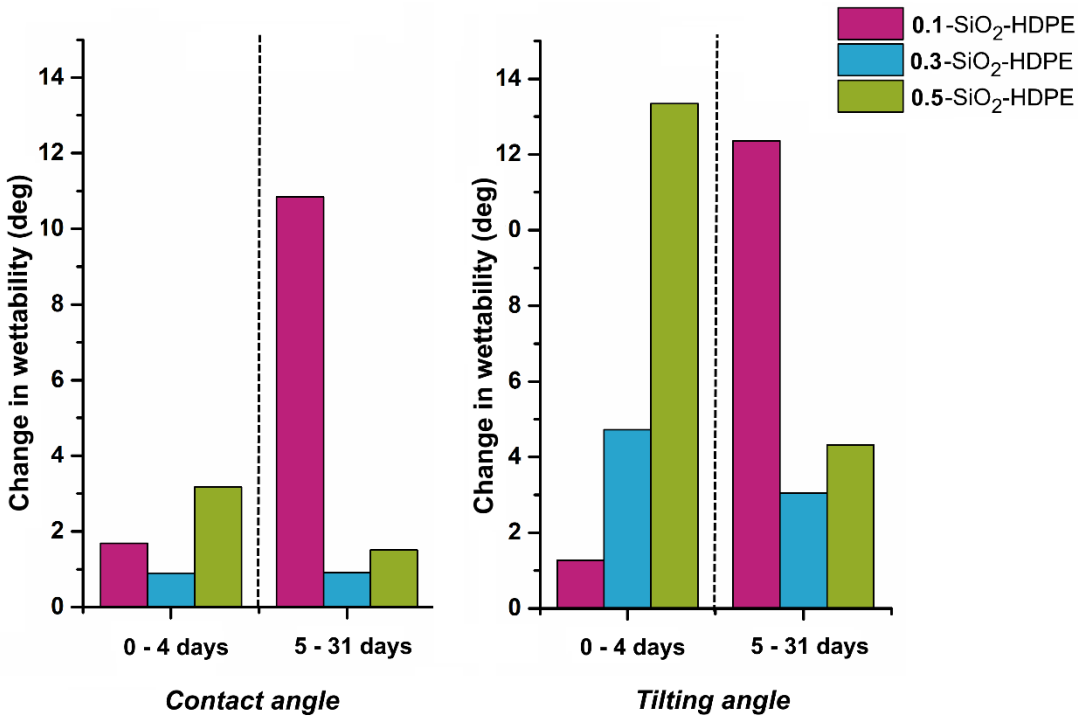

Figure 4.16: Bar chart showing the change in wettability (decrease in contact angle and increase in tilting angle) of CNF-containing surface coatings, during short-term and long-term submersion periods [0-96 hour periodic submersion (day 0-4) vs 27-day continuous submersion (day 5-31)] at a hydrostatic pressure of 0.196 kPa (2 cm depth).

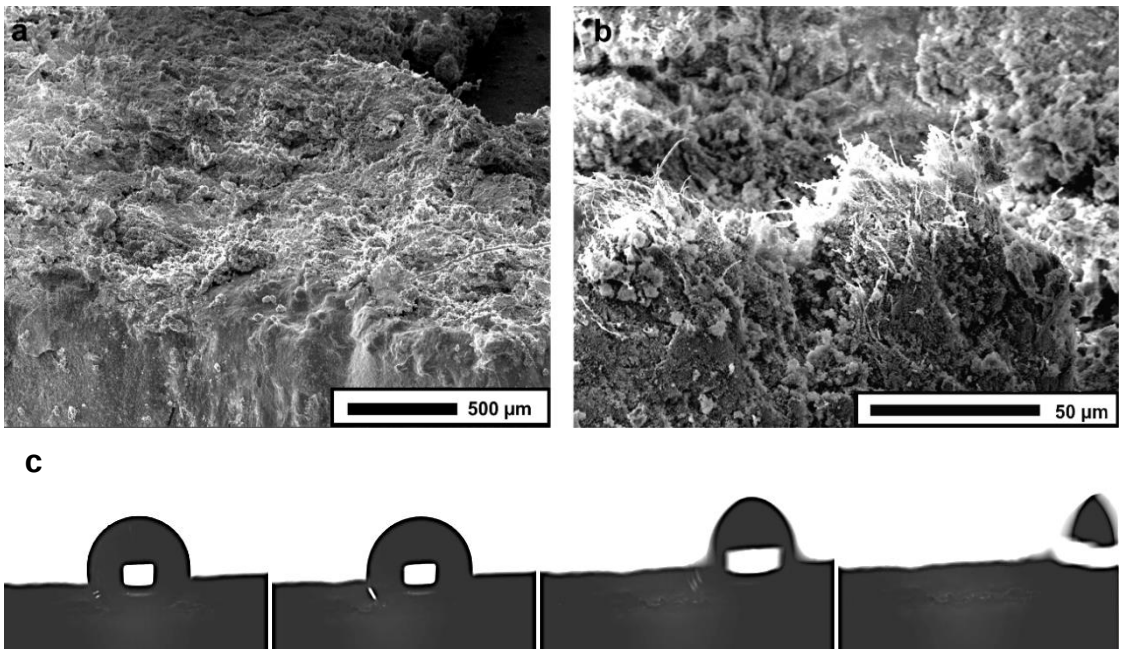

Figure 4.17: SEM micrographs of **0.5**-SiO_2-HDPE tilted at a 55° angle; (**a**) showing the surface morphology and (**b**) highlighting the CNF presence on the external surface. (**c**) Digital images showing the movement of a water droplet on the surface of **0.5**-SiO_2-HDPE, after 31 days of submersion in distilled water (2 cm depth), as the stage is tilted.

4.3.4.2.2 Plastron Stability at 7.85 kPa

Throughout section 4.3.4.2.1, surface coatings were only subject to mild hydrostatic pressure. To assess the performance of coatings under more challenging conditions, the submersion depth was increased from 2 cm to 80 cm, subsequently enhancing the hydrostatic pressure acting on the liquid-vapour interface from 0.196 kPa to 7.85 kPa. Here, two sets of experiments were carried out in parallel, similar to those conducted in section 4.3.4.2.1;

Sample set 1: Periodic measurements were taken at 24-hour intervals, for a maximum of 96 hours (short-term testing), which involved the recovery and re-submersion of the same samples. Conducted for **all** surface coatings.

Sample set 2: Continuous measurements were taken, where individual samples were submerged for discrete periods of time – either 1, 2 or 4 weeks (long-term testing) – and were removed from the solution, only, at the end of the testing period for immediate measurements. Conducted for **CNF-containing** surface coatings.

It was important to probe both periodic and continuous measurements, in order to deduce and minimise any disturbances to the plastron.

Sample set 1

When conducting periodic measurements, samples were all attached to the same weighted support that was then lowered into a large cylinder filled with distilled water, and brought to the surface only to conduct each measurement (see Fig. 4.18 for set-up). In doing so, it was anticipated that additional plastron destabilisation would likely occur, due to continuous change in hydrostatic pressure during the removal and re-submersion cycle, presenting increasingly challenging circumstances. The resultant surface wettability data is displayed below in Table 4.09.

Figure 4.18: Image showing the set-up for periodic submersion measurements of sample set 1, during testing at 7.85 kPa (80 cm depth). Inset; image of the tested samples and sample support/holder.

Table 4.09: Recorded static contact angles and tilting angles for all coatings in **sample set 1**, fabricated from slurries with a dried formulation content of [0.30 g composite/4 mL xylene], before and after periodic submersion at a hydrostatic pressure of 7.85 kPa for a time period of 96 hours:

CNF content	*Initial static contact angles*	*Recorded static contact angle after 96 hours of underwater submersion*	*Initial tilting angles*	*Recorded tilting angle after 96 hours of underwater submersion*
SiO_2-HDPE	152° ± 7	66° ± 68	16° ± 1	90° ± 0
0.1-SiO_2-HDPE	155° ± 2	143° ± 4	18° ± 7	90° ± 0
0.3-SiO_2-HDPE	156° ± 1	152° ± 2	11° ± 2	45° ± 18
0.5-SiO_2-HDPE	156° ± 3	152° ± 3	5° ± 1	40° ± 22

In sample set 1, **0.5**-SiO_2-HDPE was found to exhibit the most consistent plastron stability, with respect to static and dynamic wettability measurements. Whereas, SiO_2-HDPE and **0.1**-SiO_2-HDPE underwent a wetting state transition after only a number of days (≥ 48 hours), marked by tilt angles that exceeded 90°. Interestingly, **0.1**-SiO_2-HDPE was found to display greater plastron stability than SiO_2-HDPE (see Fig. 4.19) – contrasting to what was observed during long-term testing at low hydrostatic pressure. Subsequently, highlighting that CNFs are able to provide some order of structural support for the air cavities within coatings, preventing them from collapsing and/or slowing the movement of air from within pockets to the surface; at greater hydrostatic pressures, structural support appears to outweigh the adhesion of water, through the presence of polar groups on surface fibres, for these systems. **0.3**-SiO_2-HDPE and **0.5**-SiO_2-HDPE displayed surface superhydrophobicity after 96 hours, mimicking what was observed during the extended testing at low hydrostatic pressure, and underlining the benefit of CNF-induced stabilisation and resilience (see Fig. 4.21). Measurements in sample set 1 generally displayed a greater magnitude of change in tilting angles, most likely due to the repeated removal and re-submersion of samples to record measurements (see Fig. 4.22)

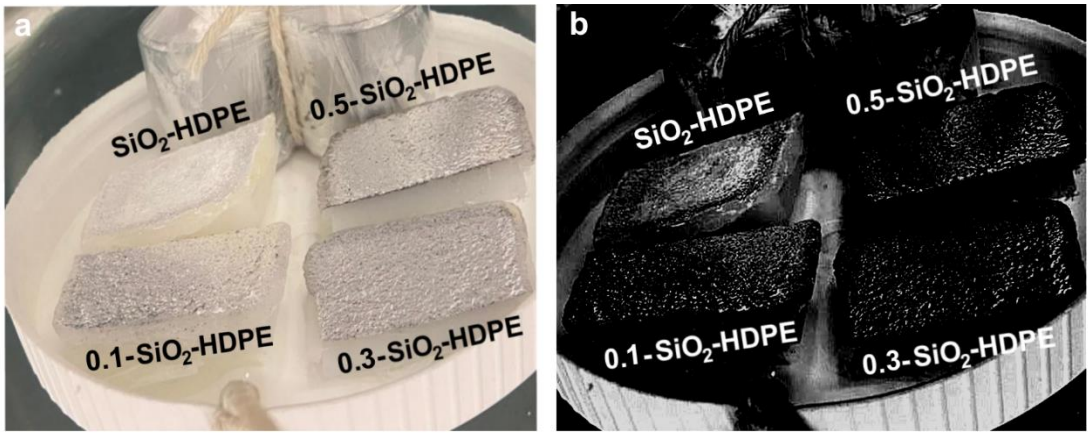

Figure 4.19: Images showing the mirrored appearance of the plastron, while submerged at a hydrostatic pressure of 7.85 kPa (80 cm depth), after 96 hours; (**a**) the original image and (**b**) converted into black and white to highlight the loss of interfacial air at the surface of SiO_2-HDPE. Individual surface coatings are labelled.

Sample set 2

During continuous submersion testing, individual samples were attached to separate weighted supports and lowered into the cylinder, under the same conditions as sample set 1 (see Fig. 4.20). This was an optimised approach, relative to the approach used for the first set of measurements (sample set 1), to minimise any disturbances to the plastron. Wettability data

was recorded immediately after samples were recovered, and is presented below in Figure 4.21/4.22. All results presented were based on multiple measurements across 1 sample, for each submersion period (1, 2 or 4 weeks). Following the removal of samples that had been continuously submerged for 4 weeks, samples were left under ambient conditions for 30-minute and 60-minute intervals to investigate plastron recovery, and determine whether plastron decay primarily occurs at the uppermost surface layers.

Figure 4.20: Images showing the set-up and individual weighted supports for continuous submersion measurements of sample set 2, during testing at 7.85 kPa (80 cm depth).

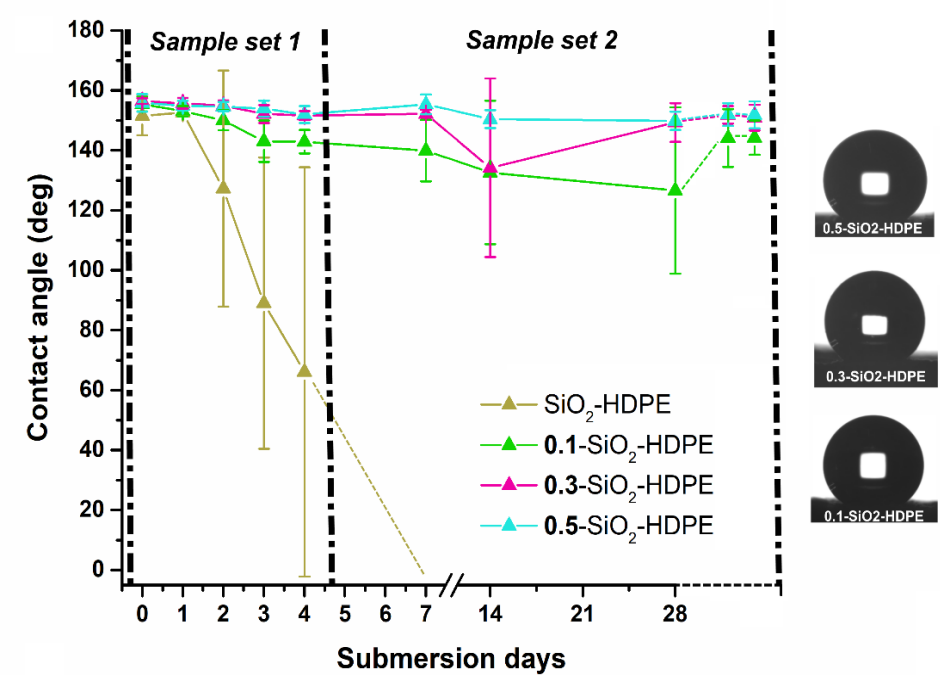

Figure 4.21: The static underwater plastron stability of coatings that have been submerged in distilled water at increased hydrostatic pressure (7.85 kPa, 80 cm depth); monitored periodically for 96 hours (sample set 1, **solid lines**) and continually submerged for 1-4 weeks (sample set 2, **solid lines**). Samples that were submerged continuously for 4 weeks were left under ambient conditions, and measurements were recorded at 30-minute and 60-minute intervals, post-removal (**dotted lines**). Insets; digital images of a water droplet resting on the highlighted coating (after 4 weeks of continuous submersion). Multiple measurements were taken across a single sample for sample set 1, and across one sample per submersion period for sample set 2 (1, 2 or 4 weeks).

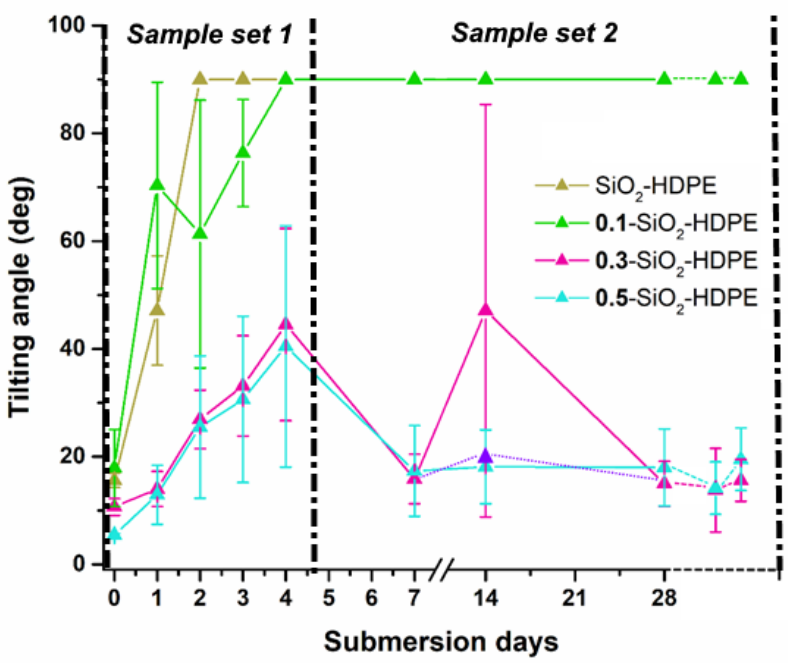

Figure 4.22: The static underwater plastron stability (tilting angles) of coatings that have been submerged in distilled water at increased hydrostatic pressure (7.85 kPa, 80 cm depth); monitored periodically for 96 hours (sample set 1) and continually submerged for 1-4 weeks (sample set 2, **solid lines**). Samples that were submerged continuously for 4 weeks were left under ambient conditions, and measurements were recorded at 30-minute and 60-minute intervals, post-removal (**dotted lines)**. Data plotted when excluding large tilting angle values for **0.3**-SiO_2-HDPE is represented by the **purple dotted line**. Multiple measurements were taken across a single sample for sample set 1, and across one sample per submersion period for sample set 2 (1, 2 or 4 weeks).

Continual sample submersion showed promising results as **0.5**-SiO_2-HDPE exhibited a static contact angle of 150° ± 3 and tilting angle of 18° ± 7, after 4 weeks of continuous submersion. In addition, these materials were found to remain fully operational as self-cleaning coatings – tested with simulated dirt particles using external falling water droplets (see Fig. 4.23). **0.1**-SiO_2-HDPE displayed results that aligned with the initial periodic testing of sample set 1 and long-term testing at low hydrostatic pressure, losing superhydrophobicity and displaying a tilting angle of >90° after 1 week of continuous submersion (contact angle of 127° ± 28 after 4 weeks). **0.3**-SiO_2-HDPE displayed similar plastron stability to **0.5**-SiO_2-HDPE, yielding a contact angle of 149° ± 6 and a tilting angle of 15° ± 4 after 4 weeks of continuous submersion. Thus, it can be deduced that an increased CNF loading has an overall positive effect on the long-term underwater stability and performance of superhydrophobic coatings, even during submersion at greater hydrostatic pressures. However, **0.3**-SiO_2-HDPE appeared to exhibit greater coating variability. Whereby, some areas appeared more susceptible to wetting/air depletion than others, highlighted during measurements taken at week 2 (**pink solid line**, Figure 4.22). As discussed previously, obtaining exact morphological replicas of

coatings is incredibly difficult, due to the nature of the deposition process and dried formulation approach. Therefore, each independent sample used may show varied susceptibility to air depletion, which is likely related to coating thickness and the channel of nanopores present within the bulk surface coating. The averaged tilt angle at week 2 for **0.3**-SiO_2-HDPE included two large values (87° and 90°), due to reduced plastron stability in particular regions across the surface. Hence, significantly increasing the apparent overall tilting angle. When discounting these from the averaged value, it is apparent that the fit of the line is more appropriate (**purple dotted line,** Fig. 4.22), following the general 'trend' for high CNF content coatings. The submersion performance of coatings with the highest CNF content (**0.5**-SiO_2-HDPE) suggests that CNFs may contribute toward coating reproducibility, through more effective adhesion/dispersion of components.

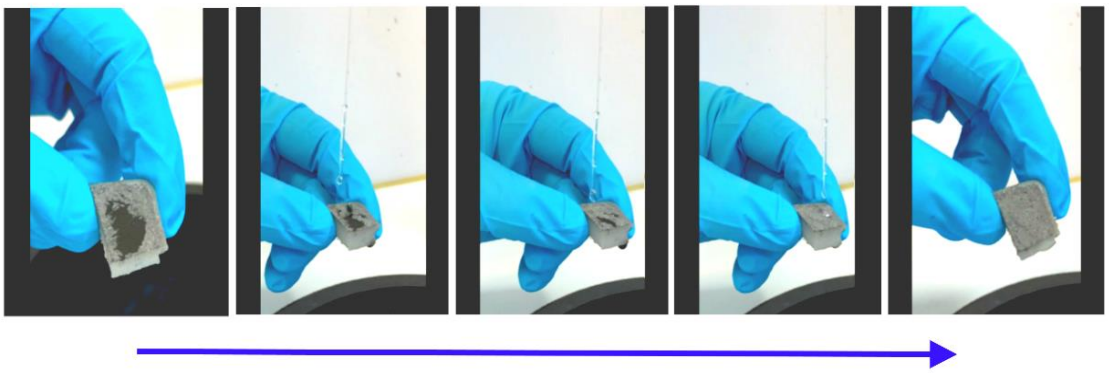

Figure 4.23: Self-cleaning action of **0.5**-SiO_2-HDPE after 4 weeks of continual submersion, at a hydrostatic pressure of 7.85 kPa (80 cm depth). Simulated dirt particles (MnO_2) were deposited onto the surface and falling water droplets dispensed from a pipette were used to remove them.

After the recovery of samples within sample set 2, samples were left under ambient conditions and wettability measurements were recorded after 30-minute and 60-minute intervals. No significant change in surface wettability was observed for coatings with greater CNF loadings. However, **0.1**-SiO_2-HDPE displayed an enhancement in surface hydrophobicity from 127° ± 28, during the initial removal, to 144° ± 6 after 60 minutes under ambient conditions (see Table 4.10). Subsequently, suggesting that plastron decay may occur predominantly at, and in some cases may be limited to, the exterior layer(s) of the surface. For partial interfacial air regeneration to occur over a short period of time, it is likely that air is still somewhat present, deeper within the cavities of the surface coating. This aligns well with what was observed in section 4.3.4.2.1, where all surface coatings were able to withstand short-term submersion at low hydrostatic pressure, without any substantial change in surface hydrophobicity.

Table 4.10: Recorded static contact angles and tilting angles for all coatings in sample set 2, fabricated from slurries with a dried formulation content of [0.3 g composite/4 mL xylene], after continuous submersion at a hydrostatic pressure of 7.85 kPa and time period of 4 weeks:

CNF content	*Recorded static contact angle after 4 weeks of underwater submersion*	*Recorded static contact 60 minutes after removal*	*Recorded tilting angles after 4 weeks of underwater submersion*	*Recorded tilting angles 60 minutes after removal*
0.1-SiO_2-HDPE	127° ± 28	144° ± 6	90° ± 0	90° ± 0
0.3-SiO_2-HDPE	149° ± 6	151° ± 4	15° ± 4	16 ° ± 4
0.5-SiO_2-HDPE	150° ± 3	152° ± 4	18° ± 7	20° ± 6

4.3.4.2.3 Reflectivity Measurements

In the literature, a well-established method of assessing the underwater plastron stability of a superhydrophobic material is by monitoring reflectivity at the liquid-vapour interface, over time. Due to the difference in refractive index between two mediums – in this case, water and air – reflectance can be observed at the interface when incidence light is applied to the surface. As the plastron reflects light, its degradation can be identified by the disappearance/reduction in the intensity of reflected light.

In collaboration with Imperial College London, reflectivity measurements were recorded by Aleksandra Fedosyuk (Edel Research Group) to probe the plastron stability of **0.5**-SiO_2-HDPE over a series of weeks. For these measurements, the sample was adhered within a plastic cuvette (1cm x 1cm) and filled with distilled water to simulate shallow submersion; the water layer between the sample surface and the cuvette wall was measured to be between 1.2-1.3 mm thickness, respectively (see Fig. 4.24 inset). Ideally, we aimed to design an experiment that would allow us to monitor the total internal reflectance at the liquid-vapour interface at variable submersion depths (incident light > 48.5° relative to perpendicular to the surface in each case). However, after unsuccessful attempts at manually angling optical probes in a reproducible manner to emit and detect full reflectance, we decided to compromise by using a UV spectrometer equipped with an integrating sphere attachment (see Fig. 2.24). Subsequently, this restricted the sample size, submersion depth and reflected light, so that complete reflectance was not achievable due to a smaller angle of incidence. Nonetheless, a reflectance signal could be observed when using this set-up (specular and diffuse reflectance, referenced against an aluminium mirror).

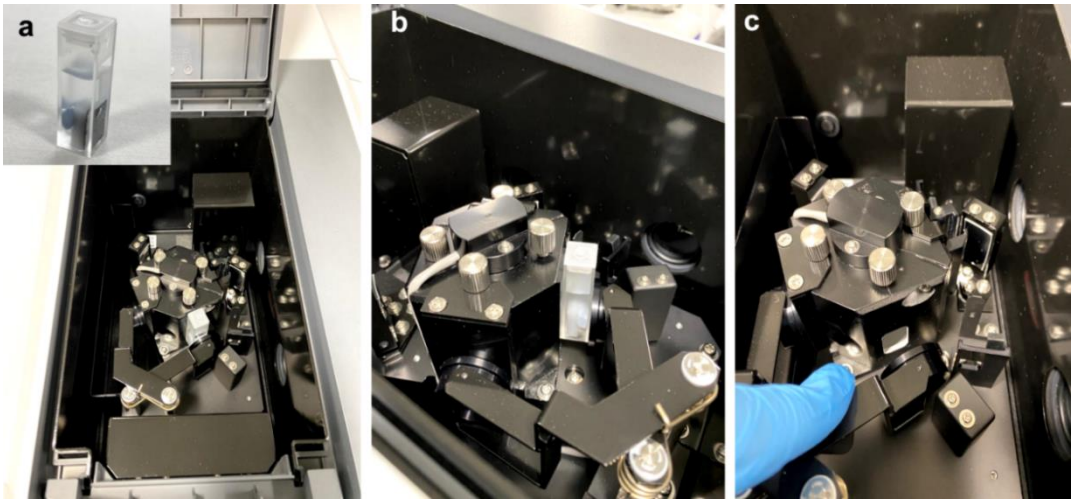

Figure 4.24: (**a/b**) Images showing the placement of the cuvette within the spectrophotometer during reflectivity measurements. (**c**) Image highlighting the exposure window of the spectrophotometer, without the sample present. Inset; image of the sample (**0.5**-SiO_2-CNF, 1 x 1.5 cm) within the cuvette.

Measurements from different positions across the surface were collected for every set of reflectance measurements, and later averaged to yield the average reflectance at the specified submersion period. The average reflectance was then baselined against the average initial reflectance at day zero for every set of measurements, to determine the relative change in reflectivity, over the optical range 400-1400 nm (ΔR, see Fig. 4.25). Following this, the data was then averaged over the whole optical range (400-1400 nm), as seen in Figure 4.26, to show the general change in reflectivity, over time. The average change in reflectivity (ΔR) was deduced to be -0.31% after continuous submersion of the surface coating in a cuvette of water for 49 days. Overall, this was judged as a negligible change in reflectivity (<1%), indicating the limited loss of the plastron and aligning well with the reported contact angles above in sections 4.3.4.2.1 and 4.3.4.2.2. Although fluctuations could be observed and a general decline in reflectance could be seen over time, this change was not significant enough to report plastron degradation within the examined time frame.

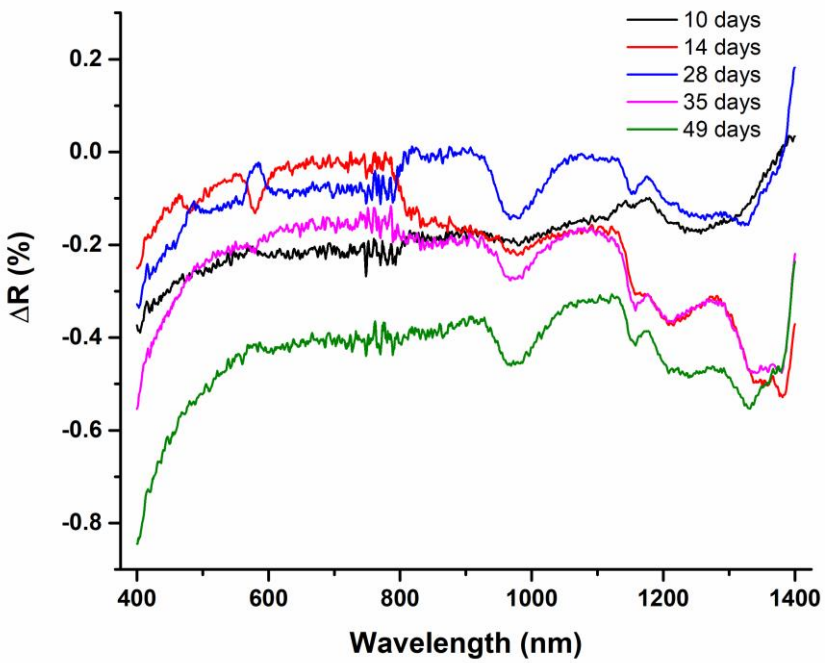

Figure 4.25: The average change in reflectivity (ΔR) of **0.5**-SiO_2-HDPE, over the optical range 400-1400 nm (baselined against initial reflectance measurements from day zero), for coatings with different submersion periods.

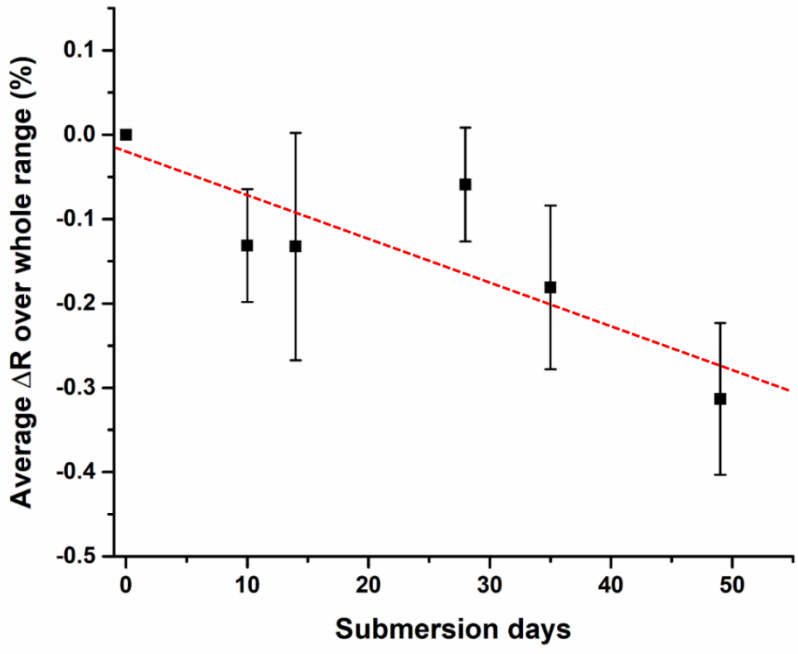

Figure 4.26: The average change in reflectivity (ΔR) of **0.5**-SiO_2-HDPE as a function of submersion time, averaged over the optical range 400-1400 nm (baselined against initial reflectance measurements from day zero).

4.4 Conclusions

Here, novel design and deposition approaches were employed, and the use of a high-strength additive was investigated to elevate the real-world potential of conventional SPNC coatings. Within this work, we aimed at integrating long-lasting protective mechanisms – e.g. self-cleaning abilities – into polymeric materials, by means of enhancing the inherent resilience of composite coatings. The main outcomes are detailed below:

Unique Design and Deposition Approach – An alternative approach that was first trialled in chapter 2, and involved the use of a hot press deposition process/dried SPNC formulations, was used and optimised. This deposition process allowed for high processing temperatures that were suspected to facilitate a strong integration between the surface coating and polymeric substrate. Furthermore, this approach promoted the bulk of incorporated fibres to reside at the substrate-coating interface, which was confirmed *via* cross-sectional SEM imaging and attributed to the use of slurries that comprised components with different inherent surface chemistries. Subsequently, resulting in suspected phase separation and preferential fibre positioning. Although this approach was only carried out with one SPNC system as proof of principle (SiO_2-HDPE), it is anticipated that this could be relevant to a range of SPNC materials, and could be employed widely as a method of coating thermoplastic substrates with superhydrophobic composite material (providing thermal degradation is not initiated at the melting temperature of the polymer).

Physical Resilience and CNF Loading – The link between physical resilience and CNF loading was unveiled during abrasive wear testing. After identification of the optimal dried formulation content within slurries, i.e. [0.30 g/4 mL xylene], extended abrasion testing was carried out, where physical resilience was seen to increase in line with CNF loading. Coatings that comprised no fibres displayed a loss in superhydrophobicity after ~ 60 abrasion cycles. Superhydrophobicity was maintained for all coatings that contained fibres but enhancements in tilt angles could be observed, indicative of a change in wetting mechanism from Cassie-Baxter to Wenzel, or the adoption of intermediate wetting state during later cycles. Although CNF-containing coatings underwent a change in wetting behaviour after heavy abrasive wear (after 100 abrasion cycles), they remained efficient as self-cleaning materials in the early stages of abrasion (0-40/60 cycles). This signifies a substantial increase in mechanical strength of SiO_2-HDPE-CNF materials, when compared to coatings fabricated in the absence of fibres (i.e.. SiO_2-HDPE) and their solution-based equivalents. Thus, the utilization of fibres was found to dramatically improve the abrasive wear susceptibility of SPNC coatings.

CNF-Induced Underwater Stabilization – In addition to having improved physical resilience, coatings also displayed excellent underwater stability. After carrying out periodic and continuous testing at two different hydrostatic pressures (0.196 kPa and 7.85 kPa), it was concluded that coatings displayed high underwater stability due to two factors:

(i) The presence of a continuous system of nanopores within the bulk dried coating, that acts to facilitate the entrapment/slow movement of air. The stability can be intensified further by the addition of a high-strength additive which acts to reinforce the pores and provide further support, in this case, CNFs.

(ii) The use of unmodified CNFs appeared to induce a direct stabilising effect on the liquid-vapour interface, in coatings with a higher CNF loading. It was anticipated that this was through pinning of the interface, similar to that of the *Salvinia* effect, due to the small percentage of polar groups on the surface of fibres ~ < 2% (confirmed *via* XPS analysis).

Generally, a reduced presence of CNFs was found to be superior for short-term underwater applications. However, coatings with greater CNF loadings were found to dramatically prolong the long-term underwater stability – verified by retaining their functionality as self-cleaning coatings, after 4 weeks of continuous submersion at a depth of 80 cm. This was expected to be due to a mixture of morphological change (dependent on CNF loading), and the stabilisation effects stated above. In studying the underwater stability over different experimental conditions, the benefits and implications associated with CNF addition/content were uncovered, allowing for the prediction of optimal formulation compositions for future work (application dependent).

Potential for Self-Healing Properties – It was suspected that partial regeneration of interfacial air occurred in the absence of any chemical or mechanical regenerative mechanisms, when leaving samples that had been continually submerged for 4 weeks to stand under ambient conditions, for short periods of time (up to 60 minutes). Therefore, implying that air depletion is somewhat limited to the external coating layer(s), and that air entrapped within the nanopore system of the bulk coating may be stable over time. Although in-depth analysis was not conducted, the increase in contact angle that was observed for **0.1**-SiO_2-HDPE indicated that coatings could have intrinsic regenerative properties. However, further investigation would be required in order to confirm this.

To conclude, it has been shown that a combination of factors e.g. the use of SPNC formulations in their 'dried' form, high temperature depositions, and incorporation of a high-strength additive can be used to enhance the inherent resilience of conventional SPNC coatings. Furthermore, successful integration of CNFs demonstrates further opportunities to incorporate different additives into SPNC systems, to impart superior resilience and/or additional functionalities (providing system compatibility). The self-cleaning performance of coatings remained strong after weeks of continuous submersion or moderate abrasive wear (40-60 cycles – found to physically damage the surface of flat HDPE). Hence, the coatings presented within this chapter have demonstrated realistic commercial potential and have exhibited greater resilience than many synthetic coatings documented within the literature, thus opening future applications as resilient superhydrophobic materials.

4.5 References

1 M. Biron, *Thermoplastics and thermoplastic composites*, William Andrew, 2018.

2 R. W. Lang, A. Stern and G. Doerner, *Die Angew. Makromol. Chemie Appl. Macromol. Chem. Phys.*, 1997, **247**, 131–145.

3 P. K. Mallick, in *Materials, Design and Manufacturing for Lightweight Vehicles*, Elsevier, 2010, pp. 174–207.

4 A. Riveiro, A. Chantada, R. Soto, J. del Val, F. Arias-González, R. Comesaña, M. Boutinguiza, F. Quintero, F. Lusquiños and J. Pou, in *Materials for Biomedical Engineering*, Elsevier, 2019, pp. 29–56.

5 F. Ahmad, I. Singh and P. K. Bajpai, *Reinf. Polym. Compos. Process. Charact. Post Life Cycle Assess.*, 2019, 1–20.

6 G. Sui, W. H. Zhong, X. Ren, X. Q. Wang and X. P. Yang, *Mater. Chem. Phys.*, 2009, **115**, 404–412.

7 G. G. Tibbetts, M. L. Lake, K. L. Strong and B. P. Rice, *Compos. Sci. Technol.*, 2007, **67**, 1709–1718.

8 T. Ojeda, A. Freitas, K. Birck, E. Dalmolin, R. Jacques, F. Bento and F. Camargo, *Polym. Degrad. Stab.*, 2011, **96**, 703–707.

9 R. K. Krishnaswamy, *Polymer (Guildf).*, 2005, **46**, 11664–11672.

10 R. S. Devi, R. Ramya, K. Kannan, A. R. Antony and V. R. Kannan, *Mar. Pollut. Bull.*, 2019, **138**, 549–560.

11 W. Wang, K. Lockwood, L. M. Boyd, M. D. Davidson, S. Movafaghi, H. Vahabi, S. R. Khetani and A. K. Kota, *ACS Appl. Mater. Interfaces*, 2016, **8**, 18664–18668.

12 S. S. Latthe, R. S. Sutar, V. S. Kodag, A. K. Bhosale, A. M. Kumar, K. K. Sadasivuni, R. Xing and S. Liu, *Prog. Org. Coatings*, 2019, **128**, 52–58.

13 L. Cao, A. K. Jones, V. K. Sikka, J. Wu and D. Gao, *Langmuir*, 2009, **25**, 12444–12448.

14 J. P. Rothstein, *Annu. Rev. Fluid Mech.*, 2010, **42**, 89–109.

15 H. Y. Erbil, A. L. Demirel, Y. Avcı and O. Mert, *Science (80-.).*, 2003, **299**, 1377–1380.

16 K. Maghsoudi, E. Vazirinasab, G. Momen and R. Jafari, *Ind. Eng. Chem. Res.*, 2020, **59**, 9343–9363.

17 A. Biswas, I. S. Bayer, A. S. Biris, T. Wang, E. Dervishi and F. Faupel, *Adv. Colloid Interface Sci.*, 2012, **170**, 2–27.

18 S. F. Toosi, S. Moradi, M. Ebrahimi and S. G. Hatzikiriakos, *Appl. Surf. Sci.*, 2016, **378**, 426–434.

19 Y. Lee, S. Park, K. Kim and J. Lee, *Adv. Mater.*, 2007, **19**, 2330–2335.

20 E. Puukilainen, T. Rasilainen, M. Suvanto and T. A. Pakkanen, *Langmuir*, 2007, **23**, 7263–7268.

21 F. Vüllers, G. Gomard, J. B. Preinfalk, E. Klampaftis, M. Worgull, B. Richards, H. Hölscher and M. N. Kavalenka, *Small*, 2016, **12**, 6144–6152.

22 M. N. Kavalenka, A. Hopf, M. Schneider, M. Worgull and H. Hölscher, *Rsc Adv.*, 2014, **4**, 31079–31083.

23 M. Röhrig, M. Mail, M. Schneider, H. Louvin, A. Hopf, T. Schimmel, M. Worgull and H. Hölscher, *Adv. Mater. Interfaces*, 2014, **1**, 1300083.

24 Y. Lu, S. Sathasivam, J. Song, C. R. Crick, C. J. Carmalt and I. P. Parkin, *Science (80-.).*, 2015, **347**, 1132–1135.

25 V. Tuukka, B. Chris, A. Piers, F. Sami, I. Olli and R. R. H. A., *Adv. Mater.*, **23**, 673–678.

26 H. Xu, C. R. Crick and R. J. Poole, *J. Mater. Chem. A*, 2018, **6**, 4458–4465.

27 Y. Xue, P. Lv, H. Lin and H. Duan, *Appl. Mech. Rev.*, 2016, **68,** 030803.

28 B. V. Hokmabad and S. Ghaemi, *Sci. Rep.*, 2017, **7**, 1–10.

29 HDPE Boats - Tideman Boats, https://tidemanboats.com/high-density-polyethylene-boats-hdpe/.

30 S. Liu, X. Liu, S. S. Latthe, L. Gao, S. An, S. S. Yoon, B. Liu and R. Xing, *Appl. Surf. Sci.*, 2015, **351**, 897–903.

31 D. W. Clegg and A. A. Collyer, *Mechanical properties of reinforced thermoplastics*, Springer, 1986, vol. 326.

32 S. Yang, J. Taha-Tijerina, V. Serrato-Diaz, K. Hernandez and K. Lozano, *Compos. Part B Eng.*, 2007, **38**, 228–235.

33 S.-S. Yao, F.-L. Jin, K. Y. Rhee, D. Hui and S.-J. Park, *Compos. Part B Eng.*, 2018, **142**, 241–250.

34 M. H. Al-Saleh and U. Sundararaj, *Carbon N. Y.*, 2009, **47**, 2–22.

35 N. Forintos and T. Czigany, *Compos. Part B Eng.*, 2019, **162**, 331–343.

36 S. Ye, B. Wang, Y. Shi, B. Wang, Y. Zhang, Y. Feng, W. Han, C. Liu and C. Shen, *Compos. Commun.*, 2020, **21**, 100378.

37 P. Wang, W. Wei, Z. Li, W. Duan, H. Han and Q. Xie, *J. Mater. Chem. A*, 2020, **8**, 3509–3516.

38 M. Donati, C. W. E. Lam, A. Milionis, C. S. Sharma, A. Tripathy, A. Zendeli and D. Poulikakos, *Adv. Mater. Interfaces*, 2021, **8**, 2001176.

39 A. Baldelli, J. Ou, D. Barona, W. Li and A. Amirfazli, *Adv. Mater. Interfaces*, 2021, **8**, 1902110.

40 X. Liu, K. Chen, D. Zhang and Z. Guo, *Coatings*, 2021, **11**, 95.

41 M. Peng, Z. Liao, J. Qi and Z. Zhou, *Langmuir*, 2010, **26**, 13572–13578.

42 K. L. K. Lim, Z. A. M. Ishak, U. S. Ishiaku, A. M. Y. Fuad, A. H. Yusof, T. Czigany, B. Pukanszky and D. S. Ogunniyi, *J. Appl. Polym. Sci.*, 2005, **97**, 413–425.

43 K. Golovin, M. Boban, J. M. Mabry and A. Tuteja, *ACS Appl. Mater. Interfaces*, 2017, **9**, 11212–11223.

44 I. V Krasnikova, I. V Mishakov and A. A. Vedyagin, in *Carbon-Based Nanofiller and Their Rubber Nanocomposites*, Elsevier, 2019, pp. 75–137.

45 Y. Yang, Z. Ren, S. Zhao and Z. Guo, *Ind. Eng. Chem. Res.*, 2020, **59**, 6172–6182.

46 W. Barthlott, T. Schimmel, S. Wiersch, K. Koch, M. Brede, M. Barczewski, S. Walheim, A. Weis, A. Kaltenmaier and A. Leder, *Adv. Mater.*, 2010, **22**, 2325–2328.

47 D. J. Babu, M. Mail, W. Barthlott and J. J. Schneider, *Adv. Mater. Interfaces*, 2017, **4**, 1700273.

Chapter 5

Investigating the Viability of Sulfur Copolymers Within Superhydrophobic Materials Design

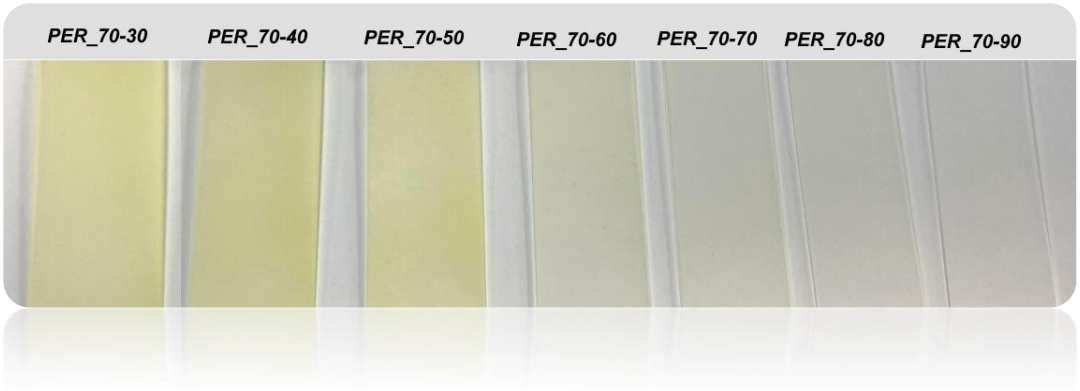

Contributions:

Powder X-ray Diffraction Measurements were carried out by Amy Lunt (Chong Research Group) at the University of Liverpool).

Antibacterial Preparation, Testing and Analysis was carried out by Romy Dop (Hasell Research Group) at the University of Liverpool

5.1 Introduction

The field of superhydrophobic materials design is continuously expanding, with innovative research being carried out to improve the versatility, sustainability and resilience of synthetic water repellent coatings, with examples being outlined in the experimental chapters thus far (versatility chapters 2 and 3, and resilience chapters 3 and 4). As we move into a future that is more conscious about recyclability and sustainability, research into developing functional coatings from waste by-products and natural compounds is on the rise, to address the mounting concerns and find alternative options.[1–4] This chapter combines the use of elemental sulfur – a by-product from the oil refining and gas processing industries – with a naturally occurring crosslinker, and explores the possibility of designing functional superhydrophobic materials from these sulfur-based polymers.[5,6] As elemental sulfur is an intrinsically hydrophobic material that has been shown to have inherent photocatalytic and antibacterial properties (see section 5.1.1 below), it was anticipated that functional superhydrophobic coatings with superior UV stability to conventional TiO_2 based photocatalytic/antimicrobial superhydrophobic materials, may be attainable.

5.1.1 Elemental Sulfur

Elemental sulfur (S_8) is an intrinsically hydrophobic, pale yellow, crystalline material that primarily exists as the α-sulfur polymorph at ambient temperature – a crown-shaped 8-membered ring structure of S atoms. While other polymorphs exist, particularly β and γ polymorphs, the α molecular configuration is most common.[7] it is an inexpensive and heavily abundant by-product of the oil and gas refining industries as sulfur is a primary component of fossil fuel, hence its removal is imperative in reducing sulfur dioxide emissions.[5] Consequently, this generates a large stockpile of unused material, reported by Karunarathna *et al*. to be > 7 million tonnes, annually, after industrial consumption for the production of sulphuric acid, fertilizers, vulcanized rubber, etc… (see Fig. 5.01) [8,9]

Figure 5.01: A stockpile of elemental sulfur produced from the hydrodesulfurisation process in petroleum refining. Figure taken from ref [10].

Although a large stockpile remains, sulfur has been shown to have interesting intrinsic properties. For example, Lui *et al.* and Peyman *et al.* have both independently reported powdered elemental sulfur to be photocatalytically active under visible and UV radiation, by demonstrating the degradation of commercially available dyes (Rhodamine B and Methyl Violet); it was suspected that these both proceeded *via* hydroxyl radical-mediated processes.[11,12] Furthermore, it is well-documented that sulfur has antibacterial and antifungal properties, whereby it has been shown to display substantial activity towards several strains of bacteria; many mechanisms have been proposed, including deactivation of SH enzyme systems within bacterial cells, and crosslinking between sulfur free radicals and proteins/lipids.[13,14] However, the exact mechanism is yet to be definitively established. Despite sulfur being proven to be a highly promising and natural waste material, employment in its elemental form has great limitations; it has restricted solubility in organic solvents, significantly reducing the ability to process the material, and despite being able to form polysulfides *via* ring-opening polymerisation (formation of diradicals at temperatures > 159°C), depolymerisation rapidly occurs when polymers reach ambient temperature.[15] In light of this, more practical methods that could be used to successfully consume and exploit the inherent properties of elemental sulfur have emerged in recent years, primarily, the synthesis of high sulfur content polymers *via* a process termed inverse vulcanisation. Pyun *et al.* first reported this revolutionary process in 2013, and documented how simple organic crosslinkers could be used to stabilise linear sulfur chains, in the absence of complimentary solvents, to form polymers that were later discovered to have a wide range of functional properties (see

Fig. 5.02).[6] Subsequently, this has led to sulfur copolymers receiving significant industrial and commercial interest in application areas such as, mercury capture and filtration applications, thermal imaging and optical applications, and antibacterial surfaces.[10,16–18]

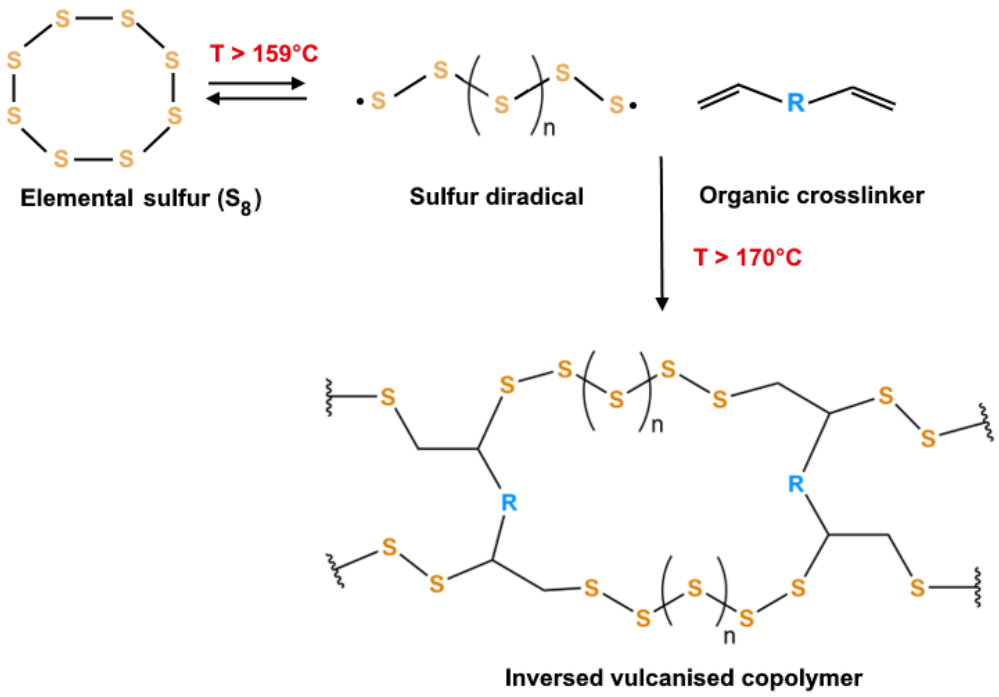

Figure 5.02: Schematic detailing the inverse vulcanization radical mechanism, used to synthesise stable copolymers from elemental sulfur and simple organic crosslinkers (containing vinyl groups), at elevated temperatures (~ 170°C).[6]

5.1.2 The Use of Sulfur-based Compounds in Superhydrophobic Materials

A large proportion of research that has employed sulfur-based compounds for use in synthetic superhydrophobic materials, has been focused on thiol-ene click chemistry. Generally, this involves the reaction between a thiol group (S-H) and an alkene (C=C), and is typically used to link carbon-based molecules together, in contrast to bridging polysulfide chains.[19] When subject to photo- or thermal- initiation, thiol free radical addition across carbon-carbon double bonds takes place, subsequently resulting in a straightforward method to synthesise macromolecules or polymer networks.[19] Commonly, acrylates and methacrylates have been employed as they allow for networks with tuneable surface chemistries, and are capable of connecting chemical groups or nanoparticles to an underlying surface.[20–22] Although thiol-ene click chemistry has been widely explored and has been typically used to fabricate superhydrophobic materials with enhanced durability, due to the presence of covalently boned

networks, the functional benefits of elemental sulfur are not directly extended to the resultant material.

The use of elemental sulfur in superhydrophobic materials is more limited; Lantos *et al.* reported the use of elemental sulfur nanoparticles in Ag-TiO_2 (silver-titanium dioxide) coatings to promote dual superhydrophobicity and visible light-activated photocatalytic activity, while maintaining high UV stability.[23] Although, sulfur was only used here as a hydrophobic, non-photodegradable filler to enhance surface roughness and to provide a desirable low surface energy; no testing was carried out to probe the inherent properties that sulfur nanoparticles may introduce into superhydrophobic coatings. Due to the majority of reported photocatalytic and antimicrobial superhydrophobic coatings comprising either TiO_2 or silver Ag nanoparticles – both intrinsically hydrophilic materials – UV-induced transitions in surface wettability often take place, leading to a rapid loss in superhydrophobic performance (as seen in chapter 3). Lantos *et al*. suggested that the intrinsic hydrophobicity and non-photodegradable nature of elemental sulfur could result in coatings with excellent degradation stability.[23] It was found that coatings that comprised 90 wt % sulfur and 10 wt % Ag-TiO_2 exhibited significant photocatalytic activity and degraded ~ 68.9 % of gaseous ethanol under blue LED light (405 nm), while retaining superhydrophobicity. Nonetheless, these materials were reported to have high contact angle hysteresis and to demonstrate Wenzel wetting, while also displaying limited mechanical resilience (superhydrophobicity was lost after a single tape test), likely related to the high powdered content.

5.1.3 The Feasibility of Designing Superhydrophobic Materials from Sulfur Copolymers

With an apparent lack of research into the employment of elemental sulfur and/or inverse vulcanised sulfur polymers within the field of superhydrophobic materials design, the question is raised as to whether this could be an area of overlooked opportunity. The non-photodegradable nature of sulfur and its stability towards photo-induced changes in surface wettability has been previously demonstrated, where it has been reported that interactions between elemental sulfur and water molecules are very limited due to a lack/absence of hydrogen bonding sites.[24] It is anticipated that this, combined with the inherent photocatalytic and antibacterial behaviour of sulfur, could be used to generate high-performance superhydrophobic materials, without the need for superfluous and/or expensive additives (e.g. TiO_2, Ag etc.). The most feasible route of introducing elemental sulfur into formulations would likely be in nanoparticulate form, due to the processability issues discussed above. However, the generation of high powder content coatings typically leads to poor mechanical

resilience. Therefore, a polymer-nanoparticle composite system, consisting of an inverse vulcanised sulfur polymer and inorganic metal oxide nanoparticles, may be more suitable. To the best of our knowledge, superhydrophobic coatings designed from inverse vulcanised sulfur copolymers have not been reported in the literature to date, and thus, were explored in this chapter.

5.1.4 Chapter Aims

Within this chapter, the primary aim was to fabricate a functional superhydrophobic material that displayed both photocatalytic and antibacterial activity, while existing as a high performance, UV stable material with self-cleaning abilities. The fabrication of superhydrophobic coatings, designed from sulfur-based polymers and hydrophobic silica (SiO_2) nanoparticle composites, was trialled and reported for the first time, to the best of our knowledge. Coatings were subject to photocatalytic testing (*via* a series of dye degradation tests) and antimicrobial testing (*via* assessment of both solution and surface bacterial attachment/growth), to assess the functional capabilities of coatings. Furthermore, surface wettability studies were carried out to govern the wetting behaviour of materials, upon exposure to high-intensity UV irradiation (254 nm, 8W), to track the UV stability of materials and their susceptibility to photodegradation.

To achieve this, the following objectives were met:

- Establishment of a suitable crosslinker that is capable of generating soluble sulfur copolymers.
- The synthesis of a range of sulfur copolymers that comprise varied weight percentages of elemental sulfur: organic crosslinker.
- Materials characterisation of all sulfur copolymers.
- The fabrication and optimisation of SiO_2-sulfur copolymer systems, to assess the wettability and functionality of materials.
- Performance of dye degradation studies on coatings, under intense UV exposure (254 nm, 8W), to establish whether coatings are photocatalytically active.
- Subject coatings to UV stability testing, *via* prolonged exposure to intense UV irradiation (254 nm, 8W), to probe their susceptibility to UV-induced changes in surface wettability over time.
- Performance of antibacterial studies to determine whether superhydrophobic coatings are more efficient than flat sulfur surfaces.

5.2 Materials and Methods

5.2.1 Materials

Elemental sulfur (S_8, sublimed powder, reagent grade, ≥ 99.5%) was purchased from Brenntag UK & Ireland. Silicon dioxide nanopowder (SiO_2, 10-20 nm), hexamethyldisilazane (HMDS, reagent grade, ≥99%), (S)-(–)-perillyl alcohol (≥ 95%), titanium dioxide (TiO_2, Aeroxide P25, 21 nm), 1H, 1H, 2H, 2H-perfluorooctyltriethoxysilane (FAS, 98 %) and 2-hydroxyethyl cellulose (M_v ~ 90000) were purchased from Sigma Aldrich. Sylgard-184 (Silicone elastomer) was purchased from Ellsworth Adhesive Ltd. Resazurin (sodium salt, pure) was purchased from Acros Organics. Glycerol (99.5%) was purchased from Alfa Aesar. Tetrahydrofuran (THF, 99+ %, extra pure, stabilized with BHT), toluene (99.8+ %), chloroform ($CHCl_3$, 99.8%) and ethanol (analytical reagent grade) were purchased from Fisher Scientific Limited.

5.2.2 Synthesis of Sulfur-Perillyl Alcohol Copolymers

Elemental sulfur was heated to >170℃ in an aluminium heat block, with continuous mechanical stirring (15 g in total, see Table 5.01). Once visibility molten, marked by a change in appearance from a pale yellow powder to a deep yellow/orange liquid, the perillyl alcohol (PER) crosslinker was added, and the solution was left to mechanically stir at 800 rpm until the reaction had almost gone to completion (20-25 minutes). At this point, the liquid had intensified in colour and appeared to be more viscous (deep red, dependent on the amount of crosslinker added). The prepolymer was then transferred into a silicone mould and left to cure in the oven at 140℃ for 18 hours.

Table 5.01: Sulfur-perillyl alcohol polymer mass summary for varying weight percentages:

Wt % Sulfur	*Total mass (g)*	*Mass sulfur (g)*	*Mass perillyl alcohol (g)*
50 (**PER_50**)	15.00	7.50	7.50
60 (**PER_60**)	15.00	9.00	6.00
70 (**PER_70**)	15.00	10.50	4.50
80 (**PER_80**)	15.00	12.00	3.00
90 (**PER_90**)	15.00	13.50	1.50

5.2.3 Hydrophobization of SiO_2 Nanoparticles

This was carried out as described in earlier chapters. See 'Functionalisation with HMDS' in chapter 2, section 2.2.3.1 for the experimental procedure.

5.2.4 Preparation of Superhydrophobic PER-Sulfur-SiO_2 Coatings

PER polymer (PER_50, PER_60, PER_70) was finely ground using a pestle and mortar, and dissolved in chloroform (30 mL) with the aid of mechanical stirring. Once fully dissolved, an intense yellow clear liquid was obtained, to which HMDS-functionalised SiO_2 nanoparticles were added and the suspension was continuously stirred for a further 2 hours before deposition. Following this, the coating was deposited as stated in section 5.2.7, where the deposition was carried out at a moderate temperature of ~ 60℃, to facilitate solvent removal. See Table 5.02 below for formulation details:

Table 5.02: PER-sulfur-SiO_2 formulation summary for varying weight percentages. The example amounts displayed below are for PER_60, however, these are also applicable to PER_50 and PER_70 formulations:

Wt % PER_60	*Wt % SiO_2*	*Total mass (g)*	*Mass SiO_2 nanoparticles (g)*	*Mass PER (g)*
70	30 (**PER_60-30**)	0.50	0.15	0.35
60	40 (**PER_60-40**)	0.50	0.20	0.30
50	50 (**PER_60-50**)	0.50	0.25	0.25
40	60 (**PER_60-60**)	0.50	0.30	0.20
30	70 (**PER_60-70**)	0.50	0.35	0.15
20	80 (**PER_60-80**)	0.50	0.40	0.10
10	90 (**PER_60-90**)	0.50	0.45	0.05

5.2.5 Preparation of SiO_2-PDMS Composite Coating

PDMS (0.2905 g) was dissolved in n-hexane (30 mL), with the aid of mechanical stirring. When visibly dissolved, marked by the formation of a clear, colourless solution, HMDS-functionalised SiO_2 nanoparticles (0.2 g, 15 nm) were added, and the suspension was left to stir for a further three hours. Following this, the coating was deposited as stated in section 5.2.7, where the deposition was carried out at room temperature, and samples were left under ambient conditions for 48 hours to allow time for polymer curing.

5.2.6 Preparation of TiO_2-FAS Composite Coating

TiO_2 nanoparticles (0.23 g, 21 nm) were added to a solution of FAS (0.076 mL) in ethanol (12.5 mL), and left to mechanically stir overnight. Following this, the coating was deposited as stated in section 5.2.7, where the deposition was carried out at room temperature and coatings were left to dry for 15 minutes.

5.2.7 Coating Deposition

A compression pump and airbrush kit was purchased from Voilamart. The spraying nozzle, pressurised by air at 2 bar, was used at a distance of approximately 4 cm away from the substrate surface. Suspensions (described in sections 5.2.4 - 5.2.6, 30 mL) were firstly sonicated, and then spray-coated onto glass substrates (Thermo scientific 76 x 26 mm) in a diagonal motion, periodically across the surface. This was repeated a total of three times for each sample to ensure even coverage.

5.2.8 Materials Characterization

Surface morphologies of coatings were analysed using a scanning electron microscope (SEM, Tescan FIB SEM S8000G) operating at an acceleration voltage of 5-10 kV. Samples were vacuum sputter coated in a thin layer of chromium using a Quorum S150T ES sputter coater, to improve electrical conductivity. Fourier Transform Infrared (FTIR) measurements were taken using a Bruker Optics' Vertex 70 over a range of 500 to 4000 cm^{-1}. UV-Vis absorbance spectra were obtained using a Cary 5000 UV-Vis-NIR Spectrometer in the range of 300-800 nm. Baselines were recorded for solid samples using a coated sample of either PER-60-60, SiO_2-PDMS or TiO_2-FAS, in the absence of any dye solution, and distilled water was used for liquid samples (demountable cuvette). Differential scanning calorimetry (DSC) measurements were performed on a TA instruments discovery series DSC 25, using a heat-cool-heat method with heating and cooling rates of 10 °C/min, from −80 to 150 °C. Powder X-ray diffraction (PXRD) measurements were carried out by **Amy Lunt** (Chong Research Group) at the University of Liverpool. Data was collected in transmission mode on a Panalytical X'Pert PRO MPD equipped with a high throughput screening XYZ stage, X-ray focusing mirror and PIXcel detector, using Cu Kα radiation. Data was recorded using loose powder samples held on thin Mylar film in aluminium well plates, over the range 4-40° in ~0.013° steps over 60 minutes.

5.2.9 Contact Angle Measurements

Static contact angle measurements were taken using a DSA100 Expert Drop Shape Analyser (Kruss GmbH) in the sessile drop operating mode with Young-Laplace fitting and manual assignment of the baseline. 6 μL water droplets were dispensed from a Hamilton microliter syringe with a 30 gauge dispensing tip directly onto the surface and at least 5 contact angle measurements, from evenly distributed positions across the surface, were taken and averaged for every reported contact angle. Tilting angles were recorded manually by dispensing a water droplet on the surface and tilting the surface at 2°/s, recording the angle at which the droplet began to roll. At least 5 measurements, from evenly distributed positions across the surface, were taken and averaged for every reported tilting angle. For powders that were pellet pressed, 5 measurements were taken from 5 separate pellets.

5.2.10 Pellet Pressing of Powders

A small mass of powder was inserted into a hydraulic press, under a pressure of 2 tons for approximately 30 seconds, before obtaining a 7 mm diameter pellet.

5.2.11 Solubility Studies

PER polymers (100 mg, PER_50, PER_60, PER_70, PER_80 and PER_90) were weighed out in triplicate, into pre-weighed vials. See Table A1 in section 2.5 for details regarding weights. Chloroform, tetrahydrofuran and toluene (5 mL) were added to a sample of each copolymer, and the polymer was sonicated to ensure complete dissolution, before being left to stir under ambient conditions for 2 hours. Following this, the solution was pipetted through a filter into a new pre-weighed vial and left under ambient conditions in the fume hood for 48 hours to allow for solvent evaporation. Before weighing, the vials were heated in the over for a further 2 hours (above the boiling point of each solvent), to ensure complete solvent removal. The mass of the polymer and vial was weighed and subtracted from the initial vial mass, allowing for the weight percentage of recovered polymer to be determined. Any loss of soluble material within the filter was negligible and all samples were carried out in triplicate.

5.2.12 Dye Degradation Studies

5.2.12.1 Formulating Intelligent Ink

Intelligent ink was formulated as reported by Mills *et al*., using a reduced concentration of dye.[25] Briefly, an aqueous solution of hydroxyethyl cellulose (3 g, 1.5 wt %), glycerol (0.3 g) and resazurin dye (Rz) were mixed in a vial to give a deep blue solution. In order to ensure the spreading of the dye solution across the surface, ethanol was added to the formulated solution. Due to differences in surface hydrophobicity, PER-60-60 and SiO_2-PDMS/TiO_2-FAS samples required individually tailored dye formulations, to tune surface tension and induce spreading across the coated surface. However, the concentration of dye remained constant (0.238 mg/mL). PER_60-60 dye contained 1 mg Rz per 1 mL ethanol, and SiO_2-PDMS/TiO_2-FAS dye contained 1.7 mg Rz per 4 mL ethanol, with other formulation components remaining constant.

5.2.12.2 UV Lamp Set-up

Samples were positioned within a container, on top of which the UV lamp was situated (6.8 cm above coated slides), where it could emit radiation to the samples *via* a rectangular cut out in the container, sized to fit the parameters of the lamp (20 x 5 cm). The Spectroline ENF-280c UV lamp was used with an emitted light of 254 nm wavelength (8W power).

5.2.12.3 Testing using Intelligent Ink

Intelligent ink was deposited onto the surface of the coated sample (0.5 mL), and was then placed in an oven at 60℃ for 5 minutes to remove any excess water and prevent the movement of dye solution. The sample was placed under the UV lamp (λ - 254 nm) and irradiated for a stated period of time, following which the coated sample was attached vertically to the sample holder (ensuring the dye was placed within the exposure window), to record absorbance spectra. This was repeated during stated time intervals (dependent on the sample) to track the redox behaviour/degradation of the dye, marked by a colour change from blue to pink. Coated samples in the absence of any dye solution, were used to measure the baseline and all testing was carried out in triplicate.

5.2.12.4 Testing using Resazurin Dye

An aqueous solution of Rz dye was formulated (1 mg in 20 mL distilled water), in the absence of hydroxyethyl cellulose and glycerol. Four droplets (per measurement, total 80 μL) were placed on the surface of the coated sample using a calibrated pipette, following which the sample was exposed to UV radiation (245 nm) for a stated period of time. After the stated exposure period, a pipette was used to withdraw the droplets from the surface and dispense them into a quartz demountable cuvette (0.5 mm path length). The demountable cuvette was then positioned within the sample holder, so that absorbance spectra could be recorded. This was repeated during stated time intervals (dependent on the sample) to track the redox behaviour/degradation of the dye, marked by a colour change from blue to pink. Distilled water was used to measure the baseline and all testing was carried out in triplicate.

5.2.13 Antibacterial Studies

5.2.13.1 Bacteria Preparation, Storage and Enumeration

All antibacterial preparation, testing and analysis were carried out by **Romy Dop** (Hasell Research Group) at the University of Liverpool. Glycerol stocks of *Staphylococcus aureus* (*S. aureus*) strain USA300 were stored at -80℃ for long term storage. For experimental use, frozen glycerol stocks of *S. aureus* were defrosted and spread onto lysogeny broth (LB) agar plates that were incubated overnight and stored at 5℃. Bacterial cultures were prepared by swabbing one colony into 10 ml LB broth followed by overnight incubation at 37℃. Colony-forming units (CFU) were enumerated by serially diluting the cultures in phosphate-buffered saline (PBS) onto LB agar, using the Miles and Misra method.[26,27] CFU/cm^2 and CFU/ml were calculated using the following equation:

$$\boldsymbol{CFU} = [(\text{no. of colonies} \times \text{dilution factor}) / (\text{volume of culture plate})]$$

5.2.13.2 Viable Cell Enumeration Assay

S. aureus USA300 was used to evaluate the antibacterial efficiency of the materials cut into 1 x 1 cm^2 squares, using uncoated glass as a negative control. 1 cm^2 samples were placed in separate wells of a 24-well plate. Overnight cultured bacteria prepared in LB broth were diluted to 10^5 CFU/mL (OD600 = 0.001). Diluted bacterial solution (0.5 mL) was added to each sample in the 24-well plate and allowed to incubate statically for 5 h at 37℃. After

incubation, the bacterial solution surrounding each sample was removed and the viable cells in solution were enumerated after serial dilution of the solution in PBS onto LB agar, using the Miles and Misra method (20 μL in 180 μL PBS for each dilution). To enumerate the cells adhered to the sample surfaces, the samples were gently rinsed with 1 mL of PBS to remove any planktonic cells and were vortexed in 1 mL of LB broth for 10 s to remove any adhered cells. The vortexed solution was serially diluted in PBS and the viable cells associated with the sample surface were enumerated using the Miles and Misra method on LB agar, as above. All samples were tested in technical triplicate.

5.3 Results and Discussion

5.3.1 Synthesis of Inverse Vulcanised Sulfur Copolymers

5.3.1.1 Crosslinker Selection

Generally, superhydrophobic materials that can be applied *via* conventional and convenient deposition techniques i.e., spray coating or dip-coating, require components to be stably suspended or fully solvated, as seen throughout this thesis so far. Although sulfur appears to display great potential as a component for superhydrophobic materials design, as discussed throughout section 5.1, it is extremely difficult to process in its elemental form due to its limited solubility in common solvents (see Fig. 5.03). Typically, the formation of a cross-linked material promotes insolubility, as the introduction of physical crosslinking points make dissolution increasingly difficult. However, in this case, it has been shown that crosslinkers can be used to generate sulfur copolymers with varying degrees of solubility.[28] To enhance the processability of elemental sulfur, an organic crosslinker was introduced and a series of sulfur copolymers were synthesised, *via* a process termed inverse vulcanisation (refer to section 5.1.1). This is a straightforward process and requires an elevated temperature of ≥ 159℃ to initiate ring-opening polymerisation of the S_8 monomer. Diradical sulfur monomers are then formed, and can go on to react with small unsaturated organic molecules, resulting in a 'crosslinked' polymer network (refer back to Fig. 5.02).

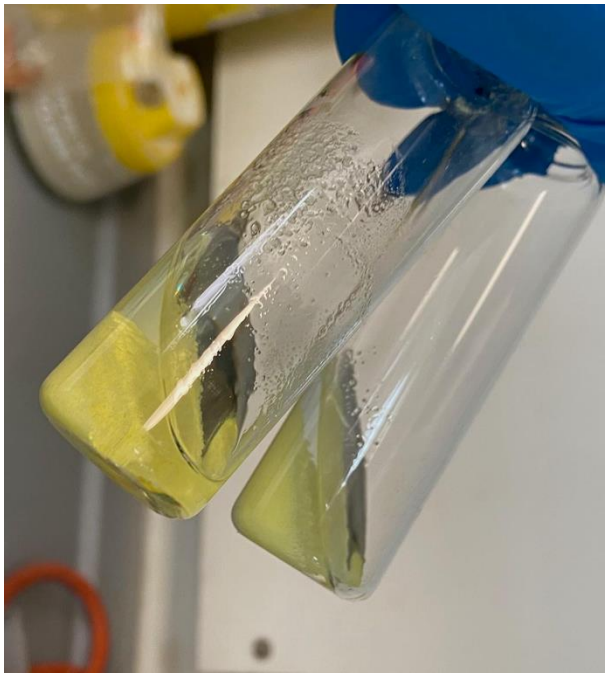

Figure 5.03: Image highlighting the limited solubility of elemental sulfur in toluene (**left**) and chloroform (**right**) at 80℃.

Limonene – a naturally derived crosslinker – has recently received much attention in the field of sulfur polymers, where it was reported by Smith *et al*. to form a low molecular weight polysulfide with an inherently low glass transition temperature (T_g, -21℃ for 50 wt % sulfur polymer).[29] The glass transition temperature is a particularly useful technique, commonly used to characterise sulfur copolymers, as it can be employed to determine the temperature at which amorphous materials transition from a glassy/brittle state into a rubbery or viscous state.[30] Here, a low T_g value is indicative of a polymer that may have weaker intermolecular interactions/lower degree of crosslinking, and thus, can undergo this transition at lower temperatures. Subsequently, signifying that a linear or hyperbranched polymer may have been formed (rather than a heavily crosslinked polymer), therefore, increasing the probability of solubility. However, if the T_g value is too low, it may not be suitable for application use, as it may lack structural integrity. Perillyl alcohol (PER), an alternative bioderived crosslinker and metabolite of limonene (similar chemical structure, see Fig. 5.04), was selected for this work, as it was reported by Parker *et al*. to form sulfur copolymers that displayed high solubility in a number of solvents and thermoplastic behaviour (e.g. the ability to be re-processed/recycled).[31] It is likely PER-sulfur copolymers take on a similar polymeric structure to limonene-sulfur copolymers, yet have been shown to generate materials with more moderate T_g values (20℃ for 50 wt % sulfur polymer).[31] Hence, providing additional structure to the polymer at room temperature, without suggesting the formation of a heavily crosslinked network.

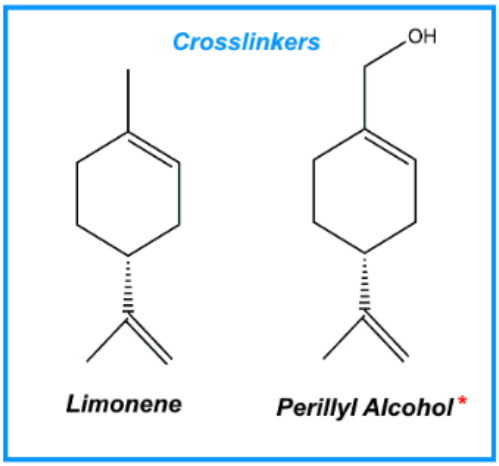

Figure 5.04: Chemical structures of crosslinkers limonene and perillyl alcohol. *Perillyl alcohol was used as the crosslinker within this work and limonene is displayed for comparative purposes only.

5.3.1.2 Materials Characterization

To probe the stability of different copolymers, based on their sulfur content, an array of sulfur-PER polymers were fabricated and examined, which spanned the range of 50-90 wt%

elemental sulfur (termed PER_50, PER_60, PER_70, PER_80 and PER_90). The process of crosslinking was marked visibly by a deepening ruby red colour, in line with an increasing weight percentage of PER crosslinker, as seen in Figure 5.05 and Figure 5.06b. This change in physical appearance from pale yellow to ruby red is further highlighted in the UV-Vis absorbance spectra, displayed in Figure 5.07. It can be seen in Figure 5.07a that elemental sulfur absorbs lower wavelength of light than PER_60 (see Figure 5.07b), with the absorption edge shifting to a higher wavelength for PER_60, subsequently verifying the observed change in physical appearance.

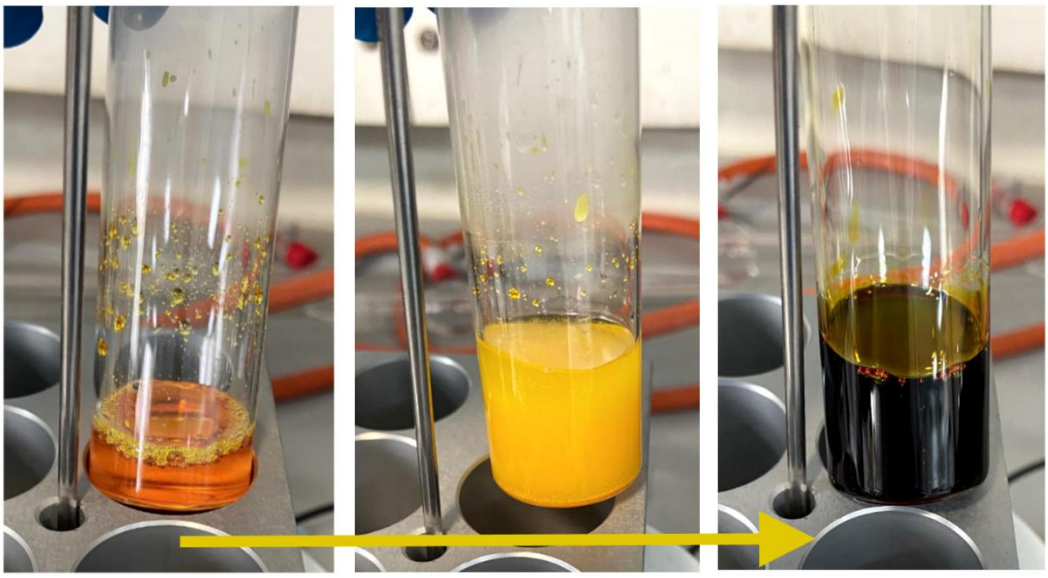

Figure 5.05: Images highlighting the visual changes that occurred when synthesising PER_60, *via* inverse vulcanisation at >170℃. Initially, the formation of molten sulfur resulted in an orange/yellow solution (**left**), which turned cloudy yellow after the addition of PER crosslinker (**middle**), before finally reaching a deep ruby red, viscous liquid (**right**).

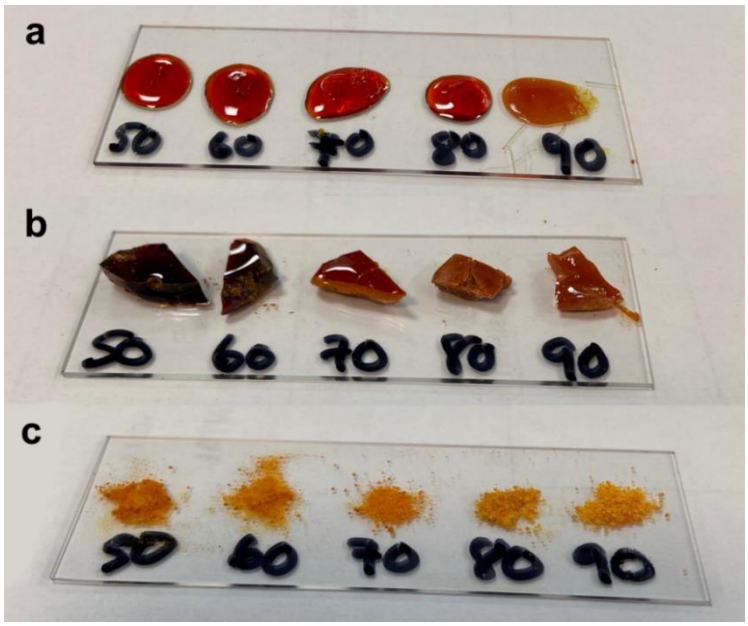

Figure 5.06: Images showing the visual appearance of PER-sulfur polymers (50-90 wt % sulfur); (**a**) after melting at >170℃, (**b**) after reaching ambient temperature, and (**c**) after being finely ground with a pestle and mortar.

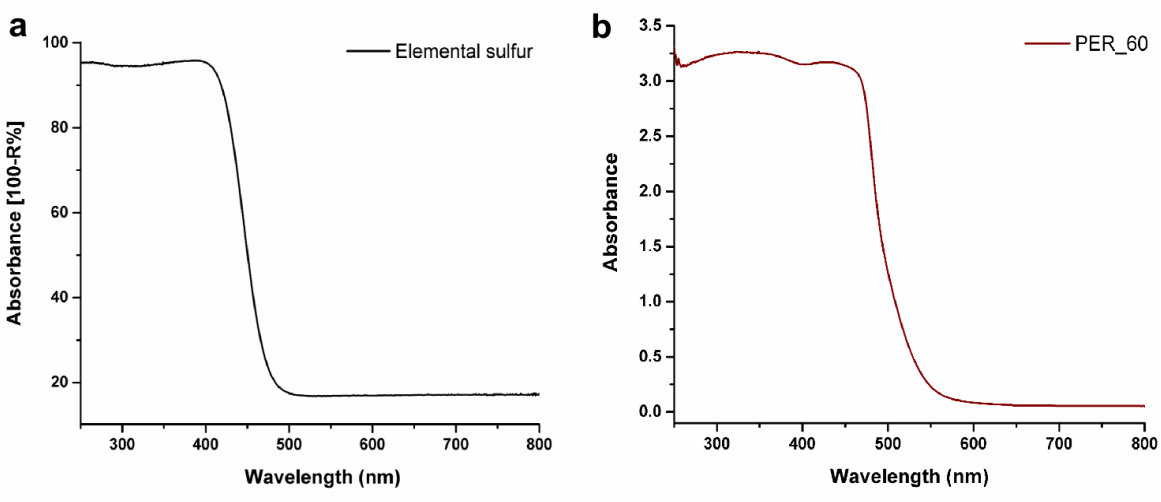

Figure 5.07: UV-Vis absorption spectra of; (**a**) elemental sulfur – obtained by subtracting the diffuse reflectance spectrum [100 – R%] – and (**b**) PER_60 polymer.

Fourier-transform infrared spectroscopy (FTIR) was used to detect physical crosslinking within the polymer matrix, between polysulfide chains and organic PER molecules (see Fig. 5.08). It can be seen from Figure 5.08 that signals representative of C=C-H stretching (3082 cm^{-1}) and C=C stretching (1643 cm^{-1}), present in the spectrum of pure PER, were significantly reduced in all spectra of the copolymers. Subsequently, this indicates a reduction in unsaturated hydrocarbons, confirming that crosslinking had taken place and resulted in the formation of C-S bonds. The newly formed C-S bonds could be identified by the appearance of a signal at 704 cm^{-1}, that was not present in the pure PER spectrum, but could be observed in the spectra of all copolymers. Peak intensity was seen to decrease for copolymers that comprised the highest sulfur content (PER_80 and PER_90), which was anticipated as the weight percentage of crosslinker, and therefore, the number of unsaturated hydrocarbons available for crosslinking had decreased.

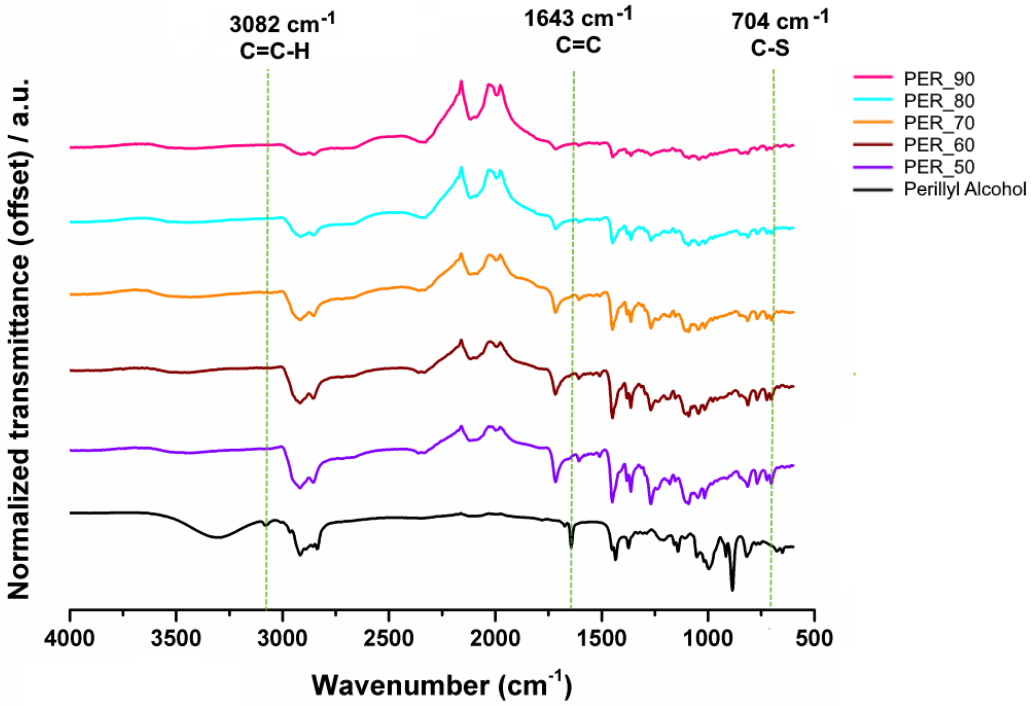

Figure 5.08: Stacked FTIR spectra of PER-sulfur polymers (50-90 wt % sulfur), where peaks that are suggestive of inverse vulcanisation are highlighted; reduction in C=C-H (3082 cm^{-1}), reduction in C=C (1643 cm^{-1}) and presence of C-S (704 cm^{-1}).

Materials were further characterised using differential calorimetry (DSC) and powder x-ray diffraction (PXRD). DSC can be used to track the thermal transitions of a polymer with both amorphous and crystalline domains, and hence, can be used here to identify whether sulfur copolymers are stable and fully crosslinked, or whether crystalline sulfur is still traceable. As seen in Figure 5.09, no peak representative of crystalline sulfur (~105-115℃) was detectable in PER_50, PER_60 and PER_70. Subsequently, indicating that at these mass ratios, PER molecules had homogenously reacted with elemental sulfur to form stable polymers. However, when increasing the sulfur content further (PER_80 and PER_90), a peak that can be attributed to the melting transition of crystalline sulfur (~105-115℃) was seen to appear and intensify. Therefore, highlighting that PER_80 and PER_90 polymers were not stable, likely due to the low weight percentage of crosslinker used, and that crystalline sulfur was leaching from the resultant polymer (depolymerisation). In line with this, T_g values were seen to decrease as the weight percentage of elemental sulfur was increased (see Table 5.03); PER_50 was found to have a T_g value of 26℃, while PER_90 displayed a T_g value of -25℃, indicating that polymers with a higher PER content appeared to be more resistant to changes

in physical state. Thus, suggesting the formation of polymers with stronger intermolecular interactions/higher degree of crosslinking.

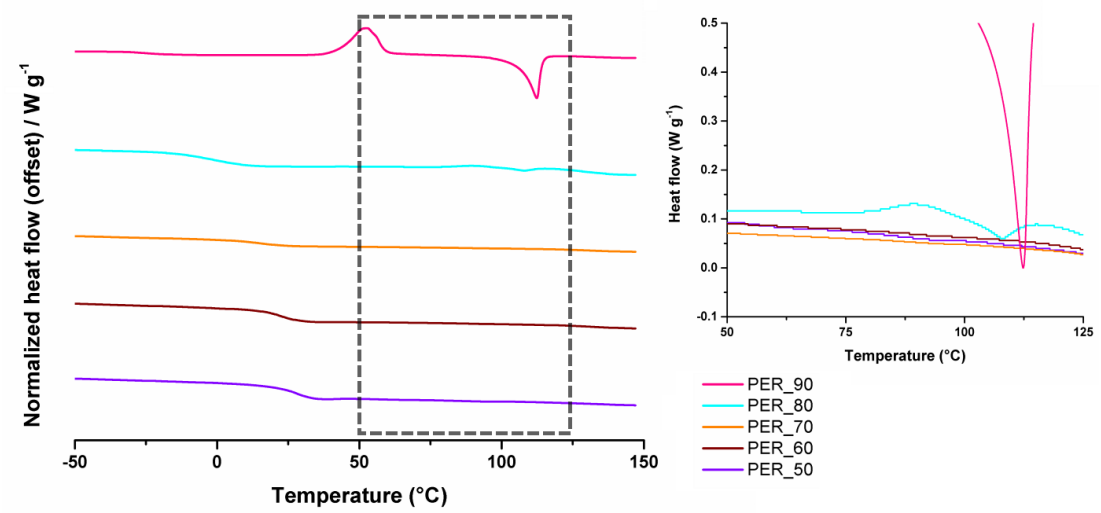

Figure 5.09: Stacked DSC curves of PER-sulfur polymers (50-90 wt % sulfur). Inset; magnified region (50-125℃) of overlaid curves to better highlight peaks that are indicative of elemental sulfur (melting of crystalline sulfur) at ~ 105-115℃ for PER_80 and PER_90 polymers.

Table 5.03: Measured glass transition temperatures of PER-sulfur polymers (50-90 wt % sulfur, calculated from DSC curves):

PER-sulfur polymer	*Glass transition temperature (T_g)*
PER_50	26℃
PER_60	22℃
PER_70	15℃
PER_80	-1℃
PER_90	-25℃

Complementary to DSC data, PXRD was employed as a tool to detect crystalline sulfur within polymers, where measurements were taken by Amy Lunt (Chong Research Group). The same trend was observed here, where PER_50, PER_60 and PER_70 were found to be amorphous with no distinct crystalline peaks (see Fig. 5.10). However, signs of crystallinity were observed for PER_80 and PER_90, reiterating that crystalline sulfur was present, and that these polymers had undergone depolymerisation. It was anticipated that sulfur leached from within the polymer was no longer the stable α-polymorph, but the γ-polymorph, marked by a change

in peak pattern, and suggested to be due to the slow cooling of unstable sulfur within the polymer matrix (PER_80/PER_90 *vs* α-sulfur in Fig. 5.10).[31,32]

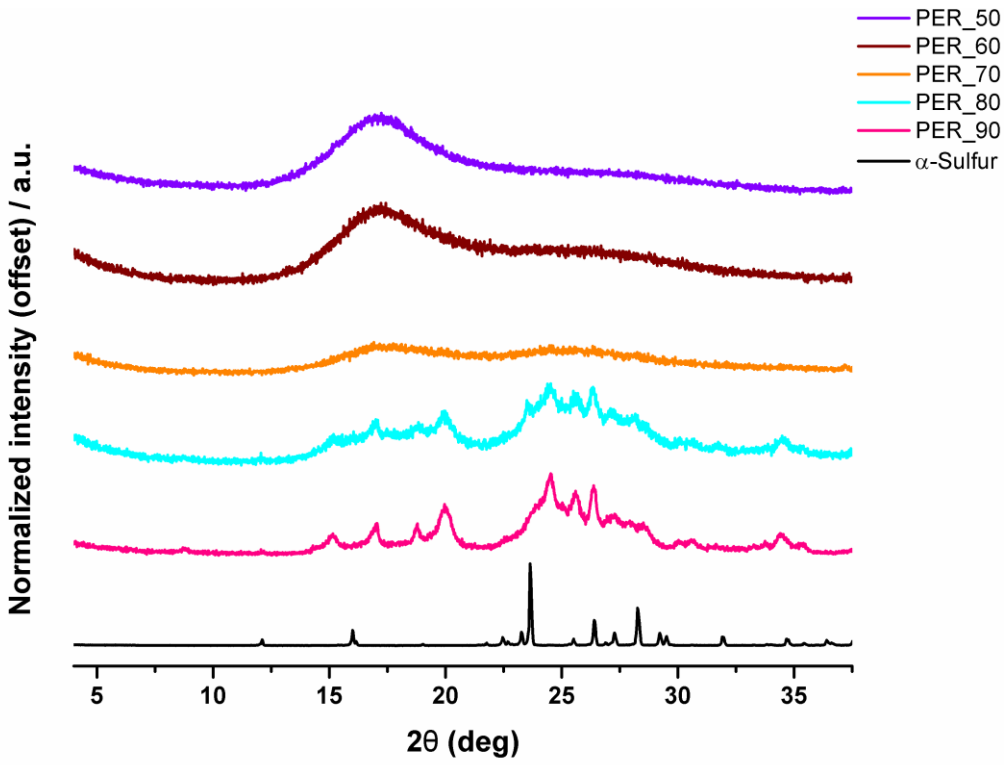

Figure 5.10: Stacked PXRD patterns of PER-sulfur polymers (50-90 wt % sulfur) and elemental sulfur.

The wettability of each material was examined, where flat surfaces were used to avoid any intensification in contact angle, as a result of surface roughness. Smooth surfaces were achieved by melting a thin layer of sulfur/polymer onto a glass slide, or pellet pressing loose material, in the case of powdered sulfur (see experimental section 5.2.10, made for comparative purposes). The resultant static contact angles and dynamic tilting angles are presented as follows in Table 5.04:

Table 5.04: Recorded static contact angles and tilting angles of smooth PER-sulfur polymers:

PER-sulfur polymer	*Recorded static contact angle*	*Recorded tilting angle*
Sulfur (pellet)	105° ± 2	>90°
Sulfur (melted)	98 ° ± 3	>90°
PER_50	76° ± 4	>90°
PER_60	80° ± 3	>90°
PER_70	78° ± 3	>90°
PER_80	76° ± 7	>90°
PER_90	82° ± 6	>90°

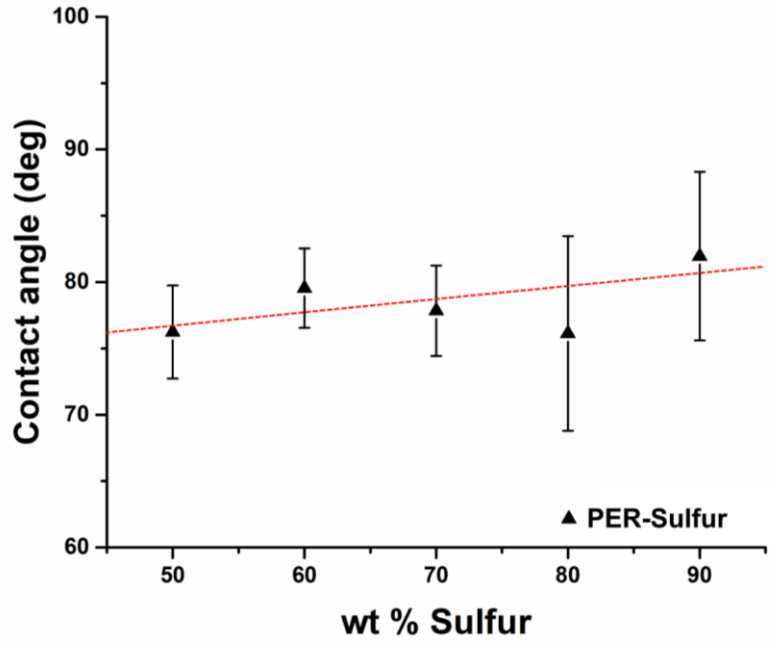

Figure 5.11: Plotted static contact angles for PER-sulfur polymers with different weight percentages of elemental sulfur (50-90 wt % sulfur).

In line with the literature, α-sulfur was found to be hydrophobic, displaying a contact angle of 105° ± 2 for the pressed pellet sample, and a slightly lower contact angle of 98 ° ± 3 for the smooth sulfur surface (difference due to unavoidable surface roughness of pellet pressed surface). On the other hand, PER-sulfur copolymers exhibited collectively lower contact angles, showing a slight trend between increasing weight percent of sulfur and enhanced hydrophobicity (see Fig. 5.11). However, this cannot be said definitively, as the range of recorded static contacts for PER-sulfur polymers was very small, and values did not deviate significantly (76-82°). Although the chemical structure of PER primarily comprises

hydrocarbons, it also contains a terminal hydroxyl group. Hence, this likely contributed towards the overall decrease in contact angle for all sulfur copolymers, due to the introduction of polar groups. Furthermore, tilting angles were determined to be >90° in all cases, signifying that water droplets were fully adhered to the surface, exhibiting a Wenzel wetting state. This was unsurprising due to the intrinsic wettability of copolymers, and lack of surface roughness. However, it was anticipated that superhydrophobicity and a stable Cassie-Baxter wetting state could be attained if surface roughness was induced, due to polymers being situated on the border between hydrophilic (<90°) and hydrophobic (>90°).

5.3.1.3 Solubility Studies

To enable the formation of SPNC formulations, it was imperative that a suitable solvent, capable of fully solvating PER-sulfur polymers, was identified. With aid of the current literature, the selection of common solvents was narrowed down to chloroform, toluene and tetrahydrofuran (THF). Samples comprising 100 mg copolymer/5 mL solvent were made up, and solubility testing was carried out, as stated in section 5.2.11. Briefly, polymers were initially sonicated to encourage dissolution, before being mechanically stirred under ambient conditions for a further two hours. Following this, samples were filtered, left to stand in the fume hood for 48 hours, and then heated for the further two hours to ensure complete solvent removal and recovery of the soluble fraction of material.

Table 5.05: Averaged solubility testing results of PER-sulfur polymers (100 mg/5 mL solvent), carried out as described in section 5.2.11:

PER-sulfur polymer	*Solvent*	*Recovered polymer (%)*
PER_50	Chloroform	97 ± 3
PER_60	Chloroform	96 ± 3
PER_70	Chloroform	96 ± 3
PER_80	Chloroform	86 ± 5
PER_90	Chloroform	77 ± 3
PER_50	Toluene	97 ± 3
PER_60	Toluene	85 ± 2
PER_70	Toluene	75 ± 4
PER_80	Toluene	61 ± 1
PER_90	Toluene	72 ± 2
PER_50	THF	94 ± 4
PER_60	THF	95 ± 3
PER_70	THF	92 ± 5
PER_80	THF	88 ± 5
PER_90	THF	70 ± 5

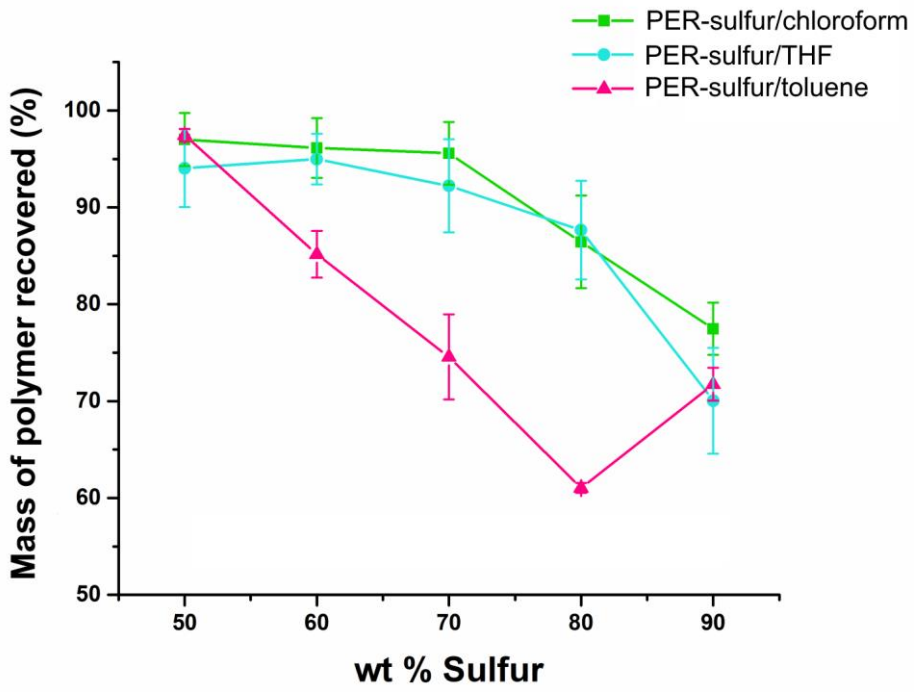

Figure 5.12: Solubility testing results for all PER-sulfur polymers (100 mg/5 mL, PER_50, PER_60, PER_70, PER_80 and PER_90) in chloroform, toluene and THF.

It can be seen from Table 5.05 and Figure 5.12 that chloroform was the most successful solvent, demonstrating the highest mass percentages of recovered polymer across the range of copolymers examined; 97 % ± 3 polymer for PER_50, 96 % ± 3 for PER_60, 96 % ± 3 for PER_70, 86 % ± 5 for PER_80 and 77 % ± 3 for PER_90. Polymer recovery was collectively lower for other trialled solvents, toluene and THF. However, the same general trend was apparent across all tested solvents, whereby the solubility of the copolymer decreased, in line with increasing sulfur content. In particular, PER_80 and PER_90 displayed low solubility, which suggests that either (**i**) these polymers underwent extensive crosslinking, leading to the synthesise of a higher molecular weight polymer, that was consequently more difficult to solubilise, or (**ii**) high sulfur content polymers are inherently more unstable, and sulfur may have leached out of the polymer due to depolymerisation (elemental sulfur is insoluble in common organic solvents, as seen in section 5.3.1). It is more likely that the latter has taken place, as peaks that were representative of crystalline sulfur were apparent in DSC traces and PXRD patterns for PER_80 and PER_90. Furthermore, the T_g values of these polymers were reduced compared to PER_50, PER_60 and PER_70, indicative of weaker intermolecular interactions/lower degree of crosslinking.

Nonetheless, PER_50, PER_60 and PER_70 polymers were found to be soluble, and could therefore, be implemented in SPNC systems. It was suggested by Parker *et al*. that the surprising solubility of PER copolymers may be attributed to hydrogen abstraction, which subsequently leads to dehydrogenation of the cyclic system within PER monomers (refer back to Fig. 5.04 for crosslinker chemical structure).[31] This would then form an aromatic derivative, preventing crosslinking from taking place, and increasing the chance of synthesising a more linear or hyperbranched polymer – which may explain the susceptibility of copolymers to dissolution.

5.3.2 Introducing Superhydrophobicity

5.3.2.1 Fabrication

Similar to chapters 2 and 4, the introduction of inorganic metal oxide nanoparticles was primarily to induce surface texturing, as this is a fundamental requirement to achieve surface superhydrophobicity. Therefore, silica nanoparticles (SiO_2, 15 nm) were utilized as they can be easily functionalised to ensure surface hydrophobicity and are not activated by UV irradiation (see chapter 2 for analysis of HMDS-functionalised SiO_2). PER-sulfur polymers were initially dissolved in chloroform, followed by the addition of HMDS-functionalised SiO_2 nanoparticles, to generate formulations that could later be applied to substrates *via* spray-

coating, at a moderate temperature of 60℃ (quick exposure to speed up solvent removal). Due to issues related to the solubility and stability of high sulfur content polymers i.e., PER_80 and PER_90 (see sections 5.3.1.2 and 5.3.1.3), it was decided that these would not be suitable for superhydrophobic materials fabrication, and so coatings were fabricated using PER_50, PER_60 and PER_70 polymers, only. As seen in previous experimental chapters (chapters 2-4), it is often crucial that the optimal theoretical polymer thickness ($\mathbf{r}_{poly}$) and polymer:nanoparticle ratio is determined, to generate materials with high performance properties. However, in this case, examination of $\mathbf{r}_{poly}$ values was more difficult, due to the formation of copolymers with no established density values. Although not as precise, the weight percentage of SiO_2 nanoparticles in the system was varied as a method of optimising coatings for proof of principal work; an array of formulations were made up, comprising 30-90 wt % SiO_2, to unveil optimal formulation compositions through morphological assessment, and static and dynamic wettability measurements (see Fig. 5.13).

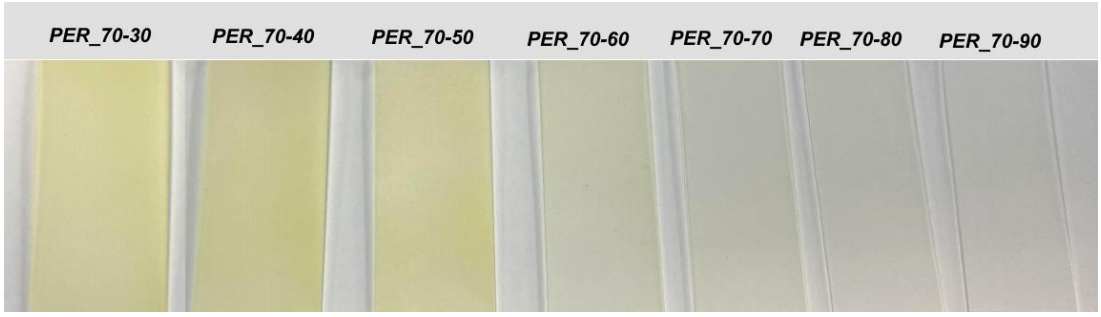

Figure 5.13: Images showing the physical appearance of PER_70-SiO_2 coatings when the weight percentage of SiO_2 was increased from 30 wt % (PER_70-30) to 90 wt % (PER_70-90).

5.3.2.2 Morphology

SEM microscopy was used to assess the morphology of PER-sulfur-SiO_2 composite coatings, where a difference in surface morphology was detected for coatings that comprised different copolymers, in addition to coatings with varying SiO_2 weight percentages. Across all coatings, SiO_2 nanoparticles were seen to provide a roughened surface architecture, of which the extent of surface roughness varied, dependent on the weight percentage of SiO_2 as seen in Figure 5.14.

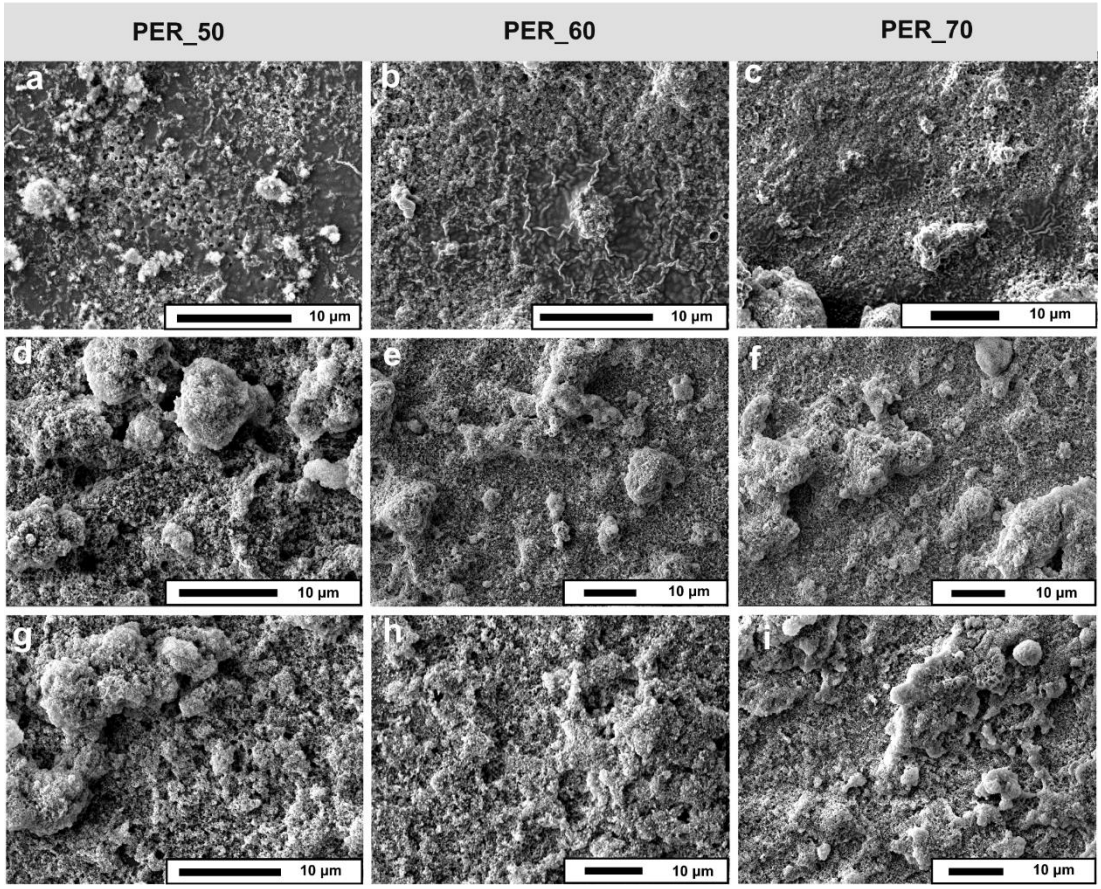

Figure 5.14: Top-down SEM micrographs showing the morphology of (**a**) PER_50-30, (**b**) PER_60-30, (**c**) PER_70-30, (**d**) PER_50-60, (**e**) PER_60-60, (**f**) PER_70-60, (**g**) PER_50-90, (**h**) PER_60-90 and (**i**) PER_70-90. Scale bars are shown.

Formulations with lower SiO_2 nanoparticle loadings all displayed dense polymer regions, where surface roughness was heavily compromised, particularly in coatings that comprised 30 wt % SiO_2 (PER_50-30, PER_60-30 and PER_70-30). PER_60-30 and PER_70-30 appeared to display a more homogenous morphology, despite exhibiting an excess of polymer in parts, as the majority of SiO_2 aggregates appeared to be visually coated with polymer. PER_50-30, on the other hand, seemed to undergo some order of phase separation, as aggregates that had a visually different texture could be frequently identified throughout the coating ('fluffy', brighter regions due to lack of polymer coating, see red highlighted regions in Fig. 5.15a/b). This is likely related to crosslinker loading, as PER_50-30 comprised the greatest overall mass of crosslinker within any formulation, leading to a more significant difference in interfacial tensions/energies between formulation components. Surface uniformity, in terms of the adhesive interaction between polymer and particles, generally appeared to improve as the SiO_2 loading was increased, with coatings >50 wt % SiO_2 displaying no visible flattened polymer regions or obvious polymer-particle separation across all copolymers (see Fig. 5.15c/d for PER_50 example).

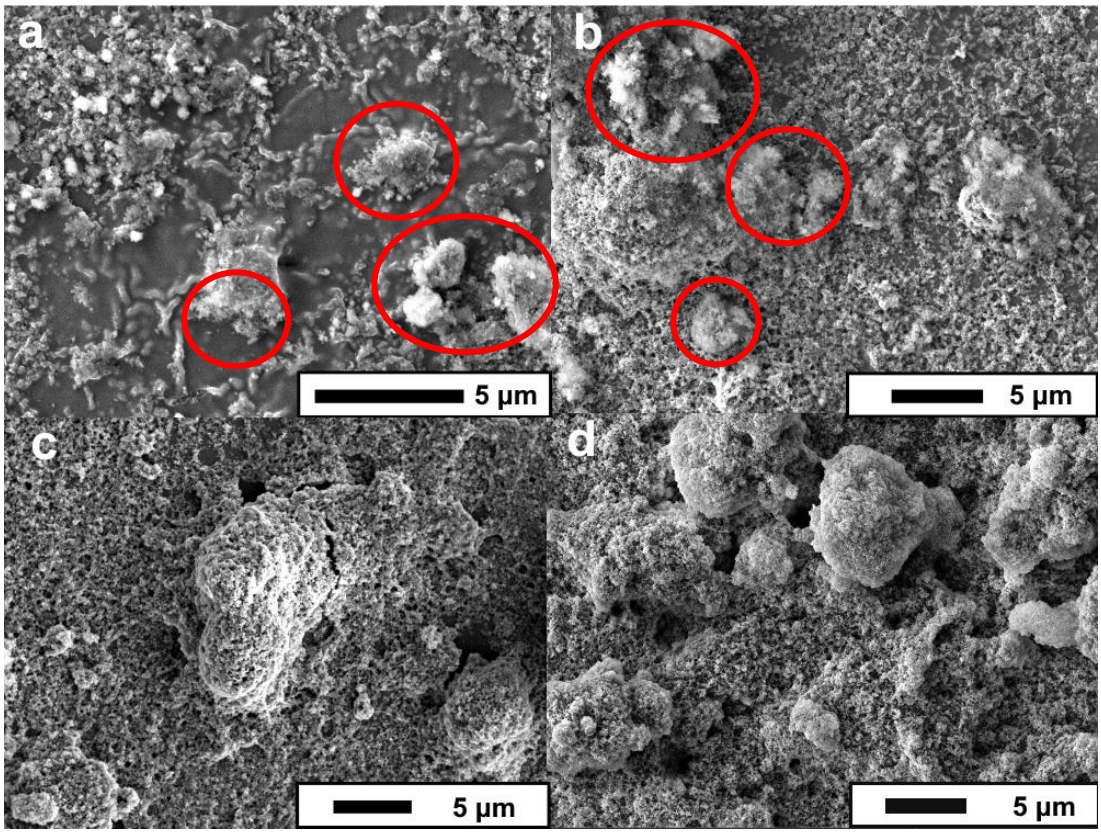

Figure 5.15: Top-down SEM micrographs highlighting the change in surface morphology of PER_50-SiO_2 coatings, when the weight percentage of SiO_2 nanoparticles was increased from 30 wt % to 60 wt %; (**a**) PER_50-30, (**b**) PER_50-40, (**c**) PER_50-50 and (**d**) PER_50-60. Scale bars are shown. Red highlighted regions indicate areas where aggregates of uncoated SiO_2 nanoparticles likely resided.

Interestingly, elemental sulfur appeared to be present in all surface coatings that were fabricated from PER_70. This indicated that although PER_70 appeared to be initially stable (confirmed *via* DSC, PXRD and solubility testing), the sulfur content may have been too high to endure re-processing of the material, which subsequently, had led to the precipitation of crystalline sulfur particles. Generally, the presence of elemental sulfur throughout the surface of coatings was seen to decrease, as the weight percentage of PER_70 was decreased; small sulfur particles were abundantly present in coatings that comprised ≤50 wt % SiO_2, and larger sulfur fragments could be seen, extremely sparsely, on the surface of coatings with ≥60 wt % SiO_2 (see Fig. 5.16). Elemental sulfur could not be identified in coatings fabricated from PER_50 and PER_60 copolymers, suggesting that these polymers were stable and depolymerisation did not readily occur during the re-processing of the materials.

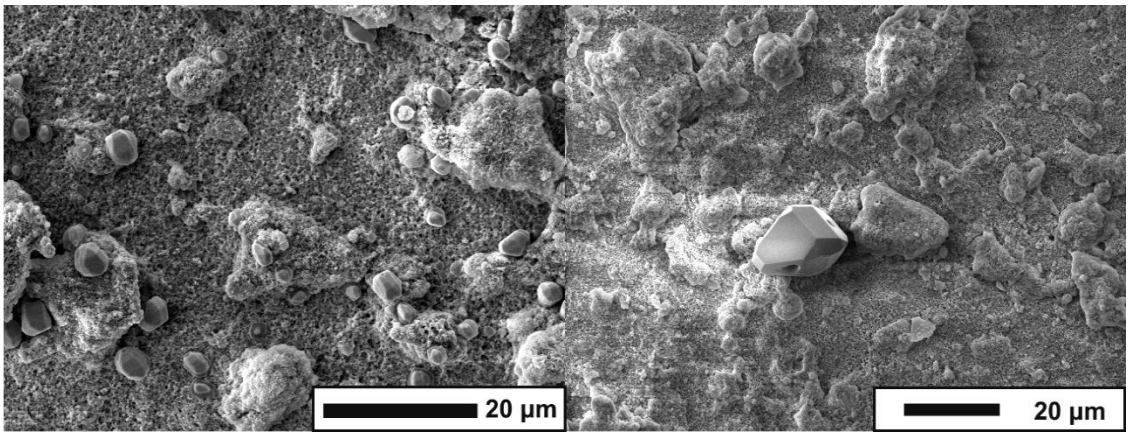

Figure 5.16: Top-down SEM micrographs of PER_70-40 (**left**) and PER_70-70 (**right**), highlighting the size/distribution of elemental sulfur particles that had leached from the polymer during re-processing. Scale bars are shown.

5.3.2.3 Surface Wettability

Static and dynamic wettability measurements were conducted to probe any trends in surface hydrophobicity between different PER-sulfur-SiO_2 systems. It is apparent from Figure 5.17 that two extremes exist within the range of formulations trialled; at low SiO_2 weight percentages, the surface predominantly consists of polymer. Therefore, two contributing factors likely result in the comparatively low static contact angles and high tilting angles that were observed (Wenzel wetting) i.e., reduced surface roughness due to the presence of excess polymer (confirmed *via* SEM imaging), and increased surface polarity, as a result of the chemical structure of the crosslinker. This is similar to the work reported in previous experimental chapters (chapters 2-4), in particular chapter 4, where unfunctionalised carbon nanofibers were introduced into coatings. However, as the crosslinker is homogenously positioned throughout the entire external coating, it is anticipated that this would have more of a profound effect on surface hydrophobicity.

As the weight percentage of SiO_2 was increased to ≥50 wt %, coatings increasingly displayed Cassie-Baxter wetting behaviour, as the surface interaction with water became progressively limited. This was marked by a decrease in tilting angle to ~ 5-6° for coatings that comprised 90 wt % SiO_2 (see Table 5.06 and Fig. 5.17). An enhancement in the mass of nanomaterial subsequently heightened hierarchical surface roughness, and therefore, the ability to trap air within the porosity of the surface and generate a substantial liquid-vapour interfacial area. Furthermore, increasing the sulfur content of coatings generally resulted in higher static contact angles i.e., PER_70 > PER_60 > PER_50. As the static contact angles, and hence, the inherent wettability of flat PER polymers were previously determined to be fairly consistent

(see section 5.3.1.2), it is anticipated that PER_70 composites resulted in greater hydrophobicity due to the presence of sulfur particles. It was suspected that elemental sulfur had leached from the polymer during reprocessing, acting to somewhat enhance hierarchical surface roughness.

Table 5.06: Recorded static contact angles and tilting angles of low, mid and high SiO_2 content PER-sulfur-SiO_2 coatings (30, 60 and 90 wt % SiO_2):

PER-sulfur-SiO_2 coating	*Recorded static contact angle*	*Recorded tilting angle*
PER_50-30	116° ± 8	>90°
PER_60-30	117° ± 6	>90°
PER_70-30	120 ° ± 7	>90°
PER_50-60	162° ± 2	10° ± 2
PER_60-60	166° ± 2	9° ± 2
PER_70-60	167° ± 2	14° ± 4
PER_50-90	168° ± 2	8° ± 3
PER_60-90	168° ± 1	6° ± 1
PER_70-90	169° ± 1	6° ± 3

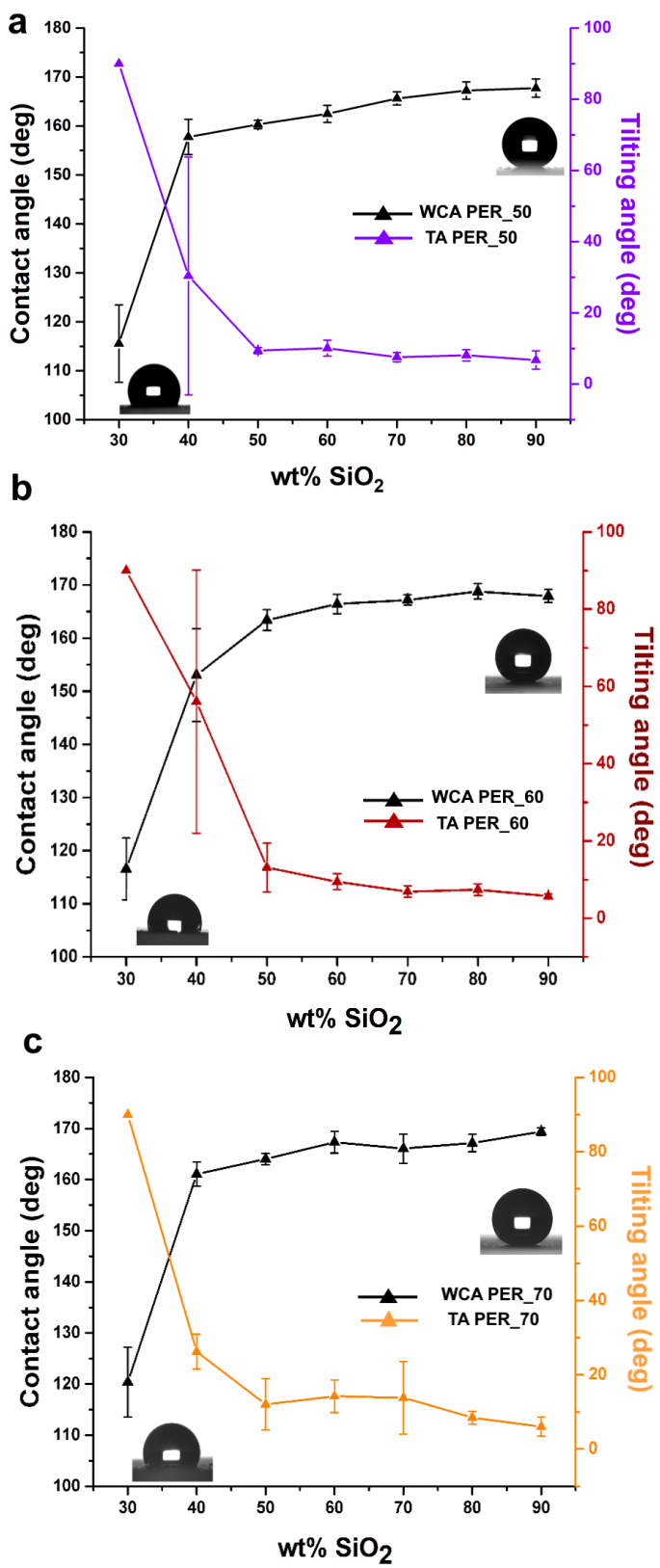

Figure 5.17: Plotted wettability data to highlight the change in static contact angle and tilting angle (TA) of coatings, when increasing the weight percentage of SiO_2 nanoparticles from 30 wt % to 90 wt %, for (**a**) PER_50, (**b**) PER_60 and (**c**) PER_70 composite materials.

Furthermore, a change in self-cleaning functionality was observed for PER-sulfur-SiO_2 systems that comprised varying SiO_2 loadings. Consistent with the wetting state transition from Wenzel to Cassie-Baxter, the performance of coatings improved considerably as the SiO_2 loading was enhanced (coatings that generally comprised ≥50 wt % SiO_2), as seen in Figure 5.18. Limited water adhesion to the surface, due to the presence of interfacial air, facilitated the rolling motion of deposited water droplets across the surface, resulting in the successful removal of simulated surface-bound contaminants.

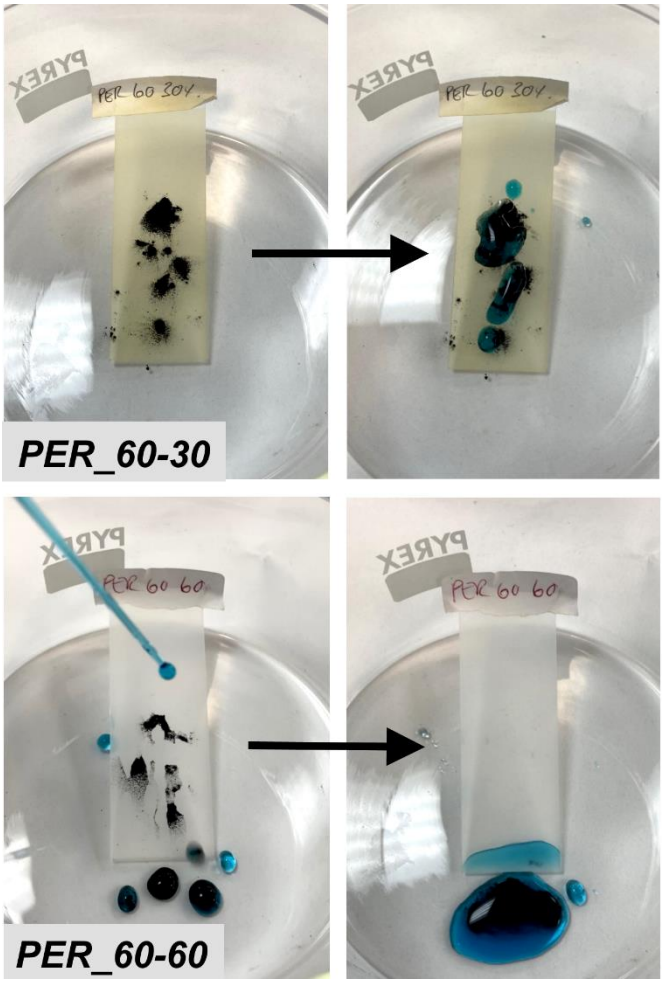

Figure 5.18: Images showing the self-cleaning performance of PER_60-30 coatings (static contact angle of 117° ± 6 and TA of 90°) *vs* PER_60-60 coatings (static contact angle of 166° ± 2 and TA of 9° ± 2). Manganese dioxide (MnO_2) was used to simulate dirt particles on the surface of materials, and methylene blue dye was used to better visualise distilled water droplets.

5.3.3 Dye Degradation Studies

5.3.3.1 Selection of PER-Sulfur-SiO_2 Coating

When determining the optimal coating to examine, to assess the photocatalytic and antibacterial activity, two primary factors needed to be considered; the initial wetting behaviour of the coating, and the relationship between surface hydrophobicity and polymer content. Ultimately, it was a trade-off between finding a surface that existed in a stable Cassie-

Baxter wetting state, and one that had a substantial polymer content (without compromising superhydrophobicity), so that the resultant coating would be sufficiently active, while remaining functional as a high-performance material. With that in mind, it was decided that PER_60-60 would be the ideal choice, as it:

- comprised a relatively high polymer content.
- exhibited extreme water repellency and presented a stable Cassie-Baxter wetting state (confirmed *via* low tilt angle of $9° \pm 2$).
- was fabricated from a stable sulfur copolymer (confirmed *via* DSC, PXRD and solubility studies). Therefore, limiting depolymerisation and improving surface homogeneity (confirmed *via* SEM imaging).

5.3.3.2 Testing using Intelligent Ink

To assess the photocatalytic activity, dye degradation studies were conducted using an ink formulation that was developed by Mills *et al*. for assessing photocatalytic films, termed 'intelligent ink'.[25] Intelligent ink is made up using the redox dye Resazurin, that when formulated as an aqueous solution, gives an intense blue colour. In the presence of a photocatalyst, the dye proceeds *via* a novel photo-reductive mechanism, whereby resazurin is irreversibly reduced to resorufin, marked by a visible colour change from blue to pink (see Fig. 5.19).

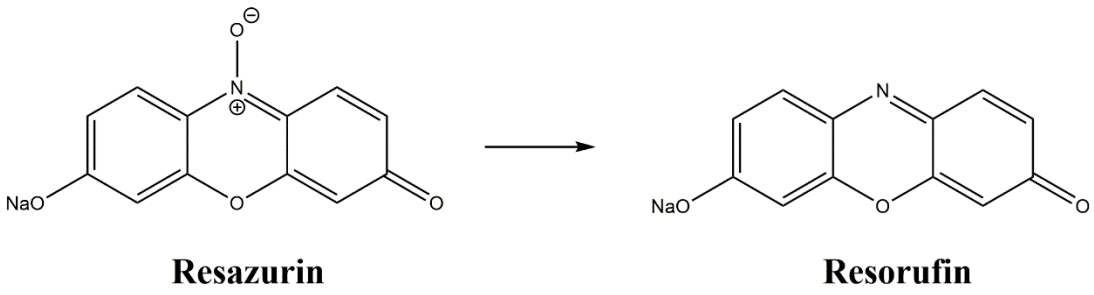

Resazurin **Resorufin**

Figure 5.19: Chemical structure of redox dye, Resazurin, and its reduction product, Resorufin.

This dye formulation has been commonly used to assess the photocatalytic activity of semi-conductor films, particularly titanium dioxide (TiO_2, anatase), which is known to be a strong photocatalyst and reported to degrade resazurin in a matter of minutes.[25] However, here, it was employed to probe the photocatalytic behaviour of PER_60-60. The dye was formulated as stated in experimental section 5.2.12.1, where 1 mL was pipetted onto the surface of PER_60-60 samples, followed by a short heating period of 5 minutes at 60℃, to promote water

evaporation and thicken the dye formulation (avoid movement of dye during vertical measurements). Coatings were stood vertically in the UV-Vis apparatus to record measurements, and measurements were taken after timed periods of irradiation to track any changes in absorbance (10-minute intervals up to 50 minutes).

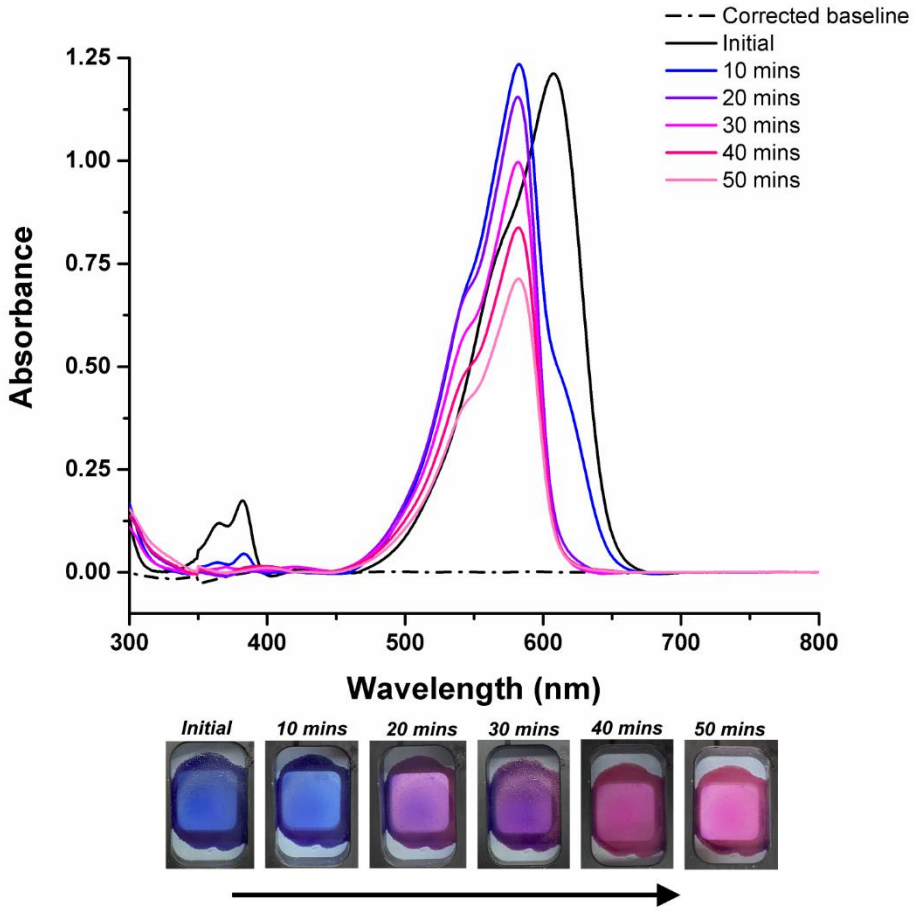

Figure 5.20: Overlaid UV-Vis absorbance spectra of intelligent ink on the surface of PER_60-60 after each 10 minute irradiation interval, up to 50 minutes of UV exposure (254 nm, 8W), and corresponding images showing the visual appearance of dye after each irradiation period. All spectra have been baseline corrected in Origin.

It can be seen from Figure 5.20 that a visual colour change from blue to pink had occurred within the 50 minute testing period, supported by a change in absorbance spectra where the disappearance/reduction of peaks at 608 nm and 382 nm, and appearance of peaks at 582 nm and 543 nm was apparent – evidence that the reduction of resazurin had taken place. It must be noted that although the reduction reaction did take place, the dye was not fully degraded in the examined time frame (marked by the incomplete disappearance of peaks and intensely coloured appearance), due to the dye formulation being highly concentrated. Nonetheless, the rapid peak shift from 608 nm to 582 nm, suggests that the redox reaction predominantly

occurred during the initial 20 minutes of irradiation. To better visualise the peak shift, measurements were recorded at 2-minute intervals, between 0-20 minutes (see Fig. 5.21).

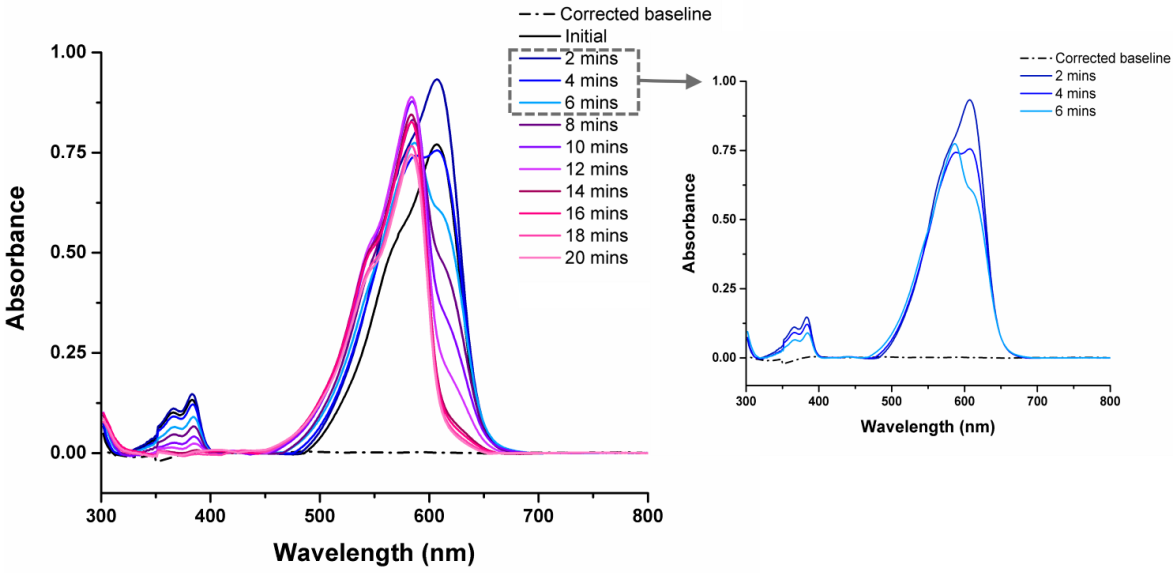

Figure 5.21: Overlaid UV-Vis absorbance spectra of intelligent ink on the surface of PER_60-60 after each 2 minute irradiation interval, up to 20 minutes of UV exposure (254 nm, 8W). Selected region of 2-6 minutes UV exposure overlaid, highlighting the peak shift from 608 nm to 582 nm. All spectra have been baseline corrected in Origin.

Photoreduction appeared to be initiated after 4 minutes of UV exposure, where the recorded absorbance spectrum displayed peaks at both 608 nm and 582 nm. Although this seemingly provided evidence that PER_60-60 was active as a photocatalyst, and can successfully reduce intelligent ink, it was important to test the dye formulation on a sample that is known to display no photocatalytic activity, to assess the stability of the dye under intense irradiation. For this, a SiO_2-polydimethylsiloxane (SiO_2-PDMS) coating that comprised hydrophobic SiO_2 nanoparticles [15 nm, pre-functionalised with hexamethyldisilazane (HMDS], coated with thermoset polymer PDMS, with a theoretical polymer thickness ($\mathbf{r}_{poly}$) value of 5 nm, was employed. This coating displayed a comparable static contact angle of 165° $\pm$ 2, and is stable when exposed to UV irradiation, therefore, no redox reaction or colour change was expected to take place.

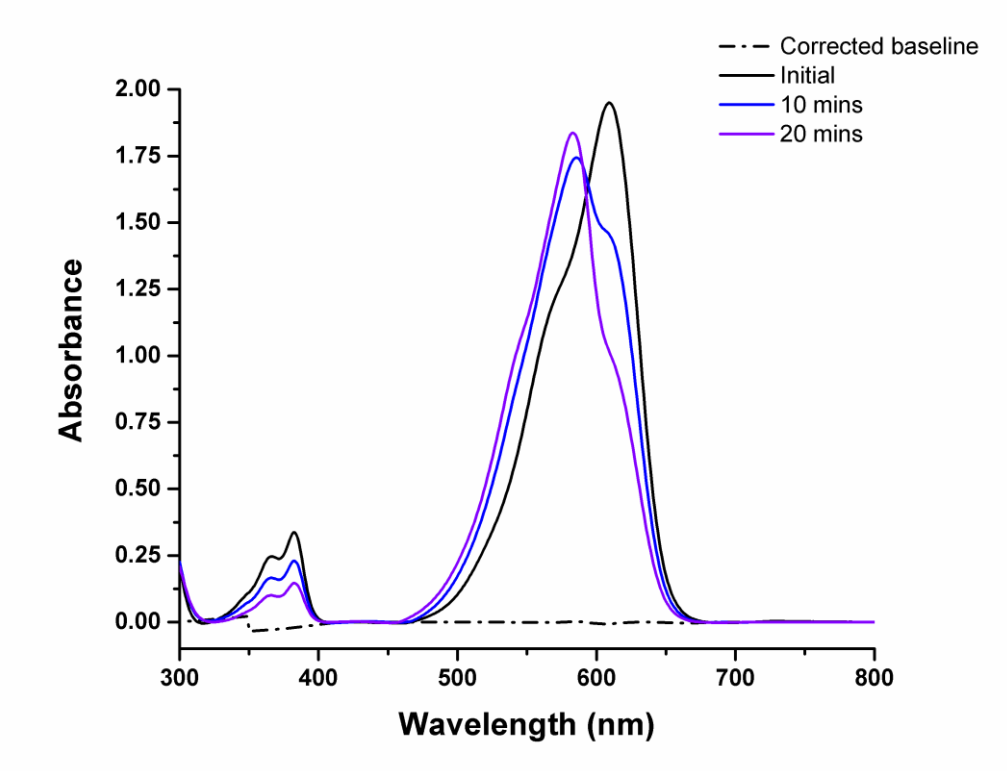

Figure 5.22: Overlaid UV-Vis absorbance spectra of intelligent ink on the surface of SiO_2-PDMS after each 10 minute irradiation interval, up to 20 minutes of UV exposure (254 nm, 8W). All spectra have been baseline corrected in Origin.

Interestingly, during the early stages of irradiation, it became quickly apparent that the deposited dye was beginning to transform into the redox product, resorufin (see Fig. 5.22). This was indicated by the peak shift from 608 nm to 582 nm, but also a noticeable reduction in the absorbance peak at 382 nm, as seen with PER_60-60, suggesting that intelligent ink was not stable under the wavelength of UV (254 nm) that was being used. As a result, the above findings could not be used to definitively prove that PER_60-60 was in fact photocatalytic, and a new testing method needed to be deduced.

5.3.3.3 Testing using Resazurin Dye

In light of the stability issues that surrounded intelligent ink, an aqueous solution of resazurin dye in the absence of the additional additives was trialled (glycerol and 2-hydroxyethyl cellulose), to limit the number of formulation components and independently assess whether the dye itself was unstable. The drawback of this, however, is that a thickened dye solution was not attained, and so the previous application method that used deposit dye (heating to remove residual water and vertically placing samples into the UV-Vis to record spectra) could

no longer be implemented. To overcome this, an optimized testing method was implemented that involved depositing the dye solution in droplet formation onto the surface of the sample. A total of sixteen 20 μL droplets were deposited onto the sample, and four droplets were pipetted into a demountable cuvette after each irradiation period to record a UV-Vis absorbance spectrum (10-minute intervals up to 40 minutes). A demountable cuvette enables the examination of small volumes of liquid as it has a path length of 0.5 mm, with a minimum volume of ~ 80 μL – as opposed to the generic 1 cm path length cuvettes. As a result, absorbance spectra are typically 20x more diluted, leading to lower absorbance values, although this does not affect the spectral signals. Four 20 μL droplets of aqueous dye appeared to be the best method for recording spectra, to allow for good contact between the surface and droplet, while meeting the minimum requirement of 80 μL for each measurement. To assess the stability of the new dye formulation (1 mg resazurin in 20 mL distilled water), this method was trialled with SiO_2-PDMS over an exposure period of 40 minutes.

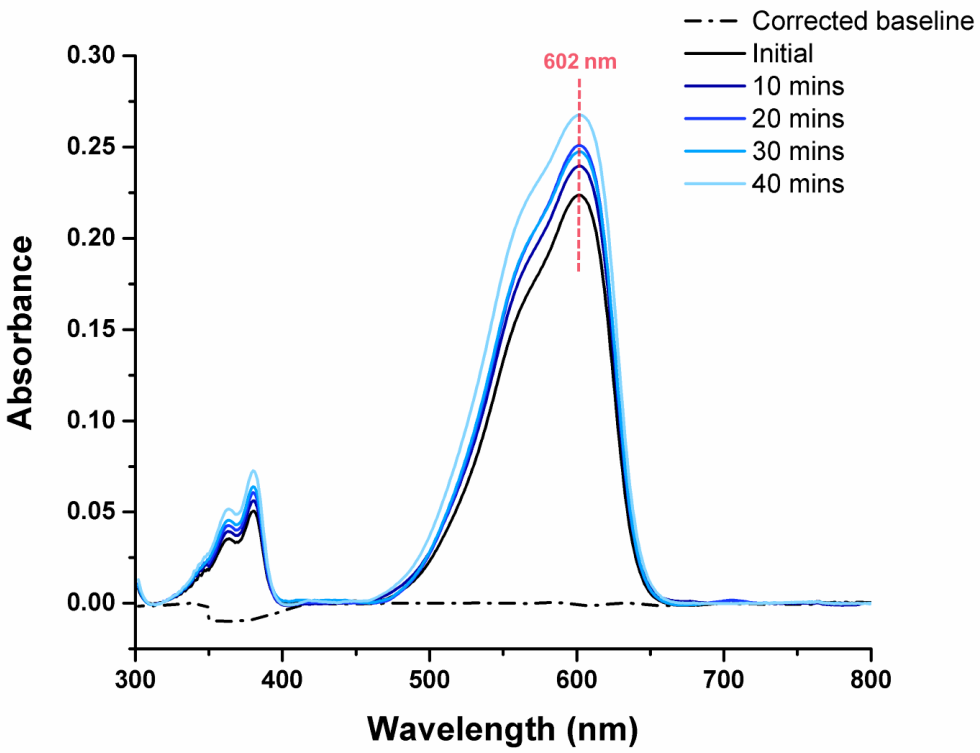

Figure 5.23: Overlaid UV-Vis absorbance spectra of aqueous resazurin dye droplets (1 mg per 20 mL), removed from the surface of SiO_2-PDMS after each 10 minute irradiation interval, up to 40 minutes of UV exposure (254 nm, 8W). The highlighted absorption peak is at 602 nm, showing that no peak shift has occurred over time. All spectra have been baseline corrected in Origin.

It can be seen from Figure 5.23 that there is no sign of a peak shift from 602 nm to lower wavelengths during the full irradiation period, and that complete flattening of the peak at 380 nm did not occur. Thus, indicating that the aqueous dye solution appeared to be relatively stable when exposed to 254 nm radiation, within the tested time period. Additionally, the dye retained its intense blue colour after 40 minutes of exposure, suggesting that significant photoreduction did not take place. It can be seen, however, that some variation in peak height was apparent over time for both peaks. This could be explained by differences in concentration/volume of dye during the exposure period, and the method used to collect the testing samples; ideally, using a humid environment to limit water evaporation during testing would have been considerably more efficient. However, the discovery of a covering material that allowed full transmittance of 254 nm light presented challenges, and the exposure period was considered to be relatively short, therefore, it was decided that conducting the experiment without a cover shouldn't have impacted the peak intensity profoundly. Nonetheless, it cannot be ruled out that the chemical reduction of the dye molecules may have been initiated through interactions with the sulfur polymer surface (see below).

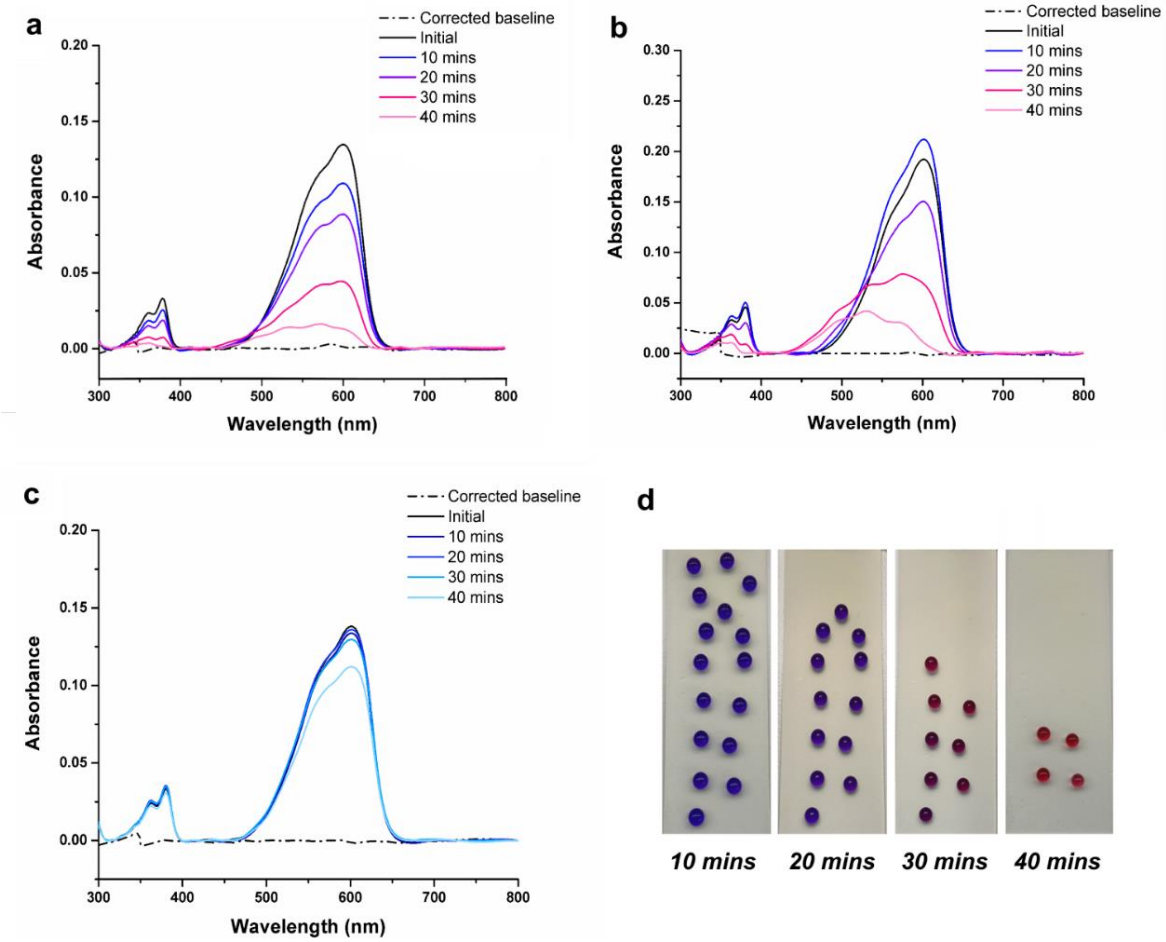

Figure 5.24: Overlaid UV-Vis absorbance spectra of aqueous resazurin dye droplets (1 mg per 20 mL), removed from the surface of (**a**) flat elemental sulfur, (**b**) PER_60-60 under standard conditions (254 nm, 8W) and (**c**) PER_60-60 when left in the dark. (**d**) Images of dye droplets on the surface of PER_60-60 after exposure to 10-40 minutes of UV (left to right, 254 nm). All spectra have been baseline corrected in Origin.

After achieving a stable dye solution, elemental sulfur (a flattened surface obtained from melting and manually spreading molten sulfur across a glass slide) and PER_60-60 coatings were examined, *via* the same method. From Figure 5.24a/b, similar peak reductions (~602 nm ~380 nm) and peak enhancements (~572 nm and ~532 nm) that were originally observed when employing intelligent ink, were apparent for both examined materials. The percentage difference in peak height was calculated for two different sets of peaks; [602 nm (*initial*): 572 nm (*after full UV exposure*)] and [380 nm (*initial)*: 362 nm (*after full UV exposure*)], where elemental sulfur displayed peak reductions of 88 % (602 nm: 572 nm) and 86 % (380 nm: 362 nm), and PER_60-60 peak reductions of 84 % (602 nm: 572 nm) and 77 % (380 nm: 362 nm). Although the photoreduction mechanism occurred in both elemental sulfur and PER_60-60, confirmed by a visual colour change (see Fig. 5.24d), elemental sulfur could be seen to be

more photocatalytically efficient within the exposure time, evident by the advanced decrease in peak intensity and paler pink appearance of the resultant dye droplets (see Fig. 5.25 b/c – appearance comparison). Nonetheless, the performance of both materials was comparable, despite PER_60-60 only comprising 40 wt % PER-sulfur copolymer, as both materials promoted the reduction of resazurin to resorufin. Interestingly, for PER_60-60, surface hydrophobicity was seen to be upheld after the full exposure periods, as droplets were observed to remain on the surface with no indication of spreading/wetting (see section 5.3.3.4 for further discussion).

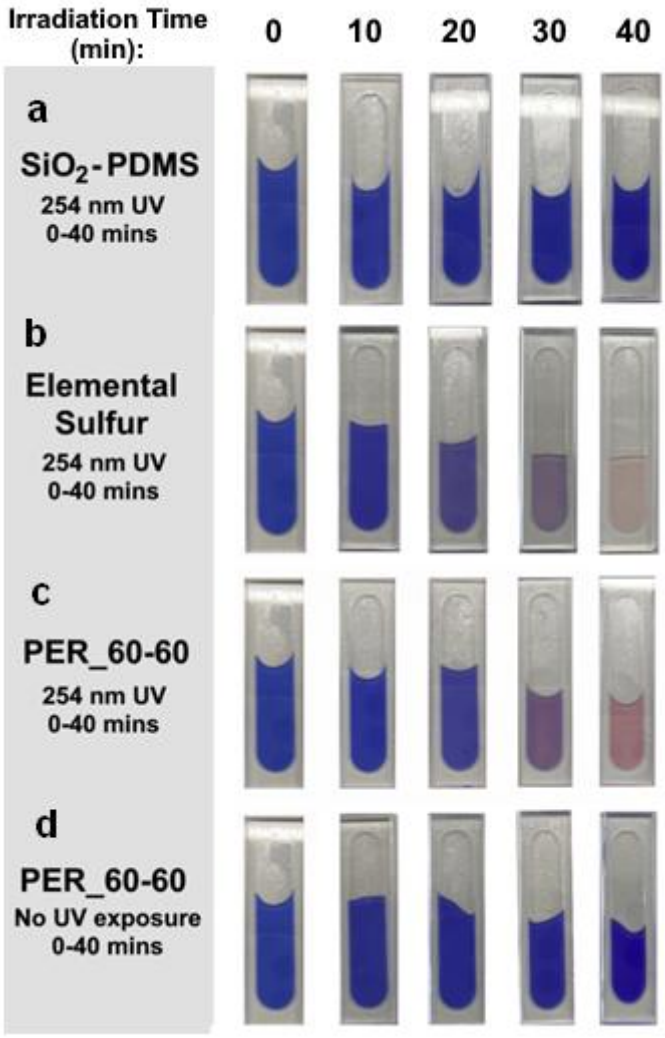

Figure 5.25: Images displaying the physical appearance of the dye sample (loaded into a demountable cuvette) after each irradiation period; (**a**) SiO_2-PDMS, (**b**) elemental sulfur, (**c**) PER_60-60 and (**d**) PER_60-60 under dark conditions. All conditions for each set of sample measurements are stated on the left-hand side and irradiation time is stated above.

To certify that the dye was truly being reduced by photogenerated species, and not chemically reacting with the surface of films, dye droplets were deposited onto the surface of PER_60-60 and coatings were kept in the dark (exposure to light of PER_60-60 coatings was avoided for

7 days prior to use). As seen in Figure 5.24c, signals indicative of the reduced product resorufin were not present after 40 minutes of UV exposure, and coatings did not appear to visually change colour (see Fig. 5.25d). Although there was a slight decrease in peak height at 602 nm, the shape of the peak maintained consistency and no significant decrease in peak height at 380 nm was observed, so therefore, it is unlikely that this is related to resazurin reduction. It is more probable that the peak reduction is consequential of issues related to the concentration/volume of the dye solution used to record the measurement, due to the nature of the process. However, it is not possible to rule out that the surface of the coating may be active after a prolonged period, and dye degradation may also proceed *via* a chemical mechanism. Nonetheless, it can be said that within the examined time frame, the primary cause of dye degradation is due to a photocatalytic mechanism.

For comparative reasons, a superhydrophobic coating that comprised TiO_2 nanoparticles was fabricated and tested. TiO_2 nanoparticles (21 nm) were functionalised by a self-assembled monolayer of fluoroalkylsilane (FAS) molecules, *via* hydrolysis and condensation reactions, to yield a coating with a static contact angle of $162° \pm 2$. Upon subjecting TiO_2-FAS to parallel dye degradation tests, identical peak reductions (602 nm and 380 nm) and appearances (572 nm and 532 nm), like those seen for elemental sulfur and PER_60-60, were observed. Thus, highlighting that the photoreduction mechanism of dye molecules had taken place (see Fig. 5.26).

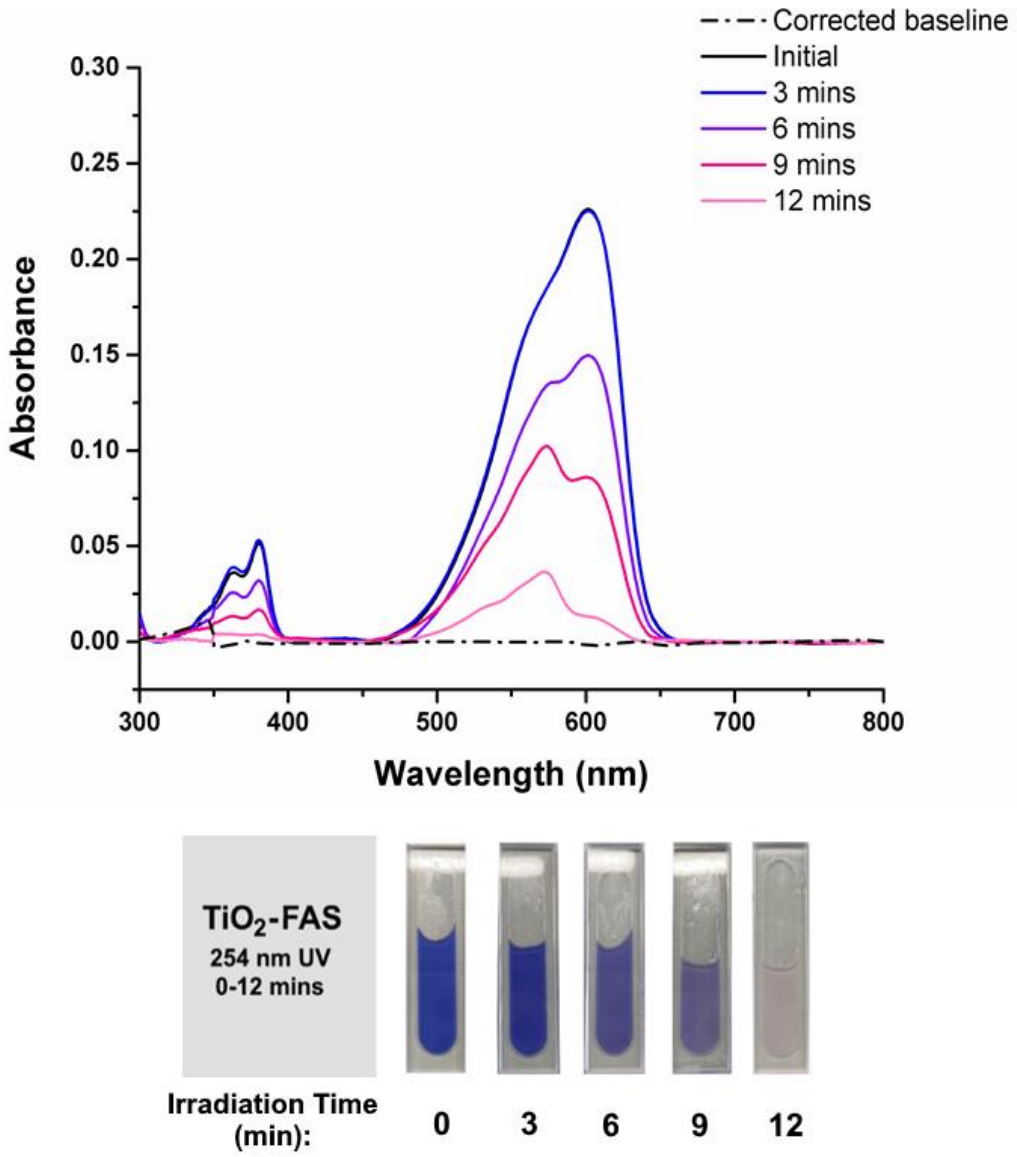

Figure 5.26: Overlaid UV-Vis absorbance spectra of aqueous resazurin dye droplets (1 mg per 20 mL), removed from the surface of TiO_2-FAS after each 10 minute irradiation interval, up to 40 minutes of UV exposure (254 nm, 8W). All spectra have been baseline corrected in Origin. Inset; Images showing the physical appearance of the dye solution (loaded into a demountable cuvette) after each irradiation period.

TiO_2-FAS was significantly more efficient as a photocatalyst, degrading the dye almost entirely within 12 minutes of exposure, with peak reductions of 84 % (602 nm: 572 nm) and 92 % (380 nm: 362 nm). However, the surface of TiO_2-FAS was found to undergo a UV-induced change in surface wettability, from superhydrophobic to superhydrophilic (static contact angle ~0°), within the same exposure time. This can be attributed to the degradation

of hydrophobic FAS molecules by liberated radicals, resulting in the regeneration of hydroxyl groups on the surface of TiO_2 nanoparticles.

5.3.3.4 UV Stability

Initially, it was important to assess the UV stability of elemental sulfur, to probe any immediate changes in surface chemistry. As UVC radiation was used here (254 nm), this does not represent the time taken for photodegradation to occur *via* exposure to solar irradiation, as only lower energy/longer wavelength radiation reaches the earth (UVA and UVB). However, this study can be used as an indicator as to what changes could occur to surface coatings, during prolonged periods of outdoor exposure. Powdered sulfur particles were pellet pressed to yield near flat, 7 mm diameter pellets that were then subjected to UV irradiation for an extended time (254 nm, see experimental sections 5.2.9, 5.2.10, and 5.2.12.2 for further details). Static and dynamic wettability measurements were initially recorded at 30-minute intervals (up to 90 minutes), and then taken every hour after this. Elemental sulfur was found to be intrinsically hydrophobic throughout the entire testing period (see Fig. 5.27a), where the static contact angle varied very little (standard deviation of 1.5), highlighting excellent stability against intense UV irradiation.

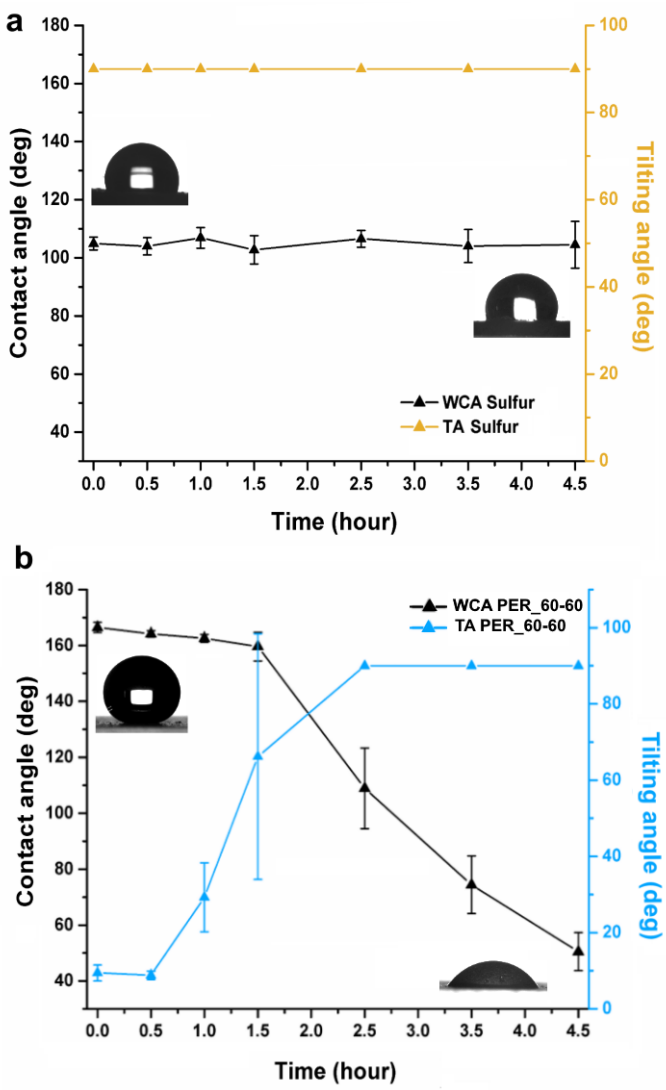

Figure 5.27: The change in static contact angle and tilting angle with UV irradiation time (254 nm, 8W) for (**a**) sulfur (7 mm diameter pellet, one measurement per pellet, total of 5 readings/pellets per data point) and (**b**) PER_60-60. Inset; corresponding digital image of a water droplet on the surface of sulfur and PER_60-60 at 0 hours and 4.5 hours.

Although PER_60-60 initially displayed a stable Cassie-Baxter wetting state, susceptibility towards UV-induced degradation was apparent, over time. Before irradiation, a static contact angle of 166° ± 2 and tilt angle of 9° ± 2 was recorded and the coating appeared to show high stability for ~ 90 minutes, before undergoing a complete wetting state transition from Cassie-Baxter to Wenzel, after 2.5 hours of irradiation (contact angle of 109° ± 14 and tilt angle of 90°). After which, further decreases in surface hydrophobicity were observed, resulting in a final reading of 51° ± 7, after 4.5 hours of exposure. It was anticipated that UV-induced hydrophilicity was due to the susceptibility of the organic crosslinker to photodegradation; it is likely that exposure to intense UV not only promotes degradation of the deposited dye, but also facilitates the breakdown of physical crosslinks between sulfur and PER, resulting in the production of organic contaminants, and therefore, changes in surface wettability.

Throughout section 5.3.3.3, it was clear that resazurin underwent a redox reaction, reported to be a photoreduction by Mills *et al.*, whereby photogenerated electrons or other generated

species e.g. $O_2^{-}\cdot$ or $HO_2\cdot$ act to irreversibly reduce resazurin dye. Under these circumstances, there is reported to be a requirement for a sacrificial electron donor to irreversibly react with photogenerated holes – in the case of intelligent ink, this was the additive glycerol.[25] However, as the dye formulation was modified and additives were removed to ensure UV stability under intense radiation, it is likely that photogenerated holes were reacting with moisture or adsorbed hydroxyl groups to generate OH· radicals (particularly in the case of TiO_2-FAS, as TiO_2 is intrinsically hydrophilic and may have had remaining surface-bound hydroxyl groups). Liu *et al*. documented the photocatalysis of elemental sulfur in aqueous suspensions and suggested that upon photoexcitation α-sulfur can liberate OH· radicals, while retaining its stability (detection of very little sulfur-containing ions present in solution after irradiation). The production of OH· radicals was confirmed by the generation of 2-hydroxyterephthalic acid, from a basic solution of terephthalic acid (*via* reaction with liberated OH· radicals), and was detected by an emitted fluorescence signal.[11] Although other radical species were likely present at the surface interface during irradiation, the reduction of resazurin was seen to proceed. However, the presence of other radical species may have contributed towards the degradation of the organic crosslinker, in the case of PER_60-60.

Owed to PER_60-60 coatings displaying good stability towards UV degradation within the initial 90 minutes of irradiation (compared to TiO_2-FAS coatings which turned superhydrophilic within 12 minutes), it is expected that the presence of sulfur decelerated the rate of photodegradation, due to its non-photodegradable nature. However, over time, the presence of organic contaminants, and breakdown of the PER crosslinker inevitability encouraged surface hydrophilicity. Figure 5.28 depicts stacked FTIR spectra of PER_60, PER_60-60 before UV exposure, and PER_60-60 after 4.5 hours of UV irradiation, where a substantial reduction in peaks is apparent after UV exposure (black line). Subsequently, indicating that full or partial photodegradation of the crosslinker may have taken place (peaks are diluted compared to pure PER_60, due to the large presence of SiO_2). Furthermore, the weak signal at $\sim$760 cm^{-1} that is characteristic of Si-C stretching – present from HMDS-functionalised SiO_2 – appeared to have reduced in peak intensity after exposure to UV (red line *vs* black line), suggesting that the degradation of hydrophobic $–CH_3$ groups, that were grafted onto SiO_2 nanoparticles, may have also occurred. Therefore, further contributing towards the change in surface wettability.

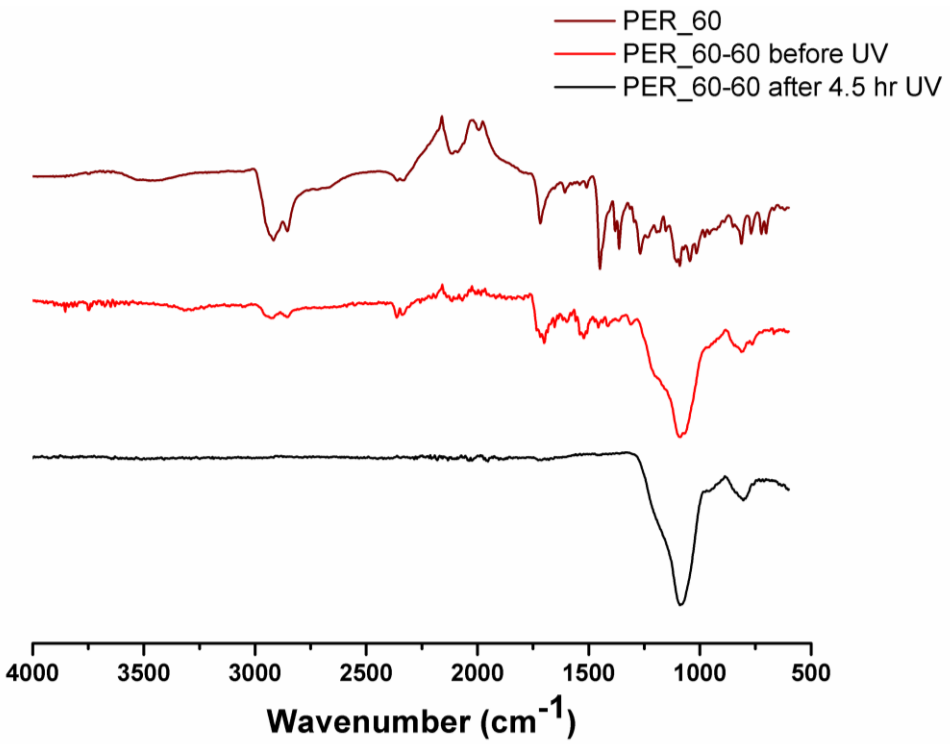

Figure 5.28: Stacked FTIR spectra of PER_60 (**maroon line**), PER_60-60 before UV irradiation (**red line**) and PER_60-60 after 4.5 hours of UV exposure (**black line**).

5.3.4 Antibacterial Studies of PER_60-60

In addition to studying the UV-activated photocatalytic behaviour of surface coatings, we also probed the antibacterial activity under ambient conditions (no direct source of visible or UV radiation). It has been reported by Smith *et al*. that high sulfur content polymers [sulfur-diisopropenyl benzene (DIB) copolymer and sulfur-dicyclopentadiene (DCPD) copolymer] display antibacterial properties when exposed to *E. coli* and *S. aureus* bacteria strains.[18] However, the polymeric samples that were tested here were flat bulk polymer samples. Hence, we speculate that the intrinsic antibacterial nature of sulfur/sulfur polymers, combined with the well-established self-cleaning behaviour of superhydrophobic surfaces, could generate materials with superior antibacterial/self-cleaning properties. The commonly used *S. aureus* bacteria strain was employed for testing, and both solution effects and surface effects of bacterial growth/adhesion were investigated, where all preparation, testing and analysis was performed by Romy Dop (Hassel Research Group). In doing so, we aimed to elucidate the growth of bacteria within the solution, but also the attachment of bacteria to the surface of each coating. Here, plain glass was used as a negative control, alongside elemental sulfur, flat PER_60 polymer and superhydrophobic PER_60-60 which were all tested in triplicate, following the method stated in section 5.2.13.

The bacterial solution was applied to 1 cm^2 samples in a 24-well plate that was then statically incubated at 37℃ for 5 hours. Serial dilutions of each bacterial solution were then performed using phosphate-buffered saline (PBS), and deposited onto separate agar plates in segments (Miles and Misra method), before being incubated overnight to enable colony growth. The segment that comprised a minimum of 30 colony forming units (CFU) and a maximum of 300 CFU was used to calculate the CFU/mL, and for solution-based bacteria, this corresponded to a serial dilution of 5 for all samples (see Fig. 5.29). In order to investigate the surface effects, surfaces were rinsed with 1 mL PBS to remove any planktonic cells, and then vortexed in 1 mL LB broth to extract adhered cells. The vortexed solution was serially diluted in PBS using the same method, as stated above. Here, 4 serial dilutions were required for glass, 3 were required for elemental sulfur and flat PER_60 polymer, and 1 was required for superhydrophobic PER_60-60. CFUs were counted from sectors of the agar plate that corresponded to the necessary serial dilutions, and from these CFU/cm^2 could be calculated (see Fig. 5.29).

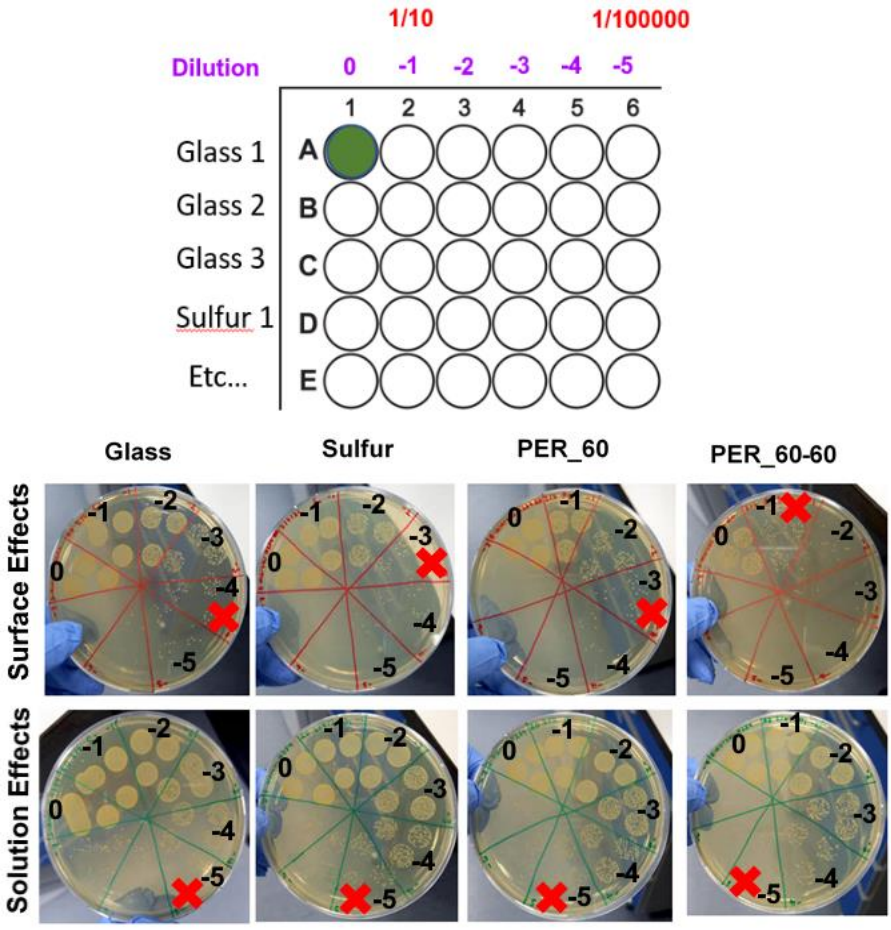

Figure 5.29: Illustration showing serial dilutions *via* Miles and Misra method of bacterial solution in PBS (20 μL in 180 μL PBS per dilution), and images of one agar plate for each sample with specimens from the initial solution and labelled serial dilutions, consecutively deposited into a sector to investigate solution-based effects and surface-based effects. Red crosses mark the serial dilution used for CFU count and analysis.

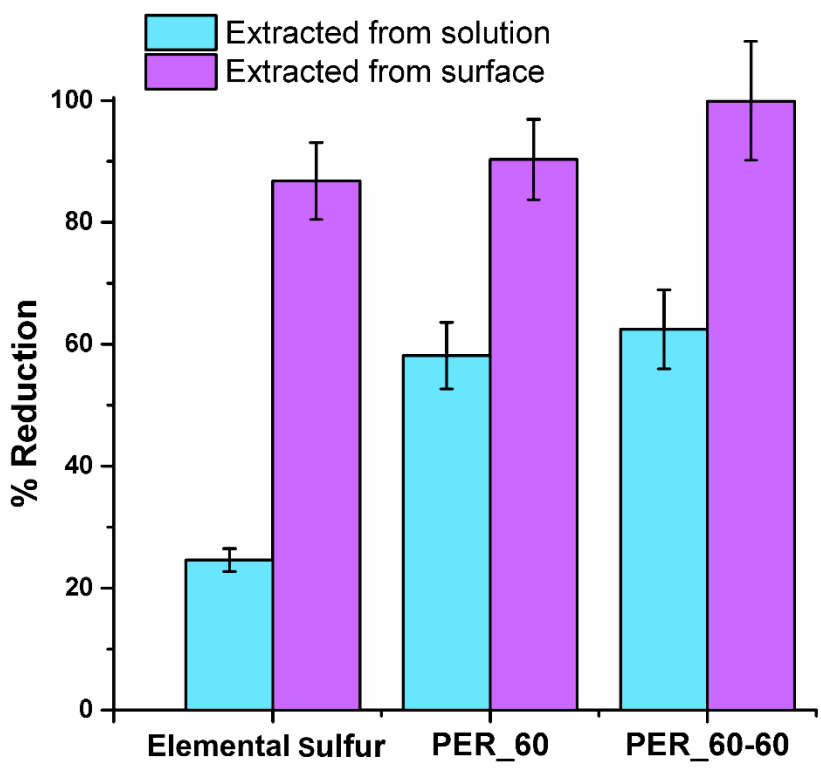

Figure 5.30: Bar chart displaying the % reduction of bacteria (determined *via* CFU/mL or CFU/cm^2) found in solution and extracted from the surface of elemental sulfur, flat PER_60 and superhydrophobic PER_60-60, in reference to the negative control (plain glass).

It can be seen in Figure 5.30 that a reduced presence of bacteria was detected in solutions that sulfur-based materials were submerged in, with elemental sulfur displaying a 24.58 % reduction, flat PER_60 displaying a 58.14 % reduction, and superhydrophobic PER_60-60 showing a 62.46 % reduction, when compared to the negative control (plain glass). Considering this, it is likely that sulfur-based materials either inhibited the growth of bacteria/biofilms or a significant number of bacteria were adhered to the surface of each material, and hence, not accounted for in the external solution. When later examining the bacteria extracted from each surface, it could be seen that the bacterial reduction was even more significant, suggesting that sulfur-based materials possessed an intrinsic antibacterial nature and limited both, surface and solution bacterial growth. The same trend in behaviour seemed to be apparent when considering surface growth: elemental sulfur < flat PER_60 < superhydrophobic PER_60-60 as an 86.79 % reduction was determined for elemental sulfur, 90.29 % reduction for flat PER_60, and 99.89 % reduction for superhydrophobic PER_60-60, when probing bacteria attachment to the surface. This can be better visualised when plotting the log reduction of each sample, as seen in Figure 5.31.

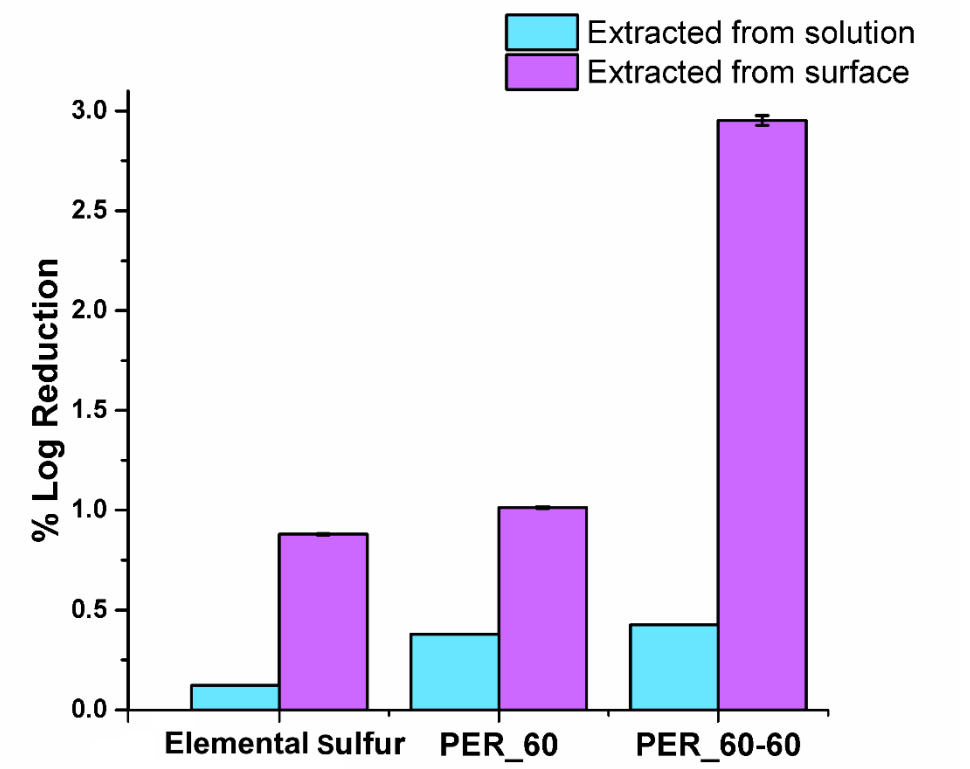

Figure 5.31: Bar chart displaying the log % reduction of bacteria (determined *via* CFU/mL or CFU/cm^2) found in solution and extracted from the surface of elemental sulfur, flat PER_60 and superhydrophobic PER_60-60, in reference to the negative control (plain glass).

As bacterial solutions are highly concentrated, plotting the log reduction allows us to better differentiate between the three surfaces, particularly when comparing surface effects. Here, it is now clear that the superhydrophobic coating was significantly more effective in reducing bacterial attachment and growth, when compared to flat elemental sulfur and sulfur polymer surfaces (% reductions in reference to the negative control). This may have been expected as the bacterial solution was aqueous, and the surface had extreme water repelling properties. However, as stated earlier, superhydrophobic PER_60-60 also had the lowest number of detectable bacterial CFUs in solution; it is anticipated that the superhydrophobic coating presented a reduced surface area for bacterial attachment and nucleation points, due to the large presence of interfacial air pockets, and intrinsic Cassie-Baxter wetting behaviour. This, combined with the ability of inverse vulcanized sulfur polymers to kill bacteria – suggested to occur *via* homolytic S-S bond cleavage of polysulfide linkages, by Smith *et al*., who studied the antibacterial nature of DIB and DCPD copolymers – is believed to be the primary reason behind the superior antibacterial nature of PER_60-60.[18] As DIB and DCPD are both molecules that generate more heavily crosslinked sulfur copolymers, it was further anticipated that the PER crosslinker could form a copolymer that displayed increased antibacterial

activity, due to having longer polysulfide linkages within the 'crosslinked' network (unlikely to be fully crosslinked due to high solubility).[18,29] However, as further work to distinguish between live and dead cells, and comparative work studying a range of crosslinkers was not carried out due to time constraints, we cannot definitively state this. Yet, it can still be said with certainty that superhydrophobic sulfur polymer materials were found to be more effective in limiting bacterial growth than flattened sulfur polymer surfaces.

5.4 Conclusions

Throughout this chapter, we investigated the feasibility of designing superhydrophobic surface coatings from PER-sulfur polymers (used to coat SiO_2 nanoparticles), and examined the photocatalytic and antibacterial properties of resultant coatings, arising from the combined effects of synthetically induced surface superhydrophobicity and the intrinsic nature of sulfur/sulfur polymers. The key discoveries are outlined below:

Fabricating Superhydrophobic Coatings from PER-Sulfur Copolymers – For the first time, to the best of our knowledge, it was shown that PER-sulfur copolymers can be used to design superhydrophobic coatings. Here, a series of coatings were successfully fabricated, employing SiO_2 nanoparticles as a roughening agent, where static contact angles as high as $169° \pm 1$ (tilt angle $6° \pm 3$) were observed and coatings displayed stable Cassie-Baxter wetting behaviour/self-cleaning properties (with the exception of coatings that comprised 30 and 40 wt % SiO_2). The use of a crosslinker that could generate soluble sulfur copolymers, and discovery of a solvent capable of dissolution – in this case chloroform (recovered polymer mass percentages of 97 % $\pm$ 3 for PER_50, 96 % $\pm$ 3 for PER_60, 96 % $\pm$ 3 for PER_70, 86 % $\pm$ 5 for PER_80 and 77 % $\pm$ 3 for PER_90) – were imperative to the design of superhydrophobic sulfur polymer composites. PER_50 and PER_60 coatings were found to be stable *via* DSC, PXRD and SEM. However, elemental sulfur could be detected in higher sulfur content polymers, either initially or after reprocessing, as there was likely not enough crosslinker present to stabilize sulfur chains, so these coatings were not selected for further investigation.

PER-Sulfur-SiO_2: Photocatalytic Nature – The photocatalytic behaviour of superhydrophobic PER_60-60 was uncovered *via* a series of dye degradation tests on the commercially available dye, resazurin. It was discovered that the coating was sufficiently active under 254 nm UV light, as the photoreduction of aqueous resazurin occurred within a 40-minute exposure window (intense blue colour to pink). Although chemical reduction of the dye *via* interactions with the polymer surface could not be definitively excluded, it was proven that within the stated exposure period that redox reactions were kept to a minimum, and photocatalysis was the primary mechanism of degradation. The photocatalytic activity of PER_60-60 was found to be comparable to that of flat elemental sulfur, however, both displayed lower activity than TiO_2-FAS which displayed full dye degradation within 12 minutes of irradiation. Interestingly, PER_60-60 coatings retained their extreme water repellency throughout the UV exposure period, where droplets could be observed to have a high static contact angle after the photoreduction process had taken place, likely due to the

non-photodegradable nature of sulfur. Hence, sulfur has been used here as an active component that also acts to preserve surface hydrophobicity.

PER-Sulfur-SiO_2: UV Stability – Following photocatalysis studies, UV stability testing was carried out on PER_60-60 and flat elemental sulfur to better understand each surface. Though elemental sulfur was found to be intrinsically hydrophobic, photocatalytically active, and to display a high stability towards self-degradation (i.e., degradation of surface hydrophobicity through UV-induced changes in chemical structure), it could not be independently employed as a SiO_2 composite due to issues surrounding processability. Coatings exclusively fabricated from elemental sulfur were very mechanically weak and droplet-surface adhesion was strong – highlighted by a tilt angle that consistency exceeded 90° (Wenzel wetting). Furthermore, these concerns extend to the use of sulfur nanoparticles, as we have seen from previous studies on the resilience of superhydrophobic coatings, designed from powdered materials, that the mechanical resilience is extremely limited. On the other hand, PER_60-60 was observed to display initial high stability (~ 90 minutes), before considerably declining between 90 minutes and 2.5 hours of UV exposure. It was anticipated that photodegradation of the PER crosslinker may have occurred over time, leading to UV-induced changes in surface wettability. Furthermore, there was evidence to suggest that photodegradation of the hydrophobic coating that surrounded SiO_2 nanoparticles may have also taken place, contributing towards this. However, this work is proof of principle that sulfur copolymers have the potential to display simultaneous photoactivity and superhydrophobicity.

PER-Sulfur-SiO_2 – Antibacterial Properties – Both, bacterial solution effects and bacterial surface effects were found to be significantly reduced for the superhydrophobic PER_60-60 coating, when compared to flat elemental sulfur, flat PER_60 polymer and the negative control (plain glass). Elemental sulfur and a limited number of sulfur copolymers (flattened surfaces) have already been shown to actively kill *S. aureus* bacteria in the literature, so it was anticipated that the antibacterial nature of sulfur polymers, collective with the reduced solid-vapour interface obtained when inducing surface superhydrophobicity, further diminishes bacterial attachment and growth. The extreme water repellence of the surface provides an initial barrier against interaction with the aqueous bacterial solution, following which, the large liquid-vapour interfacial area alleviates pinning points on the surface for bacteria to attach and initiate growth. Subsequently, generating a triple action, high performance antibacterial surface.

Overall, we have shown that PER-sulfur polymers can be used to manufacture multi-functional, synthetic superhydrophobic materials. More specifically, that sulfur-based materials have great potential in developing coatings that can display simultaneous

photocatalysis and superhydrophobicity, which currently, is not being reported without the use of potentially carcinogenic and expensive metal/metal oxides. The work here is proof of principle that this class of materials, obtained from natural and waste by-products, can be employed to design superhydrophobic materials with a wide range of prospective applications (self-cleaning, antibacterial, photocatalytic etc.). Although PER_60-60 was shown to be susceptible to photodegradation after a short period of time, upon exposure to intense UV irradiation (254 nm), the reported work paves the way for the development of superhydrophobic materials using a range of sulfur copolymers, and investigation into the link between UV stability and structure of the crosslinked polymer network.

5.5 References

1 M. Ghasemlou, F. Daver, E. P. Ivanova and B. Adhikari, *J. Mater. Chem. A*, 2019, **7**, 16643–16670.

2 Q. Shang, C. Liu, J. Chen, X. Yang, Y. Hu, L. Hu, Y. Zhou and X. Ren, *ACS Sustain. Chem. Eng.*, 2020, **8**, 7423–7435.

3 Q.-Y. Cheng, X.-L. Zhao, Y.-X. Weng, Y.-D. Li and J.-B. Zeng, *ACS Sustain. Chem. Eng.*, 2019, **7**, 15696–15705.

4 S. M. R. Razavi, J. Oh, S. Sett, L. Feng, X. Yan, M. J. Hoque, A. Liu, R. T. Haasch, M. Masoomi and R. Bagheri, *ACS Sustain. Chem. Eng.*, 2017, **5**, 11362–11370.

5 J. Lim, J. Pyun and K. Char, *Angew. Chemie Int. Ed.*, 2015, **54**, 3249–3258.

6 W. J. Chung, J. J. Griebel, E. T. Kim, H. Yoon, A. G. Simmonds, H. J. Ji, P. T. Dirlam, R. S. Glass, J. J. Wie and N. A. Nguyen, *Nat. Chem.*, 2013, **5**, 518–524.

7 J. J. Germida and H. H. Janzen, *Fertil. Res.*, 1993, **35**, 101–114.

8 M. S. Karunarathna, M. K. Lauer, T. Thiounn, R. C. Smith and A. G. Tennyson, *J. Mater. Chem. A*, 2019, **7**, 15683–15690.

9 Sulfur - Periodic Table - Royal Society of Chemistry, https://www.rsc.org/periodic-table/element/16/sulfur.

10 M. J. H. Worthington, R. L. Kucera and J. M. Chalker, *Green Chem.*, 2017, **19**, 2748–2761.

11 G. Liu, P. Niu, L. Yin and H.-M. Cheng, *J. Am. Chem. Soc.*, 2012, **134**, 9070–9073.

12 V. A. Peyman and S. Azizian, *Photochem. Photobiol.*, 2020, **96**, 1191–1199.

13 L. Libenson, F. P. Hadley, A. P. McIlroy, V. M. Wetzel and R. R. Mellon, *J. Infect. Dis.*, 1953, 28–35.

14 S. Saikia and P. N. L. Lens, *Synthesis and Application of Sulfur Nanoparticles*, IWAP online, 2020.

15 V. S. Wadi, K. Halique and S. M. Alhassan, *Ind. Eng. Chem. Res.*, 2020, **59**, 13079–13087.

16 J. J. Griebel, S. Namnabat, E. T. Kim, R. Himmelhuber, D. H. Moronta, W. J. Chung, A. G. Simmonds, K. Kim, J. Van Der Laan and N. A. Nguyen, *Adv. Mater.*, 2014, **26**, 3014–3018.

17 T. Hasell, D. J. Parker, H. A. Jones, T. McAllister and S. M. Howdle, *Chem. Commun.*, 2016, **52**, 5383–5386.

18 J. A. Smith, R. Mulhall, S. Goodman, G. Fleming, H. Allison, R. Raval and T. Hasell, *ACS omega*, 2020, **5**, 5229–5234.

19 C. E. Hoyle and C. N. Bowman, *Angew. Chemie Int. Ed.*, 2010, **49**, 1540–1573.

20 Y. Fang, C. Liu, M. Li, X. Miao, Y. Pei, Y. Yan, W. Xiao and L. Wu, *Ind. Eng. Chem. Res.*, 2020, **59**, 6130–6140.

21 B. J. Sparks, E. F. T. Hoff, L. Xiong, J. T. Goetz and D. L. Patton, *ACS Appl. Mater. Interfaces*, 2013, **5**, 1811–1817.

22 H. Zhang, Y. Ma, J. Tan, X. Fan, Y. Liu, J. Gu, B. Zhang, H. Zhang and Q. Zhang, *Compos. Sci. Technol.*, 2016, **137**, 78–86.

23 E. Lantos, L. Mérai, Á. Deák, J. Gómez-Pérez, D. Sebők, I. Dékány, Z. Kónya and L. Janovák, *J. Mater. Sci. Technol.*, 2020, **41**, 159–167.

24 S. K. Brossard, H. Du and J. D. Miller, *J. Colloid Interface Sci.*, 2008, **317**, 18–25.

25 A. Mills, J. Wang, S.-K. Lee and M. Simonsen, *Chem. Commun.*, 2005, 2721–2723.

26 A. A. Miles, S. S. Misra and J. O. Irwin, *Epidemiol. Infect.*, 1938, **38**, 732–749.

27 A. J. Hedges, *Int. J. Food Microbiol.*, 2002, **76**, 207–214.

28 D. J. Parker, H. A. Jones, S. Petcher, L. Cervini, J. M. Griffin, R. Akhtar and T. Hasell, *J. Mater. Chem. A*, 2017, **5**, 11682–11692.

29 J. A. Smith, X. Wu, N. G. Berry and T. Hasell, *J. Polym. Sci. Part A Polym. Chem.*, 2018, **56**, 1777–1781.

30 J. C. Dyre, *Rev. Mod. Phys.*, 2006, **78**, 953.

31 D. J. Parker, S. T. Chong and T. Hasell, *RSC Adv.*, 2018, **8**, 27892–27899.

32 N. N. Greenwood and A. Earnshaw, *Chemistry of the Elements*, Elsevier, 2012.

Chapter 6

Conclusions & Future Work

6.1 Summary

The primary focus of this thesis was to investigate the use of different superhydrophobic polymer-nanoparticle composite (SPNC) systems to target routes of improving the hydrophobic performance, all-around durability, and subsequently, the real-world viability of these synthetic materials. A range of approaches were taken throughout this work including coating optimization (**chapter 2**), the discovery of suitable component substitutes (**chapter 3**), employment of a high-strength additive (**chapter 4**), use of alternative deposition approaches (**chapter 4**), and investigation into new materials for superhydrophobic materials design (**chapter 5**). Overall, we were able to demonstrate efficient methods of improving UV durability, physical strength and underwater stability, while preserving the functional properties of coatings for extended periods of time, enhancing the potential impact of the developed coatings.

6.2 Conclusions & Future Work

The initial work of this thesis detailed the development of a methodology that enabled the systematic optimisation of superhydrophobic coating components. It was well-documented by Golovin *et al*. that understanding components within a superhydrophobic system – in their case, polymers and small organic molecules – is crucial to targeting materials with high functionality and mechanical durability.[1] Although heavily documented in the literature, a universal method of systematically optimising SPNC systems was largely lacking. In most work, some extent of optimisation is carried out, generally through varying the weight percentage of one component in the system, however, this then complicates comparative assessment between systems that comprise different components (e.g. different sized particles or type of polymer).[2-6] Hence, developing an approach to comprehensively assess and compare various polymer systems in parallel, allowing for direct comparison, may shed more light on how the resultant properties of coatings relate to the size and type of components used (**chapter 2**). In this chapter, consistent morphological differences between thermoplastic and thermoset systems were discovered, that were seen to impact the overall hydrophobicity and functionality of individual coatings. Thus, leading to an independent range of optimal theoretical polymer thickness ($\mathbf{r}_{poly}$) values for each polymer category. Thermoset polymer, polydimethylsiloxane (PDMS), was observed to uniformly coat silica nanoparticles (SiO_2, 15 nm and 250 nm), while thermoplastic polymers could be seen to portray the role adhesive, binding particle aggregates together in a non-homogenous manner. It was anticipated that the observed structural differences were due to variations in surface energies between the hydrophobic polymers and HMDS-functionalised SiO_2 nanoparticle/solvent systems.

Therefore, highlighting considerations that must be made before designing a SPNC coating; for example, how does the intrinsic wettability and physical properties of the polymer affect the optimal $\mathbf{r}_{poly}$ range, and is the resultant morphology suitable to the desired application (e.g. work in chapter 4 benefited from incomplete particle coverage due to the nature of the deposition technique used). Through a systematic evaluation of SPNC systems, using the proposed SPNC design principle, trends in functionality could be easily identified and a facile comparison of thermoset and thermoplastic systems was possible. It is believed that this design principle could be extended to a wide range of SPNC systems, and could therefore, be used to aid the future of superhydrophobic materials optimisation, allowing for better comparison within the wider literature.

Further work in this area would include the use of complementary characterisation techniques, such as atomic force microscopy (AFM), to measure surface roughness more quantitatively, and in-depth analysis into the relationship between the intrinsic wettability of polymers (within the sub-categories) and optimal $\mathbf{r}_{poly}$ range/coating architecture, as assessment over a wider range of polymers (hydrophobic and hydrophilic) may be beneficial in developing our understanding. Furthermore, the measurement of tilt angles after surfaces had been abraded (Fig. 2.26, abrasion of coatings deposited *via* hot press) and measurement of advancing contact angles, receding contact angles and CAH for all reported systems, would shed more light on the interaction between the abraded surface and deposited water droplets.

Following this, substitute inorganic oxide particles were probed for their use in aesthetically pleasing superhydrophobic coatings, which was inspired by the known issues associated with UV-induced changes in surface wettability when using the wide-spread pigment, titanium dioxide (TiO_2, **chapter 3**). Although the brightest white pigment in current use, TiO_2 is an efficient photocatalyst and is widely known to initiate surface superhydrophilicity when employed in superhydrophobic materials, after undergoing exposure to UV light.[3,4,7,8] Molecularly functionalised TiO_2 composites have been reported to lose all functionality in as little exposure time as 10 minutes in simulated sunlight, rendering coatings completely unusable.[8] Though efforts have been made to overcome these weaknesses, most routes to success generally involve multi-step modification processes, and can frequently involve the use of fluorinated chemicals that carry a negative impact on the environment. Hence, new methods of imparting UV stability into pigmented superhydrophobic materials require further investigation. In chapter 3, we shed light on the degree of photodegradation and type of hydrophobic coating used to coat nanoparticles (molecular *vs* polymeric), identifying PDMS as a hydrophobic agent that is capable of suppressing photodegradation and extending the performance of photoactive superhydrophobic materials. It was suggested that a combination of high particle surface coverage, inherent stability towards oxidative degradation, backbone

flexibility and establishment of the optimal $\mathbf{r}_{poly}$ value/range, enabled PDMS to display high chemical stability. Coatings were found to be functional after 250 hr of UV exposure ($\mathbf{r}_{poly}$ value of 6 nm), while molecular coatings could be seen to undergo full surface degradation within 90 minutes, underlining the benefit of polymeric composites. Furthermore, cerium oxide (CeO_2) and TiO_2/CeO_2 hybrids were investigated for their use as alternative pigments to exclusive TiO_2, and found to be more inefficient as photocatalysts. Subsequently, resulting in enhanced UV stability and advanced protection against UV-induced surface hydrophilicity, while demonstrating that hybrid formulations can be used to fine-tune pigmentation and susceptibility of films to changes in surface wettability. However, issues related to the functionalisation of CeO_2 particles resulted in the use of a dual solvent system of n-hexane and ethanol that was later suspected to play a part in the premature photodegradation of CeO_2-PDMS composite coatings, particularly those with low $\mathbf{r}_{poly}$ values. After further investigation, it was shown that altering the solvent system can have a profound impact on the resultant coatings (polymer solubility and particle suspension), underlining the importance of system compatibility. Overall, this is a step forward in addressing the stability issues that surround the use of TiO_2 as the primary pigment within pigmented superhydrophobic coatings, and demonstrates the importance of considering a range of inorganic metal oxide/hybrid systems when designing high performance materials.

Further work that could be carried out to improve current findings would include, synthesising and hydrophobising CeO_2 nanoparticles *in-situ*, to avoid issues associated with the post-functionalisation of as-received CeO_2 nanoparticles, and to enable comparison between these and the as-received CeO_2-based systems (as-received particles were utilized originally to promote commercial use). Furthermore, an investigation into different sized inorganic metal oxide particles could be beneficial, as the particle size is widely reported to influence the rate of photocatalysis.

To further target the increased real-world application of superhydrophobic materials, and address issues associated with plastic waste and production, work was carried out on enhancing the general durability of superhydrophobic coatings, designed to protect the widely employed plastic, high-density polyethylene (HDPE, **chapter 4**). Although superhydrophobic coatings can impart several desirable functionalities (self-cleaning abilities, antimicrobial, etc.), the primary challenge stopping their widespread commercial use is their susceptibility to chemical, physical and underwater degradation.[9,10] Nonetheless, incorporating superhydrophobicity into the surfaces of bulk polymer substrates *via* direct roughening, has been frequently demonstrated using techniques such as hot moulding/embossing, use of a 'pulling' technique (stretching hot material into fibre-like features) and the use of anodized moulds.[11-13] However, in most cases, these fine surface architectures still need to be validated

under real-world conditions. Here, we took the alternative approach of using an external superhydrophobic coating, where the intrinsic resilience of the coating could be tuned to provide superior physical properties. The combination of a high temperature deposition technique, capable of processing dried formulations, and employment of a high-strength additive (carbon nanofibres, CNF), allowed for the facile development of superhydrophobic SiO_2-HDPE coatings that displayed strong mechanical resilience and long-term underwater stability. It was anticipated that the physical strength of materials arose from the targeted deposition of fibres at the interface, between the substrate and dried composite. Subsequently, promoting excellent integration between coating and substrate, and providing a secondary layer of surface coating that could provide additional surface roughness when subject to abrasive wear. Coatings remained efficient as self-cleaning materials in the early stages of abrasion (0-40/60 abrasion cycles), where they were seen to undergo a wetting state transition from Cassie-Baxter to Wenzel, after further abrasion; underlining a significant enhancement in the mechanical strength of materials, when compared to coatings that comprised no fibres, and conventional solution-based SiO_2-HDPE coatings. Furthermore, the short-term and long-term underwater stability of coatings were studied at two different hydrostatic pressures (0.196 kPa and 7.85 kPa), where the formulation/deposition approach and use of unmodified fibres were believed to induce underwater plastron stabilization. The repeated deposition of dried nanomaterial allowed for a continuous system of nanopores to be generated throughout the surface, preventing the rapid escape of entrapped air. Additionally, the employment of unmodified fibres provided structural reinforcement for these pores, especially at greater hydrostatic pressures, and acted to pin and stabilize the liquid-vapour interface, through interactions between polar groups on the surface of fibres (< 2%) and the surrounding water molecules. It was believed that this is a similar effect to the *Salvinia* effect (a natural example of a superhydrophobic surface with excellent air retention and underwater stability).[14] For short-term applications it was shown that a lower fibre content is beneficial, due to the initial attractive interactions between surface-exposed fibres and water molecules. However, for long-term submersion, it was found that a higher loading of fibres provided the greatest air retention, as a result of the induced stabilization effect, where **0.5**-SiO_2-HDPE was seen to retain its functionality as a self-cleaning coating after 4 weeks of continual submersion (at a submersion depth of 80 cm). In summary, this demonstrates how a simple additive can be used to generate high performance materials – highlighting the potential for other additives to be incorporated – and how fibres can be effectively used to secure external superhydrophobic coatings onto polymeric substrates, expanding the current application of fibres within the field of superhydrophobic materials design. Thus, presenting great potential for designing truly resilient superhydrophobic materials, where it is believed that these dried composite systems could be extended to other common thermoplastic systems, e.g. polypropylene. Within this

work, coatings also displayed initial signs of being self-healing materials, where partial regeneration of static superhydrophobicity could be seen over a short period of time (60 minutes) for coatings with low CNF contents.

To fully understand this and discover the true potential of these dried composite systems, repeat submersion measurements would need to be carried out to verify preliminary work, and more detailed experiments probing whether air-layer regeneration can occur over time, would be required. It is anticipated that regeneration could be evaluated *via* static and dynamic contact angle measurements during exposure to different environments (heat, air, inert atmosphere etc.).

Finally, an investigation into the use of more sustainable polymers for superhydrophobic materials design was carried out (**chapter 5**). To address the huge stockpile of elemental sulfur – an intrinsically hydrophobic, naturally occurring material that has been shown to display photocatalytic behaviour and antibacterial properties, and is a by-product of the petrochemical industries – inverse vulcanised sulfur copolymers were investigated for their use in superhydrophobic materials for the first time, to the best of our knowledge.[15-18] To date, most sulfur compounds that have been utilized within the field of superhydrophobic materials design, are compounds that comprise thiol groups and have been employed to facilitate thiolene click chemistry, with very little reported research focused on incorporating elemental sulfur or inverse vulcanised sulfur polymers into highly water repellent materials.[19-21] Lantos *et al.* carried out initial work within this area and reported the use of elemental sulfur particles to achieve superhydrophobic/photoactive coatings with enhanced UV stability (sulfur-Ag-TiO_2), taking advantage of the non-photodegradable nature and inherent hydrophobicity of elemental sulfur.[22] However, resultant coatings displayed high contact angle hysteresis, likely due to the presence of hydrophilic particles (Ag-TiO_2) and lack of other hydrophobic agents within the composite. It is anticipated that due to the solubility issues that surround elemental sulfur and varied solubility of sulfur copolymers, that little focus has been paid to the potential benefit of incorporating these materials into superhydrophobic coatings.[23,24] Here, it was shown that an organic crosslinker, in this case, the naturally-derived molecule perillyl alcohol, could be used as a route to solubilising sulfur *via* the introduction of organic groups, and suspected low degree of crosslinking/formation of a hyperbranched polymer (as opposed to a highly crosslinked polymer). Optimal polymers were established through a combination of high solubility and high sulfur content, in addition to their ability to show high stability during the initial and re-processing procedures, which was confirmed *via* a series of characterisation techniques (50-70 wt % elemental sulfur). While high sulfur content polymers (80-90 wt % elemental sulfur) were partially insoluble and unstable, due to having a reduced mass of crosslinker. Furthermore, we demonstrated that SiO_2 nanoparticles could be introduced to

promote superhydrophobicity, and highlighted that although polymers may appear initially stable they can undergo depolymerisation during reprocessing, as particles of elemental sulfur that had leached from the polymer were detected on the surface of coatings that comprised the 70 wt % elemental sulfur copolymer. Coatings primarily displayed Cassie-Baxter wetting behaviour and efficient self-cleaning properties, however, high polymer loadings i.e., ≤ 40 wt % SiO_2, were found to promote water adhesion due to limitations in surface roughness. When assessing the functional properties of a representative sulfur-perillyl alcohol-SiO_2 coating (60 wt % elemental sulfur copolymer, 60 wt % SiO_2 = PER_60-60), it was found to be multifunctional and display not only high superhydrophobicity and low contact angle hysteresis, but also efficient photocatalysis and antibacterial behaviour. Through assessment of both surface and solution effects, bacterial attachment/growth was found to be lowest for PER_60-60, in comparison to flat elemental sulfur, flat sulfur-perillyl alcohol copolymer (60 wt % elemental sulfur) and the negative control (plain glass). Overall, a 62.46 % reduction of bacteria in solution and 99.89 % bacterial reduction on the surface was found, in comparison to the negative control, underlining the benefits of combining an active antibacterial agent with extreme surface roughness (limited area for bacterial attachment and growth due to the large liquid-vapour interface). Furthermore, as a significant challenge within the field of superhydrophobic materials design, is the fabrication of synthetic materials that display dual photocatalysis and superhydrophobicity, the non-photodegradation nature of sulfur was of particular interest. Although these coatings were found to be successful and able to initiate the photoreduction mechanism of the dye resazurin within 40 minutes of exposure to UV light (254 nm, 8W) – being around 4 times less efficient than the widely established photocatalyst TiO_2 and comparable to that of flat elemental sulfur – there was anticipated to be a trade-off between polymer solubility (weight percentage of crosslinker) and UV stability. It was suspected that exposure to intense UV not only promoted dye degradation, but also facilitated the breakdown of physical crosslinkers within the polymer matrix, resulting in the production of organic contaminants and eventually UV-induced changes in surface hydrophobicity. PER_60-60 coatings were able to withstand ~90 minutes of UV before significant changes in surface hydrophobicity were seen to take place, where a change in wetting behaviour from Cassie-Baxter to Wenzel was initiated from the ~60-minute mark. Unfortunately, due to time constraints, only one coating was selected for functional examination, and so a comprehensive understanding of the relationship between UV stability and crosslinker composition/weight percent was unable to be deduced.

To further aid our understanding and promote better functional use of inverse sulfur copolymers within superhydrophobic materials, additional research into alternative crosslinkers and the assessment of coatings with various sulfur-crosslinker-SiO_2 compositions

would need to be carried out. For example, examination of crosslinkers that form more extensively crosslinked networks, as it is anticipated that these would provide greater resistance against photodegradation. However, the relationship between crosslinking and solubility would need careful consideration, as this is foreseen to be a limitation here. Although a comprehensive study has not been completed, the preliminary work carried out here demonstrates that inverse vulcanised sulfur polymers have great potential in developing highly water repellent materials with superior functional properties, particularly dual photocatalysis and superhydrophobicity, as surfaces retained their superhydrophobicity, while simultaneously facilitating the photoreduction mechanism of the dye. Thus, paving the way for further investigation and providing more sustainable raw materials options for superhydrophobic materials design, offering alternatives to the potentially carcinogenic and expensive metal/metal oxides that are frequently employed to impart photocatalytic and/or antibacterial properties.

6.3 References

1 K. Golovin, M. Boban, J. M. Mabry and A. Tuteja, *ACS Appl. Mater. Interfaces*, 2017, **9**, 11212–11223.

2 Z. Liu, H. Wang, E. Wang, X. Zhang, R. Yuan and Y. Zhu, *Polymer (Guildf).*, 2016, **82**, 105–113.

3 X. Ding, S. Zhou, G. Gu and L. Wu, *J. Mater. Chem.*, 2011, **21**, 6161–6164.

4 Y. Qing, C. Yang, Y. Sun, Y. Zheng, X. Wang, Y. Shang, L. Wang and C. Liu, *Colloids Surfaces A Physicochem. Eng. Asp.*, 2015, **484**, 471–477.

5 E. M. Baba, C. E. Cansoy and E. O. Zayim, *Prog. Org. Coatings*, 2016, **99**, 378–385.

6 S. S. Latthe, R. S. Sutar, T. B. Shinde, S. B. Pawar, T. M. Khot, A. K. Bhosale, K. K. Sadasivuni, R. Xing, L. Mao and S. Liu, *ACS Appl. Nano Mater.*, 2019, **2**, 799–805.

7 G. E. Morris, W. A. Skinner, P. G. Self and R. S. C. Smart, *Colloids Surfaces A Physicochem. Eng. Asp.*, 1999, **155**, 27–41.

8 S. Nishimoto, M. Becchaku, Y. Kameshima, Y. Shirosaki, S. Hayakawa, A. Osaka and M. Miyake, *Thin Solid Films*, 2014, **558**, 221–226.

9 C. R. Crick, in *Superhydrophobic Surfaces-Fabrications to Practical Applications*, IntechOpen, 2018.

10 H. Y. Erbil, *Langmuir*, 2020, **36**, 2493–2509.

11 K. Maghsoudi, E. Vazirinasab, G. Momen and R. Jafari, *Ind. Eng. Chem. Res.*, 2020, **59**, 9343–9363.

12 F. Vüllers, G. Gomard, J. B. Preinfalk, E. Klampaftis, M. Worgull, B. Richards, H. Hölscher and M. N. Kavalenka, *Small*, 2016, **12**, 6144–6152.

13 E. Puukilainen, T. Rasilainen, M. Suvanto and T. A. Pakkanen, *Langmuir*, 2007, **23**, 7263–7268.

14 W. Barthlott, T. Schimmel, S. Wiersch, K. Koch, M. Brede, M. Barczewski, S. Walheim, A. Weis, A. Kaltenmaier and A. Leder, *Adv. Mater.*, 2010, **22**, 2325–2328.

15 J. Lim, J. Pyun and K. Char, *Angew. Chemie Int. Ed.*, 2015, **54**, 3249–3258.

16 G. Liu, P. Niu, L. Yin and H.-M. Cheng, *J. Am. Chem. Soc.*, 2012, **134**, 9070–9073.

17 V. A. Peyman and S. Azizian, *Photochem. Photobiol.*, 2020, **96**, 1191–1199.

18 L. Libenson, F. P. Hadley, A. P. McIlroy, V. M. Wetzel and R. R. Mellon, *J. Infect. Dis.*, 1953, 28–35.

19 Y. Fang, C. Liu, M. Li, X. Miao, Y. Pei, Y. Yan, W. Xiao and L. Wu, *Ind. Eng. Chem. Res.*, 2020, **59**, 6130–6140.

20 B. J. Sparks, E. F. T. Hoff, L. Xiong, J. T. Goetz and D. L. Patton, *ACS Appl. Mater. Interfaces*, 2013, **5**, 1811–1817.

21 H. Zhang, Y. Ma, J. Tan, X. Fan, Y. Liu, J. Gu, B. Zhang, H. Zhang and Q. Zhang, *Compos. Sci. Technol.*, 2016, **137**, 78–86.

22 E. Lantos, L. Mérai, Á. Deák, J. Gómez-Pérez, D. Sebők, I. Dékány, Z. Kónya and L. Janovák, *J. Mater. Sci. Technol.*, 2020, **41**, 159–167.

23 V. S. Wadi, K. Halique and S. M. Alhassan, *Ind. Eng. Chem. Res.*, 2020, **59**, 13079–13087.

24 D. J. Parker, H. A. Jones, S. Petcher, L. Cervini, J. M. Griffin, R. Akhtar and T. Hasell, *J. Mater. Chem. A*, 2017, **5**, 11682–11692.

Appendix

A.1 Chapter 2 Appendix

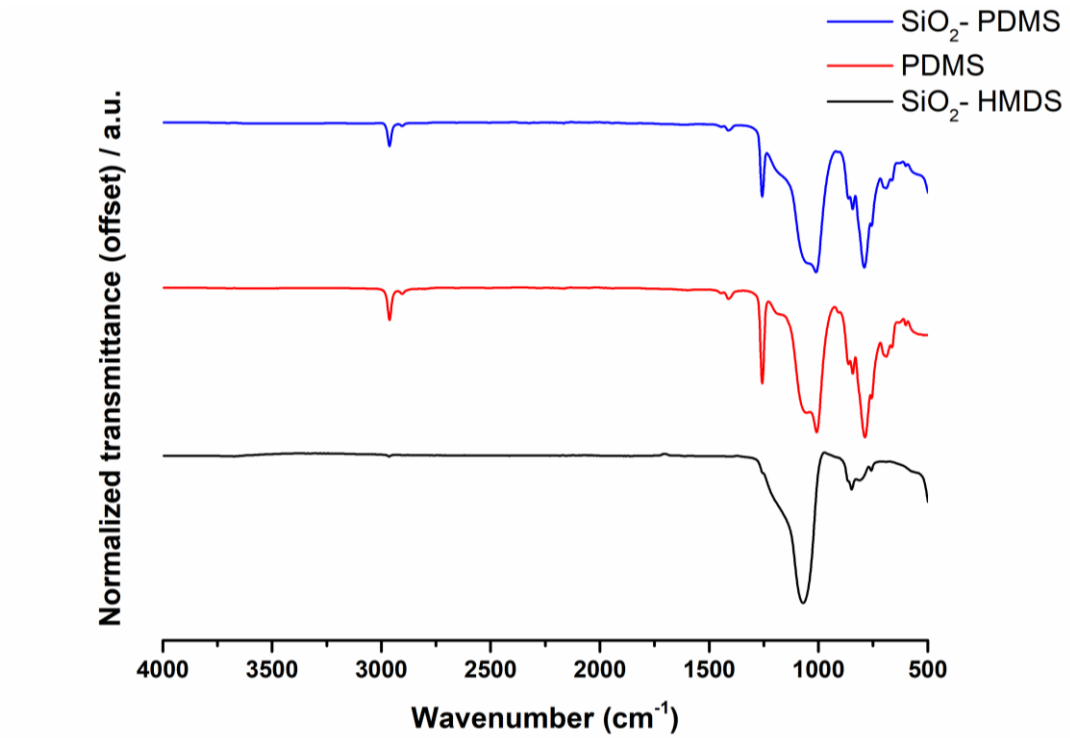

Figure A1: Stacked FTIR spectra of SiO_2-PDMS composite ($\mathbf{r}_{sphere}$ = 125 nm, **blue line**), PDMS (**red line**) and HMDS-functionalised SiO_2 nanoparticles ($\mathbf{r}_{sphere}$ = 125 nm, **black line**).

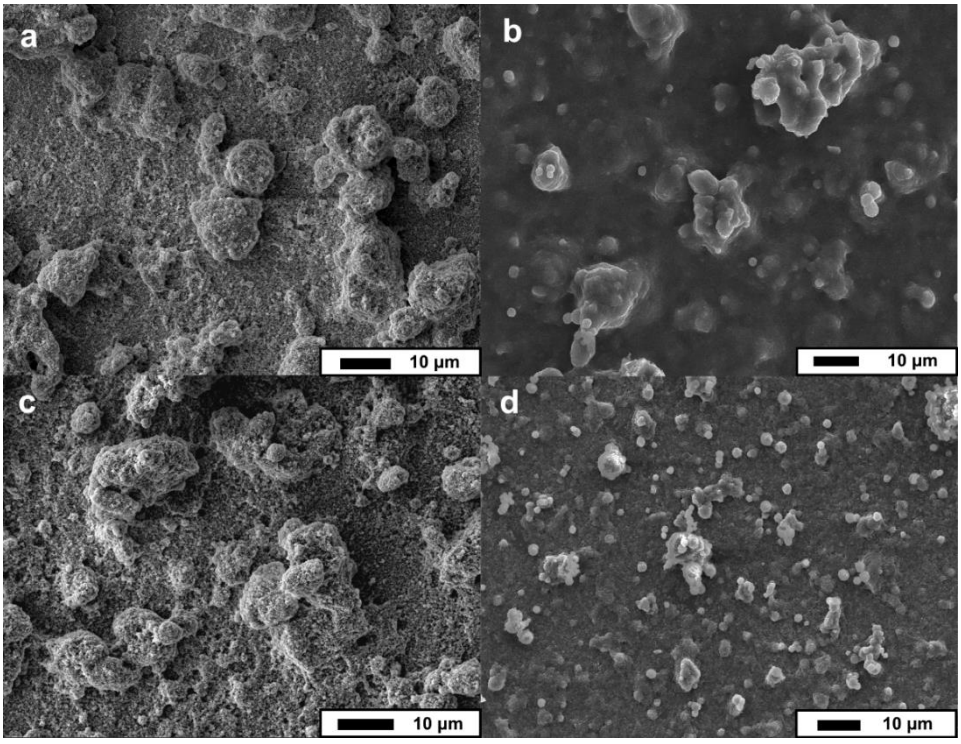

Figure A2: Lower magnification SEM micrographs of SiO_2-PDMS SPNCs, deposited *via* spray-coating from a hexane solution, for comparative purposes; (**a**) $\mathbf{r}_{sphere}$ = 7.5 nm and $\mathbf{r}_{poly}$ = 6 nm; (**b**) $\mathbf{r}_{sphere}$ = 7.5 nm and $\mathbf{r}_{poly}$ = 8 nm, (**c**) $\mathbf{r}_{sphere}$ = 125 nm and $\mathbf{r}_{poly}$ = 80 nm and (**d**) $\mathbf{r}_{sphere}$ = 125 nm and $\mathbf{r}_{poly}$ = 120 nm. Scale bars are shown.

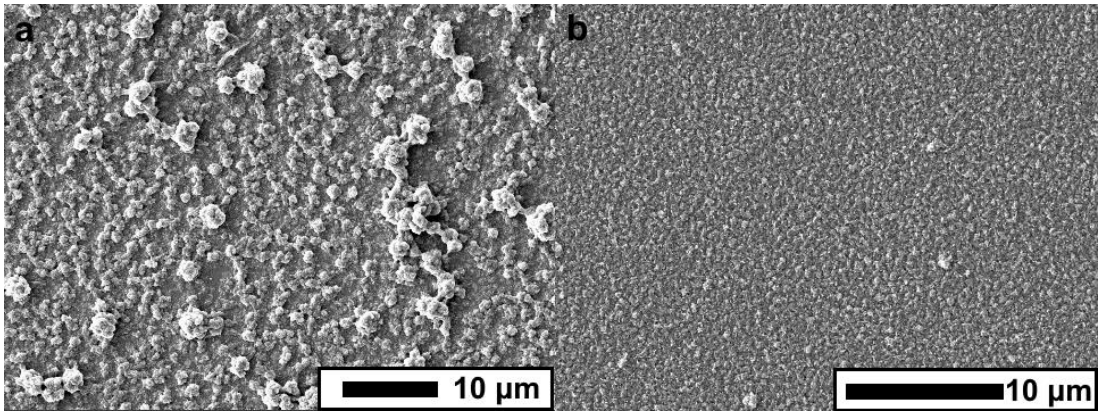

Figure A3: SEM micrographs of a polypropylene coating (in the absence of any roughening agents), deposited *via* dip-coating from a xylene solution; (a) in regions where a roughened microstructure was visible and (**b**) in regions were a flatter morphology was apparent. Scale bars are shown.

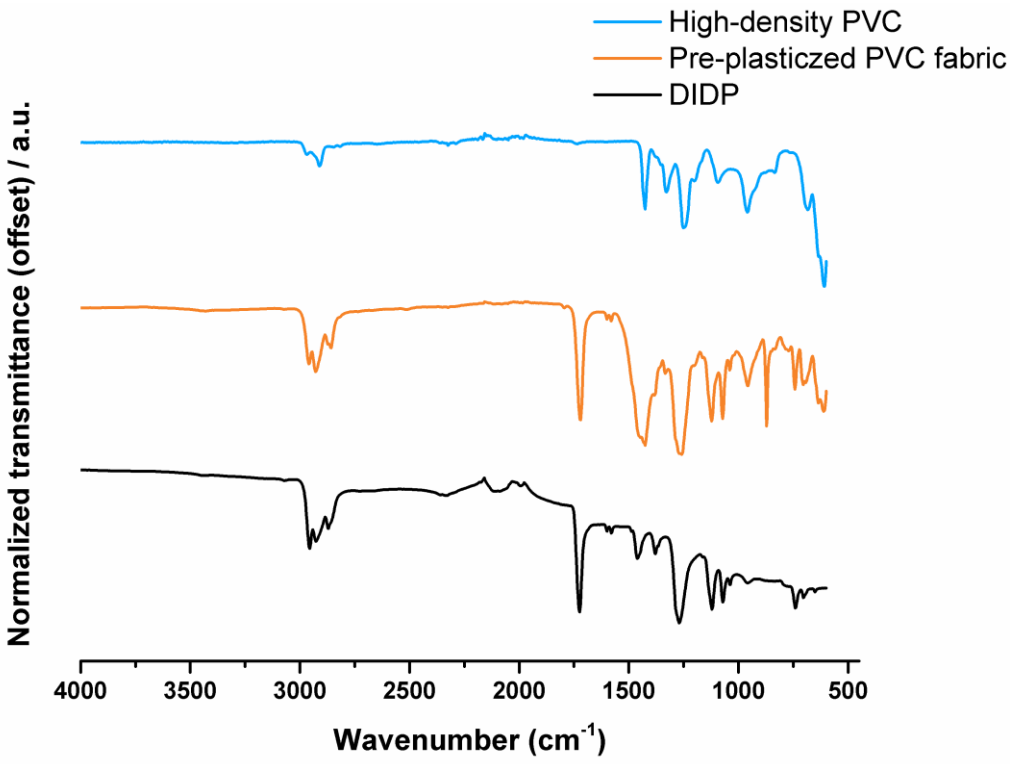

Figure A4: Stacked FTIR spectra of DIDP, bought-in pre-plasticized PVC fabric and high-density PVC. Vibrational bands characteristic of phthalate esters were apparent in both DIDP and the pre-plasticized PVC fabric; 1720 cm^{-1} representative of the ester (-COOH), 1579 cm^{-1} and 1599 cm^{-1} representative of the aromatic ring quadrant stretching vibrations, and 742 cm^{-1} characteristic of the ortho-substituted aromatic ring.[40]

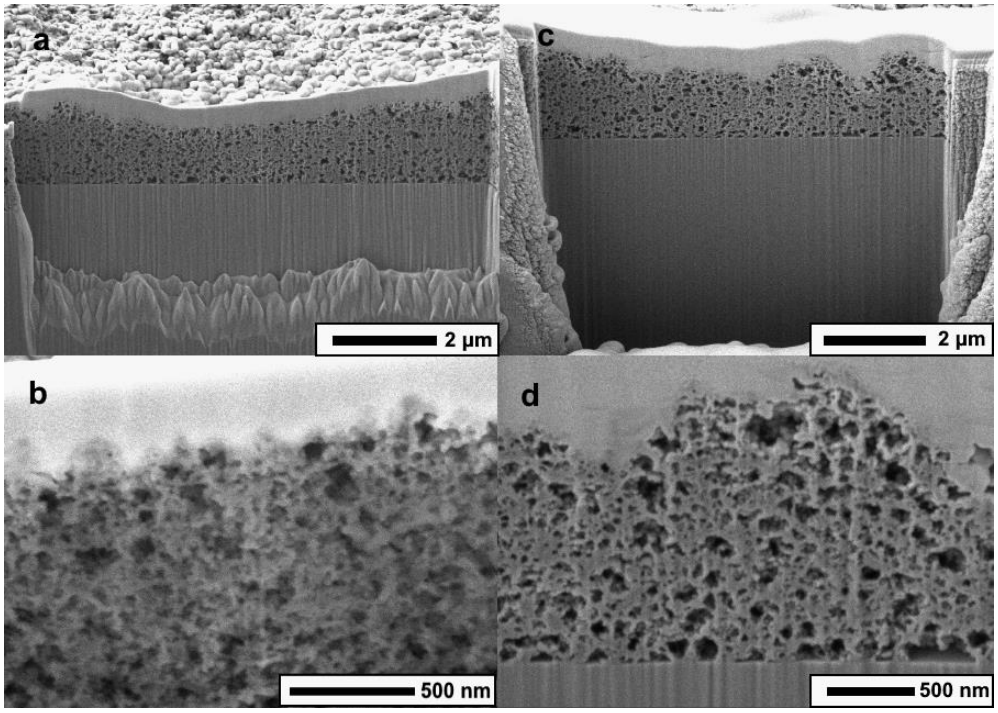

Figure A5: SEM micrographs of FIB-prepared cross-sections of SiO_2-PVC coatings, prepared on silicon wafer *via* spray-coating from THF solutions, with a platinum strap applied to the surface before milling for protection; (**a, b**) 15 nm nanoparticle diameter and (**c, d**) 250 nm nanoparticle diameter at low and high magnifications. Scale bars are shown.

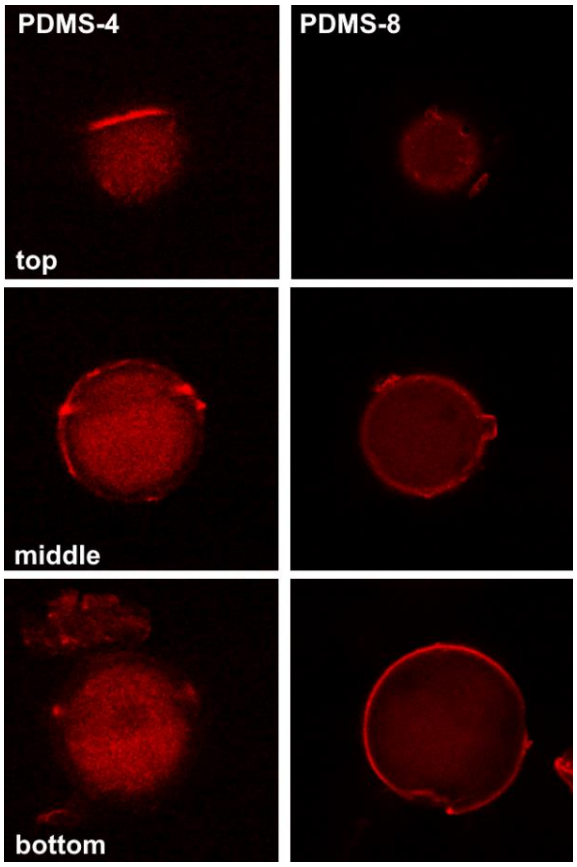

Figure A6: Confocal fluorescence microscopy images, detailing z-stack slices at the top, middle and bottom of a SiO_2 microparticle, coated with PDMS and stained with Nile Red; PDMS-4 (**left**) and PDMS-8 (**right**).

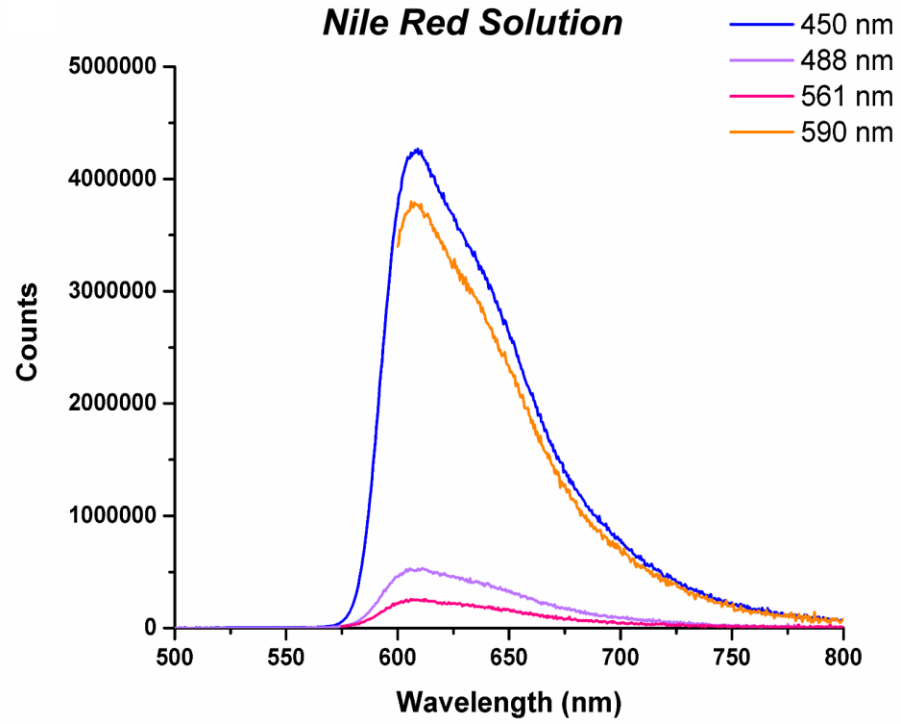

Figure A7: Overlaid fluorescence emission spectra of Nile Red dye solution (0.196 mM, chloroform), using excitation wavelengths of 450 nm, 488 nm, 561 nm and 590 nm.

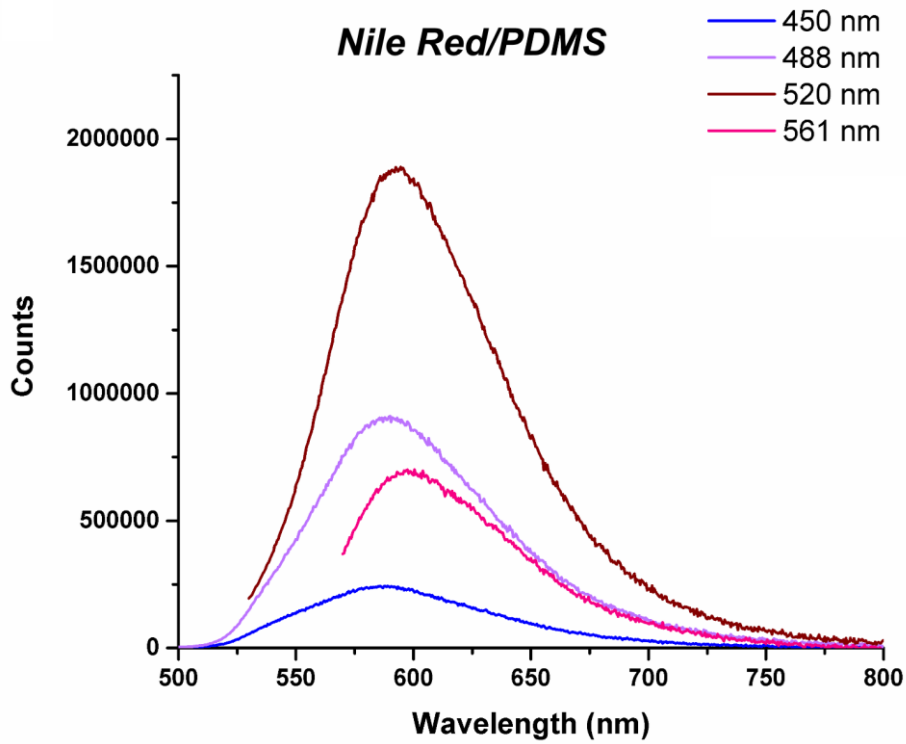

Figure A8: Overlaid fluorescence emission spectra of PDMS polymer stained with Nile Red dye [fabricated in the same way as PDMS-8 samples for confocal fluorescence, but without SiO_2 microparticles], using excitation wavelengths of 450 nm, 488 nm, 520 nm and 561 nm.

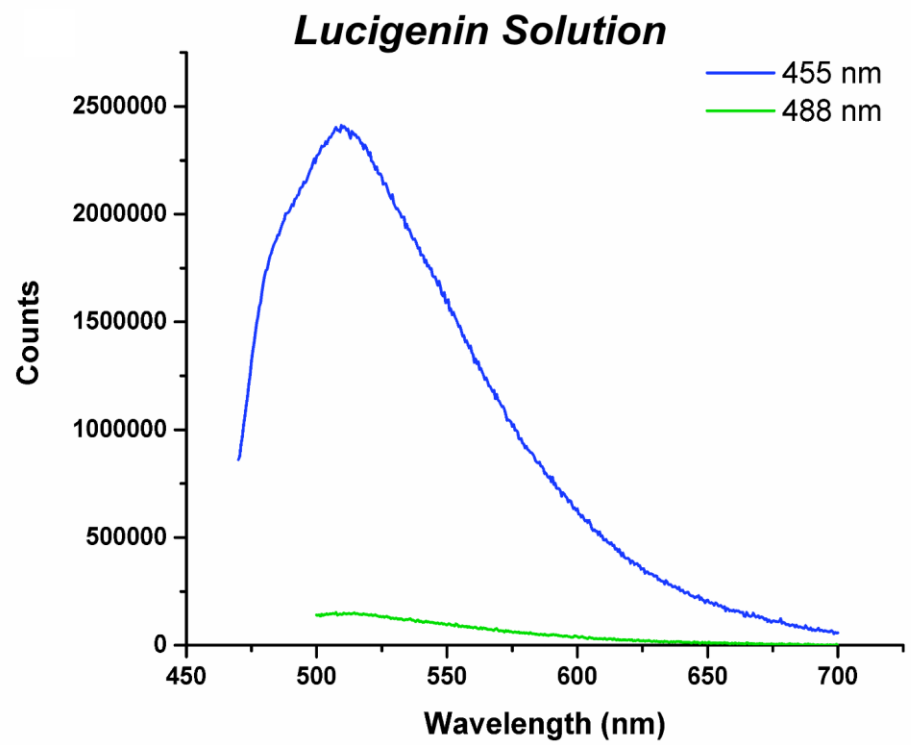

Figure A9: Overlaid fluorescence emission spectra of Lucigenin dye solution (0.196 mM, THF/H_2O), using excitation wavelengths of 455 nm and 488 nm.

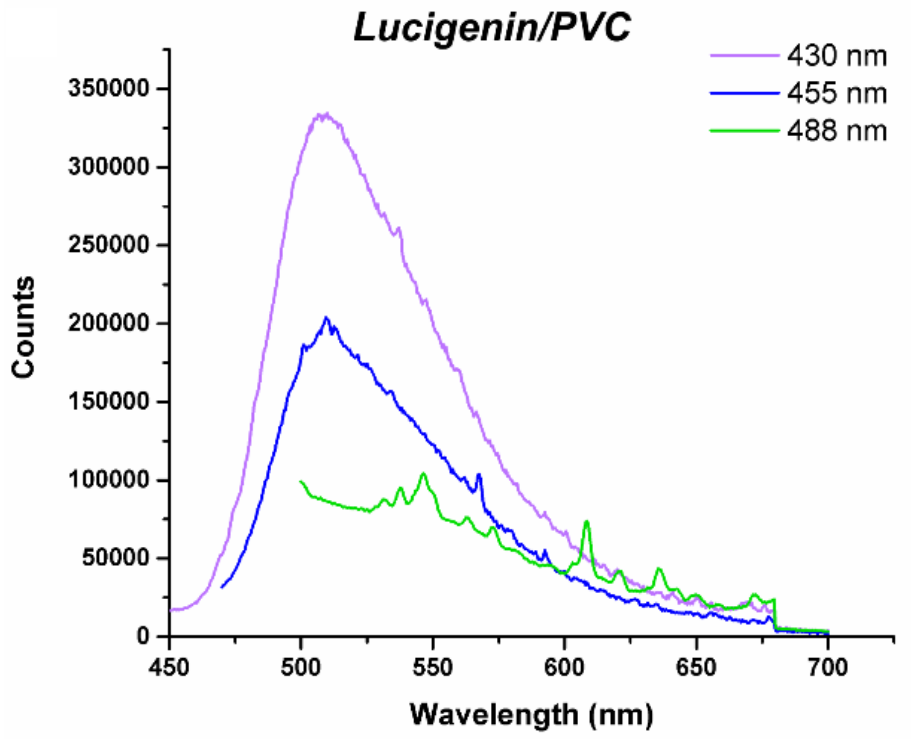

Figure A10: Overlaid fluorescence emission spectra of PVC polymer stained with Lucigenin dye [fabricated in the same way as PVC samples for confocal fluorescence, but without SiO_2 microparticles], using excitation wavelengths of 430 nm, 455 nm and 488 nm.

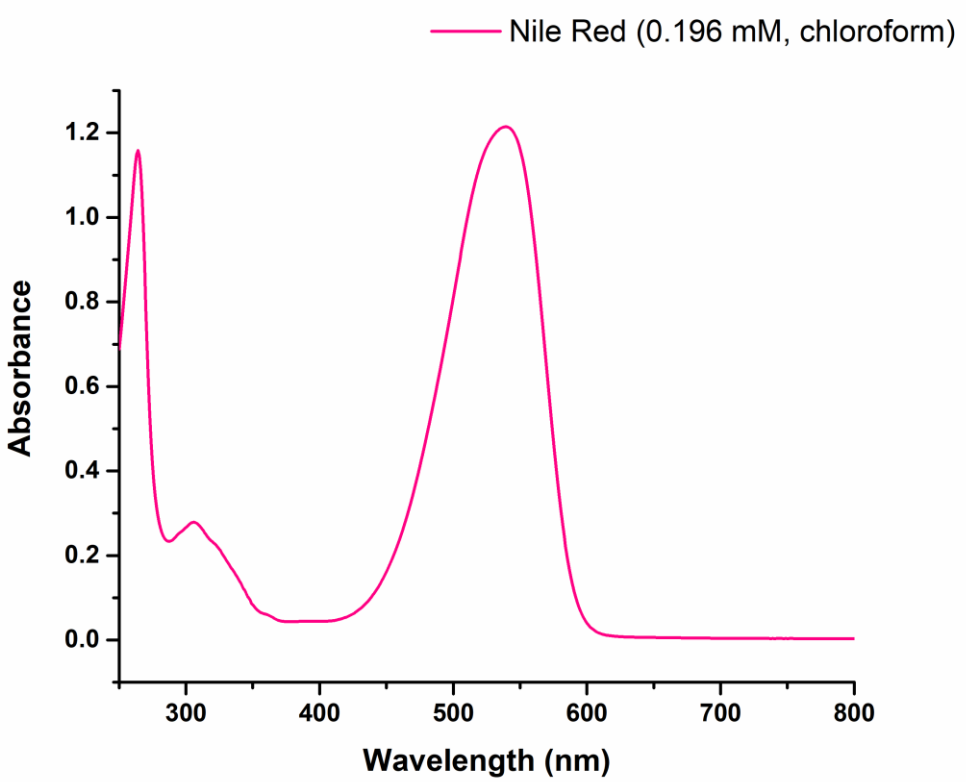

Figure A11: UV-Vis absorption spectra of Nile Red dye solution (0.196 mM, chloroform).

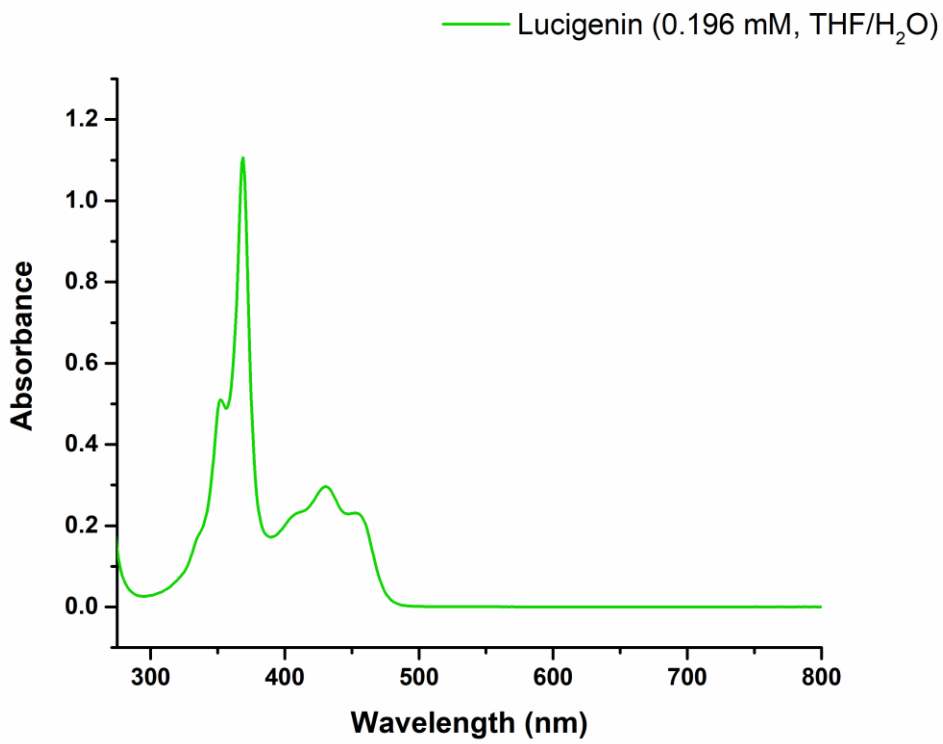

Figure A12: UV-Vis absorption spectra of Lucigenin dye solution (0.196 mM, THF/H_2O).

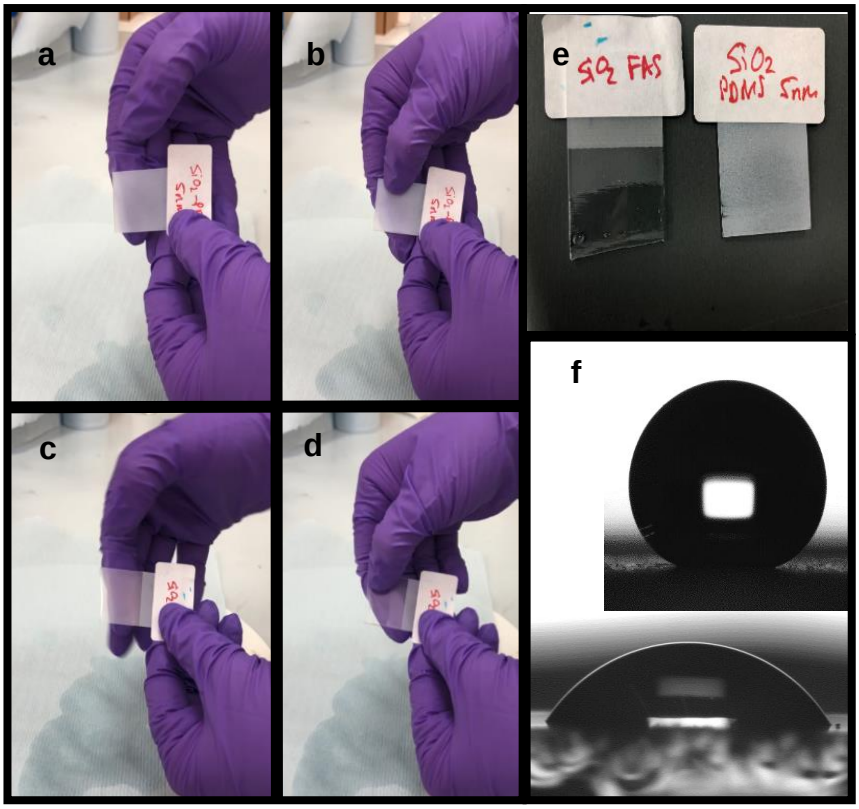

Figure A13: Images depicting; (**a, b**) SiO_2-PDMS ($\mathbf{r}_{sphere}$ = 7.5 nm, $\mathbf{r}_{poly}$ = 5 nm) before and after finger wipe; (**c, d**) SiO_2-FAS ($\mathbf{r}_{sphere}$ = 7.5 nm) before and after finger wipe; (**e**) both samples after finger wipe. (**f**) Water droplets on SiO_2-PDMS (**top**) and SiO_2-FAS (**bottom**) after finger wipe.

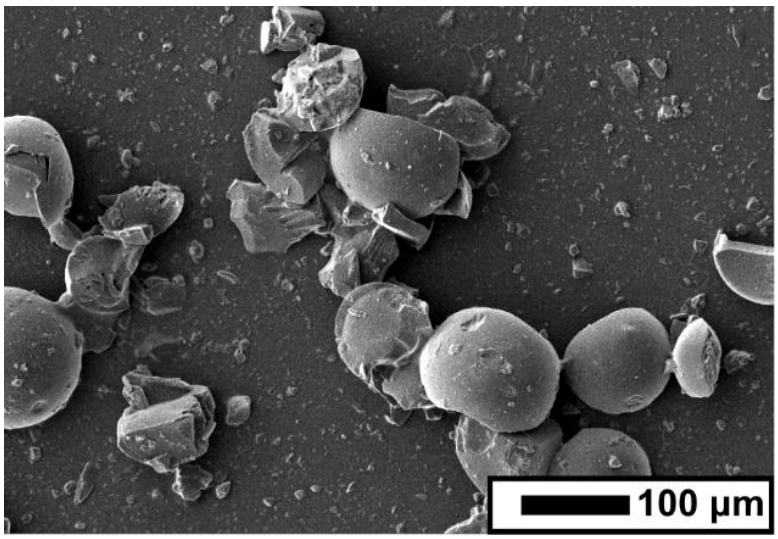

Figure A14: SEM micrographs of the scaled-up SiO_2-PVC thermoplastic SPNC system, deposited via drop-casting from a THF/H_2O solution, highlighting fractured SiO_2 microparticles (particle diameter is 40-75 µm). Scale bar is shown.

Table A1: Recorded static contact angles for varying dip-coating settings (emersion rate; time in suspension; withdrawing rate; drying time before next iteration) for SiO_2-polyethylene SPNC formulations ($\mathbf{r}_{poly}$ = 1.5 nm, $\mathbf{r}_{sphere}$ = 7.5 nm), dip-coated from a xylene solution using 6 iterations.

Emersion rate	*Time in suspension (s)*	*Withdrawing rate*	*Drying time before next iteration (s)*	*Recorded static contact angle*
75	10	50	10	164
75	10	50	20	164
75	5	50	10	157
75	5	50	20	160
75	20	50	10	164
150	10	50	10	159
150	10	50	20	162
150	5	50	10	158
150	5	50	20	160
150	20	50	10	163
300	10	50	10	162
300	10	50	20	161
300	5	50	10	164
300	5	50	20	163
300	20	50	10	164

*50 = 760 mm/min; 75 = 1530 mm/min; 150 = 8000 mm/min; 300 = 22000 mm/min

Table A2: Recorded static contact angles for iterations ranging 6IT-8IT (emersion rate 1530 mm/min; time in suspension 10 seconds; withdrawing rate 760 mm/min; drying time before next iteration 10 seconds) for a SiO_2-polyethylene SPNC formulation ($\mathbf{r}_{poly}$ = 1.5-3 nm, $\mathbf{r}_{sphere}$ = 7.5 nm), dip-coated from a xylene solution.

$\mathbf{r}_{poly}$	*Iteration*	*Recorded static contact angle*
1.5 nm	6 IT	162° ± 1
1.5 nm	7 IT	165 ° ± 2
1.5 nm	8 IT	161° ± 3
2 nm	6 IT	161° ± 2
2 nm	7 IT	162° ± 3
2 nm	8 IT	160° ± 2
3 nm	6 IT	156° ± 3
3 nm	7 IT	161° ± 2
3 nm	8 IT	160° ± 2

Table A3: Calculated surface free energy values and static contact angles for flat thermoset and thermoplastic polymers (measured *via* the drop shape analyser using water and diiodo-methane solvents, OWRK model).

Polymer	*Recorded static contact angle (water)*	*Recorded static contact angle (diiodo-methane)*	*Surface free energy (mN/m)*
PDMS	104° ± 2	77° ± 3	19.98 ± 2.11
PVC	91° ± 3	34° ± 3	42.97 ± 1.56
Polyethylene	80° ± 6	49° ± 2	39.24 ± 3.41
Polypropylene	103° ± 2	58° ± 1	29.95 ± 0.83

Table A4: Measured particle diameters of as-received SiO_2 microparticles; manually measured using the Image J tool and SEM images, with a ruler that was calibrated against the SEM scale bar, for a sample size of 50 particles.

*SiO_2 particle size (**μ**m)*		
80.33	28.3	54.3
68.85	29.51	23.59
32.83	55.69	45.01
40.98	49.31	26.48
73.77	60.79	50.29
62.3	31.15	51.24
19.88	36.84	48.41
19.94	38.38	23.64
39.34	79.59	57.96
32.79	59.21	42.62
31.15	60.66	54.07
62.3	34.85	46.94
68.85	33.1	*Average = 45.1 ± 16*
41.02	23.18	
50.82	61.25	
32.79	29.05	
31.32	44.75	
67.21	25.05	
44.29	46.89	

A.2 Chapter 3 Appendix

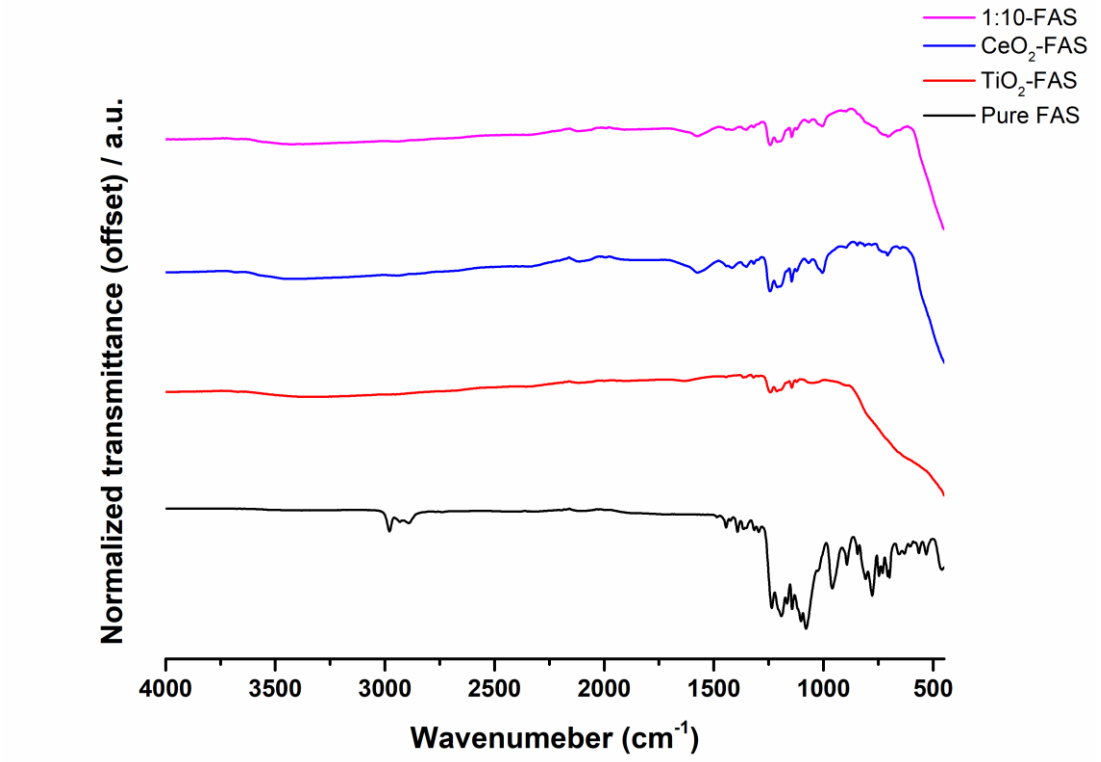

Figure A1: Stacked FTIR spectra of FAS composite coatings, prior to any UV exposure.

Expected signals were present in coatings. Pure FAS sample displayed vibrational bands representative of alkyl groups (-CH_2) between 2978-2891 cm^{-1}, bands at 1236 cm^{-1}, 1192 cm^{-1}, 1144 cm^{-1} and 1103 cm^{-1} characteristic of -CF_2 vibrations, bands at 1100 cm^{-1} and 960 cm^{-1} corresponding to Si-O-Si/Si-O-aliphatic vibrations and additional bands at 890 cm^{-1}, 845 cm^{-1} and between 808-705 cm^{-1}, representative of –CF_3 vibrations.[31] Additional peaks can be seen, characteristic of the metal oxide component; TiO_2-FAS showed a peak at ~800-450 cm^{-1} which was characteristic of the Ti-O/Ti-O-Ti stretching vibration and CeO_2-FAS/1:10-FAS spectra comprised a peak at ~560-450 cm^{-1} which can be owed to O-Ce-O stretching.[37,31] Signals representative of FAS within composite coating spectra appear relatively weak and the vibrational bands characteristic of alkyl groups were absent. This can be attributed to the self-assembled monolayer of FAS molecules, subsequently reducing the intensity of vibrational bands. It must be noted that impurity peaks at ~ 2400 cm^{-1} representing CO_2 can be seen in spectra.

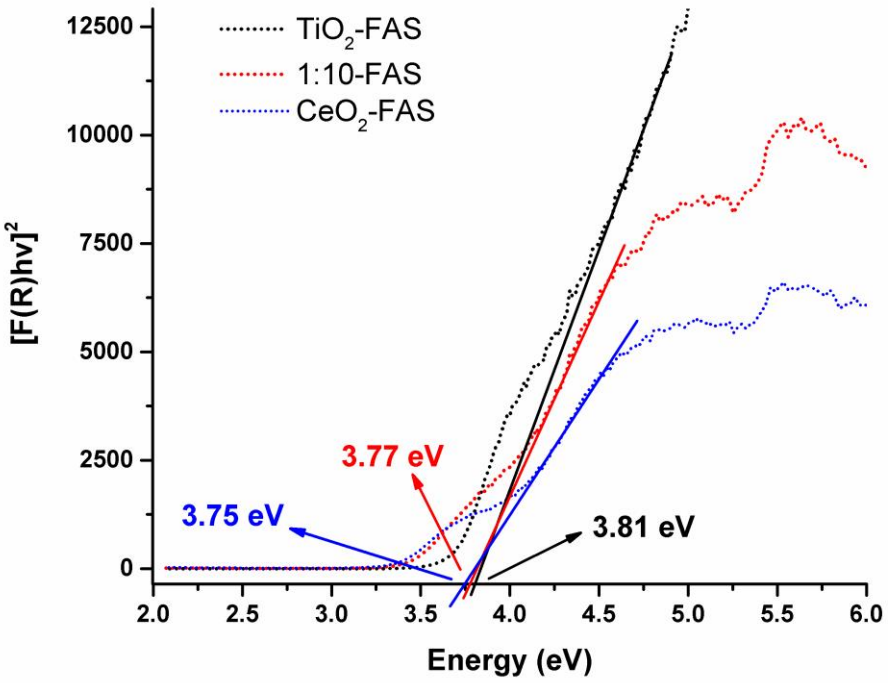

Figure A2: Band gap energies of TiO_2-FAS, CeO_2-FAS and 1:10-FAS, calculated using the Kubelka-Munk theory, where TiO_2-FAS was found to have an E_g value of 3.81 eV, CeO_2-FAS was found to have an E_g value of 3.75 eV and 1:10-FAS was found to have an E_g value of 3.77 eV.

Table A1: Measured particle diameters of as-received TiO_2 and CeO_2 nanoparticles; manually measured using the Image J tool and TEM images, with the ruler that was calibrated against the TEM scale bar, for a sample size of 50 particles per metal oxide (**left hand and middle columns**). Estimated polymer thickness for a PDMS layer surrounding TiO_2 nanoparticles; averaged over 25 measurements and measured using the same technique and S-TEM images (**right hand column**).

TiO_2 particle size (nm)	*CeO_2 particle size (nm)*	*Polymer thickness (nm)*
20.59	26.78	5.58
26.45	17.32	8.43
19.12	9.33	6.88
21.19	10.73	6.37
14.33	30.00	11.35
23.45	23.56	8.72
26.87	18.40	4.77
35.66	15.10	6.19
31.64	50.92	7.16

20.69	22.84	5.47
38.14	19.13	4.42
20.44	24.60	4.88
21.51	23.40	7.75
22.91	12.62	9.35
30.29	29.40	4.56
23.54	15.60	8.22
23.75	86.50	5.12
21.00	37.47	6.35
24.23	13.92	7.71
17.15	26.00	10.08
17.59	29.18	8.02
21.05	25.67	8.25
18.00	24.12	6.88
19.25	21.18	11.20
50.72	18.81	4.79
43.21	17.44	*Average = 7.1* $\pm$ *2*
36.36	29.28	
27.82	39.40	
13.02	28.01	
12.57	27.42	
28.19	23.12	
16.54	45.47	
27.88	37.50	
18.39	29.89	
24.30	24.24	
14.86	23.00	
24.20	66.71	
21.14	36.69	
28.52	26.40	
23.10	15.56	
25.55	25.12	
17.10	24.86	
19.90	13.40	
24.84	23.71	
28.74	15.74	

22.26	12.17
26.22	26.83
21.85	19.15
25.96	41.16
22.85	22.67
Average = 24.1 ± 7	*Average = 26.6 ±14*

Table A2: EDX data for TiO_2-PDMS, CeO_2-PDMS and 1:10-PDMS coatings, showing the element atomic ratio and approximate composition of coatings.

Coating	*Element atomic ratio (%)*				
	C K	*O K*	*Si K*	*Ti K*	*Ce K*
TiO_2-PDMS	28.12	50.14	15.01	6.73	-
CeO_2-PDMS	40.34	35.78	12.51	-	11.37
1:10-PDMS	27.68	43.70	12.11	3.77	12.74

A.3 Chapter 4 Appendix

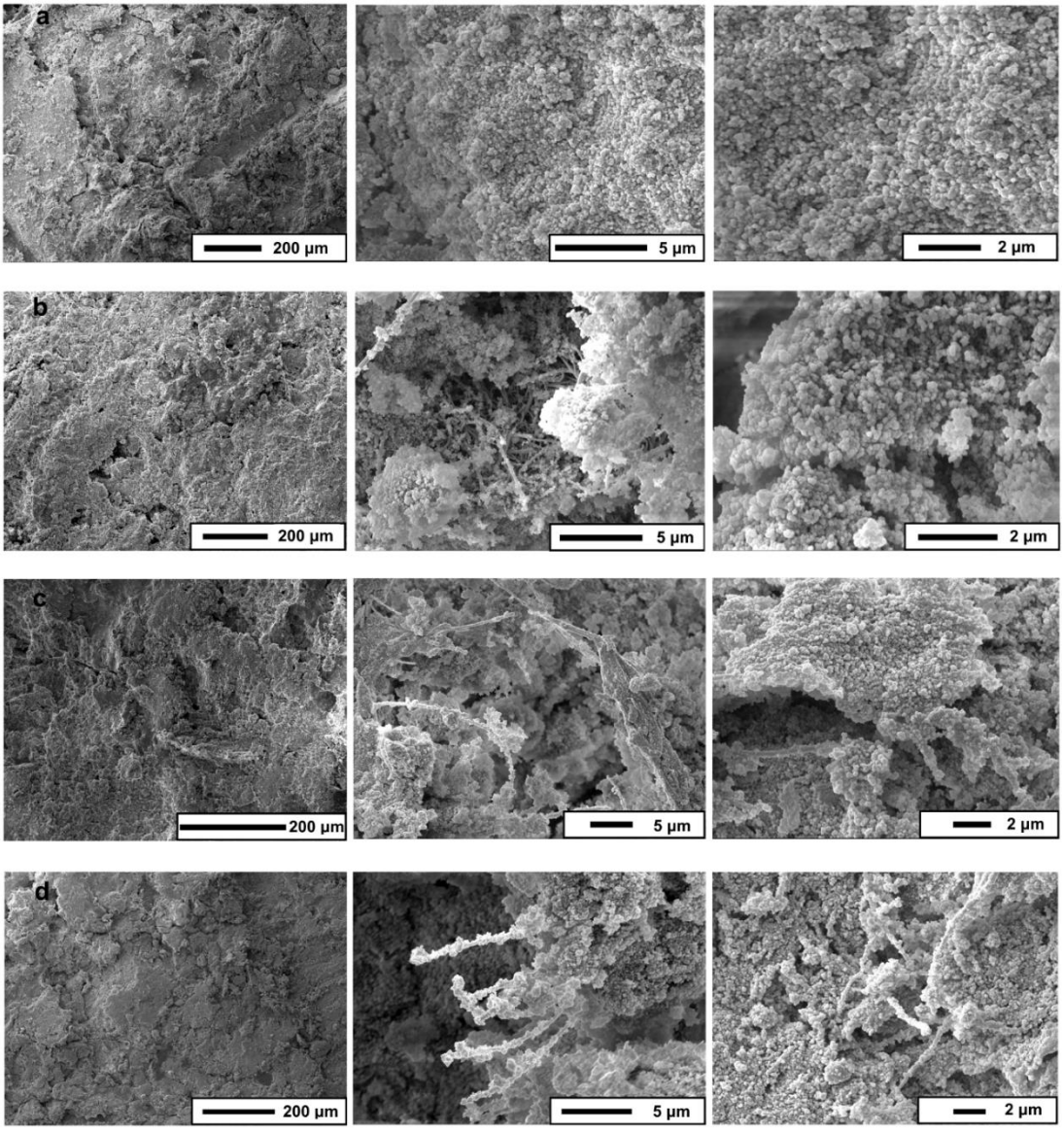

Figure A1: Top-down SEM micrographs highlighting the roughened surface morphology of coatings, at different magnifications; (**a**) SiO_2-HDPE; (**b**) **0.1-** SiO_2-HDPE; (**c**) **0.3-** SiO_2-HDPE; and (**d**) **0.5-** SiO_2-HDPE. Scale bars are shown.

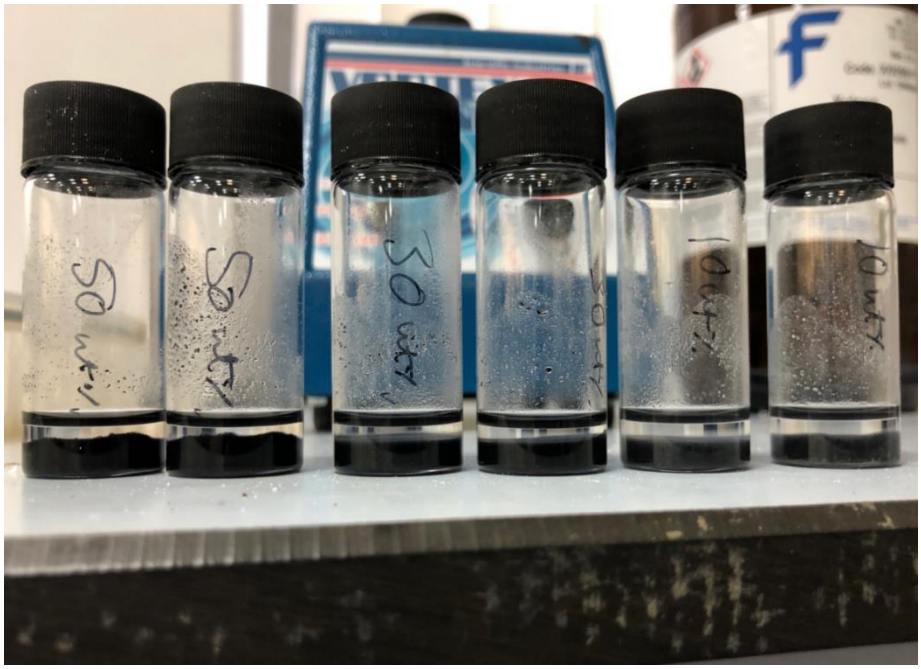

Figure A2: Image highlighting the partial phase separation of components within CNF-containing slurries, when left to stand at ambient temperature for 10 minutes; [2 vials of each, (**left**) **0.5-** SiO_2-HDPE, (**middle**) **0.3-** SiO_2-HDPE and (**right**) **0.1-** SiO_2-HDPE].

.

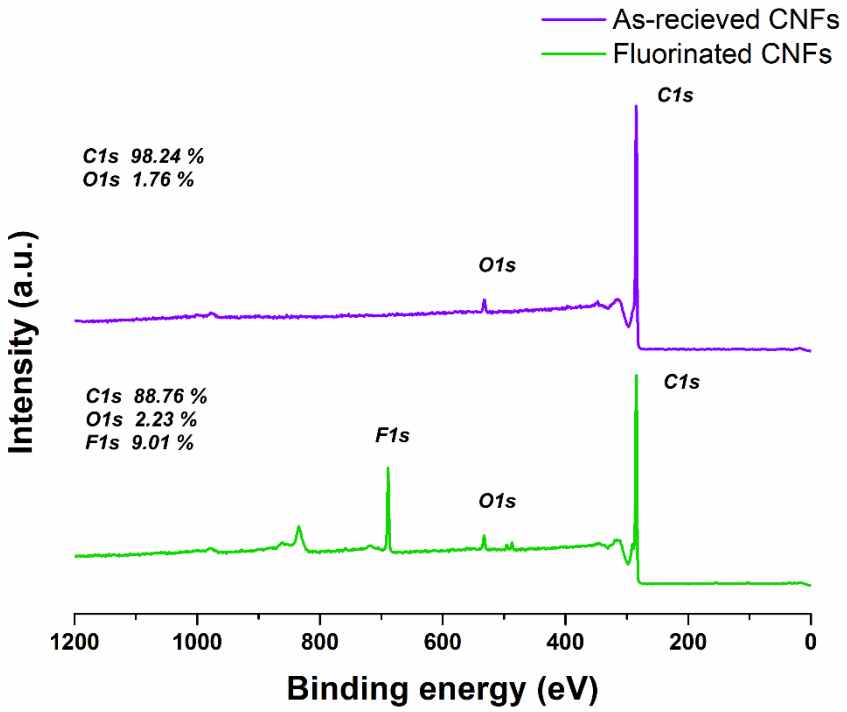

Figure A3: XPS wide scan comparison of as-received CNFs and fluorinated-CNFs, and the corresponding elemental compositions.

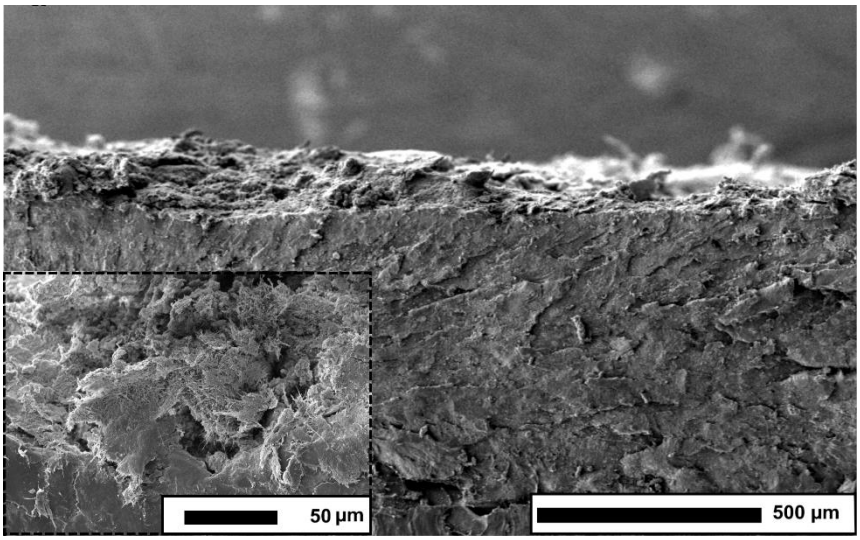

Figure A4: Cross-sectional SEM micrograph of **0.5**-SiO_2-HDPE at low magnification (obtained by fracturing samples after immersion in liquid nitrogen). Inset; high magnification image highlighting CNFs positioned deeper within the surface (obtained by fracturing samples after immersion in liquid nitrogen). Scale bars are shown.

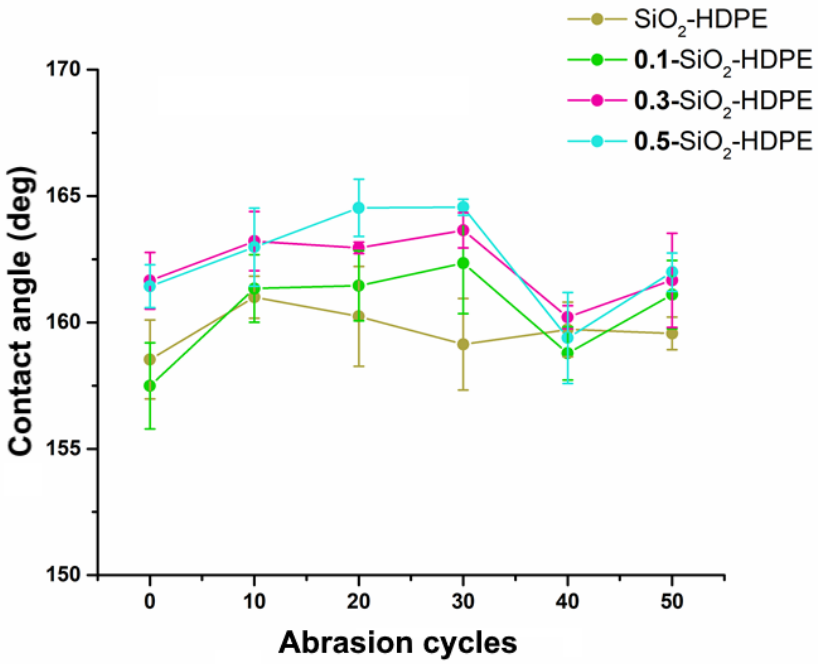

Figure A5: Preliminary abrasion results showing the change in static contact angle for all weighted coatings, fabricated using a dried formulation content of [0.3 g composite/4 mL xylene], after 50 abrasion cycles (100 g weight, P120 Al_2O_3 sandpaper).

Table A1: Recorded contact angles for coatings fabricated from slurries with dried formulation contents which vary between 0.2-0.4 g/4 mL xylene:

Dried formulation content	*CNF content*	*Initial static contact angle*	*Recorded static contact angle after 50 abrasive wear cycles*
0.2 g/4 mL	**0.1**-SiO_2-HDPE	161° ± 3	143° ± 14
0.2 g/4 mL	**0.3**-SiO_2-HDPE	159° ± 2	147° ± 12
0.2 g/4 mL	**0.5**-SiO_2-HDPE	158° ± 1	146° ± 23
0.3 g/4 mL	**0.1**-SiO_2-HDPE	160° ± 2	145° ± 22
0.3 g/4 mL	**0.3**-SiO_2-HDPE	159° ± 3	154° ± 3
0.3 g/4 mL	**0.5**-SiO_2-HDPE	157° ± 2	158° ± 5
0.4 g/4 mL	**0.1**-SiO_2-HDPE	162° ± 2	138° ± 29
0.4 g/4 mL	**0.3**-SiO_2-HDPE	161° ± 2	152° ± 10
0.4 g/4 mL	**0.5**-SiO_2-HDPE	161° ± 2	153° ± 11

A.4 Chapter 5 Appendix

Table A1: Mass data for solubility testing of PER_50, PER_60 and PER_70 in chloroform, toluene and THF (100 mg/5 mL).

Sample	*Initial Mass PER*	*Initial vial+stirrer bar mass*	*Initial filtrate vial mass*	*Filtrate vial and filtered PER mass*	*Recovered PER mass*
Sample Set 1					
50 PER CHCl3	0.1012	11.8975	10.549	10.6496	0.1006
50 PER Tol	0.101	11.9621	10.748	10.8468	0.0988
50 PER THF	0.1019	11.9695	10.444	10.5428	0.0988
60 PER CHCl3	0.1005	12.0737	10.7287	10.8278	0.0991
60 PER Tol	0.1007	12.0293	10.5328	10.616	0.0832
60 PER THF	0.1022	12.1319	10.4555	10.5556	0.1001
70 PER CHCl3	0.1014	12.0843	10.8242	10.9226	0.0984
70 PER Tol	0.1004	11.9656	10.4968	10.5675	0.0707
70 PER THF	0.1008	12.0304	10.5173	10.6103	0.093
80 PER CHCl3	0.1013	11.8969	10.4527	10.5418	0.0891
80 PER Tol	0.1006	12.0203	10.6865	10.7485	0.062
80 PER THF	0.1009	12.0218	10.4951	10.5857	0.0906
90 PER CHCl3	0.102	11.9446	10.437	10.5182	0.0812
90 PER Tol	0.1011	12.1079	10.4338	10.5075	0.0737
90 PER THF	0.1008	12.0007	10.5558	10.6273	0.0715
Sample Set 2					
50 PER CHCl3	0.101	12.2278	10.8084	10.907	0.0986
50 PER Tol	0.1018	11.867	10.7645	10.8641	0.0996
50 PER THF	0.1025	11.7417	10.4685	10.5602	0.0917
60 PER CHCl3	0.1009	12.0247	10.7403	10.8383	0.098
60 PER Tol	0.1011	12.0657	10.8235	10.9119	0.0884
60 PER THF	0.101	11.756	10.6935	10.7874	0.0939
70 PER CHCl3	0.1009	12.0311	10.7438	10.8425	0.0987
70 PER Tol	0.1008	12.1612	10.6726	10.7473	0.0747
70 PER THF	0.1015	12.1273	10.5528	10.6415	0.0887
80 PER CHCl3	0.1008	12.1263	10.8001	10.8911	0.091
80 PER Tol	0.1021	12.0093	10.7596	10.8216	0.062
80 PER THF	0.1008	12.1498	10.7544	10.8369	0.0825
90 PER CHCl3	0.1022	12.1666	10.7112	10.7913	0.0801
90 PER Tol	0.1023	11.7782	10.5144	10.5886	0.0742
90 PER THF	0.1019	12.0321	10.7024	10.7678	0.0654
Sample Set 3					
50 PER CHCl3	0.1002	11.8904	10.7411	10.8353	0.0942
50 PER Tol	0.1002	12.145	10.7431	10.84	0.0969
50 PER THF	0.1025	11.7205	10.8162	10.9143	0.0981
60 PER CHCl3	0.1011	12.0269	10.4698	10.5635	0.0937
60 PER Tol	0.1015	12.1711	10.7326	10.8193	0.0867
60 PER THF	0.1021	12.0877	10.8774	10.9734	0.096
70 PER CHCl3	0.1022	12.0241	10.7051	10.799	0.0939
70 PER Tol	0.1013	11.8325	10.7583	10.8385	0.0802
70 PER THF	0.1006	12.0103	10.9054	11.003	0.0976
80 PER CHCl3	0.102	12.0834	10.5607	10.6434	0.0827
80 PER Tol	0.1014	12.0699	10.7374	10.799	0.0616
80 PER THF	0.1025	12.0552	10.4422	10.5358	0.0936

90 PER CHCl3	0.1017	11.8825	10.6923	10.768	0.0757
90 PER Tol	0.1017	11.9875	10.7042	10.7752	0.071
90 PER THF	0.1016	11.7628	10.7312	10.8074	0.0762